Vegetation, topography and snow melt at the Forest-Tundra Ecotone in arctic Europe: a study using synthetic aperture radar

Dean, Andrew Mark

Vegetation, Topography and Snow Melt at the Forest-Tundra Ecotone in Arctic Europe: a Study using Synthetic Aperture Radar

by

Andrew Mark Dean

School of Biological and Biomedical Sciences

University of Durham

2003

Submitted in partial fulfilment of the requirements for the degree of

Doctor of Philosophy

"The incessant beep of the Global Positioning System is all the companionship I need"

Rory B. Bellows

a.k.a. Krusty the Clown

Declaration

The material contained within this thesis has not been submitted for a degree at the University of Durham or at any other university. The research reported in this thesis is the work of the author unless indicated otherwise.

Vegetation, Topography and Snow Melt at the Forest-Tundra Ecotone in Arctic Europe: a Study using Synthetic Aperture Radar

PhD Thesis Abstract

Andrew Mark Dean, 2003

This research was conducted as part of DART (Dynamic Response of the Forest-Tundra Ecotone to Environmental Change), a four year (1998-2002) European Commission – funded international programme of research addressing the potential dynamic response of the (mountain birch) forest-tundra ecotone to environmental change. Satellite remote sensing was used to map landscape scale (10^1-10^3 m) patterns of vegetation and spatial dynamics of snow melt at the forest-tundra ecotone at three sites along *ca.* an 8° latitudinal gradient in the Fennoscandian mountain range.

Vegetation at the forest-tundra ecotone was mapped using visible –near infrared (VIR) satellite imagery, with class definition dependent on the timing of the acquisition of imagery (related to highly dynamic vegetation phenology) and spatial variation in the FTE. Multi-temporal spaceborne ERS-2 synthetic aperture radar (SAR) was used for mapping snow melt. Comprehensive field measurements of snow properties and meteorological data combined with a physically based snow backscatter model indicated potential for mapping wet snow cover at each site. Significant temporal backscatter signatures enabled a classification algorithm to be developed to map the pattern of snow melt across the forest-tundra ecotone. However, diurnal and seasonal melt-freeze effects relative to the timing of ERS-2 SAR image acquisition effectively reduce the temporal resolution of data. Further, the study sites with large topographic variation and complex vegetative cover, provided a challenging operating environment and problems were identified with the robustness of classification during the later stages of snow melt because of the effects of vegetation. Significant associations were identified between vegetation, topography, and snow melt despite limitations in the snow mapping.

Acknowledgements

I would like to thank my departmental supervisors, Dr Chris Thomas and Professor Brian Huntley, for providing the opportunity to complete this research. They have given me support and productive advice throughout.

I am indebted to Ian Brown for invaluable assistance and encouragement in the face of adversity. I would also like to acknowledge members of the DART project for their interest in this part of the project and their humour.

Also, in no particular order, thanks to Stuart Wain, Mick Green, Matthias Zielke, Maria Johansson, Clare McSorely, Sean Twiss, Judy Allen, Bob Baxter, and Nick Baker, Ruth Cox, Dave Bryant, and John Bennie.

Thanks to Mum, Dad, and Alison who have always been so supportive. Especially, thanks to Gill for her wonderful love, support and patience.

Table of contents

List of figures

List of tables

Chapter 1. Introduction

In the north of Scandinavia, the treeline, the limit to which trees can grow, is generally formed by mountain birch (*Betula pubescens* ssp. *tortuosa*). The forest-tundra ecotone is the zone between the limits of continuous forest and the treeline. Beyond the treeline, vegetation is predominantly dwarf shrubs, herbs and mosses and can be loosely termed tundra. The latitudinal treeline is an exceptionally important transition zone in terms of global vegetation, climate, biodiversity and human settlement (Callaghan *et al.*, 2002a).

The third assessment of the Intergovernmental Panel on Climate Change (IPCC) reports that globally averaged surface temperature is projected to increase by 1.4 to 5.8 °C over the period 1990 to 2100[1] (Houghton *et al.*, 2001). The character of predicted future climate change is, however, distinctly non-uniform with maximum warming in high latitudes of the Northern Hemisphere (Cubasch *et al.*, 2001). Globally averaged water vapour, evaporation and precipitation are projected to increase. Results from recent Atmosphere-Ocean General Circulation Model (AOGCM) simulations indicate that it is likely that mean precipitation will increase in both summer and winter over high-latitude regions (Houghton *et al.*, 2001), although the European Arctic may have lower summer precipitation (Cubasch, 2001). Current climate trends are such that global average surface temperature has increased by 0.6 ± 0.2 °C since the late 19th century (Houghton *et al.*, 2001). Recently an increase of photosynthetic activity of terrestrial vegetation was observed from 1981 to 1991 using satellite data, with the greatest increase in the Arctic regions (Myneni *et al.*, 1997); this is interpreted as a consequence of an early disappearance of snow cover and subsequent increased temperature (Groisman *et al.*, 1994).

The feedbacks between the climate system and vegetation in high latitude regions are substantial. We know that the latitudinal treeline has been sensitive to climate changes in the past with, for example, forest expansion during a Holocene episode of climate warming that occurred between 5,000 and 4,000 years ago (Macdonald *et al.*, 1993). In the Abisko area of the Swedish Arctic, Barnekow (1999) found macrofossils of mountain birch 300-400 m above the present treeline and a pronounced expansion of Scots pine (*Pinus sylvestris*) above its present limit around 5500 B.P. It is precisely

[1] Based on a number of climate models and 35 emission scenarios.

because of this sensitivity to climate influence that reconstructions of past changes in treeline have been used to make inferences about past climates (Payette *et al.*, 1989).

Most global and regional models of vegetation redistribution resulting from global climate change suggest that an advance of the boreal forest will displace a major part of the tundra. Kaplan (2001) developed a state-of-the-art equilibrium vegetation distribution model, BIOME4, which includes several Arctic plant functional types (PFTs). Compared to the present day, the potentially forested area of the Arctic increased substantially for an increased greenhouse gas scenario[2] for 2100; tundra was correspondingly reduced. The simulated tree line was farther north than in any of the mid-Holocene simulations, and the treeline was shown to advance relative to the present in all areas. Latitudinal shifts in the location of the forest-tundra ecotone will have significant effects on carbon cycling, trace-gas exchange, and water/energy balances. The primary control of energy balance at the surface is albedo and the contrast in surface albedo between tundra vegetation and forest is considerable; it is greatest in the winter, when the tundra is snow covered but the trees of the forest protrude above the snowpack (Harding *et al.*, 2002). Earlier disappearance of snow from the tundra and a decrease in albedo of new areas of forest will cause massive changes in the energy fluxes at the surface and a positive feedback resulting in significant heating of the lower atmosphere (Harding *et al.*, 2002). However, this process might be offset by an increase in carbon sequestration and surface hydrological changes that reduce methane emissions.

The forests and tundra of northern Scandinavia are home to the Sámi people who depend for their livelihood on large herds of semi-domesticated reindeer (*Rangifer tarandus*), which migrate between summer tundra and winter forest grazing pastures. A shift in the location of the forest-tundra ecotone will also have significant impact on the livelihood of these indigenous people.

1.1 Context of research: DART project

This research was conducted as part of the DART project (Dynamic Response of the Forest-tundra Ecotone to Environmental change) (Huntley, 2003), which was funded by the European Commission as part of the Environment and Climate Programme of the

[2] An exponential "business as usual" scenario (IS92a).

4th Framework. The project commenced in April 1998 and ended in December 2002 and this research comprises Work Package 2. DART was an international programme of scientific research that aimed to increase our understanding of ecosystem dynamics at the forest–tundra ecotone in northern Europe and, in particular, to quantify the dynamics of the response of this ecotone to environmental change. A key component of the DART project was to assess the interaction between vegetation at the forest-tundra ecotone and snow-melt dynamics.

1.2 Delineation of the forest-tundra ecotone

Spatial scale is inherently involved in recognising spatial patterns on the landscape and in estimating the relationships between landscape components and environmental (and social) processes driving those patterns (Walsh *et al.*, 1999). At small scales (10^3-10^4 m) the forest-tundra ecotone is generalised as a linear boundary. At such scales, location of the treeline is controlled by macroclimate, as demonstrated by the strong inverse relationship between tree limit of the southern Swedish Scandes and shortest distance to the sea (Kjällgren and Kullman, 1998). At landscape scale (10^1-10^3 m) significant spatial variation is revealed with, for example, trees commonly following river courses and abrupt reversals of the sequence of treeline components along elevation gradients (Rees *et al.*, 2002; Walsh *et al.*, 1994). At landscape-scale, distribution of snow is perhaps the single most important variable controlling biological systems in arctic ecosystems (Walker *et al.*, 1993; Walker *et al.*, 1999). Depth and duration of snow cover are consequences of interactions between landscape-scale variability in topography, climate and vegetation. Causal relationships, however, are uncertain because the nature of the vegetation itself influences the distribution of the snow cover (Schaefer and Messier, 1995). Snow persistence has a wide variety of ecosystem influences, including effects on length of the plant growing season, soil moisture, soil chemistry, soil temperatures, depth of freezing and heat flux (Walker, 2000). Persistent snow may limit the plant growing season but, depending upon the timing, late snow melt may function as a beneficial moisture reservoir offering protection from climatic stresses, particularly wind desiccation.

1.3 Utility of remote sensing for monitoring Arctic ecosystems

The utility of remote sensing for monitoring and classification of vegetation at a range of spatial (and temporal) scales is well known. Much of the Arctic is remote and

accessible only with difficulty, remote sensing from spaceborne platforms is, therefore, likely to play a significant role in determining the dynamic of the forest-tundra boundary (Callaghan *et al.*, 2002a). Requirements for regional or global mapping are likely to limit resolution to 30 to 100 m, which precludes the identification of individual trees (Rees *et al.*, 2002). Consequently, the emphasis is on the spatial pattern of change in cover and density of trees (Callaghan *et al.*, 2002b).

Snow cover is one of the easiest types of land cover to distinguish in visible and near-infrared (VIR) imagery (Rees and Steel, 2001), although the latter suffers from several limitations: (1) Inoperability through cloud and at night; (2) Incompatibility between the temporal resolution required to reduce problems of cloud cover and the spatial resolution compatible with topographic variation in mountainous regions; (3) Inability to monitor snow cover beneath a forest canopy; and (4) Inability to distinguish different types of snow cover, especially the discrimination of wet and dry snow. As an alternative, space-borne synthetic aperture radar (SAR) with independence of cloud cover and solar illumination, and especially given sensitivity to liquid water content, offers an attractive alternative (Kasischke *et al.*, 1997).

1.4 Research aims

The aims of this research can be summarised as follows:

1. Use suitable remote sensing techniques to identify the location and landscape-scale spatial patterns of the forest-tundra ecotone in Arctic Europe at.
2. Evaluate the capability of synthetic aperture radar (SAR) to map landscape-scale snow melt dynamics at the forest-tundra ecotone in Arctic Europe.
3. Identify the correlation between location of the forest tundra ecotone and aspects of the physical environment, particularly the pattern of snow melt.

1.5 Thesis structure

Following this short introduction, this thesis is structured into a number of discrete chapters. Chapter 2 provides an introduction to research concerning snow-vegetation interaction at the forest tundra ecotone and a comprehensive review of ecological applications of SAR, in particular for snow monitoring. Chapter 3 introduces the study sites, field measurements, and the VIR and SAR remotely sensed data, which were a necessary prerequisite for this research.

The methods of processing the VIR imagery are given in a relatively short chapter 4. Following this, chapter 5 presents the SAR image processing methods required to conform the ERS-2 SAR imagery into map geometry for integration within a GIS and details of the radiometric correction of the SAR imagery. The results of the vegetation classification using VIR imagery at each site are presented in chapter 6 and in chapter 7 the results of the field measurements collected to monitor evolution of snow melt across the forest-tundra ecotone are presented. A simple snow backscatter model, which has been commonly applied in applications of SAR for snow cover monitoring, is used chapter 8 along with field measurements to investigate the nature of radar interaction the snow covered ground. Changes in SAR backscatter in relation to the change in snow properties are reported in chapter 9 and this leads to the development of a snow-mapping algorithm in chapter 10. Subsequently, chapter 11 undertakes analysis of the evolution of snow melt within biophysical zones related to topography and vegetation. The final chapter is a general discussion of research findings and discusses priorities for future research.

Chapter 2. Literature review

This chapter presents a review of important literature in the context of this research. Firstly, research into interaction between snow and vegetation, focused at the forest-tundra ecotone, is reviewed. Following this, an extensive review of radar remote sensing is undertaken, which introduces the fundamentals of radar imaging and some ecological applications of radar remote sensing with emphasis on the utility of radar for snow and forestry applications.

2.1 Snow-vegetation interaction

2.1.1 Snow-vegetation interaction

Snow cover influences plant distribution and abundance both directly and indirectly by affecting establishment, growth, reproduction and phenology of plants (Heegaard, 2002). By limiting the length of the growing season, snow indirectly controls the distribution of many plant species (Billings and Bliss, 1959; Kudo, 1991; Walker *et al.*, 1993). Snow distribution can prevent tree establishment (Billings and Bliss, 1959), but, conversely, wind exposed sites that are snow-free have extremely low winter soil temperatures and high moisture stress (Billings and Bliss, 1959; Walker *et al.*, 1993). Therefore, a late-lying snowpack may offer beneficial protection, being a valuable moisture reservoir and also a potentially large source of nitrogen for supporting plant growth (Bowman, 1992).

Several studies have combined measurements with manipulations of seasonal distribution of snow cover and temperature at plot scales (<10 m^2). Snow fences have long been used to manipulate the amount of snow distributed by wind in open environments (Daly, 1984), but experiments at the Arctic forest tundra ecotone have been more limited. Considerable plasticity in growth and phenology of Alpine and Arctic plants in response to the manipulated snow and temperature has been recorded (Galen and Stanton, 1995; Walker *et al.*, 1999) and Walker *et al.* (1999) reported the death of the dominant tundra species within three years of a manipulated shortened growing season. The DART project, focusing on Arctic Europe, has conducted experiments to modify the rate at which the snow melts, extending or decreasing the period of snow cover (Huntley, 2003). This includes erecting artificial canopies of dead birch trees to examine how the canopy alters snow accumulation and melting.

Preliminary results suggest that the "fake forest" favourably increased temperature as a result of lower albedo of the forest microclimate, accelerating phenology of birch saplings in spring and early summer (Molau, *pers. comm.*).

2.1.2 Scale dependence

Vegetation at the forest tundra ecotone exhibits hierarchically-scaled spatial heterogeneity, with plant community mosaics at landscape scales and variation in the predominant mosaic elements at regional to Pan-Arctic scales; this heterogeneity reflects hierarchically-scaled spatial and temporal environmental heterogeneity (Baxter, *pers. comm.*). Spatial patterns in the landscape may be discernable only at certain measurement scales and ranges of measurement scales; landscapes appear homogeneous at some scales but heterogeneous at others (Walsh *et al.*, 1999). Therefore, defining an appropriate measurement scale is particularly important, because we must capture the natural spatial variability at an appropriate scale given the processes we wish to study.

The term scale refers to a characteristic length or time (Blöschl, 1999). It is useful to define: (1) process scale, which refers to the spatial dimension of natural variability; (2) measurement scale, which relates to the spatial dimension of a measurement structure; and (3) model scale that relates to the spatial dimension of a model (Blöschl, 1999). Measurements can be undertaken at various scales, depending on the generality with which we wish to model the ecological processes under examination (Chapin III *et al.*, 1996). For example, if a snow pack is investigated in great detail, the spatial variation of the hydrologic environment means that the numbers of possible flow paths for melt water or gas exchange is enormous (Blöschl, 1999). A coarser measurement scale may make the patterns of snow melt more predictable by averaging out spatial variation and decreasing noise (Wiens, 1989).

With remote sensing, the measurement scale is defined by the spacing, extent, and resolution of the imagery: Spacing is equal to the pixel size; the extent is effectively the swath width; and the resolution is the ability of a sensor to distinguish two closely spaced objects or lines as two rather than one object or line. Alternately, it is the smallest object or narrowest line a sensor can detect. Remotely sensed data may appear complex because of the scale of natural variation relative to the resolution, noise, and sheer volume of information. Inherently related to the spatial scale achievable with space-borne remote sensing is the frequency with which observations can be made, or

the temporal resolution. The average time between successive opportunities to observe a specific location is roughly inversely proportional to the swath width (Rees *et al.*, 2002). If we are to adequately capture landscape-scale variation in snow melt patterns in relation to the structure of the vegetation at the forest tundra ecotone, data on snow cover are required at relatively high temporal and spatial scales over relatively large areas. Remote sensing is the only reasonable method for such data collection and a discussion of available remote sensing technologies is undertaken in section 2.1.3 and 2.1.4 and from section 2.2 onwards.

2.1.3 Mapping vegetation at the forest-tundra ecotone using VIR imagery

Remote sensed data have been used in a number of classification schemes at landscape, regional and global scales (Townshend *et al.*, 1991). There has been an increasing demand for remote-sensed data products for use within regional and global ecosystem models and it is recognized that many vegetation classifications are no longer an end product, but a source of initialising data for ecological modelling (Nemani and Running, 1996). Observation of vegetation assemblages provides a challenge if classification products are to be "scaled-up" and used to initialise or validate regional mechanistic models, which produce proportions of plant functional types (PFTs) for each pixel (e.g. BIOME 3 and 4; see Haxeltine and Prentice (1996); Cramer (2002); Kaplan (2001)).

Techniques to exploit data in the visible near-infrared (VIR) portion of the electromagnetic spectrum are already reasonably well established for the delineation of different Arctic vegetation types, although these techniques do generally require the input of field data (Frank, 1988; Rees *et al.*, 2002). Chapin III *et al.* {, 1996 #112} and Walker {, 2000 #147} proposed a hierarchical classification of Arctic PFTs that should be readily detectable using satellite imagery. This includes the discrimination of forest and non-forest types, and shrubs, herbs, and non-vascular PFTs. However, many classification products suffer a lack of generality because of the classes selected and uncertainty regarding their statistical characterization. Therefore, a classification may require detailed ancillary information to resolve classes for comparative studies or another application. It is important to be realistic in terms of class definition given the spatial and spectral resolution of current earth orbiting satellites; number of classes should be restricted to those with potential to have a unique spectral and/or temporal signature. Class definition is also likely to depend on timing of the acquisition of

imagery (related to solar illumination and vegetation phenology) and scale of spatial variation in the forest-tundra ecotone relative to the resolution of the sensor.

In addition to space-borne techniques, we should also consider the possibilities presented by airborne remote sensing methods (Rees *et al.*, 2002). Ortho-rectified aerial photography may be useful for mapping the forest tundra ecotone at local and regional scales, however, spectral variation amongst photographs and the fact that such products are production intensive in terms of ground control requirements, digitising, and requirement for a high resolution DEM are limitations (Baker *et al.*, 1995). Using Airborne Thematic Mapper (ATM) data, (Foody *et al.*, 1992) demonstrated the potential of using probabilistic measures of class membership from a maximum likelihood classification for modelling a forest-heathland ecotone in the UK. New developments in air-borne remote sensing such as laser height profilers (e.g. LIDAR - Light Detection and Ranging) and use of "fuzzy" classifications offer potential for improved models of the three-dimensional patterns (Callaghan *et al.*, 2002) and density gradient of the forest-tundra ecotone.

2.1.4 Mapping snow cover using VIR imagery

Routine snow survey and snow gauge data provided by meteorological stations establish temporal ground snow cover conditions but they lack a spatial dimension. Reliable spatial information can only reasonably be acquired through remote sensing, with VIR and active and passive microwave systems having considerable potential. Snow cover is one of the easiest types of land cover to distinguish in VIR imagery because snow has a very high albedo throughout the visible wavelengths, unless the surface has acquired a covering of dust (Rees and Steel, 2001a). Historically, the only serious problem was with snow/cloud discrimination; in the visible and thermal infrared wavelengths snow and clouds have similar reflected and emitted longwave terrestrial radiance. Discrimination between snow and cloud can be achieved using observations in the near infrared where the albedo of snow cover is comparatively very low. For example, Dozier (1984) used band 5 (1.55 – 1.75 μm) of Landsat Thematic Mapper (TM), which has a spatial resolution of 30 m, to distinguish snow from cloud. Similarly, the new band 3a (1.58 – 1.64 μm) of AVHRR/3 (Advanced Very High Resolution Radiometer) onboard NOAA-17 facilitates snow discrimination, but has a resolution at nadir of 1.09 km (NOAA, 2002). MODIS (Moderate Resolution Imaging Spectroradiometer), onboard the Earth Observing System (EOS) Terra and Aqua satellites, acquires data in

36 spectral bands with high radiometric sensitivity, including band 6 (1.628 – 1.652 μm) with a spatial resolution of 500 m.

Data from relatively low spatial resolution sensors such as AVHRR are routinely used for national, regional and hemispheric scale snow mapping. Since the launch of the EOS satellites in 1999, daily snow cover mapping for the Northern Hemisphere has been performed automatically at a spatial resolution of 500 m, cloud-cover permitting, using MODIS data (Hall *et al.*, 2001). Lucas and Harrison (1994) discussed the potential application of AVHRR data for improving or replacing the UK's National Snow Survey. Landsat TM data, with the 30 m resolution that is comparable to the scale of topographic relief in many alpine regions, are routinely applied to monitoring snow cover on drainage basin scales. Indeed, the Normalized Difference Snow Index (NDSI) using TM bands 2 and 5 has been developed for monitoring and mapping of snow/ice cover (Dozier and Marks, 1987; Walsh *et al.*, 1994; Winther and Hall, 1999).

VIR sensors, however, suffer from several disadvantages that can be considered to preclude their operational use: (1) inoperability through cloud and inoperability at night; (2) incompatibility between the temporal resolution required to reduce problems of cloud cover and the spatial resolution compatible with topographic variation in mountainous regions; (3) inability to monitor snow cover beneath a forest canopy, because the received radiation will be mixed from the snow cover and the vegetation; and (4) inability to distinguish different types of snow cover, especially the discrimination of wet and dry snow. VIR methods can provide limited information on snow wetness, because the albedo of a wet snowpack is reduced, but this approach is very difficult to apply (Rees and Steel, 2001a). These problems have prompted interest in alternative space-borne methods for snow monitoring, and in particular synthetic aperture radar (SAR) systems, which are discussed in section 2.3 – 2.5.

2.1.5 Landscape scale modelling of snow-vegetation interaction at the forest-tundra ecotone

Predictive spatial modelling of vegetation is founded in ecological niche theory and environmental gradient analysis (Franklin, 1995). Models are generally based on hypotheses as to how environmental variables, or gradients, control the distribution of species and communities. There have been various attempts to model snow-vegetation interaction and vegetation responses and feedbacks to climate. Levens (1966)

formulated the principle that only two out of three model properties, generality, reality, and precision can be improved simultaneously, while the third property has to be sacrificed. This leads to a distinction of three different groups of model; analytical, empirical, and mechanistic, the choice of which has an implication for the research task.

Analytical models focus on generality and precision, and are designed to predict accurate response with simplified reality (e.g. Lokta-Volterra models: see Gillman and Hails (1997)). Empirical or statistical models forfeit generality for precision and reality. It is not possible to determine physiological cause and effect with such models, although some description of functional relationships can be achieved (Austin, 2002); their main purpose is to condense empirical facts (Wisel, 1992). Empirical techniques are static, in the sense that they consider vegetation to be in equilibrium with climate (Gottfried *et al.*, 1998). They also model the realised rather than fundamental niche due to their intrinsic empirical nature and implicitly incorporate biotic interactions and negative stochastic effects that can change from one area to another (Guisan *et al.*, 2002; Guisan and Zimmermann, 2000). Consequently, application of empirical models in different regions and at different spatial scales is limited.

Process-based or mechanistic models are based on cause-effect relationships that are biologically functional (Woodward, 1987), and are therefore considered to be realistic and general. Mechanistic models parameterise the fundamental niche and may also implement rules of competitive behaviour to predict the realized niche. Biotic relationships are likely to change over time, as demonstrated through paleoecological evidence (Huntley and Webb, 1988), and modelling the fundamental niche enables prediction of response to changing environmental conditions.

Franklin (1995) makes an important distinction between three types of environmental gradient used within predictive habitat models; resource, direct, and indirect gradients. Resource gradients refer to matter and energy consumed by plants for growth (e.g. light, water). Direct gradients include those having direct physiological impact but not consumed by plants (e.g. temperature, pH). Indirect gradients (e.g. slope and aspect) have no direct physiological influence on plant growth, and relationships with vegetation are likely to be location-specific. From a mechanistic point of view (to improve model generality), it is desirable to predict species or community distribution on the basis of resource or direct gradients, those ecological parameters that are believed

to be the causal factors for their distribution and abundance (Guisan and Zimmermann, 2000). The use of indirect gradients to replace a combination of resource and direct gradients means that a model can only be applied within a limited geographical extent without significant errors, because, for example, in a different region the same topographic gradients can reveal different resource and direct gradients. However, because of topographic controls on microclimate, direct bioclimatic parameters are often developed from spatial interpolations of climate station data based on topography (Daly *et al.*, 1994; Garen *et al.*, 1994), which introduces spatial uncertainties into microclimates because of interpolation errors and lack of sufficient data collecting stations (Joyce, 2000). In such circumstances, the use of indirect variables may produce better predictions.

In a modelling process, some sort of conceptual or theoretical model should already be proposed (Austin, 2002). A very simple conceptual model is given in figure 2.1, which illustrates that snow-vegetation associations are likely to be due to their mutual relationships with topography. It is difficult to address questions of causality with empirical approaches; causal mechanisms must be pursued by experiment or process-based modelling.

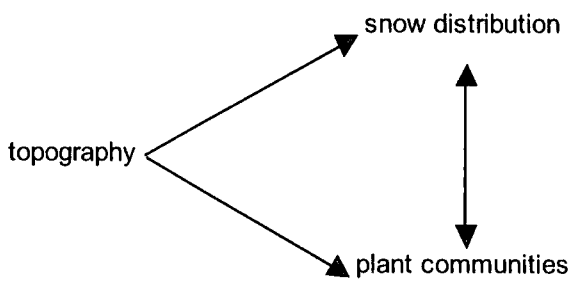

Figure 2.1. Simple conceptual model showing the interrelationship between snow, vegetation and topography.

Empirical modelling techniques have frequently been employed at landscape scales to correlate vegetation at the forest-tundra ecotone with environmental gradients, including snow melt. Many analyses are implemented within geographical information systems (GIS) and frequently utilise a digital elevation model (DEM) and data obtained from using remote sensing. Environmental gradients derived from DEMs are particularly important at landscape scales because of the importance of topography in determining important environmental gradients at such scales.

Landsat TM –derived snow maps and indirect gradients such as elevation and aspect have be used to assess the relationship between topography, snow melt (Allen and Walsh, 1993), snow avalanche (Walsh *et al.*, 1994) and the spatial composition of the Alpine forest-tundra ecotone in Glacier National park, Montana. In these studies, distinct differences in snow melt patterns relative to topography and Alpine vegetation were observed. Brown (1994) used several environmental gradients in statistical modelling (logistic regression) to predict vegetation type at treeline in Glacier National Park. The gradients included elevation and others derived from a DEM, including potential soil moisture, potential solar radiation, and potential snow accumulation; however, the model explained little of the spatial variation in vegetation types. A high resolution DEM (1 m) was used by Gottfried *et al.* (1998) to derive indirect gradients including measures of topographic roughness and curvature. The empirical model explained a significant amount of variability in plant communities and was successfully related to elevation and moisture gradients. Ostendorf and Reynolds (1998) found similar correlation with soil moisture, modelling tundra vegetation in relation to slope as a function of upslope area.

Tappeiner *et al.* (2001) aimed to model daily snow cover patterns using daily terrestrial photographic remote sensing and elevation-derived gradients and a coarse vegetation classification (forested/non-forested). In addition, a direct temperature gradient was incorporated (number of days with temperature <0 °C) regressed using elevation. An artificial neural network (ANN) modelling approach was used, which allows for non-linearity in relationships and requires no assumptions about the functional interrelations between variables. The results indicated that using topographic variables, a significant amount of spatial variation in snow cover could be explained by the model.

The relationship between snow and vegetation at the forest-tundra ecotone is usually studied at a single spatial scale of enquiry (Walker *et al.*, 1993). An exception is a study by Schaefer and Messier (1995) who examined multi-scale correlations between snow cover and tundra vegetation on Victoria Island, Arctic Canada. Scale was modified by altering the size of the sampling unit; correlation between single species and thickness of snow typically increased with a more generalised scale of analysis because of decreasing noise and averaging of spatial variation. The fact that results of statistical analyses vary according to scale is now well known (Flowerdew *et al.*, 2001). When

investigating the relationships between environmental gradients and vegetation, we must question what spatial scale is appropriate and, if necessary, the nature of a sampling scheme and the number of samples.

2.2 Synthetic Aperture Radar remote sensing

Ecologists are aware of the utility of remote sensing for studying ecological processes at a range of spatial and temporal scales. In particular, the synoptic perspective, regular and frequent coverage, and cost of remotely sensed data from space-borne sensors combine to form an attractive basis for many ecological applications. As discussed in section 2.1.3 and 2.1.4 in the context of mapping snow and vegetation at the forest-tundra ecotone, a wide range of approaches has been developed to exploit remotely sensed data collected in the VIR region of the electromagnetic spectrum (Kasischke *et al.*, 1997).

SAR systems operate in the microwave portion of the electromagnetic spectrum (approximately 1 mm to 1 m wavelength; 300 to 0.3 GHz frequency). They are active systems, transmitting microwave energy pulses and receiving the reflected energy back to a sensor. Radar is capable of penetrating the atmosphere under virtually all conditions, and is not limited by cloud cover or solar illumination, a distinct advantage over VIR sensors. Unlike passive microwave systems, space-borne SAR can achieve high spatial resolutions of around 10 m, and the discussion is primarily limited to active, space-borne SAR systems.

2.2.1 SAR imaging

Unlike most passive remote sensing techniques, SAR necessarily has an oblique view of its target, the radar beam being directed to the side of the platform trajectory. The pulse length and antenna beam width control the resolution of conventional imaging radar. The pulse length is the length of time the microwave pulse is transmitted for, and determines resolution in the range direction. The antenna beam width determines the resolution in the direction of movement of the radar platform, the azimuth direction. The antenna beam width is inversely proportional to length of the antenna, a longer antenna giving a smaller beam width and improved resolution (Lillesand and Kiefer, 1994). A SAR system is able to improve the azimuth resolution over that reasonably possible with a conventional radar system by using the forward motion of the SAR platform to create an array of short antennas through sophisticated signal processing

(Rees, 2001). This processing makes use of the Doppler shift, the decrease in the frequency of the received wave as the sensor passes a target, and requires that both phase and amplitude of the signal. Amplitude (specifically height of an electromagnetic wave) is the conventional information extracted from a radar signal. Radar phase is an additional information source (Gens and Van Genderen, 1996) and concerns the oscillation and advancement of electromagnetic waves relative to an origin. Waves are said to be "in-phase" if their origins of phase are exactly aligned. Knowledge of the phase of microwave data is fundamental to interferometric SAR e.g. Gens and Van Genderen (1996).

The amplitude, or strength, of scattering is usually expressed in terms of the backscatter cross section per unit area (sigma-nought, σ^0). Due to its range σ^0 is usually expressed in decibels:

$$\sigma^0_{dB} = 10 \cdot \log_{10}(\sigma^0) \qquad \textbf{Equation 2.1}$$

The landscape features known to affect SAR backscatter are topography, the dielectric constant of the ground surface, surface roughness and vegetation cover. The effects of landscape properties are related to the nature of SAR imaging and specific SAR system parameters: frequency, polarisation, and imaging geometry.

2.2.2 Frequency / wavelength

Frequency / wavelength is important because a microwave will interact strongly with surface components having a size comparable to that wavelength. Radar band designations for different regions within the microwave portion of the electromagnetic spectrum are given in table 2.1.

Table 2.1. Radar band designations.

Band	Wavelength λ (m)	Frequency (GHz)
Ka	0.0075 - 0.011	40 - 26.5
K	0.011 - 0.0167	26.5 – 18
Ku	0.0167 - 0.024	18 – 12.5
X	0.024 - 0.0375	12.5 – 8
C	0.0375 - 0.075	8 – 4
S	0.075 – 0.15	4 – 2
L	0.15 – 0.30	2 – 1
P	0.30 - 1	1 – 0.3

Source: adapted from (Lillesand and Kiefer, 1994)

A radar image contains different information depending on the wavelength, meaning that a composite of different bands can provide increased information content. A multi-frequency system, which can transmit microwaves of more than one wavelength, is preferable to a single-frequency radar system.

2.2.3 Polarisation

Radar polarization refers to the orientation of the transmitted and received wave, which is normally horizontal (H) or vertical (V) in orbital space-borne SAR systems. A SAR system will commonly transmit and receive either V polarized or H polarized radiation, meaning that there are four possible combinations of transmit/receive polarization; VV, HH, HV, and VH. When the transmitted radiation is in the same polarization of received radiation, the image is said to be like or co –polarized. When the transmitted radiation is the opposite polarization to the received radiation, the image is said to be cross-polarised. A polarimetric SAR is a system capable of measuring a full polarization signature of the ground surface and the change in the degree of polarization (depolarisation) (CCRS, 2002). Ratios of different polarisation measurements do not require radiometric terrain correction (Shi and Dozier, 1997), which is similar to the use of band ratios for VIR imagery.

Polarization of a SAR system needs to be considered in the context of the geometric structure of the object under study. If a surface object has a vertical structure, such as a cereal crop, then vertically polarized microwaves will interact strongly with the crop. Conversely, horizontally polarized energy will not interact with the crop and will scatter

from the ground underneath. Consequently, the different scattering behaviour of like- and cross- polarized radar systems in relation to the characteristics of the ground surface can increase the information content of a resulting image.

2.2.4 Radar geometry

Given the side-looking imaging technique of SAR, σ^0 is subject to variations due to topography; several authors have reported a significant relationship between image backscatter values and geometric parameters derived from topography (Bayer *et al.*, 1991; Domik *et al.*, 1988; Hinse *et al.*, 1988; Rees and Steel, 2001b). The incidence angle, θ, defined by the incident radar beam and the normal to the ground surface, is typically used to describe radar geometry (figure 2.2). The incidence angle changes across the radar image swath, but for space-borne SAR this tends to be small, perhaps in the order of several degrees (Laur *et al.*, 1998). The interaction between the oblique viewing geometry of SAR and changes in topography means that SAR imagery is subject to a number of interrelated geometric and radiometric distortions: foreshortening and range-scale expansion, layover and shadowing, and high and low –lighting.

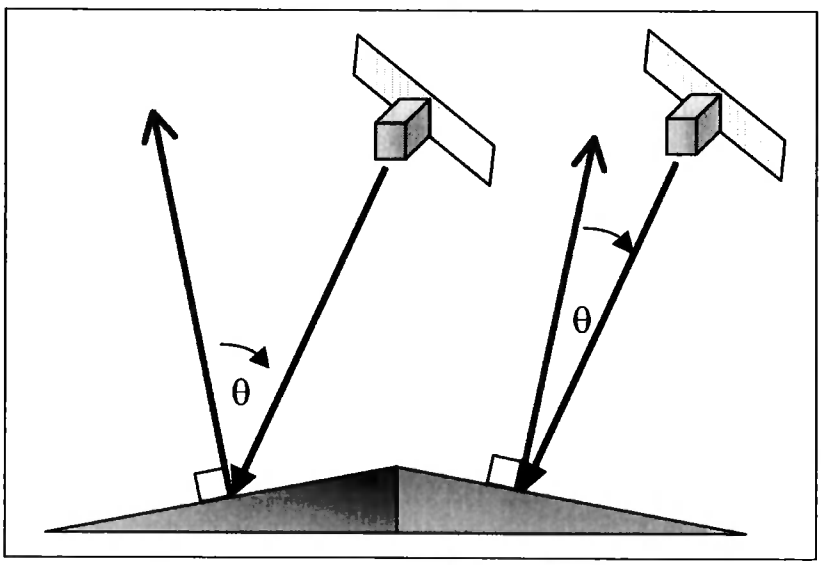

Figure 2.2. Schematic diagram showing (local) incidence angle θ, which is defined by the incident radar beam and the normal to the ground surface.

Foreshortening is a geometric distortion resulting in terrain features that appear to lean towards nadir. It is the result of the range of different targets being similar because of differences in the height of the terrain. This results in compression or foreshortening of the slope surface on the image compared to a flat surface and similarly, a slope facing away from the sensor may be elongated (range-scale expansion). An extreme form of foreshortening that can occur in more mountainous terrain is layover, in which a slope is

so steep that it is imaged in reverse order and parts of the terrain are superimposed in the image. If one part of the terrain prevents the energy of the radar from reaching another, then shadowing will occur, with the consequence that no signal at all can be detected from the shadowed region (Rees and Steel, 2001b). High and low –lighting is a radiometric distortion in which the variation in the strength of backscattering received from surface depends on the slope because an unusually large number of scatterers in the terrain contribute to the backscatter measured for a given pixel (Rees and Steel, 2001b).

In general, we expect that σ^0 should be decrease with increasing incidence angle. Previous studies have investigated empirical and physically based backscatter models to "correct" such topographic effects on backscatter (Bayer *et al.*, 1991; Goering *et al.*, 1995; Goyal *et al.*, 1998; Rees and Steel, 2001a). In the models that have been developed, the variation in backscatter explained by incidence angle depends on the SAR system parameters (frequency, polarisation), the resolution of the topographic data, and land surface characteristics. Such models are evaluated in detail in chapter 8. Local incidence angle also varies depending on the ascending or descending orbit of the (polar-orbiting) satellite platform at the time of acquisition. Combination of ascending and descending scenes has been used to reduce the effects of layover and shadow in mountainous areas (Haefner *et al.*, 1993); however, this assumes that there are no significant differences in land surface attributes between acquisitions.

Incidence angle can have an indirect effect on backscatter because it can, in part, determine the "path length" of the radiation through a surface feature. However, other factors are important in determining the amount of surface scattering and the angle of refraction at a boundary such as a vegetation canopy or snowpack. In general, a SAR with a relatively steep angle will tend to have greater penetration than one that is more oblique from the nadir because of a reduced path length through a surface target.

2.2.5 Speckle

As a consequence of the coherent imaging technique, SAR imagery is subject to an undesirable multiplicative noise called speckle (Rees and Steel, 2001a). Scatter from each target within a pixel is coherently summed for all scatterers. Speckle is produced because backscatter can be either high or low depending on the particular phase relationships between the reflected waves from different parts of the pixel (Wooding,

1995). A process called multi-looking is used to introduce incoherent averaging into the resulting image by taking several independent sub-samples and averaging the resulting backscatter. Applying a spatial filter can reduce speckle further (Shi and Fung, 1994), but this effectively reduces spatial resolution and can reduce the texture information in an image (Collins *et al.*, 2000).

2.2.6 Surface Roughness

Within an imaged pixel, there is small-scale variation in the relief of a terrain surface known as surface roughness. The roughness of a surface can be described by the standard deviation of the surface height, Δh, but this must be considered relative to the wavelength λ of the radar system. The Rayleigh criterion is usually used to classify a surface as smooth or rough (Ulaby *et al.*, 1982):

$$\Delta h < \frac{\lambda}{8\cos\theta} \qquad \textbf{Equation 2.2}$$

The spatial dimension of the irregularities is determined by the surface correlation length l, which is used to quantify the distance beyond which variation is approximately statistically independent. A very smooth surface may produce specular scattering, whereas an ideally rough surface may produce Lambertian scattering (Rees, 2001; Ulaby *et al.*, 1982).

2.2.7 Permittivity

Permittivity affects the amount of radiation reflected and the amount refracted across the interface between air and the lower target or medium. The relative permittivity is also known as the dielectric constant, and is the permittivity of the lower medium *relative* to the permittivity of "free space". If the surface medium absorbs energy from the wave then a complex number must be used to represent the dielectric constant (Rees, 2001). The real part ε' (permittivity) is the measure of how easily the energy passes across the interface, while the imaginary part ε'' (usually referred to as the loss factor) describes how much energy is absorbed by the medium. The complex number is represented as:

$$\varepsilon = \varepsilon' - i\varepsilon'' \qquad \textbf{Equation 2.3}$$

The dielectric constant depends, among other variables, on the water content of a surface medium; the more liquid water in the lower medium the greater the reflection. The Fresnel reflection coefficient is a suitable measure of reflectivity given the

dielectric constant (see Appendix A). Increased liquid water also increases the imaginary part of the dielectric constant.

2.2.8 SAR system development

Several space-borne and airborne SAR systems have been developed throughout the last two decades. Much early research was conducted with the NASA Jet Propulsion Laboratory (JPL) AIRSAR, which is an air-borne, fully polarimetric SAR operating at P-band (0.68 m wavelength), L-band (0.24 m), and C-band (0.056 m). AIRSAR research generally focused on assessing potential applications of future space-borne SAR systems. Seasat, launched by NASA in 1978, was the first civilian space-borne SAR system and was designed to obtain high-resolution imagery of the sea surface and sea ice. Seasat carried an L-band, HH polarised SAR with a resolution of 25 metres. However, it failed after 109 days of operation and, as an experimental mission, there was no replacement.

Further space-borne radar experiments were carried out in the early 1980s onboard the American space shuttles, using SIR –A and –B (Shuttle Imaging Radar). Both SIR experiments carried an L-band SAR with HH polarization. The SIR-B antenna could be tilted to direct signals toward the earth at varying look angles, ranging from 15 to 60°. This allowed the investigation of the impact of varying incidence angles on backscattering returns, and provided the opportunity to acquire stereo radar imagery and imagery at different range resolutions (Lillesand and Kiefer, 1994). The deployment of SIR-C and X-SAR during 1994 enabled evaluation multi-frequency, polarimetric space-borne SAR data. This system comprised a C and L –band fully polarimetric SAR and an X-band SAR that collected HH and VV polarised data (Lillesand and Kiefer, 1994). The ground coverage of the SIR-C/X-SAR experiment was limited because the shuttle orbit limited data collection between 57 °N/S and because of concentration on specific test sites.

Table 2.2. System parameters for space-borne SAR.

Satellite	ERS-1, ERS-2	JERS-1	Radarsat-1	Envisat
Agency	European Space Agency (ESA)	National Space Development Agency of Japan (NASDA)	Canadian Space Agency (CSA)	European Space Agency (ESA)
SAR Instrument	AMI – Active Microwave Instrument			ASAR – Advanced SAR
Period of operation	1991-2000 1995-present	1992-1998	1995-present	2002-present
Wavelength (cm)	5.65	23.5	5.65	5.65
Frequency (GHz)	5.3	1.275	5.3	5.3
Band	C	L	C	C
Polarisation	VV	HH	HH	HH+VV+HV+VH
Incidence angle[1]	23°	40°	20-60°	15 to 45°
Swath width[1]	100 km	75 km	50-500 km	100-400 km
Return Period[1,2]	35 days	44 days	1 to 24 days	35 days
Spatial resolution[1]	30 m	18 m	8-100 m	30-1000 m

Table 2.3. Future space-borne SAR systems.

Satellite	Radarsat-2	ALOS
Agency	CSA	NASDA
SAR Instrument	SAR	PALSAR
Proposed launch	2003	2004
Wavelength (cm)	5.66	23.5
Frequency (GHz)	5.3	1.275
Band	C	L
Polarisation	HH+VV+HV+VH	HH+HV or VV+VH
Incidence angle[1]	10-60°	8-60°
Swath width[1]	10-500 km	40- 350 km
Return Period[2]	1-24 days	46 days
Spatial resolution[1]	3-100 m	7-100 m

[1] Dependent on imaging mode for Radarsat, Envisat and ALOS.

[2] Dependent on latitude and/or acquisition phase for ERS (e.g. ERS-1 Mission Phase B: ice phase with 3 day return period from 28/12/91 to 01/04/92)

These experiments demonstrated that multi-frequency SAR systems with combinations of polarisation offer the greatest potential for characterisation of the earth's surface and vegetation cover, compared with single channel radars alone (Schmullius and Evans, 1997). However, adequate spatial or temporal coverage can only be provided by orbital satellites (Dobson *et al.*, 1995b), which until recently have been limited to a single channel and polarisation. The most significant systems are summarised in table 2.2, with planned systems shown in table 2.3.

The launch of ERS-1 in 1991 heralded a new era in space-borne SAR imaging and since then an enormous amount of imagery has been acquired. Early space-borne SAR instruments were limited to a single frequency and polarisation, and subsequent instruments have been designed to ensure continuity with the early missions, but also to provide enhanced capabilities. ASAR and Radarsat-1 have beam shaping and steerage capabilities, allowing the selection of different swaths and incidence angles. ASAR utilises a ScanSAR technique to acquire two images of the same scene in like and cross –polarisation (ESA, 2002); Radarsat-2 and PALSAR are being developed with these capabilities. As these systems become operational, data collected at different spatial resolutions, polarisations, and frequencies will become available. Envisat also carries a VIR sensor (MERIS – Medium Resolution Imaging Spectrometer), as did JERS-1. ALOS will also carry VIR sensors for collection of data in visible and near infrared wavelengths, although the usefulness for acquiring simultaneous microwave and VIR data is limited because of the coarse resolution of the VIR data (e.g. 300m for MERIS). The highly variable SAR acquisition geometries made available by Radarsat and Envisat have intensified the need for terrain correction of scenes over mountainous terrain. The broadly unchanging geometry of ERS-1 and ERS-2 allowed multi-temporal overlay in radar geometry, whereas "mixed-mode" images require terrain correction before any overlay is possible. However, given the incidence angle of ERS, layover can be a substantial problem in mountainous terrain, whereas shadow is unlikely.

2.2.9 Resolution of Digital Elevation Models for SAR applications

For areas of high topographic variability, the accuracy of geometric and radiometric correction will be influenced by the resolution (and accuracy) of the available DEM. The interaction between the viewing geometry of SAR and topography was discussed in section 2.2.4. SAR imagery is subject to interrelated geometric and radiometric

distortions, which mean that the resolution of topographic data has implications for the quality of both radiometric and geometric correction. A physical process cannot be modelled successfully unless data are available at an appropriate scale and we must recognise that slope, including slope in the direction of the incident radar, is a property of scale. Intuitively, a DEM should at least be of comparable resolution as the SAR imagery, however, the compatibility of DEMs with SAR often varies, perhaps because of the difficulty in obtaining high-resolution data. Over-sampling a DEM to match SAR data is considered unwise (Johnsen *et al.*, 1995). Wivell (1992) rectified a Seasat image using several commonly used DEMs in an area of highly variable terrain. Variation of the horizontal, vertical, and slope resolutions and the presence of artefacts in DEMs were found to cause errors in the radiometric and geometric correction.

Numerous studies have used a DEM and topographic correction functions in order to "normalise topographic" effects. For example, Goyal *et al.* (1998) found a reduction in variance in air-borne SAR backscatter values of the order of 54% using an empirical correction model for a high resolution DEM. However, a coarse resolution DEM significantly reduced the amount of variation in backscatter explained by incidence angle to 36%, which was attributed to the SAR data resolving topographic features not resolved by this DEM (Goyal *et al.*, 1998). Other studies aiming at reductions in variance have found results between 9 and 33% (Bayer *et al.*, 1991; Goering *et al.*, 1995; Hinse *et al.*, 1988), with results clearly dependent on land surface properties; however, the influence of DEM resolution should not be dismissed. In addition to a high resolution DEM, Shi and Dozier (1997) stress the importance of accurate sensor location data in order to determine the angle of the incident radar.

2.3 SAR experiments and ecological applications

Experiments with AIRSAR and the SIR missions have shown the increased value of multi-parameter capabilities to characterise the Earth's surface and vegetation cover, compared with VIR sensors or single channel radars alone (Schmullius and Evans, 1997). Space-borne SAR systems have only recently extended to multi-polarisation capabilities, meaning that multi-temporal imagery and synergy between data from different SAR and VIR systems is often important for the successful application of SAR data (Pohl and van Genderen, 1998). However, space-borne SAR are currently limited to C-band, which is not particularly useful for many ecological applications (Rees *et al.*, 2002).

2.3.1 Land cover classification

Experiments using multi-frequency, multi-polarisation SAR data have demonstrated the potential of SAR for land cover classification and indicated the ideal configurations required for various land cover types. Data from the SIR missions and AIRSAR experiments have been successfully applied for land cover classification (Haack *et al.*, 2000; Way *et al.*, 1994), crop classification (Soares *et al.*, 1997), tropical forest classification (e.g. Nezry *et al.* (1993); Pope *et al.* (1994); Rignot *et al.* (1997)) and boreal and temperate forest classification (e.g. Rignot *et al.* (1994b); Ranson and Sun (1994); Pierce *et al.* (1998)).

One can generalise and suggest two common classification approaches for land cover classification using radar data: (1) statistical approaches, including both supervised and unsupervised clustering algorithms and textural analysis applied to multi-temporal SAR data or SAR data that is combined with VIR data; and (2) knowledge-based techniques, such as empirical or physical backscattering models and hierarchical decision trees. A classification may use a combination of the two methodologies. For example, using JERS data, Saatchi *et al.* (2000) used a supervised statistical classification followed by a rule-based approach on texture measures to discriminate sub-categories of tropical forest vegetation.

Multi-parameter experiments using AIRSAR and SIR-C/X-SAR demonstrated the limitations that the first generation of orbital satellites would have for land cover classification; a single frequency, single polarisation does not represent a suitable data source for land cover classification (Dobson *et al.*, 1995a; Kasischke *et al.*, 1997). The advantage of using a combination polarimetric L and C –band data for vegetation mapping is clear (Schmullius and Evans, 1997). For example, Pierce *et al.* (1998) were able to produce single scene classifications of boreal coniferous and deciduous forest in excess of 90 percent using L and C –bands from SIR-C/X-SAR with combinations of cross and like –polarisations. The addition of X-band (single polarisation) improved overall accuracies to 98 percent. Balzter *et al.* (2002) acquired fully polarimetric L and C –band airborne SAR over a Finnish boreal forest test site and suggest that decomposition of the polarimetric data could provide information on scattering mechanisms in the vegetation canopy and on the ground, being of great value for land cover mapping.

The Global Boreal Forest Mapping (GBFM) Project was initiated by NASDA in 1997 and substantial data was acquired over the boreal zone of Siberia, northern Europe, Canada and Alaska before the operation of the JERS-1 satellite was terminated in October 1998. The aim was to create an inventory of forest cover at 100 m resolution and to distribute image mosaics on compact disc e.g. ASF (2002). Separability between boreal tree species in ERS data may be small, because at C-band changes in backscattering are dominated by changes in the dielectric properties of the forest floor and canopy (Rignot *et al.*, 1994a). At regional scales, Kuntz and Siegert (1999) demonstrated that ERS-1/2 could be used to map basic tropical land cover types and deforestation, and Saatchi *et al.* (2000) produced a regional scale land cover map for the entire Amazon Basin using L-band JERS data, which has certainly provided the most potential for forest mapping. Texture measures have most commonly been applied to improve forest cover classification (Haack *et al.*, 2000; Saatchi *et al.*, 2000) and for monitoring deforestation (Kuntz and Siegert, 1999).

The most effective use of information derived from SAR images has occurred when combined with complementary data provided by VIR data sets; land cover classification accuracy can be improved (Kuplich *et al.*, 2000) and classes identified that are not distinguishable in the SAR or VIR data set alone (Pohl and van Genderen, 1998). Crop classification is facilitated by using VIR imagery for landscape segmentation and weather independent SAR data to create crop evolution profiles from temporal change in backscatter conditions (Brisco and Brown, 1995; Mangolini and Arino, 1998). For crop classification, ERS data alone have demonstrated potential. For example, Schotten *et al.* (1995) used multi-temporal ERS-1 data to discriminate 12 crop types in the Netherlands with 80% accuracy, and Tso and Mather (1999) discriminated crop type in the UK with accuracies of up to 75%. Fusion of VIR and SAR data has been used to improve tropical forest classification (Lozano-Garcia and Hoffer, 1993; Nezry *et al.*, 1993). Rignot *et al.* (1997) investigated SIR-C, JERS-1, SPOT XS and Landsat TM data for mapping deforestation in Brazil. The synergy of SAR data and Landsat TM imagery could reliably map additional classes, such as flooded dead forests.

Interferometric coherence has also been used as a basis for land cover classification. Behaviour of coherence from ERS-1/2 tandem mission was investigated as a function of forest-type, forest parameters, and environmental factors by Castel *et al.* {, 2000 #255} and they were able to discriminate between coniferous forest types. Strozzi *et al.* (2000)

produced land use maps of three different areas in Europe with ERS SAR interferometry with, in the best case, classification accuracies in the order of 75%, although topographic effects reduced performance.

Future SAR systems may have limited mapping capabilities when used alone (Rignot *et al.*, 1994b), but as parameters available for classification increase, with multi-frequency, multi-polarisation capabilities afforded by a combination of Envisat, Radarsat-2, and ALOS, the accuracy of land cover classification might be expected to improve. However, the complexity of land cover classification techniques may also increase, which may remove the process of data acquisition and processing from end-users.

2.3.2 Forest Biomass

Information on woody biomass in both boreal and tropical forest ecosystems is essential for studies of the global carbon cycle; remote sensing has potential to provide such data. It is generally recognized that the utility of VIR sensors to extract information on forest biomass is limited because there is a saturation effect at very low levels of biomass (Kasischke *et al.*, 1997; Sader *et al.*, 1989) and there is no direct linkage between VIR reflectance from a forest canopy and woody biomass (Cohen and Spies, 1992; Sader *et al.*, 1989). The potential of radar for derivation of forestry parameters is clear, because energy at radar wavelengths will interact with the woody components of the vegetation. In general, the total backscatter from forest is a combination of volume scatter from the canopy, surface scatter from the ground, and double-bounce scatter between the trunk and ground. At higher frequencies (e.g. X-band) scattering from the crown is important, while at lower frequencies, trunk-ground components are dominant (Stjernman, 1995). Spatial resolution of the SAR is important, because it may affect the biomass response.

Much research has been directed to evaluate the potential of linking radar backscatter to forest biomass and develop algorithms to convert backscatter intensity into biomass by regressing SAR backscatter and biomass (Wang *et al.*, 1995). The discussion here is focused on applications for boreal forests, with synthesis of some results from SIR and AIRSAR experiments and emphasis on the potential of space-borne SAR for biomass retrieval.

Polarimetric C, L, and P –band AIRSAR data and data from SIR-C/X-SAR have been used to investigate the potential of different frequencies and polarisations for biomass

estimation. Results suggest that the dynamic range of backscattering sensitivity is maximised at P-band, and then decreases with increasing frequency (Dobson *et al.*, 1992; Le Toan *et al.*, 1992; Ranson and Sun, 1994). Dobson *et al.* (1992) reports that biomass saturation level is about 200 tons/ha at P-band and 100 tons/ha at L-band. Imhoff (1995) reports saturation approximate to 100 tons/ha for P-band, 40 tons/ha for L-band, and 20 tons/ha for C-band for tropical broadleaf and coniferous forests. Using P-band HV polarised data for a mono-specific pine forest, Le Toan *et al.* (1992) were able to achieve r^2 of 0.95 for the relationship between backscatter and biomass. It is clear that cross-polarised data or combinations of polarisation are most sensitive to variations of forest biomass (Le Toan *et al.*, 1992; Ranson and Sun, 1994; Schmullius and Evans, 1997; Wu, 1987), However relationships are known to be non-linear and radar saturation with biomass means that approximately 38% of Earth's vegetated surface area containing 81% of the estimated total terrestrial phytomass have biomass densities above the saturation limit of current SAR systems (Imhoff, 1995).

The potential of C-band ERS data for biomass retrieval has been investigated through empirical studies. Kasischke *et al.* (1994) found significant linear correlations between the radar backscattering and the various components of biomass of young pine stands. In older pine forest, the backscattering is not highly correlated to biomass and the dynamic range of backscattering in boreal forest is low (Harrell *et al.*, 1997), with the signal saturating at very low biomass because of a high sensitivity to moisture conditions (Wang *et al.*, 1994). Even with polarimetric SAR, empirical studies have great difficulty in determining which part of the canopy is responsible for the backscattering and the effect of a particular forest parameter on backscatter because of inter-correlation between parameters (Le Toan *et al.*, 1992; Wang *et al.*, 1995). Physical backscatter models have been developed to explore the mechanisms of microwave scattering from forest canopies and to predict the radar backscattering as a function of the geometry and size of the forest canopies and radar system parameters (Wang *et al.*, 1995).

Using a backscatter model, SAR backscatter data from AIRSAR, and ground data, Wang *et al.* (1995) studied the influence of changes in biomass on SAR backscatter as a function of frequency and polarisation and evaluated the feasibility of deriving biomass from the radar data. Results indicated that L and P –band in cross polarisation (HV) together provides the best potential for measuring biomass. C-band was found to be

insensitive to biomass change. HH polarised L and P –band modelled returns are mainly from the trunk-ground interface, and therefore may be useful for coniferous forests where most biomass is stored in the trunk. For cross-polarised L and P –band, canopy volume scattering was dominant. Ranson and Sun (1997) found that SIR-C/X-SAR data compared favourably with AIRSAR data, with P-band providing the best results for biomass estimation. Fransson and Israelsson (1999) used a backscatter model to investigate backscatter from C-band ERS-1 and L-band JERS-1 in relation to boreal forest biomass (stem volume). JERS-1 data was superior because the ERS-1 signal saturates at such low biomass. A semi-empirical model developed by Pulliainen *et al.* (1996) further showed that the dynamic range of backscattering values of ERS-1 with changing boreal forest biomass was very small.

There is a significant variation in backscatter within forest ecosystems due to temporal changes in environmental conditions, which may obscure or enhance the biomass signature (Kasischke *et al.*, 1994). Surface moisture conditions can be a strong influence on backscatter intensity (Fransson and Israelsson, 1999), and seasonal snow cover and freeze/thawing effects cause drastic changes in backscattering (Rignot *et al.*, 1994a). Pulliainen *et al.* (1996) found that the correlation between ERS-1 backscattering and forest biomass was positive or negative depending upon canopy and soil moisture, whereas Fransson and Israelsson (1999) found that backscattering in JERS-1 data always increases with biomass. Moghaddam and Saatchi (1999) investigated canopy moisture with the aim of estimating moisture status from polarimetric C and L –band AIRSAR data. Scattering from the canopy was isolated using a classification algorithm and a model was developed to invert canopy moisture from backscatter; changes in canopy moisture were reflected by significant changes in backscatter. Such research confirms that, in particular, C-band data affords an opportunity to monitor temporal changes in forest ecosystems (Rignot *et al.*, 1994a; Way *et al.*, 1990). Literature concerning backscatter measurements from birch forest is limited. However, ground-based C-band scatterometer measurements by Stjernman (1995) over birch trees in Arctic Sweden revealed that backscatter was dominated by trunk-ground scatter component, which meant backscatter was influenced by ground properties.

Development of practical and useful inversion algorithms for inferring forest biomass from SAR data will require multiple frequencies and polarisations; the cross-polarisation and revisit capabilities offered by the new generation of space-borne SAR

systems, particularly L-band PALSAR, will be of most interest. The major challenge is estimating biomass from deciduous and coniferous and mixed species forests. Other problems relate to spatial variation of biomass within forest stands, variation due to natural disturbance, complex canopy structure and observational geometry (Balzter *et al.*, 2002).

2.3.3 Soil moisture

In the early 90s there was hope that soil moisture estimation from radar measurements could become operational; soil moisture is highly variable both spatially and temporally and therefore remotely sensed data have potential to provide spatial measurements (Engman, 1991). The theoretical basis for a relationship between soil moisture and backscatter is the sensitivity of the dielectric constant to soil water content. However, the effects of surface roughness, vegetation moisture and structure, and topography are appreciable at all frequencies and polarisations, which may mask the soil moisture signal (Engman and Chauhan, 1995; Goyal *et al.*, 1998; Macelloni *et al.*, 1999). The sensitivity of microwave backscatter to soil moisture at different frequencies and polarisations has been investigated using experimental AIRSAR and SIR-C/X-SAR, mostly over bare or sparsely vegetated soils; Co-polarised L-band has the highest soil moisture information (Lin *et al.*, 1994; Macelloni *et al.*, 1999; Shi *et al.*, 1997).

Several empirical and physical –based models have been developed to invert volumetric soil moisture from observed backscatter coefficients. Empirical models are inherently site-specific and have limited ranges of validity. Results suggest that backscattering cannot be easily converted into moisture estimates at field scale even over non-vegetated or sparsely vegetated areas because of the effect of surface roughness (Macelloni *et al.*, 1999; Moeremans and Dautrebande, 2000). However, Bindlish and Barros (2000) suggest that operational utility could be improved by re-sampling SAR data by an order of magnitude and Moeremans and Dautrebande (2000) found that at coarse regional scales, correlation between backscatter and mean soil moisture measurements was considerably improved. Multi-temporal imagery can be used to minimise the impact variables such as roughness and vegetation because these tend to change slowly with time (Engman and Chauhan, 1995).

Physical models have been used to model the interaction between soil moisture, surface roughness and vegetation; the relationship is almost certainly non-linear when surface

roughness and vegetation cover are taken into consideration (Bindlish and Barros, 2000). Theoretical surface backscatter models such as the Small Perturbation Model (SPM), Kirchhoff Physical Optics (PO) and Geometric Optics (GO) (see Rees (2001)), and Integral Equation Model (IEM) (Fung, 1994) have been developed to improve understanding of microwave surface scattering processes and the interaction between soil moisture and surface roughness at field scales. However, to different degrees, these models suffer from restrictive assumptions (Dubois *et al.*, 1995), which means that application to invert backscatter data into soil moisture is problematic.

Altese *et al.* (1996) observed that for ERS SAR the sensitivity to the roughness parameters is much higher than the sensitivity to dielectric constant, so that even a small error in the measurement of this parameter can affect the retrieved value of soil moisture significantly. Shi *et al.* (1997) found a good agreement between IEM model output and L-band measurements from SIR-C and AIRSAR. With respect to Radarsat's configuration, Biftu and Gan (1999) found that radar backscatter modelled using the IEM was highly sensitive to the RMS surface height. IEM model results from Tansey and Millington (2001) confirm that the successful monitoring of soil moisture is strongly dependent on surface roughness. Baghdadi *et al.* (2002) suggest that none of the existing models provide consistently good agreement with the measured data. Such models were originally developed to describe the scattering from bare soil surfaces only; therefore, vegetation backscatter effects are not explicitly incorporated. Empirical vegetation scattering parameterisation has been attempted with limited success (Bindlish and Barros, 2001). The future of soil moisture monitoring may depend on PALSAR, which will allow investigation of frequent repeat coverage L-band SAR for regional soil moisture monitoring.

2.4 SAR remote sensing of snow cover

The problems with remote sensing of snow cover using VIR sensors were discussed in section 2.1.4. SAR systems offer a promising alternative space-borne method for snow monitoring because, in particular, they are independent of cloud cover and solar illumination and are sensitive to the liquid water content of snow cover.

2.4.1 Passive microwave remote sensing of snow cover

It is appropriate to consider passive microwave remote sensing methods, which operate at frequencies between 5 and 100 GHz and have a strong utility for detecting wet snow

over large areas and can give an indication of snow depth for dry snow covers (Lillesand and Kiefer, 1994; Rees and Steel, 2001a). Signals still require calibration by ground snow data, but are appropriate for macro-scale hydrological investigations (Josberger and Mognard, 2002; Pulliainen and Hallikainen, 2001) and have been linked to spatially distributed snow hydrology models (Wilson *et al.*, 1999). Spatial resolution available with space-borne systems is very poor, typically a few tens of kilometres, so only airborne systems can be realistically used for landscape-scale studies.

2.4.2 SAR remote sensing of snow cover

Since the early 80's and throughout the 90's, experimental data and empirically and physically based modelling studies have demonstrated the potential of SAR for monitoring snow cover. The physical basis of snow monitoring using SAR is the change in dielectric constant that occurs due to the presence of liquid water as the snowpack begins to melt. However, as a snowpack develops, significant metamorphosis in terms of surface roughness, snow grain (scatterer) size, snow density occur in addition to the change in reflectivity and potential for dielectric loss that occur because of liquid water. The effects of frequency, polarisation, and incidence angle of the incident radar must also be considered.

A conceptual snow backscatter model introduced by Ulaby *et al.* (1982) describes scattering from snow cover as the sum of the scattering from the snow surface, the snow volume, and scattering from the underlying ground surface. The relative strength of surface and volume scattering is dependent upon the snow properties and system parameters. A more comprehensive examination of a physically based backscatter model is undertaken in chapter 8, but it is pertinent to consider key parameters and to review important research here.

Liquid water increases the real and imaginary part of the dielectric constant, increasing reflectivity of the snow surface and dielectric loss (energy absorption) within the snow volume, thereby reducing snowpack penetration depth. Dry snow is effectively transparent for X, C, and L –band SAR because the snow surface has low reflectivity and the snow volume has negligible absorption; the dominant scattering source is the snow-ground interface and there is often no significant difference in scattering from dry snow and snow-free surfaces at C-band (Bernier and Fortin, 1998; Rott and Nagler, 1992) or X –band (Fily *et al.*, 1995; Shi and Dozier, 1997).

When a snowpack is wet (typically up to 5% volumetric water), penetration depths are of the order of one wavelength (Rott and Mätlzer, 1987). Therefore, as snow melts surface scattering at the air-snow interface dominates (Rott and Nagler, 1992), but at higher incidence angles, greater than about 25° for X-band and 30° for C-band, volume scattering may dominate (Rott, 1984). The sensitivity of backscattering to water content is also influenced by wavelength; the difference between backscattering from a dry and wet snow pack increases with frequency (Ulaby *et al.*, 1986). The impact of liquid water for C and X –band SAR was monitored over a diurnal cycle by Stiles and Ulaby (1980), who observed changes in backscatter of around 2-3 dB related to increase in snow volumetric water content to 1.3 %. Snow wetness at the surface can change rapidly. Under clear skies, solar illumination may cause partial melting of the snow surface layer even though the temperature is below freezing (Koh and Jordan, 1995; Ulaby *et al.*, 1986), which can have important consequences for penetration depth, especially for shorter wavelengths.

For a dry snowpack, backscattering has been found to be independent of snow surface roughness at several incidence angles, even at high frequencies (Ulaby *et al.*, 1982). Wet snow, however, shows a significant increase in surface scattering from rough surfaces (Nagler and Rott, 2000; Rott and Davis, 1993; Ulaby *et al.*, 1982), which may be important when discriminating wet snow from bare surfaces (Shi and Dozier, 1993, 1997).

In a wet snowpack, scattering from larger individual snow grains is likely to increase, but this should be insignificant compared to dielectric losses due to liquid water in the snowpack. In modelling volume backscatter from a snowpack, snow grains are commonly assumed to be spherical and randomly oriented and liquid water is treated as uniformly distributed within the snowpack. However, a wet snowpack will be heterogeneous due to melt-freeze processes, meaning that modelling scatter from a snow volume is complicated by the presence of significant internal structure in the snow pack. An assumption of a homogenous medium may be acceptable since at C-band, the penetration depth will commonly be a few cm into a thin wet surface layer; however, at longer wavelengths backscatter may be affected by larger structures (Shi and Dozier, 1995, 1997; Shi *et al.*, 1998).

Experimental studies using airborne and space-borne multi-frequency, multi-polarised SAR has demonstrated that wet snow could be discriminated from dry snow and snow-free ground. Early studies using AIRSAR demonstrated the potential of C and X –band polarimetric measurements for mapping snow and glacier covered areas (Shi and Dozier, 1993, 1994). Such studies confirm that C–band SAR with VV and HH polarisation (approximating to ERS-1/2 and Radarsat-1) had good potential, whereas L-band HH polarised SAR (approximating to JERS) had poor potential for discrimination of wet snow from other targets. During the SIR-C/X-SAR experiment, Shi and Dozier (1997) investigated backscatter coefficients at L, C, and X –band at each combination of like and cross –polarisation (HH, HV, VH, VV). Results indicated that C-band VH and like-polarised X-band VV provided the best separation between dry and wet snow, with poor discrimination by L-band. Shi and Dozier (1997) also investigated the utility of polarisation ratios, such as depolarisation factors (HV/VV and VH/HH), and band ratios. Using band and polarisation ratios a complex decision-tree classification was undertaken, and results indicated that in addition to wet snow, it was possible to map dry snow (Shi and Dozier, 1997).

The use of single band, single polarisation SAR for snow cover mapping is usually based on temporal differences in backscattering between wet snow covered surfaces and dry snow cover or snow free surfaces (Baghdadi *et al.*, 1997; Rott and Nagler, 1995). An alternative method, comparing an image simulated from a DEM to real images to identify wet snow has also been used (Rott and Mätlzer, 1987). Since dry snow is highly transparent at microwave frequencies, it cannot usually be discriminated from snow free surfaces. However, if terrain is known to be snow covered, a backscattering characteristic of snow-free conditions can be taken to indicate snow is dry (Rees and Steel, 2001a). Development of wet snow significantly reduces backscattering in comparison to dry snow and snow-free conditions because of dielectric loss; the discrimination of wet snow is based on the difference between the two images. Two classification approaches have typically been used on the multi-temporal imagery, a statistical approach such as a supervised maximum likelihood classification and, more commonly, a rule-based approach.

Shi and Dozier (1997) suggest that accurate sensor location and a DEM of comparable resolution to image resolution are important for geometric and radiometric correction prior to snow mapping. However, an advantage of the broadly unchanging geometry of

space-borne satellites, particularly ERS-1 and ERS-2, allows multi-temporal overlay in radar geometry. Subsequently, the ratio of multi-temporal images can be applied to determine changes in the backscatter from a reference image of dry snow or snow-free conditions and to develop rules for snow cover mapping[3]. Image ratios also afford a reduction of topographic effects in SAR imagery prior to any geometric correction into map geometry. Several rule-based algorithms have been developed, which use a combination of SAR imagery, VIR imagery, and other measures. Rott and Nagler (1995) and Baghdadi *et al.* (1997) used multi-temporal ERS-1 SAR images to determine temporal changes in the backscattering coefficient from a dry snow and snow-free reference images. Both studies developed a simple classification decision tree based on typical backscatter difference of 3 dB and used masks for layover, shadow and others created from VIR imagery to improve robustness. Nagler and Rott (2000) demonstrated that an algorithm based on ratios between repeat pass SAR data with a threshold of 3 dB was also suitable for determining wet snow in Radarsat-1 data. It is clear that a dry snow image is preferable as a reference, because soil moisture variations in a snow-free image could produce ambiguities (Bernier and Fortin, 1998; Rott and Nagler, 1995). Rott and Nagler (1995) and Haefner *et al.* (1993) provide examples of combining ascending and descending orbits to reduce the effects of layover. However, such combinations suffer from significant differences in the backscatter values associated with the different local incidence angle and relative surface roughness for each scene and diurnal differences in snow dielectric properties between ascending and descending orbits.

Adam *et al.* (1997) evaluated a supervised maximum likelihood classification approach for mapping the movement of the snow line in a temperate glacier basin with ERS-1 SAR. Only a coarse definition of wet-snow, glacier ice or bedrock classes could be achieved. Texture information over the image was also employed; the principle being that snow is generally more uniform in distribution than a rock surface, and it is that these differences texture differences can improve the classification (Adam *et al.*, 1997; Shi and Dozier, 1993).

---

[3] The ratio of amplitude images (in linear scale) is the equivalent of the difference between decibel images (in logarithmic scale): logarithm theory states that $10\log_{10}(a/b) = 10\log_{10}(a) - 10\log_{10}(b)$.

The HUT (Helsinki University of Technology) empirical model, developed by Koskinen *et al.* (1997) determines the relative fraction of snow-free ground F_g by comparing the backscatter (in dB) of an ERS SAR image of interest σ^0_w with the backscatter values of two other images, one acquired at the beginning of snow-melt σ^0_i, and a snow-free image σ^0_g, from the end of snow-melt:

$$F_g = 100 \cdot \frac{\sigma_i^0 - \sigma_w^0}{\sigma_g^0 - \sigma_w^0} \qquad \textbf{Equation 2.4.}$$

2.4.3 Effects of vegetation on snow mapping

One of the unique applications of imaging radars occurs because a significant portion of the energy transmitted by these systems penetrates a vegetation canopy to the ground surface (Kasischke *et al.*, 1997). As mentioned in section 2.3.2, L and P –band SAR are significantly affected by vegetation biomass, whereas C-band is considerably less affected by biomass, but maybe attenuated by a forest canopy depending on canopy moisture (Way *et al.*, 1990).

Experiments with AIRSAR indicate that C-band, VV polarisation SAR can expect large total changes in backscatter for varied forest types as a result of ground moisture conditions (Way *et al.*, 1990; Way *et al.*, 1994). The effect of pine and mixed type forest was assessed for snow mapping with ERS SAR using the HUT model by (Koskinen *et al.*, 1997). The difference for wet snow was around 3 dB for open areas, but this difference decreased with increasing biomass, and for the most densely forested pine backscatter was independent of snow conditions. At all frequencies, the difference in backscattering between wet snow and dry snow and snow free cover decreases with increasing biomass (Koskinen *et al.*, 1999). Indeed, numerous studies simply use a VIR derived land cover data to mask vegetation types such as forest (Baghdadi *et al.*, 1997; Nagler and Rott, 2000). A model developed by Pulliainen *et al.* (1996) indicates that as the stem volume increases, the standard deviation of backscatter decreases, meaning that the ability to distinguish wet snow from other categories is reduced. However, boreal forests are relatively low density, and since C-band radar can partially penetrate through the vegetation canopy, ERS SAR has potential for monitoring the seasonal changes of boreal forests (Rignot *et al.*, 1994a). As indicated previously, Stjernman (1995) found C-band backscatter over an area of birch trees in Arctic Sweden was

dominated by diurnal variation in ground permittivity due to changes in dielectric properties of the snow cover.

2.4.4 Validation of snow mapping

Validation of SAR-derived snow maps is usually conducted using a combination of ground control data and, if available, concurrent VIR data. However, given the trade-off between satellite return frequency and resolution and the cloud attenuation of VIR sensors, the availability of concurrent VIR data at a resolution compatible with the SAR data is likely to be limited. Usually, one or two images from a VIR sensor such as Landsat TM may be used where possible (e.g. Rott and Nagler (1995); Turpin (2000); Nagler and Rott (2000)) or a comparison might be made with AVHRR data (Koskinen *et al.*, 1999). Given the canopy attenuation of VIR data, validation using VIR data is only reasonable in open areas (Koskinen *et al.*, 1999). Studies may rely on knowledge of snow conditions from concurrently collected ground control data and from weather stations. In general, good agreement is suggested between SAR and VIR derived snow mapping products (Nagler and Rott, 2000; Rott and Nagler, 1995; Turpin *et al.*, 2000), but site-specific factors can often confound separability of wet snow and snow-free ground.

2.4.5 Future research with radar for snow applications

Given the sensitivity of SAR to wet snow, there has been considerable interest in SAR capability to estimate snow water equivalent (SWE), and additional parameters such as snow depth and snow density. The availability of spatially distributed snow parameters is potentially a great resource for hydrological modelling, but this research is still experimental.

At the moment, operational snow applications are limited by using existing space-borne SAR systems. However, multi-parameter (frequency and polarisation) SAR systems could aid in production of snow products. Rott and Nagler (1995) showed the potential of SAR derived snow maps for use in modelling of runoff from snow covered areas and glaciers. More recently, Bernier *et al.* (1999) assessed the feasibility of using Radarsat-1 and ERS data to estimate the spatial distribution of SWE in a partially forested catchment in northwest Quebec. An algorithm inferring SWE from the estimated thermal resistance had a relative difference between 1 and 13% derived from snow transects. Polarimetric information could have promising applications for monitoring

SWE, snow depth and snow density. Using SIR-C/X-SAR measurements, Shi and Dozier (1995) were able to estimate snow wetness with 2.5 % RMS. Algorithms for estimating dry snow density and depth were developed by Shi and Dozier (2000a; 2000b); snow density derived from VV and HH polarization data at L-band frequency shows 13% relative error compared with field measurements. Snow depth achieved RMS error of 34 cm. The potential for ScanSAR multi-polarisation imagery onboard Envisat and Radarsat-2 will prompt more active research in using SAR this area. Interferometric SAR has also been investigated for estimation of changes in snow water equivalent in dry snow. Small changes in snow properties between Interferometric SAR image acquisitions may introduce significant phase changes; the change in the degree of coherence could allow discrimination of wet snow (Guneriussen *et al.*, 2001; Strozzi *et al.*, 1999). However, changes in amplitude of backscatter allow discrimination of wet snow, therefore computer intensive interferometric processing is perhaps redundant.

Chapter 3. Methods: Data for vegetation and snow mapping

This chapter introduces the study sites and the remotely sensed and field data, which were a necessary prerequisite for this research. Remotely sensed data have a different measurement extent, depending on the source, but the extent of each study area was defined by the extent of aerial photography, from which a high resolution DEM was to be extracted. At each study site, this area encompasses continuous birch forest, the forest-tundra ecotone and tundra vegetation beyond the treeline.

Within this area various field measurements were made for the snow cover and vegetation mapping, with emphasis given to achieving a reasonable extent and spacing of measurements given the variability in topography and vegetation and logistical constraints during the snow melt period. Some field measurements were collected continuously through the snow melt period, whereas other measurements, which could not be collected continuously, were made coincident with image acquisition. As indicated in chapter 2, the sensitivity of a snowpack to diurnal temperature change means that the temporal correspondence of measurements with image acquisition was particularly important.

3.1 Description of study sites

The DART project involved conducting experiments at study sites across gradients in both continentality and latitude within the Fennoscandian mountain range in northern Europe. This research is focused on three study sites where there is a local example of the mountain birch (*Betula pubescens* ssp. *tortuosa*) forest-tundra ecotone (figure 3.1a-d): Dovrefjell (Sør-Tröndelag, Norway), Abisko (Norbotten, Sweden) and Joatka (Finnmark, Norway). Each study site reveals different climate and geological influences on topography, vegetation and the structure of the forest-tundra ecotone. The study sites provide useful contrasts for the investigation of snow and vegetation mapping, but with large topographic variation and heterogeneous vegetation cover, provide a challenging operating environment for remote sensing. The main species in the tundra areas are: *Empetrum hermaphroditum*, *Vaccinium ulginosum*, *V. vitis-idae* and *Betula nana*, lichens and bryophytes (and additionally in Dovrefjell *Arctostaphylus uva-ursi*) (Sjogersten and Wookey, 2002). Within the forest, there may be a greater tendency towards *V. myrtillus*.

3.1.1 Joatka (69° 45' N, 24° 00' E)

Joatka is the most northerly and continental study site. Bordered on the east by the large lake Ies'javri (*ca.* 12 × 8 km) and on the west by Alta Elva (Alta river) and Joatka'javri (Joatka lake – see figure 3.2), Joatka lies towards the northern edge of the Finmarksvidda, the continental inland plateau of northernmost Norway. The birch forest is generally discontinuous and large areas of the study site are dominated by tundra, which begins to prevail above *ca.* 400 m a.s.l. Annual precipitation is 354 mm, but winters are dry (*ca.* 50 mm per month). Mean July and February temperatures are *ca.* 11 °C and –14 °C respectively, although long-term temperature records do not exist. The study site can be characterised into three distinct sub-areas:

(1) The "lowland" plateau is an undulating plain at elevations of 385-500 m a.s.l. It has numerous bogs and small shallow lakes, with glacial-fluvial ridge formations hosting typical tundra vegetation of dwarf birch (*Betula nana*) lichen heath on the ridges and often bilberry (*Vaccinium myrtillus*) in depressions, and mountain birch (*Betula pubescens* ssp. *tortuosa*) in favourable sites. Geology consists of relatively nutrient rich, basic igneous gabbro.

(2) An escarpment edge rises forming a steep south-facing slope running west to east. Elevation rises to 671 m a.s.l. and small streams are abundant and vegetation is relatively productive with herb-rich birch forest.

(3) The "highland" plateau to the north comprises relatively nutrient poor pre-Cambrian quartz rich bedrock. Vegetation is mostly bryophytes or lichen with trailing dwarf shrubs and large areas of bogs and peat.

3.1.2 Abisko (68° 21' N, 18° 49' E)

The Abisko study site, figure 3.3 and 3.4, is close to the Abisko Scientific Research Station (356 m a.s.l), which is situated on the southern shore of Lake Torneträsk. The forest-tundra ecotone is located on an undulating gentle slope of northwesterly aspect and is comprised of a patchwork of tundra and forest, with extensions of forest up to 700-800 m a.s.l. At a finer scale, the topography is "hummocky" due to till deposits, with peat formed in the depressions. A pronounced orographic effect causes a "precipitation shadow", which results in low local mean annual precipitation of 300 mm. Mean July and January temperatures at Abisko are 11 °C and –11.9 °C respectively (30 year mean 1961-90 (Andersson *et al.*, 1996)). The bedrock in the area belongs to the Scandes mountain range and is mainly hard shale.

3.1.3 Dovrefjell (62° 18' N, 09° 37' E)

Dovrefjell has long been famous as a centre of floristic diversity within Norway, partly due to the complexity of the bedrock. The E6 highway runs along the Drivdalen valley and essentially separates two areas of contrasting geology; the west side, which is dominated by acidic gneiss, and the east side underlain by carbonate-bearing rocks. The "Western Gneiss region" contrasts with the eastern "Trondheim region", the latter having a rich flora including many uncommon species, which have only been found in one or a few localities, or occur in a limited area.

The forest-tundra ecotone is narrow, given the steep slope gradient of the topography, and is typically located at 1080 m a.s.l elevation. Topography of the Western Gneiss is sharper, typified by Snøhetta (2286 m a.s.l.), whereas the younger Trondheim region has rounder landscape forms, such as Mt. Knutsø (1690 m a.s.l.). Within the Divdalen valley is Kongsvoll Biological Station (Norwegian University of Science and Technology, Trondhiem); a meteorological station at 972 m a.s.l. records mean July and January temperatures as 10.2 and –7.9 °C respectively and annual precipitation of 473 mm.

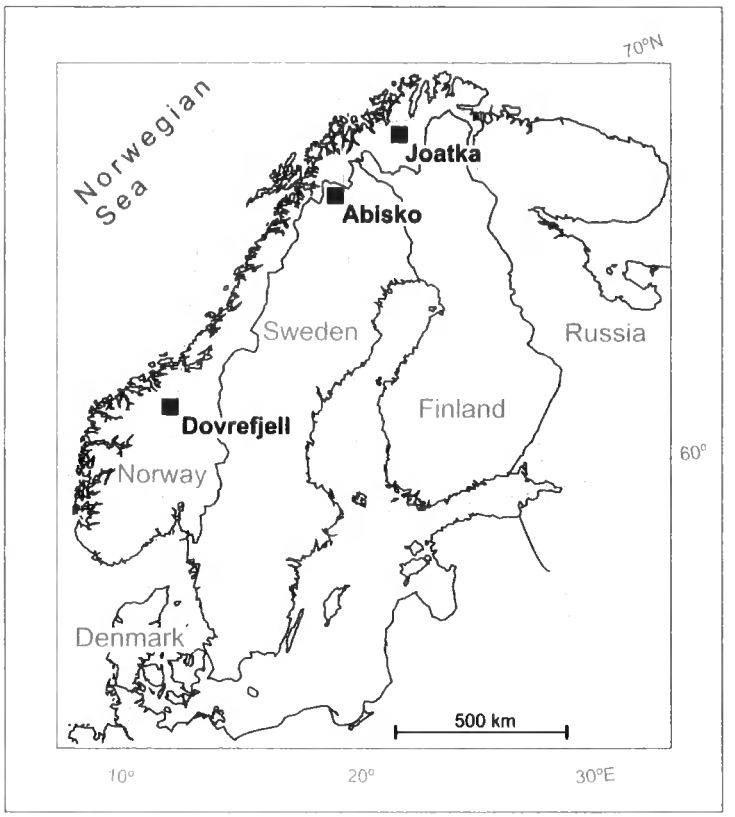

a)

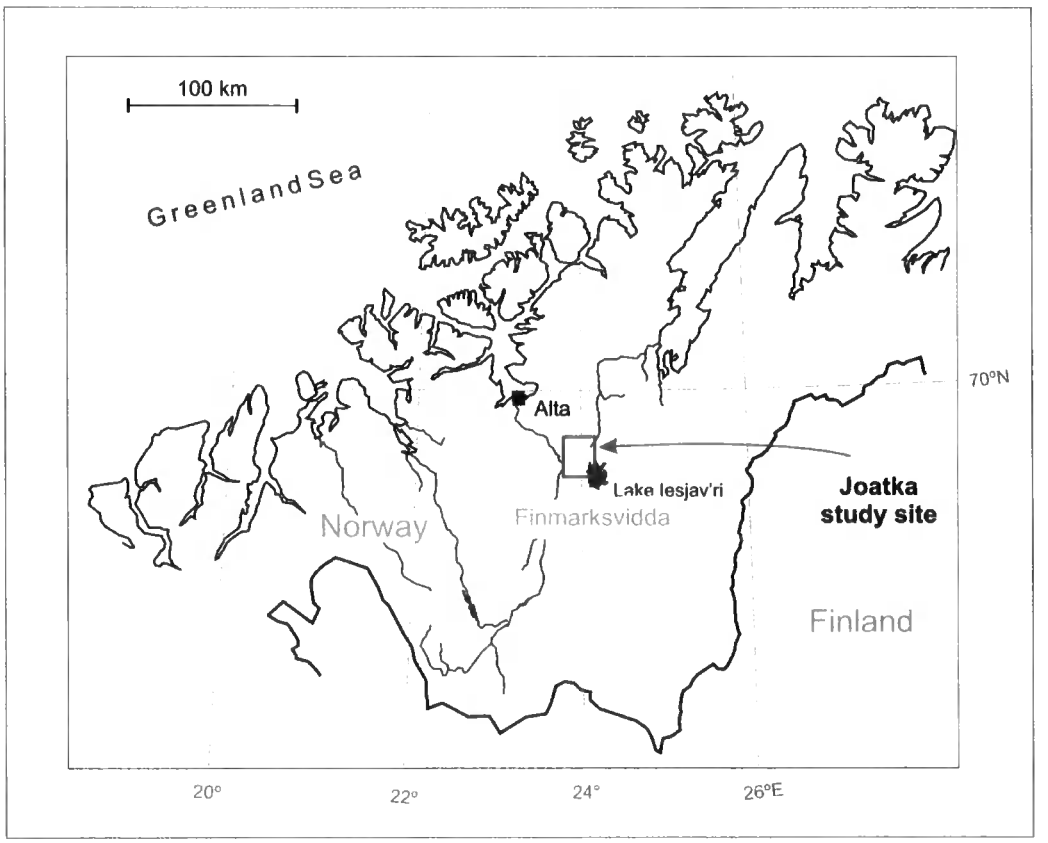

b)

Figure 3.1. Location of Study sites: (a) relative location of each site, (b) location of Joatka, (c) location of Abisko, and (d) location of Dovrefjell.

c)

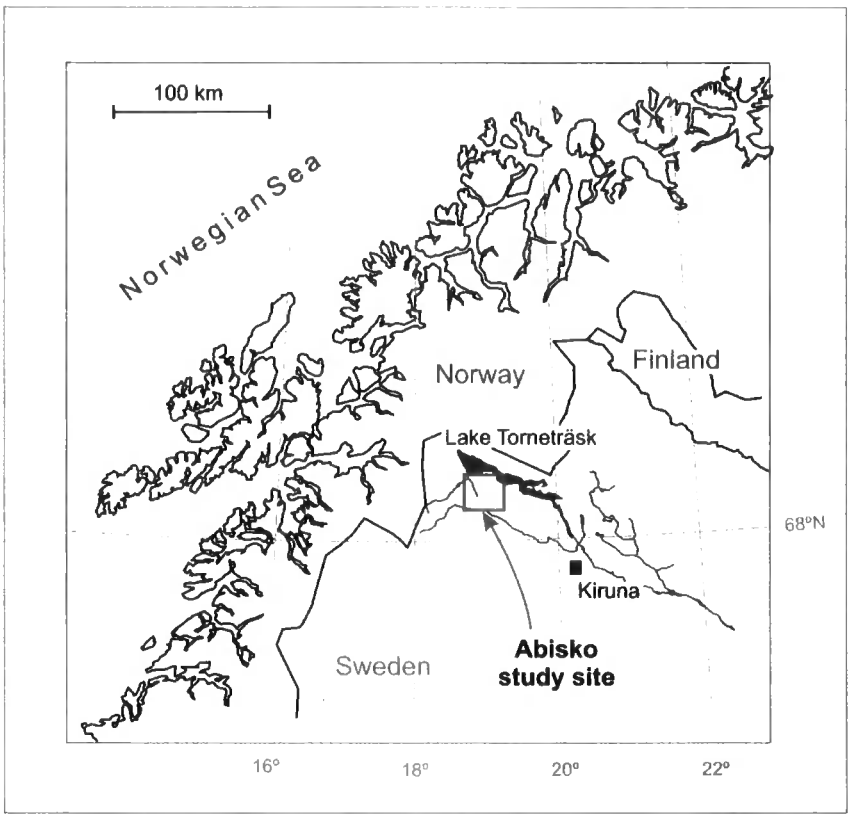
100 km
Norwegian Sea
Norway
Finland
Lake Torneträsk
68°N
Kiruna
Sweden
Abisko
study site
16°
18°
20°
22°

d)

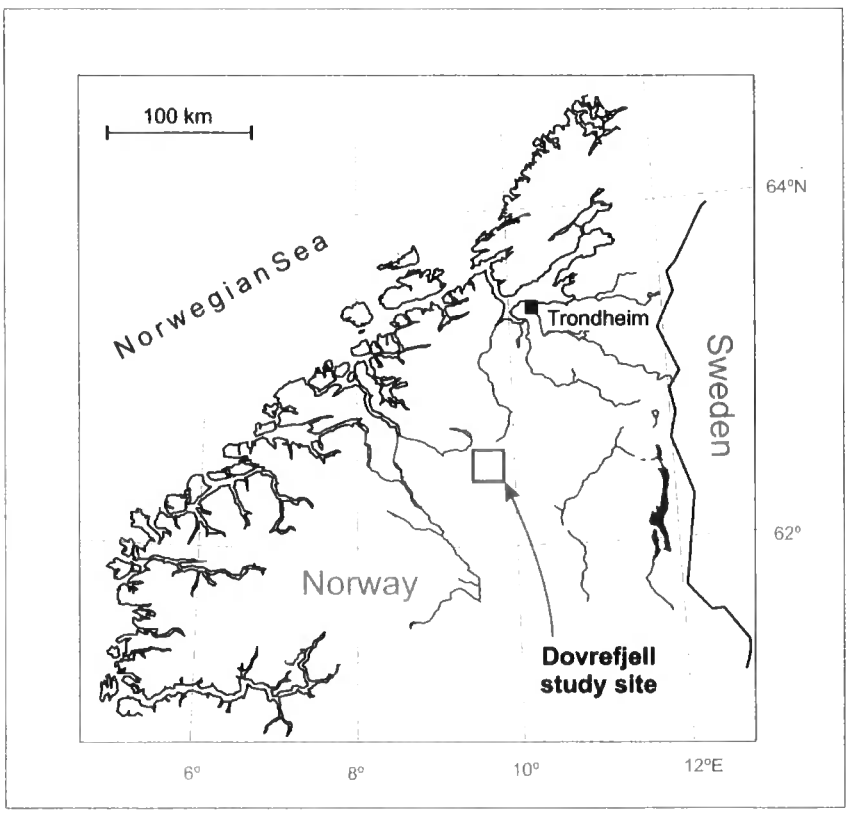
100 km
64°N
Norwegian Sea
Trondheim
Sweden
62°
Norway
Dovrefjell
study site
6°
8°
10°
12°E

Figure 3.2. Joatka Study site with field station in foreground. The tree line and study area is beyond snow-covered lake.

Figure 3.3. Abisko study site. Looking south toward treeline and Lapporten (Lapp Gate) from summit of Njulla (1169 m).

Figure 3.4. Patch of snow-free tundra at Abisko study site. Looking south toward Lapporten.

3.2 Field location measurements

For field data collection as part of the methodology for snow and vegetation mapping (discussed further in chapter 4), accurate horizontal location (x,y) data were required. For DEM extraction, accurate horizontal location and elevation (z) were required. Location was determined using the US Department of Defence global positioning system (GPS). The GPS receiver was a high performance 12-channel Trimble GeoExplorer 2, used with Trimble's GPS Pathfinder Office software (Survey Supplies Ltd., Liverpool, UK). The geodetic datum selected for all GPS measurements was WGS84.

Accuracy of GPS measurements is affected by a number of errors sources, related to the environment in which measurements are collected, atmospheric effects and satellite configuration relative to the receiver. Improved accuracy was attempted by collecting data where possible in an environment devoid of large reflective surfaces and with a clear view of the sky, reducing erroneous "multi-path" signals. Further, high accuracy was demanded from the Position Dilution of Precision (PDOP), a measure of the current satellite geometry, and signal to Noise Ratio (SNR), a measure of the strength of the satellite signal relative to the background noise. Measurement accuracy was influenced by selective availability (SA), which introduced non-systematic measurement error; SA was not deactivated until May 2000. Milbert (2000) found that 95% of GPS measurements under SA conditions fell within a radius of 45 metres of true, but without SA, 95% of the points fell within a radius of 6.3 metres.

The effects of SA and other random errors were ameliorated using two alternate methods, *position averaging* or *differential GPS*, the choice dependent on the accuracy required for the particular location measurement. The two methods are discussed below and the choice of either position averaging or differential GPS is specified in subsequent sections where each field measurement is discussed.

3.2.1 Position averaging

Taking the average of repetitive location measurements at a single location increases accuracy and precision. If the horizontal errors were not correlated, the root mean square error (RMS) would be inversely proportional to the square root of the number of measurements. However, the errors are correlated and this causes the error from averaging to decrease at a slower rate than if the errors were not correlated. When SA (Selective Availability) was on, it was noted that if one position-averaged, the RMS error when position-averaging roughly fell by the reciprocal of the square root of the number of fixes divided by twice the correlation time of the fixes (Rees, *pers. comm.*). The protocol used for location averaging was to collect a minimum of 180 (1/sec) consecutive positions, which means that the reduction in RMS error was a factor of approximately 10. Therefore, It is reasonable to assume that measurements were collected with a RMS error of less than 10 m. Repeated visits to the same site on separate occasions may further improve accuracy.

3.2.2 Differential GPS

Differential GPS is a technique that uses additional GPS measurements from a fixed "base" GPS receiver and post-processing to increase the accuracy of GPS positions. It is based on the fact that any pseudo-range errors in a GPS signal are common to all receivers within a radius of several hundred miles. Differential GPS can provide accuracies from sub-metre to around five metres, depending on the sophistication of the antenna and GPS signal used. The base receiver for each site was a permanent base station operated by the relevant national mapping agency (Sweden: Lantmäteriet, SE-801 82, Gävle; Norway: Statens Kartverk, 3504 Hønefoss). The "rover" receiver was the Trimble GPS referred to in section 3.2. In post-processing, differential correction compares the base station data with the known base station location and computes the error associated with each satellite pseudo-range. Each base station was located between 100-200 km of the study site, which helps to ensure that the signal received by the base receiver has errors representative of the rover receiver. This error is used to correct the

rover positions, improving their accuracy. Under SA conditions, August *et al.* (1994) found that 95% of locations were within 73 m of true without differential correction and within 6 m of true with correction.

Differential corrections were post-processed using Trimble Pathfinder Office software using concurrent base station files. A logging interval of one position per second was used, with at least 180 (1/sec) positions collected at a location.

3.3 Field meteorological measurements

At each study site, temperature measurements were recorded. At Abisko and Dovrefjell additional meteorological measurements were also available from the meteorological station at the respective research station: precipitation, humidity, and incoming solar radiation.

3.3.1 Temperature

Temperature measurements are useful because air temperature is the main influence on the timing and rapidity of the snow melt. Temperature monitoring at each study site was conducted using temperature loggers (TinyTag Plus: Gemini Data Loggers Ltd, Chichester, UK). These loggers were distributed in the field and maintained as part of the DART project by a number of project members, coordinated by Dr. Robert Baxter, University of Durham.

Four temperature stations were erected spanning the forest-tundra ecotone: (1) upper tundra, characterised by tundra vegetation above the treeline; (2) upper forest, characterised by a patch of forest close to the treeline; (3) lower tundra, typically an extensive tundra area within the discontinuous forest; and (4) lower forest, which is within the continuous forest. At each station, three hourly mean measures were recorded:

(1) **Air temperature** – measured from a screened logger at 2 m above ground level.

(2) **Ground surface temperature** – measured from an unscreened logger.

(3) **Soil temperature** – measured with a probe at 10 cm depth.

Ground surface and soil temperature measurements can indicate how the snowpack is acting as an insulating medium from variations in air temperature. Unscreened ground surface temperature is particularly useful because it can provide accurate information on

the duration of snow cover across the forest-tundra ecotone, which can be correlated to information in the ERS-2 SAR images. The method of determining snow cover duration is based on the amplitude of temperature variation. Beneath the snow cover, insulation causes a low amplitude response of ground temperature to variation in air temperature. In contrast, snow-free conditions reveal a significant increase in the amplitude of temperature variations, which allows the transition to snow-free conditions to be identified.

3.4 Field snowpack and ground surface measurements

Snow pits enable retrieval of several snowpack measurements that are important for interpretation of the ERS-2 SAR imagery, which were discussed in chapter 2. Snow pits were excavated to monitor the development of the snowpack at each site throughout the snow melt season. They were always excavated coincident with ERS-2 SAR image acquisition, with some additional pits excavated at other times if possible. Snowpack properties are highly variable both spatially and temporally. However, the aim is not spatial interpolation of measurement values, but to obtain representative measurements at locations across the forest-tundra ecotone. In addition, every effort was made to excavate snow pits at the same location in order to effectively monitor temporal change in snowpack properties and minimise measurement variation due to spatial variation. Fewer ground surface measurements were made when snow-free conditions had emerged because for snow mapping the emphasis is on the temporal change in snow conditions.

Field measurements were located using the US Department of Defence global positioning system (GPS) and the procedure of **position averaging**, as discussed in section 3.2.

3.4.1 Snowpack stratigraphy

The stratigraphy of the snowpack was examined following excavation of each snow pit. The mean diameter of snow grain was estimated and the complexity of the stratigraphy was recorded, in particular the evidence of melt-refreeze processes. To some extent, the complexity of stratigraphy determined the frequency of other snowpack measurements.

3.4.2 Snow permittivity and liquid water content

Determination of snow liquid water content is based on measurement of the permittivity of snow and air and, subsequently, the calculation of the snow dielectric constant. The

measurement of snow permittivity must be rapid and preferably non-destructive because of the rapid snow metamorphism at and near the melting point; any disturbance of the snow may change its structure, texture, and wetness (Denoth *et al.*, 1984)

Measurements were made using a Denoth (1994) snow dielectric moisture meter with flat capacitive sensor (figure 3.5), which allows both near surface and snow volume wetness determinations. The snow dielectric moisture meter operates at a frequency of 20 MHz, where snow density and wetness mostly control snow permittivity and the size of ice grains and liquid water distrbution can be neglected (Denoth, 1994).

Figure 3.5. Obtaining field measurements: Snow density (left) and snow permittivity using snow dielectric moisture meter (right).

The sensor is inserted horizontally into the snowpack and a measurement U is made through a tuning operation, which requires a minimum value from the mA meter. A reference measurement U_{ref} in air is also made. The dielectric constant (real part) of snow is calculated according to:

$$\varepsilon' = 1 + k \cdot \log(U/U_{ref}) \qquad \textbf{Equation 3.1}$$

where k is a sensor specific calibration factor. The relationship between snow permittivity ε', density ρ (g/cm^3), and volumetric water content W%, has been found experimentally (Denoth, 1994; Frolov and Macheret, 1999):

$$\varepsilon' = 1 + 1.92\rho + 0.44\rho^2 + 0.187W + 0.0046W^2 \qquad \textbf{Equation 3.2}$$

The calculation of the imaginary part ε'' of the dielectric constant (the loss factor), which is important for determining radar penetration depth, is more difficult. The loss factor is very sensitive to the water content and the shape of the water inclusions, meaning that a simple relationship between ε'' and liquid water content may not exist (Denoth, 1989). However, Fung (1994) introduces a relationship for calculation of ε'' for a frequency range that encompasses ERS-2 SAR, but for snow density up to only 0.38 g/cm^3:

$$\varepsilon'' = \frac{0.073\left(f/9.07\right)^2 W^{1.31}}{1+\left(f/9.07\right)^2} \qquad \textbf{Equation 3.3}$$

where frequency is expressed in GHz.

3.4.3 Snow depth

Total snow depth and depth of each measurement were made following excavation of each snow pit. All measurements are referenced relative to the snow surface. It is import to note that a wet snowpack will limit ERS-2 SAR penetration depth to around one wavelength (*ca.* 5 cm) so that spatial variation in snow depth maybe less important for a wet snowpack.

3.4.4 Snow density

Snow density (g/cm^3) was measured using a volumetric method with a cylinder of known volume and a digital balance (±1 g measurement accuracy). Cylinders of snow

were extracted throughout the profile of the snowpack, specifically where the dielectric measurements were taken.

3.4.5 Snow temperature

Temperature was taken throughout the profile of the snowpack using a digital thermometer with a needle probe (Fluke 51 J/K thermometer: RS Components Ltd., Corby, UK), which has ±0.1 °C measurement accuracy.

3.4.6 Snow and ground surface roughness

Quantitative measurements of surface roughness and correlation length of snow and ground surfaces were not acquired. However, snow surface roughness was recorded qualitatively, with interpretation of temporal change in roughness of snowpack relative to dry snow conditions. The tundra surface is assumed to remain relatively constant over the period of snow melt.

3.4.7 Ground surface / soil moisture

Since the dielectric constant of soil can influence the ERS-SAR backscatter, measurements of soil permittivity were acquired when snow-free conditions emerged. Soil permittivity was measured using a ThetaProbe (type ML2x: Delta-T Devices Ltd., Cambridge, UK), which measures volumetric soil moisture content to within 1%. The soil dielectric constant, ε_{soil}, was derived from ThetaProbe field measurements V (volts) using:

$$\sqrt{\varepsilon_{soil}} = 1.07 + 6.4V - 6.4V^2 + 4.7V^3 \qquad \textbf{Equation 3.4}$$

Volumetric soil water content W_{soil} (%) was derived from ε_{soil} using the following relationship:

$$\sqrt{\varepsilon_{soil}} = a + bW_{soil} \qquad \textbf{Equation 3.5}$$

where a and b are manufacturers constant values, which are 1.6 and 8.4 respectively.

3.5 Remotely sensed image acquisition

3.5.1 ERS-2 Imagery

ERS-2 SAR imagery provides suitable imagery for landscape-scale monitoring of snow-melt at the forest-tundra ecotone, with a spatial resolution of approximately 25 m and spatial extent of approximately 100×100 km. Table 2.2 gave details of ERS-2

parameters; as a C-band, VV-polarised SAR, ERS-2 is suitable for snow-mapping. The combination of the high latitude of the study sites and the polar orbit of ERS-2 improves the return frequency over the DART study sites. However, while coverage is achieved more frequently, images may have a different orbit track, which results in images having different imaging geometry. This precludes simple multi-temporal overlay in radar geometry for some images, which is discussed in subsequent analysis. Given the problems of large differences in imaging geometry and differences in dielectric properties between descending (daytime) and ascending (night-time) images, only descending scenes were acquired. ERS-2 SAR imagery was acquired in precision image (PRI) format through Eurimage (Via E. D'Onofrio 212, Roma 00155, Italy) and since imagery is independent of cloud cover, Eurimage gives confirmation of acquisition in advance. Because of inter-annual variation, the timing of snow melt is difficult to predict. The aim was to acquire an image of dry snow conditions and several images throughout the period of snow melt until snow-free conditions emerge.

Logistical constraints meant that field data could not be collected in the same year at each site and since image acquisition is required with concurrent field data, images were collected in different years at different site. In 1999, 5 ERS-2 SAR scenes were acquired over Joatka and 5 at Abisko. During 2000, 6 ERS-2 SAR scenes were acquired over Dovrefjell. This roughly translates to an image acquisition every 3 weeks during the melt period, which represents a good temporal resolution for remotely sensed snow mapping. Details of images are shown in table 3.1 and an example image from each satellite track is shown in figures 3.6 to 3.8.

The reference image for snow mapping should ideally be from the same track and frame as the change images. At Joatka, however, a reference image from the same orbit was not acquired for the image on 5th June, which may result in uncertainties in the analysis. However, the terrain is not extreme here and the high latitude means that the tracks overlap substantially, so that the change in imaging geometry is not large. At Abisko, there is sufficient imagery that we should be able to compare each image to a dry snow or snow-free image from the same track. An average of more than one dry snow image can be made, if available, to reduce the effects of variation in surface roughness and speckle.

Table 3.1. ERS-2 imagery acquired at each study site.

	Expected conditions	Date	Time (GMT)	Track	Frame	Coordinates of frame centre
Abisko	Reference image	02/04/99	10:10	251	2223	68°09 N, 019°14 E
	Wet snow	21/04/99	10:12	022	2223	68°09 N, 018°31 E
	Wet snow	07/05/99	10:10	251	2223	68°09 N, 019°14 E
	Wet snow	26/05/99	10:13	022	2223	68°09 N, 018°31 E
	Snow-free	11/06/99	10:10	251	2223	68°09 N, 019°14 E
Joatka	Reference image	17/01/99	09:55	394	2187	69°52 N, 024°25 E
	Wet snow	12/04/99	09:55	394	2187	69°52 N, 024°25 E
	Wet snow	17/05/99	09:55	394	2187	69°52 N, 024°25 E
	Wet snow	05/06/99	09:58	165	2187	69°52 N, 023°42 E
	Snow-free	21/06/99	09:55	394	2187	69°52 N, 024°25 E
Dovrefjell	Reference image	23/02/00	10:34	423	2349	62°06 N, 009°15 E
	Reference image	10/03/00	10:32	151	2349	62°06 N, 009°58 E
	Wet snow	29/03/00	10:34	423	2349	62°06 N, 009°15 E
	Wet snow	14/04/00	10:32	151	2349	62°06 N, 009°58 E
	Wet snow	03/05/00	10:34	423	2349	62°06 N, 009°15 E
	Snow-free	19/05/00	10:32	151	2349	62°06 N, 009°58 E

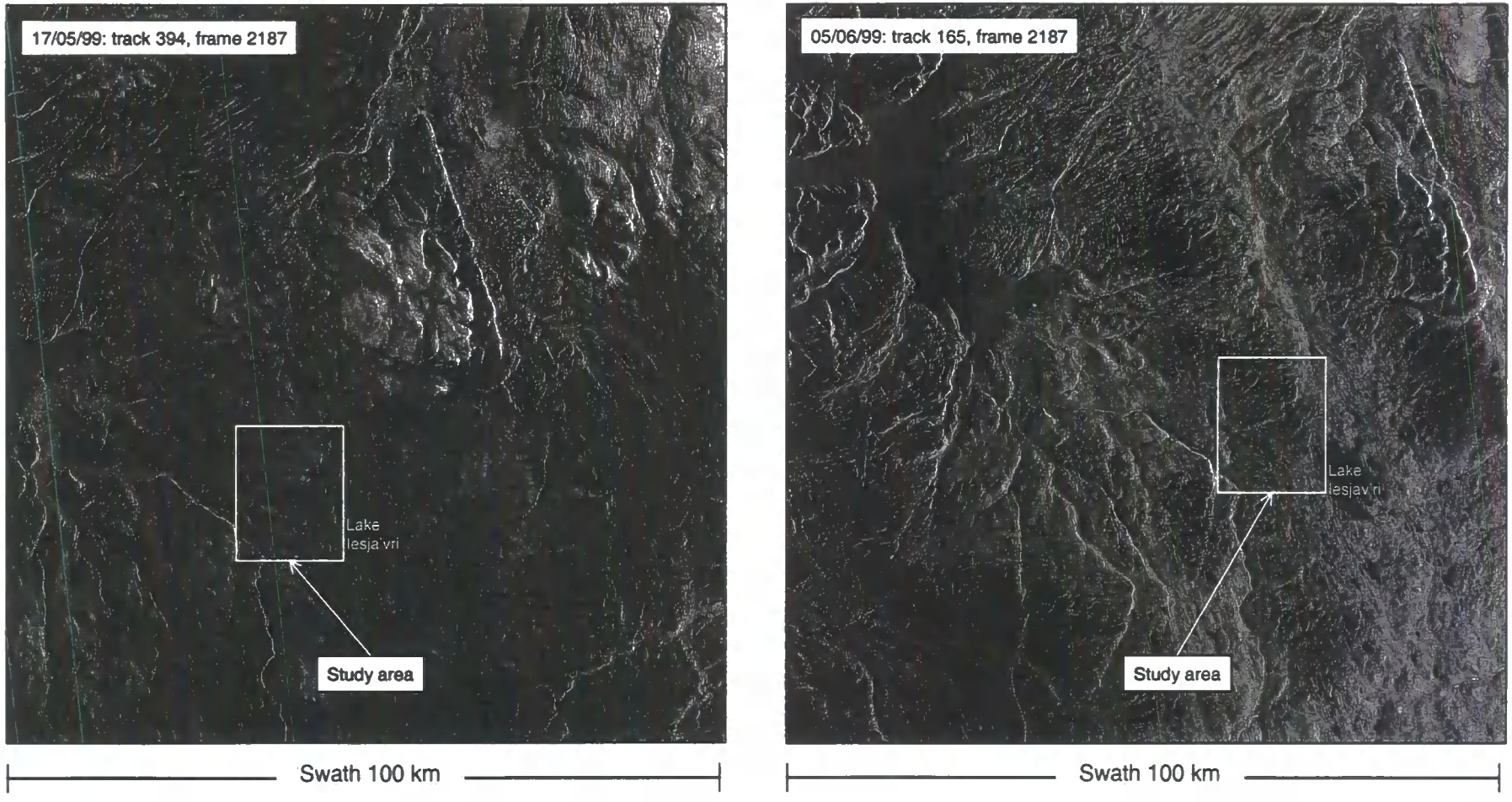

Figure 3.6. Relative location of study area within ERS-2 image frame for Joatka study site.

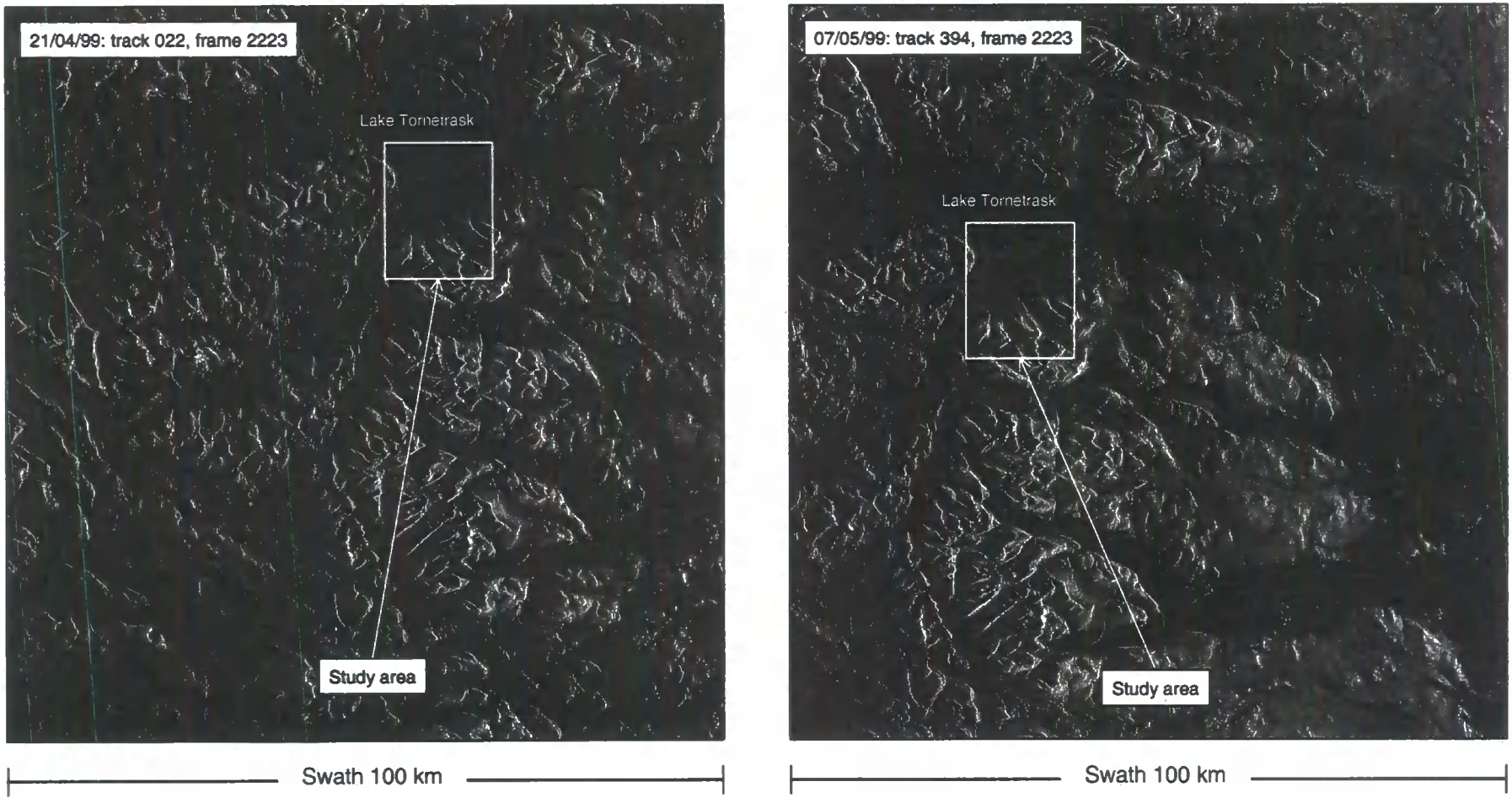

Figure 3.7. Relative location of study area within ERS-2 image frame for Abisko study site.

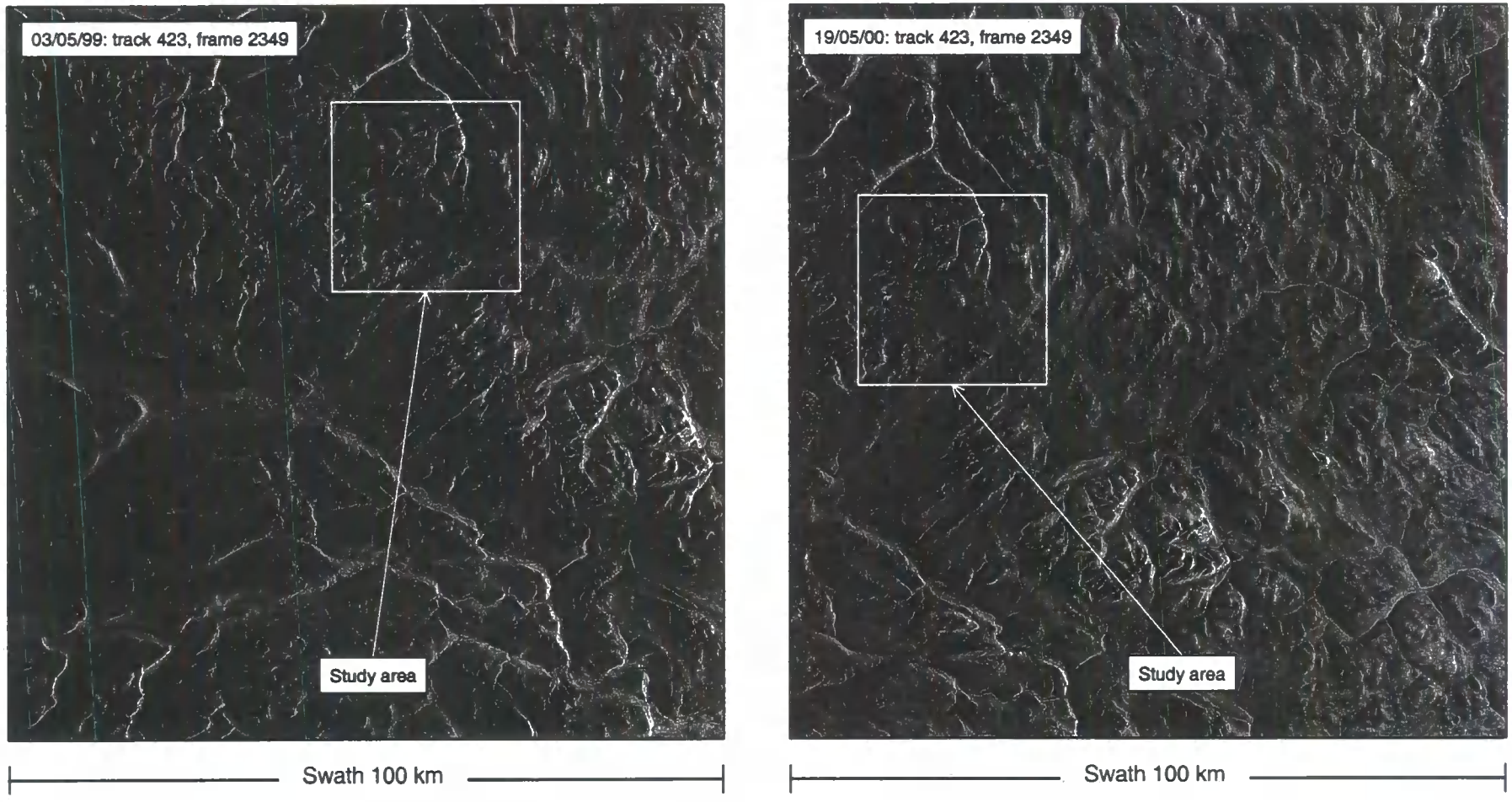

Figure 3.8. Relative location of study area within ERS-2 image frame for Dovrefjell study site.

3.5.2 Landsat TM Imagery

Landsat TM imagery provides imagery with a suitable spatial scale (30 m spatial resolution, 185 × 185 km spatial extent) for landscape-scale mapping of the vegetation at the forest-tundra ecotone. However, attenuation of VIR imagery by cloud cover despite the increased return frequency of the satellite at high latitudes (above the nominal repeat cycle of 16 days) means that the archive of Landsat TM imagery at each site is limited. Imagery had to be acquired in 1999 to meet project deadlines, and in 1999 a single Landsat ETM (Enhanced TM) with reasonable cloud cover was acquired at Abisko and Dovrefjell. At Joatka no such images were available and so an archive Landsat (5) TM image was acquired for this site. All Landsat TM imagery was from the United States Geological Survey (USGS) Earth Resources Observation Systems (EROS) Data Center. Details of imagery are given in table 3.2.

Table 3.2. Landsat TM imagery acquired at each site.

	Date	Landsat TM Sensor	Path	Row	Cloud cover % (scene average)
Joatka	16/07/87	5	195	011	10
Abisko	25/09/99	7	197	012	10
Dovrefjell	06/08/99	7	199	016	10

3.5.3 Aerial photography

A DEM at an appropriate resolution is an important prerequisite for geometric and radiometric correction of SAR imagery. Stereo aerial photography was acquired for creation of a high resolution DEM. Black and white stereo aerial diapositives were obtained for each study site from the relevant national agency; Lantmäteriet, SE-801 82, Gävle, Sweden and Fjellanger Widerøe Geomatics AS, 7486 Trondheim, Norway. Each diapositive was professionally scanned using a flatbed photogrammetric scanner (greyscale, 1000 pixels/inch) to minimise distortion; details are given in table 3.3. From the scanned photographs, given suitable horizontal and vertical locational ground control data, feasible horizontal pixel spacing for a DEM was estimated at 10 m and feasible vertical resolution at 5 m at each site. Ground control positions (GCPs) were collected using the **differential GPS** procedure, which was discussed in section 3.2.

Table 3.3. Photogrammetric values of aerial diapositives.

Study site	No. of photos	Image Scale	Camera / Lens	Calibrated focal length (mm)
Abisko	6	1:60000	Wild RC10	152.82
Joatka	9	1:40000	Wild RC5	152.51
Dovrefjell	12	1:40000	Zeiss RMK TOP 15	153.51

Since horizontal accuracy is superior to vertical accuracy in GPS positions, two types of GCPs were collected. A full GCP has accurately known horizontal and vertical components, whereas a horizontal GCP has no knowledge of the vertical component. Full GCP were taken at a number of previously surveyed locations (by a national mapping agency), where accurate elevation had been acquired using advanced surveying methods during acquisition of the photography. The geodetic datum of these elevations was WGS84, which matched the datum of GPS measurements. Typical locations were spot heights and numerous lakes.

An additional DEM of a larger area was made available at Dovrefjell, provided by Professor NR Sælthun (Norwegian Institute for Water Research, Oslo); the DEM was digitised from Statens Kartverk Dovrefjell Map Set 6 with 25 m contours.

3.6 Field vegetation survey

The aim of the vegetation survey was to record the location of vegetation communities for use as training and validation data for a supervised classification of the Landsat TM imagery. This requires sampling of vegetation communities over a large extent of each study area with a reasonable spacing of samples. The location of vegetation communities was recorded using a GPS and **position averaging** as discussed in section 3.2. The approximate location of samples was determined in advance using existing sources of spatial data that contained vegetation information: at each site the aerial photography was useful and at Dovrefjell and a 1:50,000 vegetation map (polygon-based) was available (Statens Kartverk, 3504 Hønefoss, Norway), while at Abisko a digitised 1:50,000 vegetation map was also available from Lantmäteriet.

Samples were collected during a late summer field campaign. Samples were taken from the accessible areas while ensuring sufficient spatial extent. Samples were also taken from relatively homogenous areas of vegetation, but an effort was also made to record

data for reference in more heterogeneous vegetation, to avoid optimistic bias and ensure it was representative. Collection of samples in close proximity was minimised to improve independence of samples; ignoring spatial autocorrelation might result in optimistic bias.

The vegetation survey was adapted from the hierarchical approach to classifying PFTs for Arctic ecosystems proposed by (Chapin III *et al.*, 1996; Walker, 2000), as shown in figure 3.9. A larger number of PFTs can be defined, but the final classification may be limited because of the measurement scale of Landsat TM relative to the spatial scale of variation in vegetation at each site and spectral differences between vegetation types.

3.7 Discussion

The data outlined in this chapter were required in order to fulfil the aims of the study. The data present challenges for integration because of the different measurement scales, in terms of measurement extent and resolution (pixel spacing) of the remotely sensed imagery. In addition, the temporal variation in data within and between sites demands caution. The acquisition of SAR imagery and field measurements was from a different year at Dovrefjell to Abisko and Joatka and the Landsat TM imagery was only concurrent with other data at Abisko. In particular, the archive Landsat TM imagery of Joatka must be treated with caution. However, given the slow rate of change of vegetation in Finmarksvidda, the use of this image is considered reasonable, and imagery acquired during the month where contrasts between vegetation types are maximised is probably superior to a more recent image acquired at other times.

The requirement for frequent imagery to properly monitor snow melt at the forest-tundra ecotone means that SAR imagery has been acquired under a different imaging geometry (different track). Therefore, a DEM of comparable resolution to the SAR imagery is a prerequisite to geometric and radiometric correction. Since no suitable digital elevation source was available, construction of a high-resolution DEM was required and suitable data were acquired; the aerial photography also afforded the opportunity for improved vegetation mapping.

Previous research involving radar remote sensing of snow melt has often used field data for interpretation of radar backscatter from a meteorological station a substantial distance from the study site, which is also of poor temporal resolution relative to the

image acquisition. This limits the confidence of using information obtained from the imagery in relation to changing environmental conditions. Here the focus was on concurrent field measurements within the study area.

Precautions have been taken to optimise all data quality. The errors associated with the GPS have been assessed and some propagation of error is likely during image geometric correction and in relating field measurements to the imagery. In defining the vegetation sampling protocol, it is important to consider that at landscape-scale the vegetation is often a complex mosaic and communities will often not reflect classification distinction. Further, no survey can deliver the "ground truth" needed for exact validation and no reference data can be truly representative of the entire classification. However, given the accuracy of the GPS and the nature of the data collected, it is reasonable to analyse field data in conjunction with the spatially explicit data to be generated with the GIS.

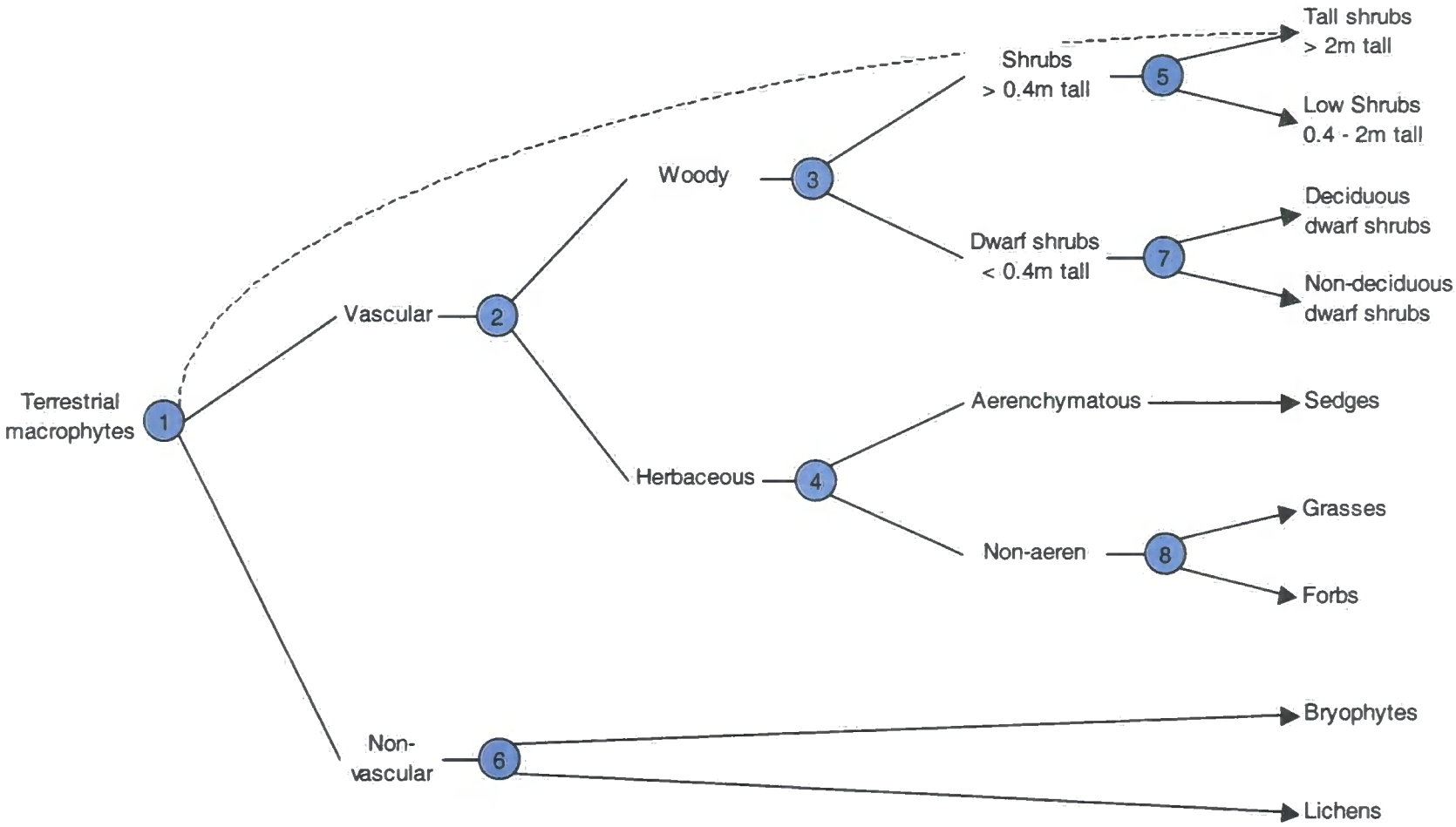

Figure 3.9. Hierarchical classification of arctic vegetation used for vegetation survey.

Chapter 4. Methods: VIR image processing

This chapter presents the image processing techniques undertaken on the VIR imagery: the aerial photography and Landsat TM imagery. A high resolution DEM was extracted for each site from the aerial photography. VIR imagery was geometrically corrected using standard image processing methods. Vegetation maps were created from Landsat TM imagery using a supervised maximum likelihood classifier (MLC) and accuracy assessment was also completed using conventional methods.

Since conversion of files between software formats can be problematic, all data were processed to conform to the relevant UTM map projection (Joatka and Abisko UTM 34N; Dovrefjell UTM 32N) with a WGS 84 datum.

4.1 DEM extraction from aerial photography

Within Erdas Imagine 8.3 (ESRI Imaging Solutions: ESRI(UK) Ltd., Aylesbury, UK) the Ortho*MAX* module was used for block triangulation and extraction of DEMs. The block triangulation procedure requires substantial manual-input; interior orientation/calibration is required using parameters from the camera calibration certificate and GCPs must be digitised between the stereo-pair photographs. The Block Tool allows the definition of different types of GCP: (c) full control point that has accurately known horizontal and vertical components, (h) horizontal control point that has no information on the vertical component, (v) vertical control point that has no knowledge of the horizontal component, and (t) tie point that simply provides a link between images. This allows the addition of tie points in locations that are difficult for ground data collection, and also the addition of an accurate vertical component to tie points which are placed at locations with an accurately surveyed height, such as lakes.

DEMs were extracted using the "DEM-Tool" at several resolutions from the original triangulation information. The software indicates the maximum resolution available, and given the high quality and density of the GCPs this was *ca.* 1 m in horizontal and vertical. However, for the requirements of this research a DEM with 12.5 m horizontal spacing and 1 m vertical precision was created. The accuracy of the DEM was estimated as *ca.* 5 m in horizontal and vertical dimensions.

4.1.1 DEM editing and evaluation

DEM extraction can produce considerable noise and errors in elevation values, this is especially noticeable on lake surfaces and if there is any cloud clover. There was little or no cloud in the photos for each study site, but the numerous lakes in each study area were not flat in the DEM and contained erroneous values because they have no features for the automatic DEM extraction to match on. PCI ImageWorks version 6.3 (PCI Geomatics: Henley on Thames, UK) provides a set of DEM editing tools for creating editing masks, interpolation, filtering, and smoothing. Corresponding ortho-photos were analysed to provide a mask for the lakes using the low grey values and distinctive low texture of lakes. Using the lakes mask, the correct elevation of large lakes was added manually from a relevant map source. For numerous small lakes interpolation was used using elevation at the shore of the lake, which resulted in a reasonably flat surface at approximately the correct elevation.

4.2 Landsat TM imagery

The focus of this research is the forest-tundra ecotone, primarily the distinction between forest and tundra and location of the treeline. However, it was interesting to consider additional classes of vegetation that form distinct parts of the landscape mosaic at each site, which are also relevant for the purposes of the DART project. Therefore, field vegetation sampling for image classification was conducted according to the hierarchical PFT classification shown in figure 3.9 (Chapin III *et al.*, 1996; Walker, 2000).

Imagery at each site was geometrically corrected and classified within Erdas Imagine 8.4 using standard techniques. In remotely sensed data classification, usually a supervised classification is performed, which, regardless of the particular technique, has three main stages:

(1) The training stage, which involves the statistical characterization of the classes that are to be mapped. This can involve characterization of reflected radiation signatures and temporal evolution of a signature and its association to various phenological attributes of a vegetation type.

(2) Pixels of unknown class membership are allocated by some predefined decision rule to the class to which they have the greatest similarity according to the training statistics.

(3) The third stage involves validation by assessing the correspondence of the known to the predicted land cover type, the most common method being a contingency table (Congalton, 1991).

Ancillary products such as a DEM are often used in attempts to improve spectral-based classifications, with data used before (e.g. stratification), during (additional bands), or following (post-classification recoding). However, no ancillary data were used in the classification process to ensure independence of vegetation data from other data sets. Further, training and reference data were separated and training data were not used in validation.

4.2.1 Training

Using an unsupervised classification (ISODATA algorithm), the nature of the spectral classes within the data was explored. Using this information and the ground control data, polygons were digitised using the onscreen editing tools with the aim of obtaining pure samples of each vegetation type in the conventional way.

The signatures were evaluated for divergence according to PFT type. The Transformed Divergence measure, which gives exponentially decreasing weight with increasing distance between classes (Erdas, 1999), identified classes that could not be separated. Training was repeated with edited, merged, and deleted samples in order to optimise the classification. The use of a single image at each site, spectral similarity of vegetation types, topographic effects, and the natural variability in the vegetation types (mosaics) meant that there were difficulties in defining suitable signatures for classification at higher levels of the PFT hierarchy.

4.2.2 Class allocation

There are numerous methodologies for the classification of remotely sensed data. The maximum likelihood classifier (MLC) was employed, which is one of the most widely used methods for supervised classification, e.g. Fuller *et al.* (1994). Using the mean spectral response and covariance matrix derived from the training statistics, the MLC determines the likelihood of each pixel belonging to each class. Unknown pixels are allocated to a class to which it has the highest likelihood of membership. Following class allocation, classes were combined to form the final classification product.

4.2.3 Evaluation

Accuracy assessment was conducted to evaluate the quality of the classified product. An error matrix was constructed, which compares the reference class values to the assigned class values in a $c \times c$ matrix, where c is the number of classes. The assessment calculated statistics of the percentage of correct correspondence (overall accuracy); total number of correctly classified cases divided by the total number of cases.

Even a completely random assignment of pixels to classes will produce correct values in the contingency table. The Kappa statistic, $\hat{k}$, is a measure of the actual agreement between reference data and the classification and the chance agreement between the reference data and a random classifier (Congalton, 1991). Conceptually, kappa can be defined as (Lillesand and Kiefer, 1994):

$$\hat{k} = \frac{correct - chance}{1 - chance} \qquad \textbf{Equation 4.1}$$

The value of kappa usually ranges between 0 and 1, with the values representing the percentage improvement over a random assignment of pixels. From a contingency table, the kappa statistic is computed (Lillesand and Kiefer, 1994):

$$\hat{k} = \frac{N \cdot \sum_{i=1}^{r} x_{ii} - \sum_{i=1}^{r} (x_{i+} \cdot x_{+i})}{N^2 - \sum_{i=1}^{r} (x_{i+} \cdot x_{+i})} \qquad \textbf{Equation 4.2}$$

where

r = number of rows in the contingency table

x_{ii} = number of observations in row i and column i (on the major diagonal)

x_{i+} = total of observations in row i

x_{+i} = total of observations in column i

N = total observations in contingency table

In considering the accuracy of classifications, only vegetation classes were included; classes such as water are relatively easy to classify and can inflate accuracy measures and are not important for this research.

4.3 Discussion

Key to the quality of SAR processing is the availability of a DEM of compatible resolution with the SAR data. With no suitable source of DEM available at Joatka and Abisko, a high-resolution product had to be produced that was compatible with the ERS-2 product. The advantage is that full control is gained over the resolution of DEM products and knowledge of the quality of inputs and methods of filtering and editing means that the limitations are known. The triangulation results indicated that the maximum resolution of DEM at each site was *ca.* 1 m in horizontal and vertical, but a conservative estimate of accuracy was 5 m horizontal and vertical. The large scale DEMs should resolve landscape features that influence the level of radar backscatter. This is essential if we are to extract the maximum possible information from the SAR data, which is required for mapping landscape-scale snow melt at the forest-tundra ecotone. At Dovrefjell, the digitised Statens Kartverk DEM is useful because of its larger spatial extent.

Chapter 5. Methods: ERS-2 SAR image processing

This chapter presents the image processing techniques required to reduce image speckle and conform the ERS-2 SAR imagery into map geometry for integration within a GIS. The first operation on the images was the application of a speckle filter. Following this, the DEMs extracted from the aerial photography were used to geometrically correct the SAR images. The final stage is the radiometric correction of the SAR imagery, which is the correction of the SAR backscatter for the variation the angle of the incident radar cause by topography. Several simple correction models for incidence angle variation are discussed.

ERS-2 imagery was received on compact disc from the UKPAF (UK Processing and Archiving Facility) as the standard ESA ERS-2 Precision Image (PRI). PRI images are geometrically corrected from slant range (range from sensor to target) to a nominal ground range (horizontal range from nadir), SAR antenna pattern gain (the change in brightness toward the near and far range of an image), and range spreading loss (Laur *et al.*, 1998). Each pixel is related to the radar brightness β^0 as follows (Laur *et al.*, 1998):

$$DN = \sqrt{\beta^0} \qquad \textbf{Equation 5.1}$$

where DN is the value of each pixel in the PRI image.

5.1 Speckle filtering

Speckle filtering was undertaken in radar geometry within ERS SAR Toolbox (ESA, 1999), a command-line driven collection of image manipulation tools developed specifically for ERS SAR data. The pre-processing at UKPAF means that the ERS-2 imagery has 3-looks, but additional speckle filtering was employed using a moving kernel of 7×7 dimension and the Gamma MAP algorithm (Capstick and Harris, 2001; ESA, 1999). A comparison of unfiltered and filtered imagery is shown in figure 5.1.

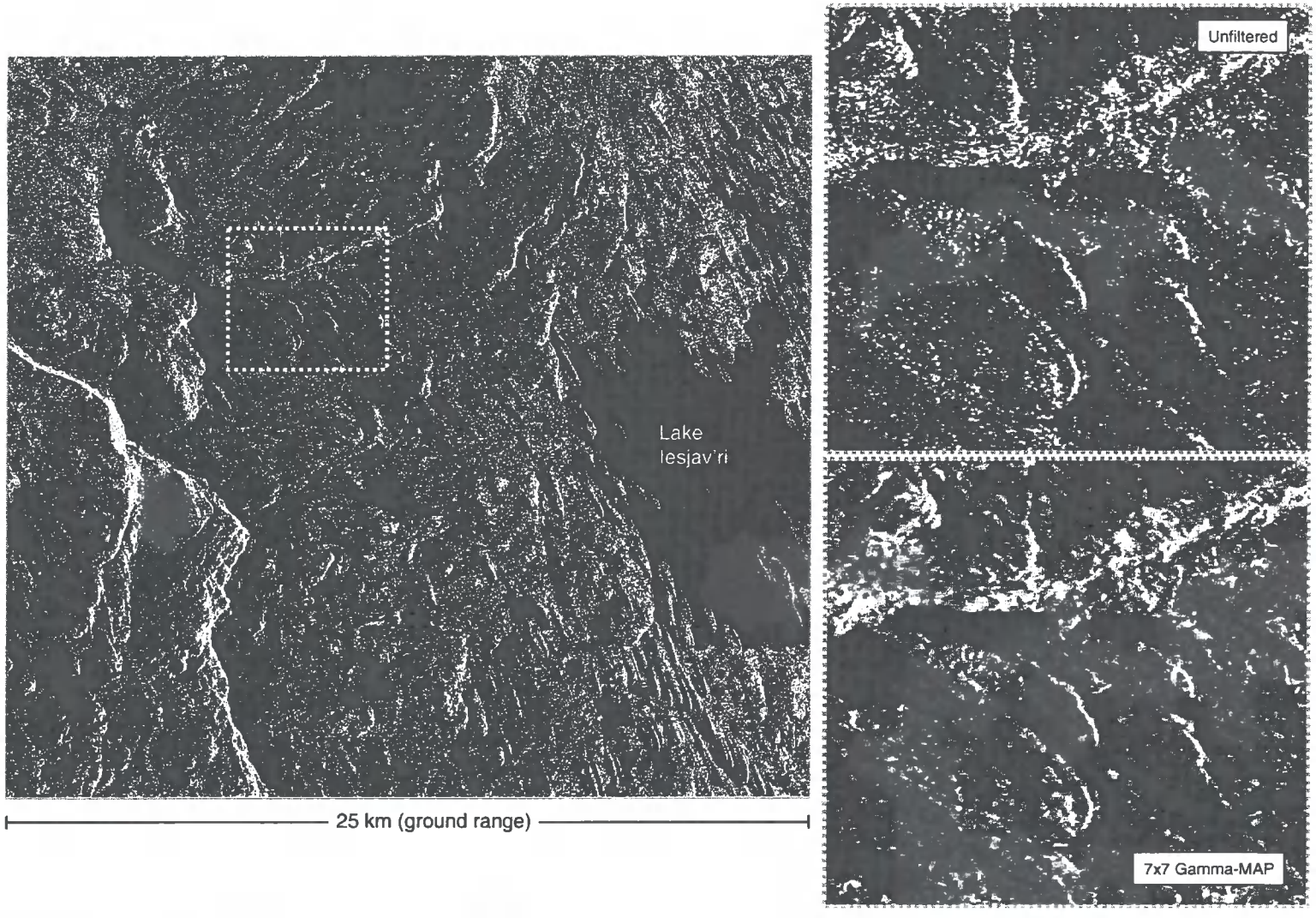

Figure 5.1. Example of Gamma MAP speckle filter of image acquired over Joatka study site.

5.2 Geometric correction

Geometric correction was undertaken using PCI EASI/PACE Version 6.3. In the first stage a simulated ERS-2 image was created for each study site using the DEM and Xpace Radar Analysis tools. The resulting ground range simulated SAR image had simulated distortions caused by the imaging geometry of the SAR system. The simulated image enabled the collection of GCPs to tie the SAR image to the DEM, which would be otherwise difficult in mountainous terrain because of the distortion in the SAR image. A particularly high number of GCPs were possible because of the high resolution of the DEM. The uncorrected SAR image, simulated SAR image, DEM, and the set of GCPs were used to transform each image into map geometry.

Production of the simulated ERS-2 images within PCI also enables production of layover and shadow masks, which are useful for incorporation into the GIS. All images were processed to conform to the relevant UTM map projection (Joatka and Abisko UTM 34N; Dovrefjell UTM 32N) with a WGS84 datum.

5.3 Incidence angle correction models

As discussed in chapter 2, the side-looking imaging technique of SAR means that backscatter will show variations due to the local incidence angle θ. A fundamental aim of most research using SAR imagery is the removal of the topographic effects because the variation in backscatter as a function of incidence angle essentially masks variation due to other factors, which are the factors of interest. The stability of ERS-2 SAR orbit means that the ratio of images relative to a reference image should, for practical purposes, remove the incidence angle dependence of ERS-2 backscatter. The ratio images can then be investigated for information content regarding snow cover. However, images were acquired from different orbits to improve temporal resolution of snow mapping, which means that investigation of the effect of incidence angle on backscatter was necessary.

Essentially, the value β^0 (equation 5.1) given by Laur *et al.* (1998) represents the incidence angle –dependent radar backscatter, which is subsequently defined as $\sigma^0(\theta)$. The simplest backscatter models interpret topographically dependent backscatter $\sigma^0(\theta)$ as being equal to topographically normalised backscatter σ_n^0 and some function of incidence angle $f(\theta)$ (e.g. Shi and Dozier (1994); Guneriussen (1997)):

$$\sigma^0(\theta) = \sigma_n^0 \cdot f(\theta)$$ **Equation 5.2**

The aim was to produce incidence angle –normalised backscatter, so equation 5.2 must be re-arranged:

$$\sigma_n^0 = \sigma^0(\theta) \cdot \frac{1}{f(\theta)}$$ **Equation 5.3**

However, the *reference* incidence angle α of ERS-2 for flat terrain is 23°. Therefore the incidence angle correction of the SAR imagery must be calculated relative to the reference incidence angle. To adjust backscatter relative to a reference incidence angle we define a correction function $c(\theta)$ that takes the reference incidence angle into account:

$$\sigma_n^0 = \sigma^0(\theta) \cdot c(\theta)$$ **Equation 5.4**

where

$$c(\theta) = \frac{f(\alpha)}{f(\theta)}$$ **Equation 5.5**

and $f(\alpha)$ is the value of function for angular dependence determined for the reference incidence angle for a horizontal surface.

5.3.1 Cosine correction

Simple surface scattering models based on a cosine function were introduced by Ulaby *et al.* (1982a; 1982b):

$$\sigma^0(\theta) = \sigma_n^0 \cos\theta$$ **Equation 5.6**

$$\sigma^0(\theta) = \sigma_n^0 \cos^2\theta$$ **Equation 5.7**

The models in equation 5.6 and 5.7 are based on theoretical surfaces that are collections of small spherical scatterers. Equation 5.6 is based on the fact that area of the surface illuminated increases with increasing incidence angle, which means that the scattering per unit area would be decreased. Equation 5.6 represents scattering based on Lambert's Law, where it is assumed that scattering is in accordance with a cosine law rather than being isotropic for each sphere. Since the incident power per unit area also decreases according to a cosine law, the product results in the angular dependence of $\cos^2\theta$. Although the Lambertian model is simple and idealised, natural physical surfaces do sometimes show this behaviour (Rees, 2001) and both models are commonly used in the remote sensing field (Ulaby *et al.*, 1982b).

A familiar application of this form of correction is topographic normalisation of VIR imagery. The cosine correction for VIR imagery assumes a surface reflects incident radiation uniformly in all directions (i.e. equation 5.6):

$$DN_n = DN\frac{\cos\alpha}{\cos\theta} \qquad \textbf{Equation 5.8}$$

where DN is the reflectance value in a VIR image and DN_n is the cosine normalised value. For solar radiation the reference incidence angle is 0°, i.e. nadir, which means that equation 5.8 is often simplified to:

$$DN_n = \frac{DN}{\cos\theta} \qquad \textbf{Equation 5.9}$$

Cosine models have been used to correct SAR data (Teillet *et al.*, 1985), where $\cos\alpha$ depends on the reference incidence angle of the SAR system. A simple cosine correction based correction for SAR imagery is:

$$\sigma_n^0 = \sigma^0(\theta)\frac{\cos^2\alpha}{\cos^2\theta} \qquad \textbf{Equation 5.10}$$

5.3.2 Inverse sine correction

Laur *et al.* (1998)[1] state that in ERS-2 imagery, the radar brightness β^0 is equal to the incidence angle –normalised backscatter coefficient σ_n^0 divided by the sine of the local incidence angle. Therefore, with reference to equation 5.2:

$$f(\theta) = \frac{1}{\sin\theta} \qquad \textbf{Equation 5.11}$$

Essentially, this model represents the angular dependence of backscatter as an inverse sine law. Therefore, inserting equation 5.11 into equation 5.5 gives the correction function as:

$$c(\theta) = \frac{\sin(\theta)}{\sin(\alpha)} \qquad \textbf{Equation 5.12}$$

Therefore, incidence angle –normalised backscatter was calculated according to:

$$\sigma_n^0 = \sigma^0(\theta)\cdot\frac{\sin\theta}{\sin\alpha} \qquad \textbf{Equation 5.13}$$

---

[1] See *Laur et al.* (1998) Section 1 – introduction, where this relationship is stated clearly for the only time in the document.

5.3.3 Modified Muhleman model

Guneriussen (1997), referring to Stiles and Ulaby (1980), introduces the modified Muhleman scattering model to describe the incidence angle dependence of backscatter[2]. The Muhleman model is an empirical model based on Bragg scattering. The Bragg scattering mechanism is largely thought to be responsible for reflection of microwave scattering from small scale (of the order of 1 cm) roughness on water surfaces, especially if the Bragg scattering has a dominant spatial frequency, in which case it is said to be resonant (Rees, 2001). As such, Bragg models have been used for ocean and geologic surfaces, with extensive research into scattering from ocean waves e.g. for ocean wind speed measurements and oil slick detection (Quilfen *et al.*, 1999). The use of the Muhleman model for monitoring snow melt by Guneriussen (1997) was novel. The model is given by:

$$\sigma^0(\theta) = \sigma_n^0 \cdot \frac{a\cos\theta}{[\sin\theta + b\cos\theta]^3} \qquad \textbf{Equation 5.14}$$

where the empirical constants for ERS are $b = 0.1$ and $a = 0.0133$ (Guneriussen, 1997). The Muhelman model can be used to create the incidence angle correction function in equation 5.5, but this is not reproduced here.

5.3.4 Empirical correction models

Often an empirical backscatter model is used to explain variance in backscatter in relation to incidence angle instead of physically based models (e.g. Bayer *et al.* (1991); Goering *et al.* (1995); Goyal *et al.* (1998); Rees and Steel (2001)). Application of empirical models has been successful, but they are obviously limited to specific locations and surface conditions.

5.3.5 Comparison of correction models

The correction function $c(\theta)$ can be graphically represented across a range of incidence angles relative to the reference incidence angle for ERS-2 ($\alpha = 23°$). If backscatter is expressed in decibels then equation 5.4 is equivalent to:

$$\sigma^0_{n\,dB} = \sigma^0_{dB}(\theta) + c_{dB}(\theta) \qquad \textbf{Equation 5.15}$$

Correction models are displayed in figure 5.2; note that at 23° each model has correction of 0 dB.

---

[2] Stiles and Ulaby (1980) does not contain any reference to the Muhleman model.

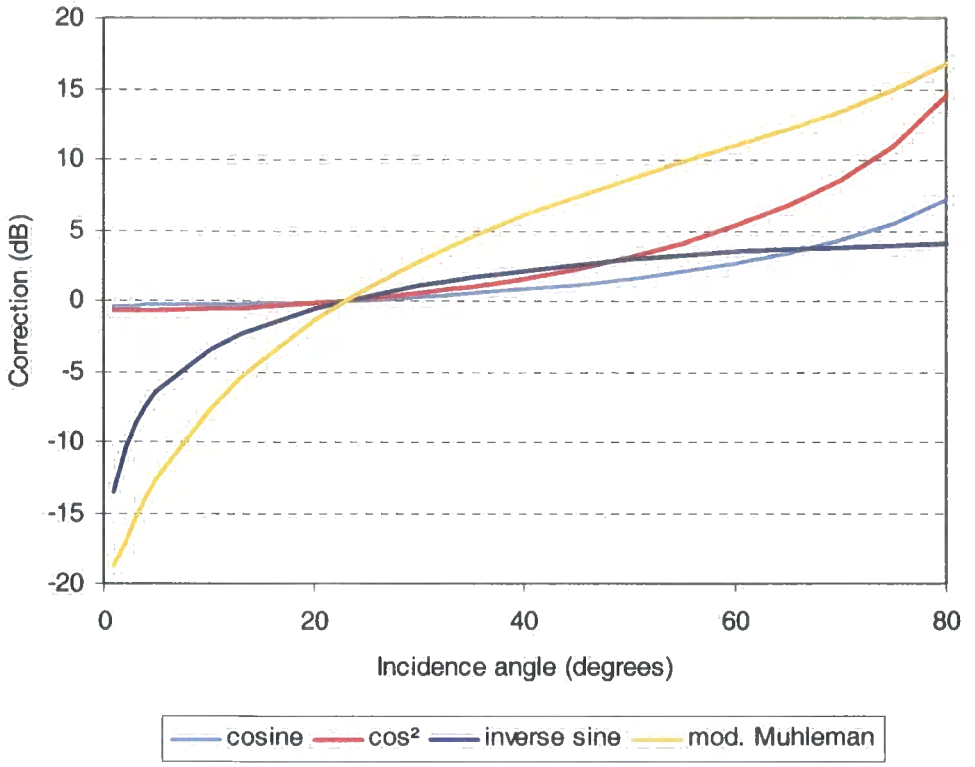

Figure 5.2. Correction functions for incidence angle for ERS SAR data.

It is clear from figure 5.2 that the choice of topographic correction model can have a significant impact on backscatter. The cosine corrections have the lowest correcting effect on backscatter values, especially over the range of incidence angles close to the horizontal plane. The Muhleman has the highest corrective effect, particularly at low incidence angles. The inverse sine correction is approximately linear between 15-35°, but increases its corrective power at low incidence angles.

5.4 Calculation of local incidence angle

In order to correct SAR backscatter using any of the models introduced in section 5.3, a map of local incidence angle was required. This involves taking into account the variation in local topography in relation to the movement of the satellite platform (the orbit vector) to produce a value of the local slope in the direction of the satellite sensor. However, at the time of analysis, no software package was available in which the incidence angle could be calculated while taking the orbit vector of the satellite into consideration.

I therefore made the decision to create a map of local incidence angle using available software in which all DEM pixels are related to one orbiting position. Given the small

study areas in this research, this assumption was considered reasonable given the simplification of processing that results. Maps of local incidence angle were created for each study area using both SAR Toolbox and PCI functionality. The SAR Toolbox Geometric Correction module can be used to determine the ERS-2 satellite position (x,y,z) for specified image rows and columns on an individual pixel basis. Using this functionality, satellite position was located for the centre of each study area for the different satellite tracks in each image. This location for the satellite was subsequently used with the PCI EASI/PACE ANG (Incidence angle) function to create a map of incidence angle based on this position.

In light of this problem in generating an incidence angle product, I decided to use the simple physical models introduced in section 5.3 to investigate the theoretical impact of the different ERS-2 image geometries on backscatter. The aim was to assess the implication of using image ratios on images from different orbit tracks that have been accurately geometrically corrected.

5.5 Effect of imaging geometry

A (dry snow) reference SAR image from the same imaging geometry was not available for one image at Joatka (05.06.99) and potentially not available at Abisko depending on snow conditions. At Dovrefjell, a reference scene was available for each image track, but the same analysis was undertaken. It was understood that the difference in the ERS-2 image track resulted in a different incidence angle for identical ground locations between the images from different tracks. Table 5.1 provides an example of difference in incidence angle for a location at the centre of each study area for different image tracks. The difference depends on latitude of the study site, because this influenced the overlap of the SAR scenes. The difference is less than 2° at Joatka and Abisko.

Table 5.1. Incidence angle for different image tracks at each study site.

Site	Centre of study area (lat., long.)	Date	Image track, frame	Image row, col	θ
Joatka	69.75 °N, 24.00 °E	21/06/99	394, 2187	5410, 4774	23.72°
		05/06/99	165, 2187	4688, 2650	21.85°
Abisko	68.35 °N, 18.81 °E	02/04/99	251, 2223	2833, 5759	24.62°
		21/04/99	022, 2223	1907, 3466	22.62°
Dovrefjell	62.3 °N, 09.61 °E	03/05/00	423, 2349	2009, 2954	22.11°
		19/05/00	151, 2349	3077, 5798	24.62°

Using θ from table 5.1 and the topographic correction models from section 3.5, the theoretical impact of the different imaging geometries can be quantified. Table 5.2 shows the value of the correction functions in decibels $c(\theta)_{dB}$ for the different image tracks used at each site. Table 5.3 shows the modelled difference in backscatter for each image track.

Table 5.2. Backscatter correction functions (dB) for incidence angle of difference image tracks relative to reference incidence angle (23°).

	Joatka		Abisko		Dovre	
Track	165	394	022	251	423	151
Incidence angle	21.85°	23.72°	22.62°	24.62°	22.11°	24.62°
Cosine	-0.036	0.024	-0.012	0.054	-0.036	0.054
Cos^2	-0.072	0.047	-0.024	0.108	-0.072	0.108
Inverse sine	-0.211	0.126	-0.068	0.278	-0.211	0.278
Muhleman	-0.525	0.318	-0.171	0.705	-0.525	0.705

Table 5.3. Modelled difference in backscatter (dB) between image tracks

	Difference in backscatter (dB)		
Model	Joatka	Abisko	Dovrefjell
Cosine	0.06	0.066	0.09
Cos^2	0.119	0.132	0.18
Sine (Laur)	0.337	0.346	0.489
Muhleman	0.843	0.876	1.23

The impact of different image track is dependent on latitude because this determines the overlap between tracks. The cosine models produce a small difference in backscatter for the different image tracks, whereas the inverse sine model gives values between 0.3 to 0.5 dB depending on the site. The Muhleman models produce the greatest difference, between 0.8 to 1.2 dB.

5.6 Implementation of incidence angle correction

The correction models in section 5.3 were used in section 5.5 to assess to assess the influence of different imaging geometry between reference and other images. Essentially, if the inverse sine correction were implemented, then the correction applied to images of different image rack would be differ by less than 0.35 dB at Joatka and Abisko. Since only Joatka and Abisko are affected by the problem of different orbit tracks for a reference and a change image, it was reasonably assumed that image ratioing of all images could be undertaken. It is very likely that the impact of geometric correction and (unresolved) speckle on backscatter will be greater than the impact of different orbit tracks.

5.6.1 Inverse sine correction

The incidence angle normalisation given in equation 5.13 was implemented within ERS SAR Toolbox. This correction was undertaken following speckle filtering but before geometric correction, meaning that the imagery is in nominal ground range. Therefore, within SAR Toolbox, flat terrain is assumed and the incidence angle only varies from approximately 19.5° at near range to approximately 26.5° at far range. In addition to equation 5.13, Laur *et al.* (1998) include a calibration constant, which is dependent on the image processing facility. Therefore, for ERS-2 PRI products, incidence angle – normalised backscatter was calculated according to:

$$\sigma_n^0 = \sigma^0(\theta) \cdot \frac{1}{k} \cdot \frac{\sin\theta}{\sin\alpha} \qquad \textbf{Equation 5.16}$$

where k is the calibration constant = 666110 for imagery pre-processed at UKPAF (UK Processing and Archiving Facility).

Following the application of this correction, the geometric correction was implemented as in section 5.2. The implementation of image processing is illustrated in figure 5.3. This figure summarises the application of the speckle filter, backscatter correction, and

image co-registration of images of the same geometry within SAR Toolbox. Co-registration involves a simple linear shift in range and azimuth between a master image and slave images and is possible because of the stability of the ERS-2 orbit.

Co-registration of images enables more efficient geo-rectification of images within PCI because only one set of GCPs is required for each image set. The simulated ERS-2 image and layover and shadow masks were created using the DEM and parameters including the ERS-2 platform heading angle, altitude above sea level, and SAR minimum look angle. The final procedure is the geometric correction of each SAR image, using the GCPs that tied the uncorrected image to the simulated image and the DEM.

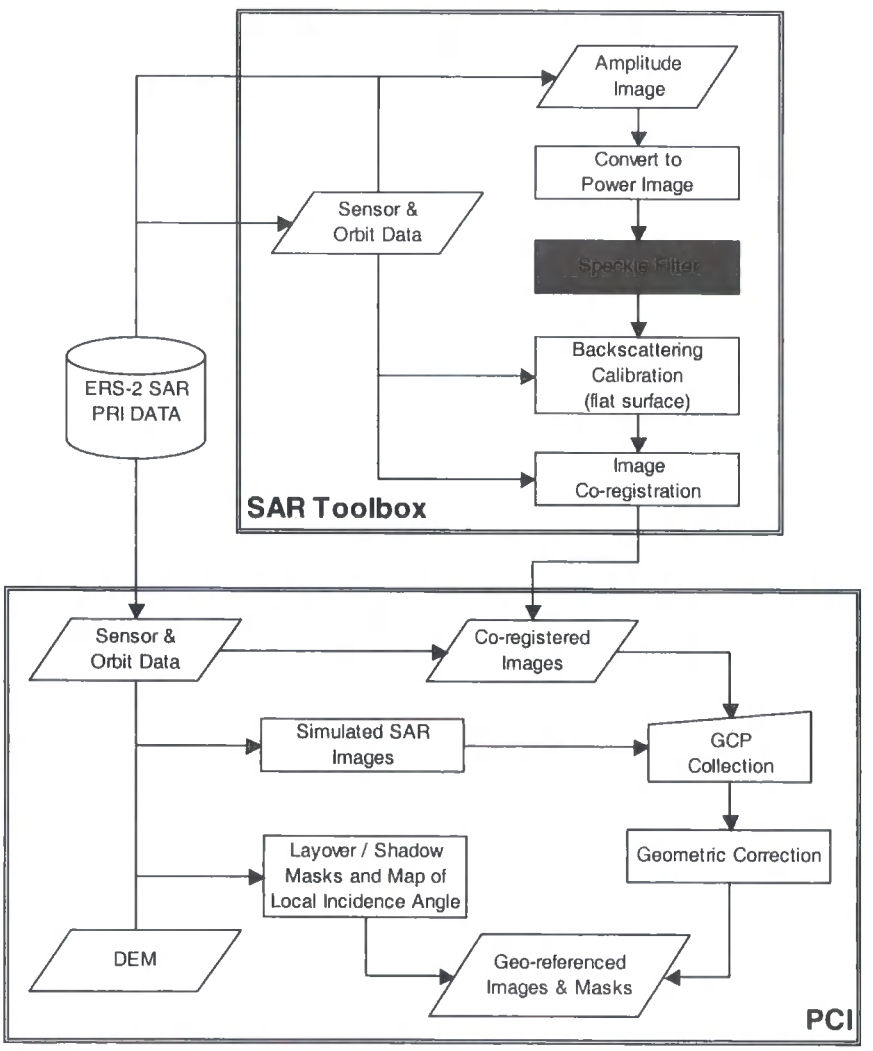

Figure 5.3. ERS-2 SAR image processing methodology.

5.7 Discussion

Topography is known to have a major influence on radar backscatter (e.g. Domik *et al.* (1988); Bayer *et al.* (1991); Hinse *et al.* (1988); Guneriussen (1997)). The removal of the topographic effects is often a primary consideration for most SAR studies because the variation in backscatter as a function of incidence angle essentially dominates variation due to other factors, which are the factors of interest.

Simple physical models are often used to "correct" images for the effects of incidence angle. However, it was shown that the magnitude of the correction of backscatter differs substantially depending on model selection, therefore the choice of model is important. Often, an empirical relationship is used, which means that correction is site specific. The comparison of correction models was conducted as part of an assessment of the impact of the different imaging geometry of the ERS-2 images at Abisko and Joatka. The impact of differences in incidence angle of 2° or less for the different image tracks was found to have a theoretical impact of less than 0.35 dB for flat terrain. However, these simple models do not take into account surface roughness. There could possibly be a change in effective surface roughness in addition to the effects of the change in incidence angle.

An examination of the correction models is relevant in the context of SAR systems in which the acquisition geometries are more variable. The image modes offered by Radarsat and Envisat can result in highly variable SAR acquisition geometries and therefore increase the need for application of incidence angle correction models for images over mountainous terrain. Consideration of which simple model to apply is more important given the very wide range of incidence angles possible with such SAR systems. Development of software tools to create accurate maps of incidence angle is required, otherwise application of SAR imagery to a study may require processing beyond the capabilities of many current users.

A correction for topographic effects must also consider the resolution or scale of the DEM. While not explicitly considered here, we must recognise that slope, including slope in the direction of the incident radar, is a property of scale. Teillet *et al.* (1985) reported that simple cosine based corrections were inadequate and over-corrected SAR data in mountainous terrain. However, a graphical representation of the cosine correction functions in figure 6.3 suggests that the cosine function is a less powerful

correction function than other models, except at very high incidence angles. Suggestions of over-correction or under-correction of terrain effects on backscatter must also consider the scale of the elevation data; a physical process cannot be modelled successfully unless data are available at an appropriate scale. For example, (Goyal *et al.*, 1998) found that DEM resolution significantly changed the amount of variation in backscatter explained by incidence angle.

In this research the geometric correction of the ERS-2 imagery was considered successful because qualitatively the ERS-2 imagery and other geo-referenced datasets were overlayed with satisfactory results. However, a quantitative assessment of accuracy of geometric correction is difficult to evaluate. The high resolution of the DEMs and creation of simulated images meant that a large number of GCPs were available The geometric correction is estimated to be accurate within 1-2 pixels in range and azimuth and the use of pixel-by-pixel multi-temporal image comparison is reasonable.

Chapter 6. Results: Vegetation and topography using VIR imagery

This chapter presents the results of the supervised classification of Landsat TM imagery at each site. The supervised maximum likelihood classification (MLC) was employed and an independent subset of the vegetation field survey data was used for training and validation. Accuracy was assessed in terms of overall correspondence and using the Kappa statistic. The classification scheme employed was a hierarchical classification of plant functional types, in which the dominant PFT in an assemblage was the allocated vegetation class in training.

High resolution DEMs were created using stereo-aerial photography. Subsequently, derivatives of elevation were created using a GIS. The aim was to create ecologically significant gradients that are important in determining the vegetation composition and the patterns of snow melt.

6.1 Topographic variables

In addition to elevation itself, derivatives of the elevation surface were calculated including slope aspect. Derivatives of elevation are calculated by relating a cell to its neighbours.

6.1.1 Elevation

There is a systematic decrease in mean surface temperature with increasing elevation and topographic relief can exert a much sharper control on surface temperature than latitude or longitude, especially in complex terrain (Joyce, 2000). In many cases elevation is used as an indirect means of accounting for the spatial variations in temperature and or precipitation (Moore *et al.*, 1991). Elevation for each study area is depicted in figures 6.1 to 6.3.

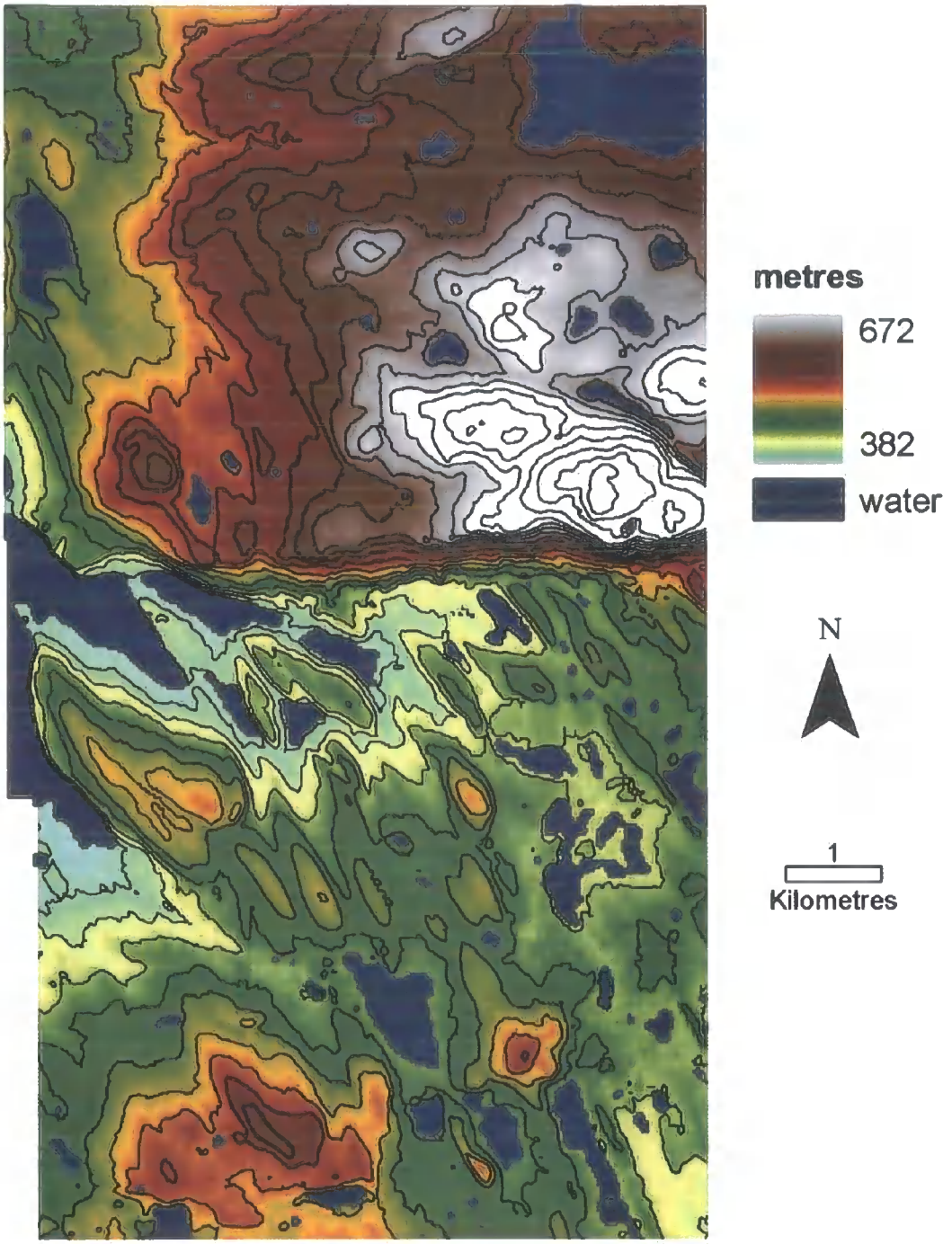

Figure 6.1. DEM created over Joatka study site with 15 m contours.

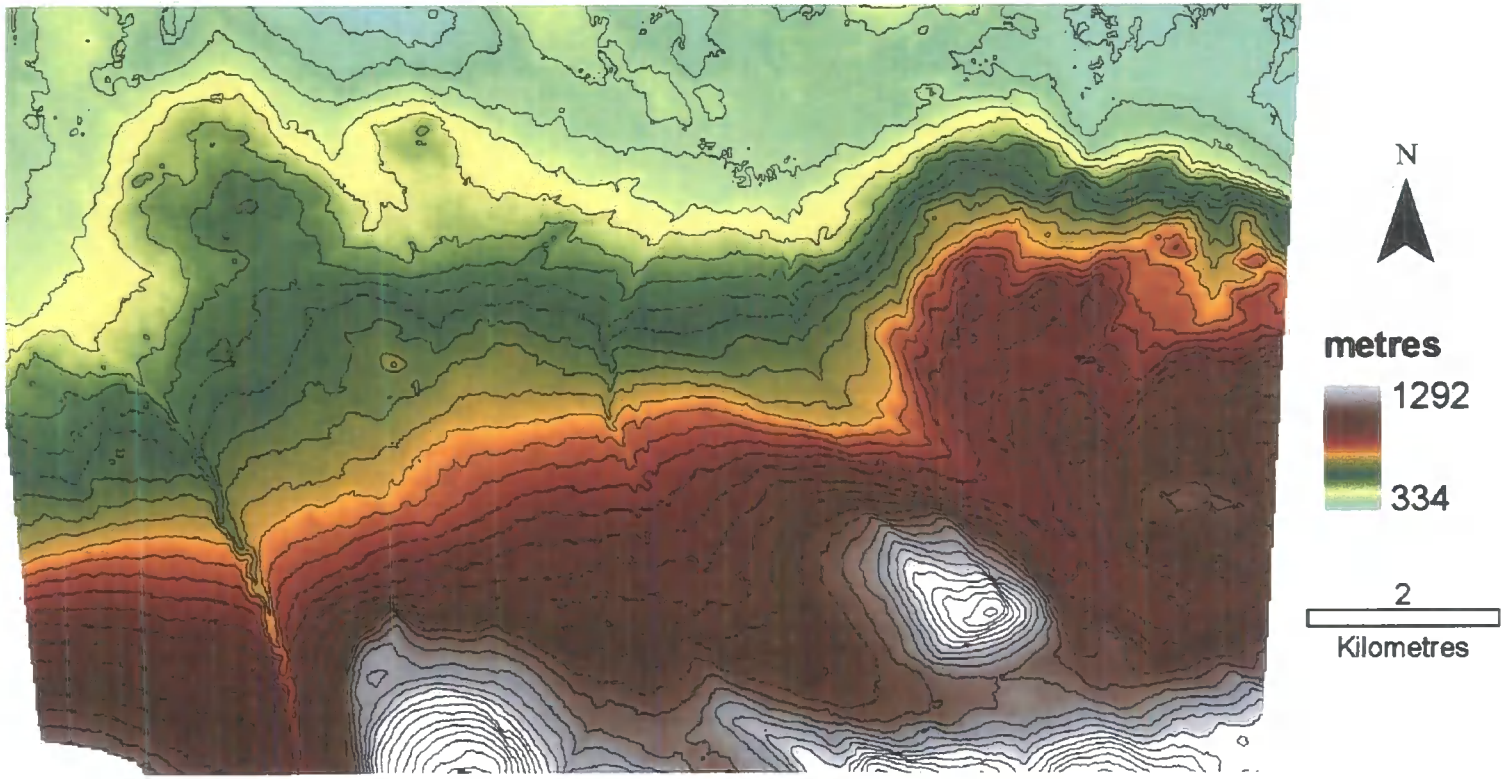

Figure 6.2. DEM created over Abisko study site with 25 m contour lines.

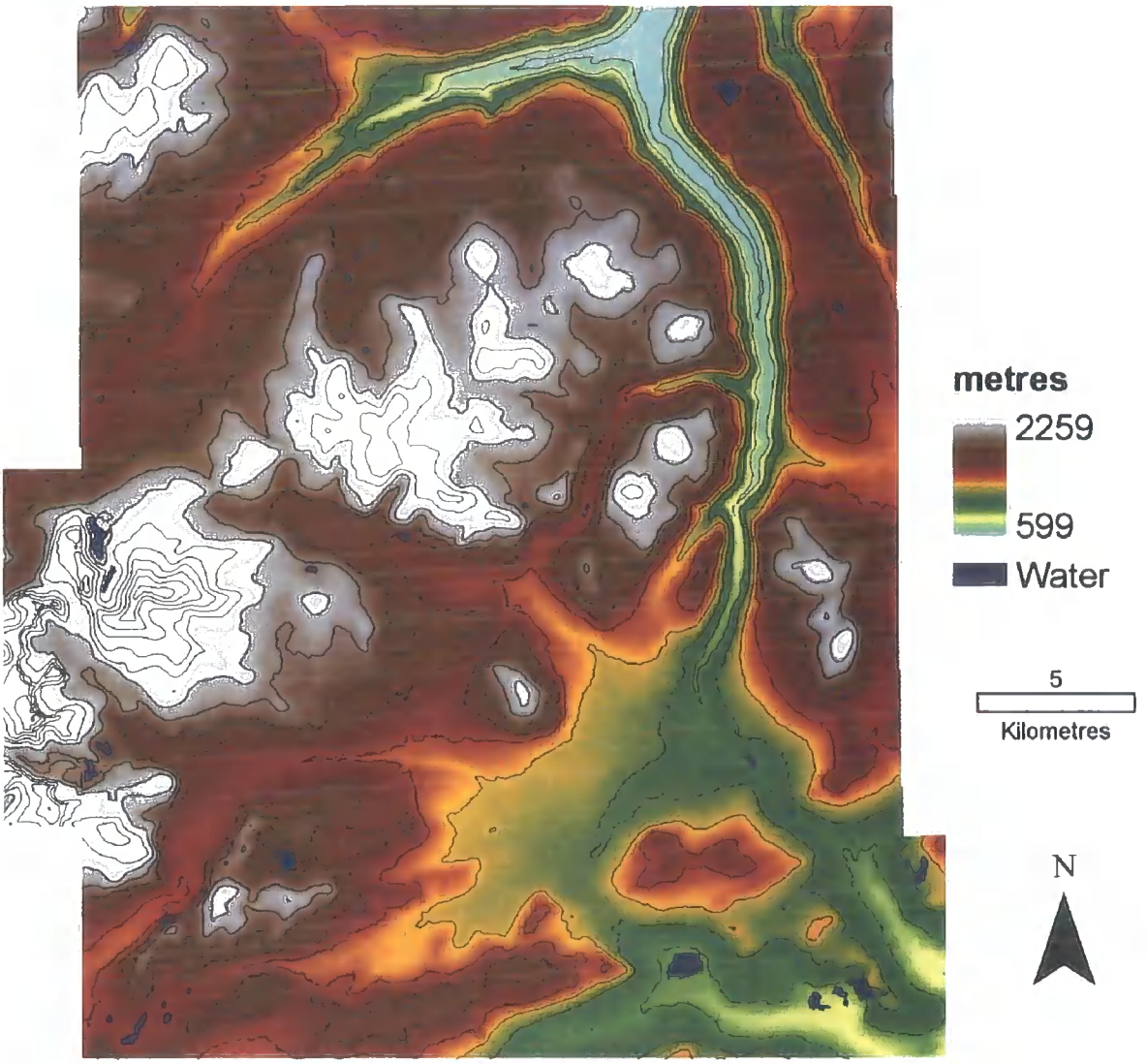

Figure 6.3. Digitised DEM over Dovrefjell study site with 100 m contour lines.

6.1.2 Slope aspect and slope gradient

Slope aspect can be an important control on direct beam solar radiation receipt at a given location, in conjunction with slope gradient. Slope aspect is the orientation of the local slope gradient. Together, these topographic variables may influence the radiation budget at the surface and hence air temperature (Joyce, 2000). Figures 6.4 to 6.6 show the resulting slope surfaces.

Slope gradient was calculated using the slope function in Arc/Info. The function returns the maximum rate of change in elevation from each grid cell to its eight nearest neighbours (3 × 3 neighbourhood). Output values range from 0 to 90 degrees. Slope aspect was calculated using the aspect function in Arc/Info. This identifies the direction of maximum slope gradient for each grid cell and is expressed in degrees from 0 to 360 degrees measured clockwise from north. Horizontal surfaces are allocated a value of –1. The positive degree values were converted to radians and a negative cosine calculated, meaning that south-facing slopes are assigned maximum values and north facing slopes minimum values. This transformation allows aspect to serve as a surrogate for incident solar radiation.

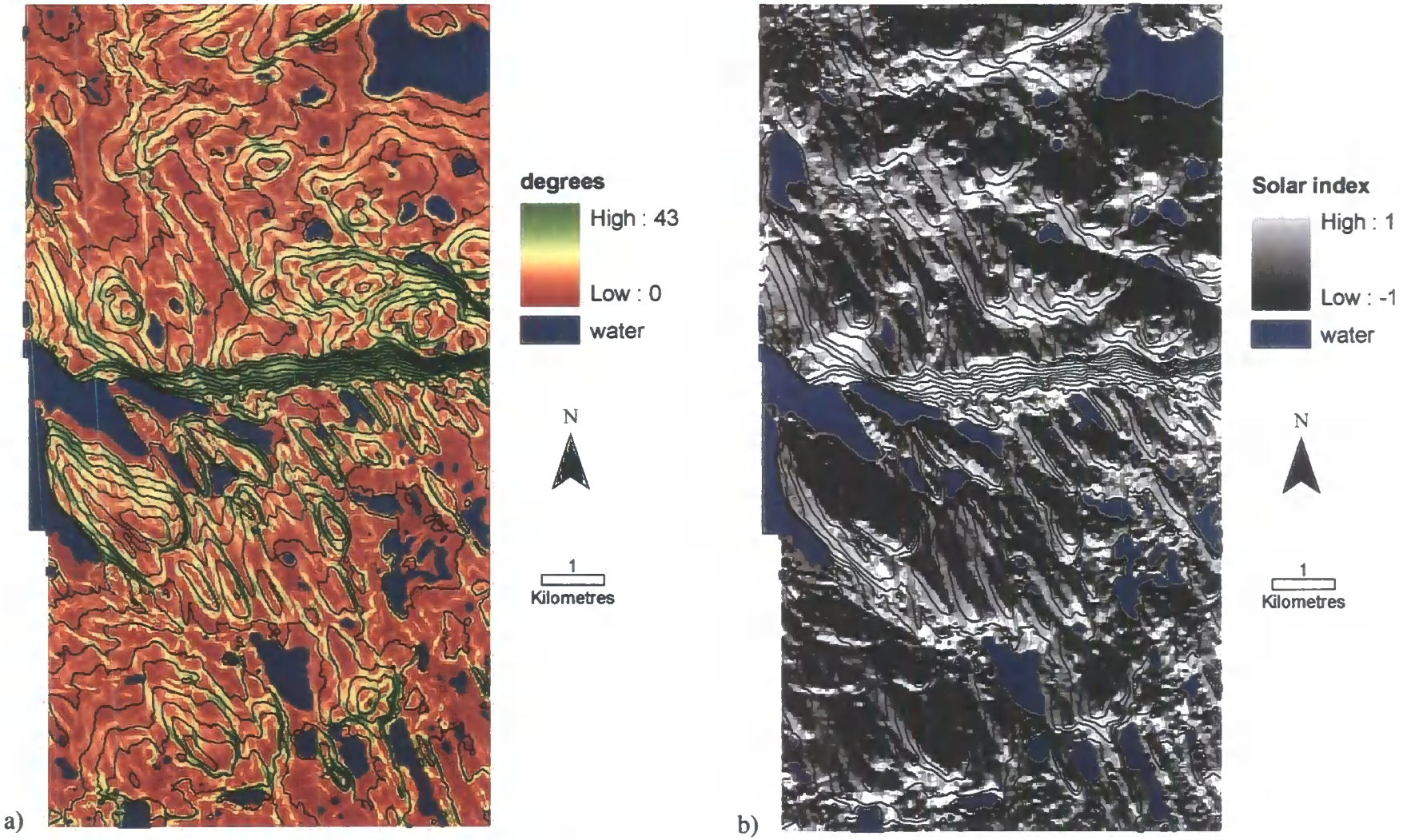

Figure 6.4. (a) Slope gradient and (b) solar radiation index derived from Joatka DEM.

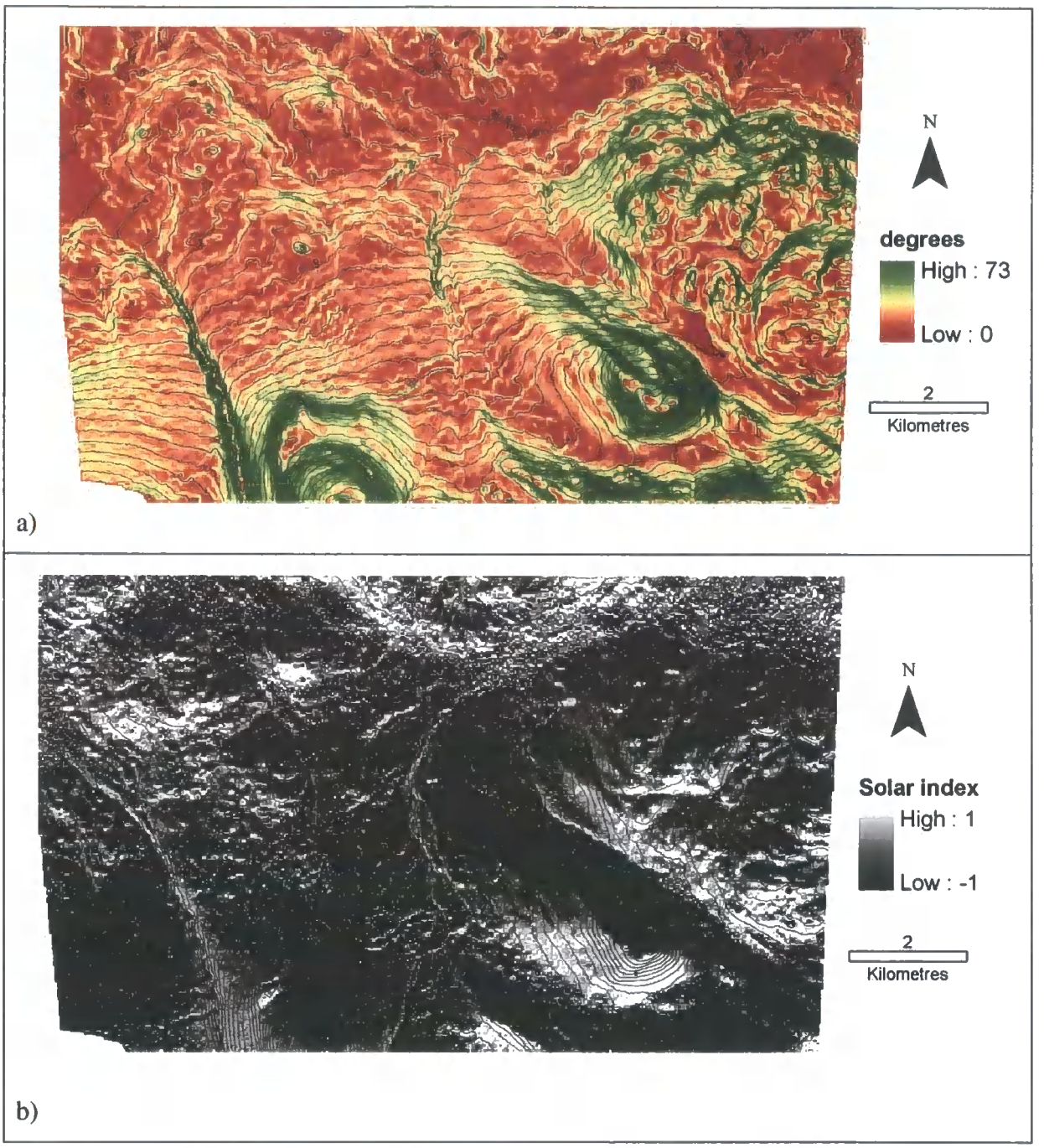

Figure 6.5. (a) Slope gradient and (b) solar radiation index derived from Abisko DEM.

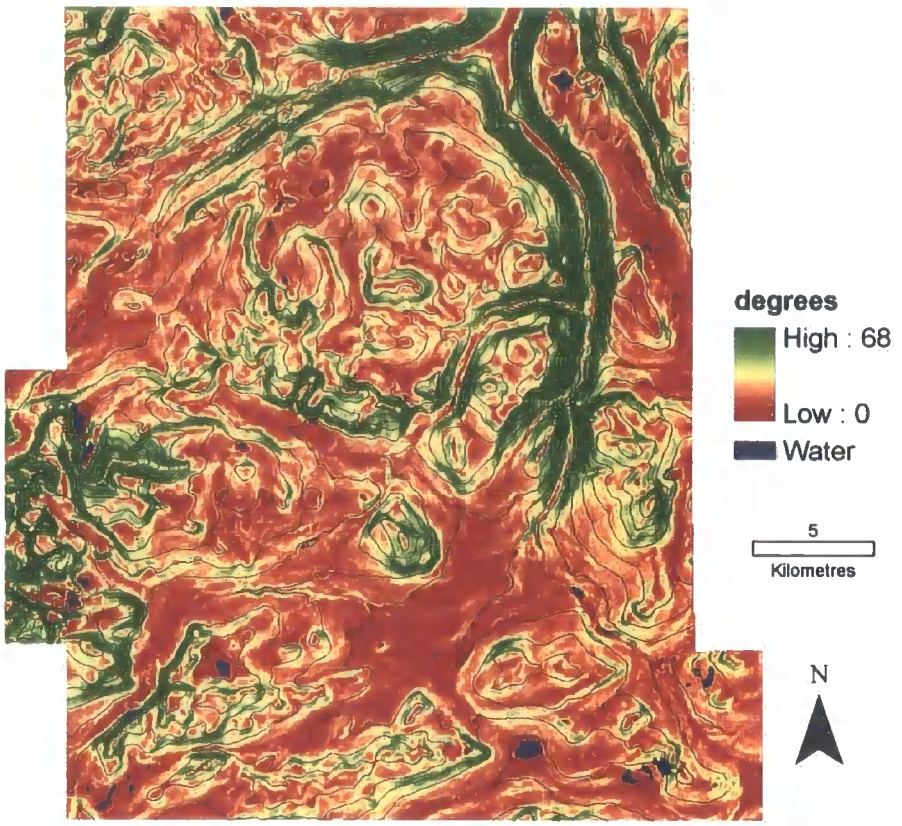

a)

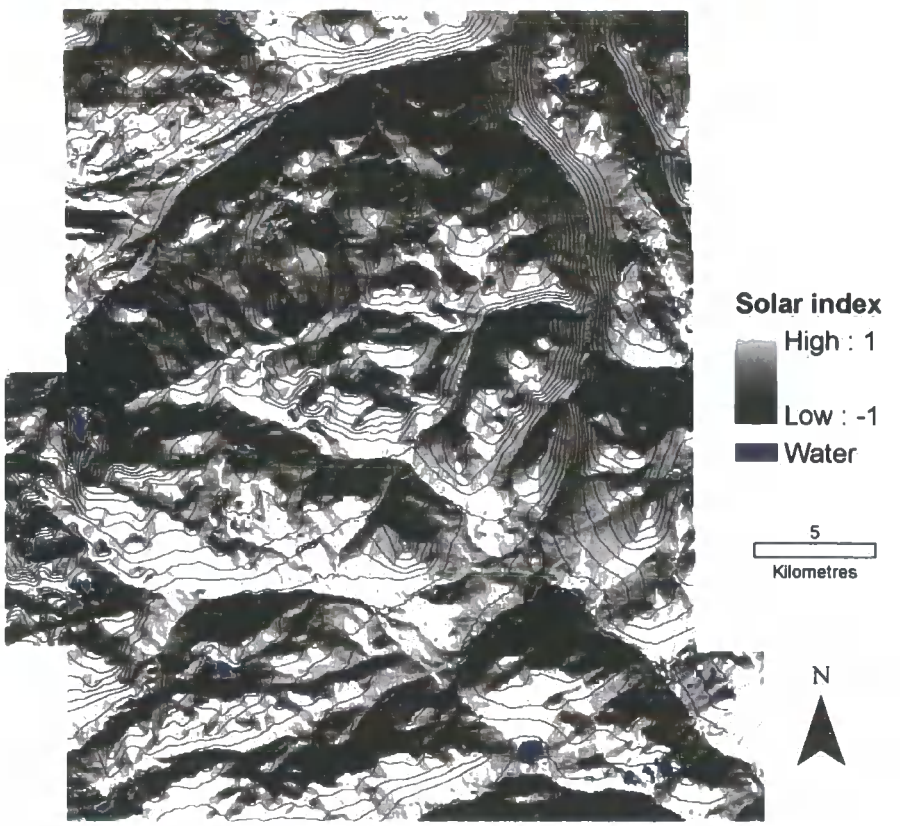

b)

Figure 6.6. (a) Slope gradient and (b) solar radiation index derived from Dovrefjell DEM.

6.1.3 Other topographic variables

There are numerous other topographic variables that can be calculated, which may be useful in explaining patterns of snow cover at the forest-tundra ecotone, for example slope curvature and topographic shelter. Slope curvature, which is the rate of change of slope for each cell, may be expected to influence wind exposure and runoff processes. Topographic shelter is the extent to which a location is surrounded by higher elevation terrain. It can affect local climate because sites surrounded with an elevated horizon may be shaded from direct solar radiation and may also have reduced exposure to high wind speeds. These topographic derivatives are discussed in chapter 11 as topographic predictors in statistical modelling of vegetation distribution.

6.2 Joatka vegetation classification

Within the study area there were only small areas of willow (low shrubs) and communities of (non-aerenchymatous) herbaceous vegetation relative to the spatial resolution of Landsat TM. For example, willow is common along the numerous small streams, but narrow communities are difficult to classify with Landsat TM. In addition, the scattered nature of the birch forest means that these elements of the treeline are also difficult to characterise given the resolution of Landsat TM. A difficulty related to spectral similarity of classes at Joatka was in separating moss heath (non-vascular bryophytes) from dwarf shrub heath (dwarf shrubs). This was related to the timing of the image and the phenology of the vegetation. Details of the PFT class and the nature of the vegetation communities are given in table 6.1.

Table 6.1. Implementation of classification: Joatka.

PFT (dominant vegetation)	Description
Tall shrubs (closed birch forest)	Birch forest (*Betula pubescens*) with dwarf shrub ground cover, primarily bilberry (*Vaccinium myrtillus*).
Tall shrubs (open birch forest)	Birch forest of lower stature, less continuous shrubs. Some erect dwarf birch (*Betula nana*) and other dwarf shrubs, including bilberry.
Low shrubs (willow)	Areas of willow (*Salix lanata* ssp.). Some erect dwarf birch and other dwarf shrubs ground cover.
Herbaceous aerenchymatous (marsh and bog)	Wetlands and some peat hummocks dominated by sedges, mainly cotton grass (*Eriophorum angustifolium*).
Prostrate and erect dwarf shrubs (dwarf shrub and moss heath)	Primarily prostrate dwarf shrubs (e.g. bilberry) and extensive moss cover.
Lichen (lichen heath)	Lichens with some prostrate dwarf shrubs (<0.1 m), e.g. crowberry (*Empetrum nigrum*) and dwarf birch. Even some scattered erect dwarf shrubs (< 0.4 m).

Table 6.2. Contingency table for classification: Joatka

		Classified					
		Birch forest	Willow	Dwarf shrub/moss	Bog	Lichen heath	Total
	Birch forest	13	1	1	0	2	17
	Willow (low shrubs)	2	5	1	0	0	8
	Dwarf shrub / moss	2	0	15	1	1	19
Ref	Bog (aeren. herbaceous)	1	0	3	9	0	13
	Lichen heath (non-vasc.)	0	0	1	0	16	17
	Total	18	6	21	10	19	74

Overall correspondence $= \frac{58}{74} = 78.4\ \%$

Kappa statistic $= \frac{74 \cdot 58 - (18 \cdot 17 + 6 \cdot 8 + 21 \cdot 19 + 10 \cdot 13 + 19 \cdot 17)}{74^2 - (18 \cdot 17 + 6 \cdot 8 + 21 \cdot 19 + 10 \cdot 13 + 19 \cdot 17)}$

$= 0.723$

Correspondence in table 6.2 shows that there is some confusion between birch forest and lichen heath because scattered birch shrubs over lichen heath may not produce a unique signature because of their spacing relative to the spatial resolution of Landsat TM. There is further confusion between bog and dwarf shrubs and willow and birch forest. Figure 6.7 shows an area of the classification at treeline. The highland plateau is correctly classified as dwarf shrub, but areas of dwarf shrub heath are also rich in bryophytes. The treeline has many extensions to the south, following distinct moisture gradients.

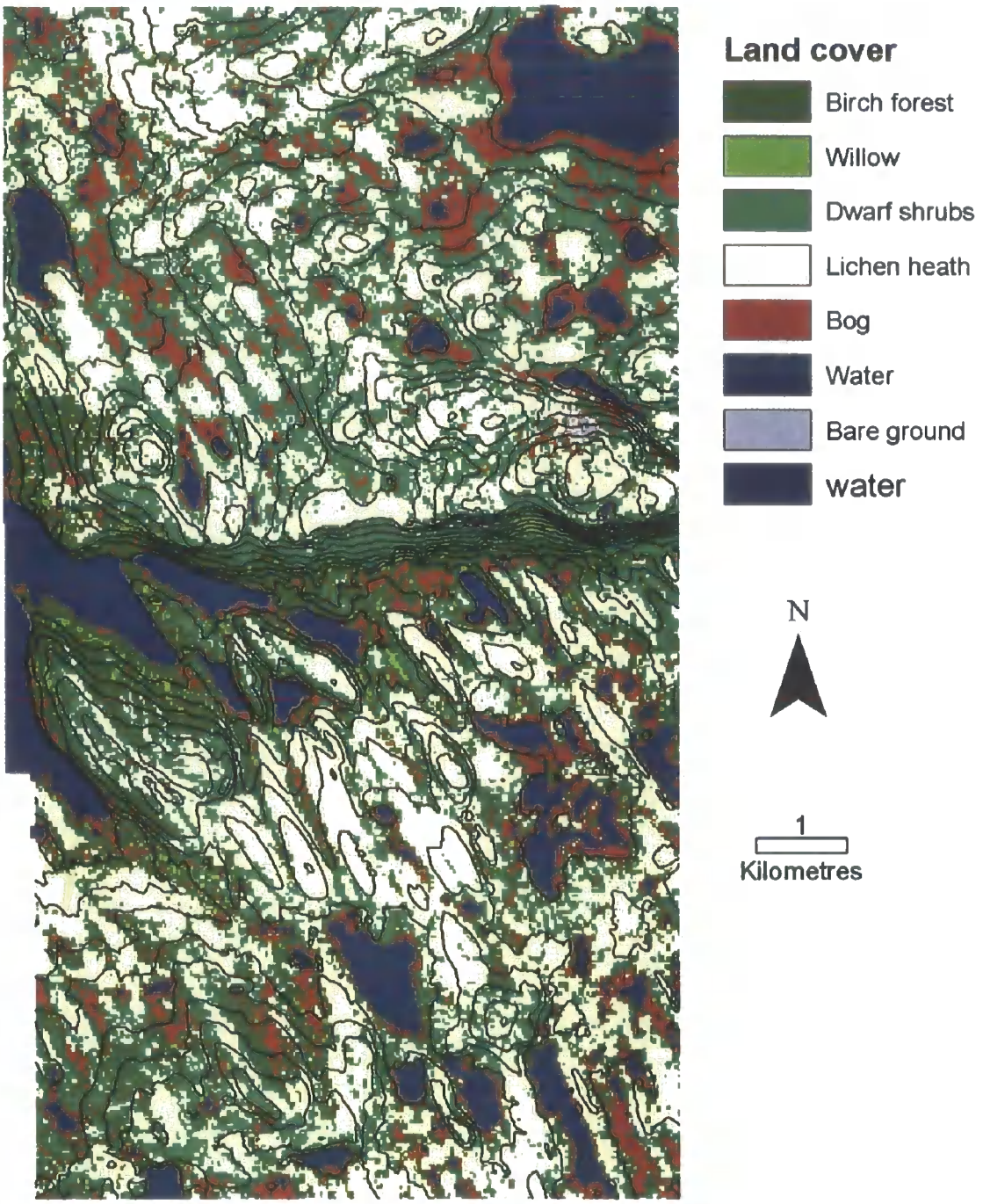

Figure 6.7. Vegetation classification at Joatka. Classification using MLC method using Landsat TM data, acquired 16/07/87.

6.3 Dovrefjell classification

The effect of slope aspect on the Landsat TM reflectance data meant that several sub-classes had to be defined to create separability between training samples. Another difficulty in data collection was distinction of a bryophyte PFT class because of the mosaic of vegetation types, specifically between moss snow bed and sedge dominated snow bed. Details of PFT classification and vegetation communities are shown in table 6.3.

Table 6.3. Implementation of classification: Dovrefjell.

PFT (land cover)	Description
Tall Shrubs (birch forest)	Birch forest (*Betula pubescens*) with dwarf shrub ground cover.
Low shrubs (willow meadow)	Willow is dominating, along with some herbs and grasses. Relatively productive communities, often found wet areas or alongside streams.
Dwarf shrubs (dwarf birch heath)	Dwarf birch and other dwarf shrubs (erect < 0.4 m). Heather (*Calluna vulgaris*) routinely present along with mosses and lichens.
Herbaceous (aerenchymatous snow bed)	Dominated by sedges (*Carex* ssp.), and often dwarf willow (*Salix herbacea*), and mosses.
Herbaceous (aerenchymatous fen and bog)	Dominated by cotton grass, with some soft rush (*Juncus effusus*).
Herbaceous (non-aeren. low herb meadow)	The vegetation is species-rich and characterised by sinewy herbs and grasses.
Non-vascular (Lichens)	Dominated by reindeer lichens (*Cladonia stellaris*).
Unvegetated	< 5 % vegetation cover.

Table 6.4. Contingency table for classification: Dovrefjell

					Class					
		Tall s	Low s	Dwarf s	Herbs na	Herbs a bog	Herbs a snow	Non v lichen	Unveg	Total
	Tall shrub	12	2	1	0	0	0	0	0	15
	Low shrub	2	7	1	1	0	0	0	0	11
	Dwarf shrub	0	3	8	2	0	0	1	0	14
	Herbs na	0	1	2	6	0	0	0	0	9
Ref	Herbs a bog	0	0	0	1	4	2	0	0	7
	Herbs a snow	0	0	0	1	2	6	0	0	9
	Non v Lichen	0	0	0	0	0	0	9	0	9
	Un-veg	0	0	0	0	0	1	0	12	13
	Total	14	13	12	11	6	9	10	12	87

$$\text{Overall correspondence} = \frac{64}{87} = 73.6\ \%$$

$$\text{Kappa statistic} = \frac{87 \cdot 64 - (14 \cdot 15 + 13 \cdot 11 + 12 \cdot 14 + 11 \cdot 9 + 6 \cdot 7 + 9 \cdot 9 + 10 \cdot 9 + 12 \cdot 13)}{87^2 - (14 \cdot 15 + 13 \cdot 11 + 12 \cdot 14 + 11 \cdot 9 + 6 \cdot 7 + 9 \cdot 9 + 10 \cdot 9 + 12 \cdot 13)}$$

$$= 0.605$$

Table 6.4 shows correspondence at Dovrefjell. Confusion is apparent between willow shrubs and birch forest, especially at the edge of the treeline and along streamsides. Further difficulties arose with separation of low shrubs and dwarf shrub heath. Significant confusion occurred between snow bed and bog, however, if these classes are merged into one class (aerenchymatous herb), then overall accuracy improves to 78.2% and Kappa to 0.744. Topographic variation has an impact important influence at Dovrefjell, the steep elevation gradient means that a more distinct treeline is present, as shown in figure 6.8.

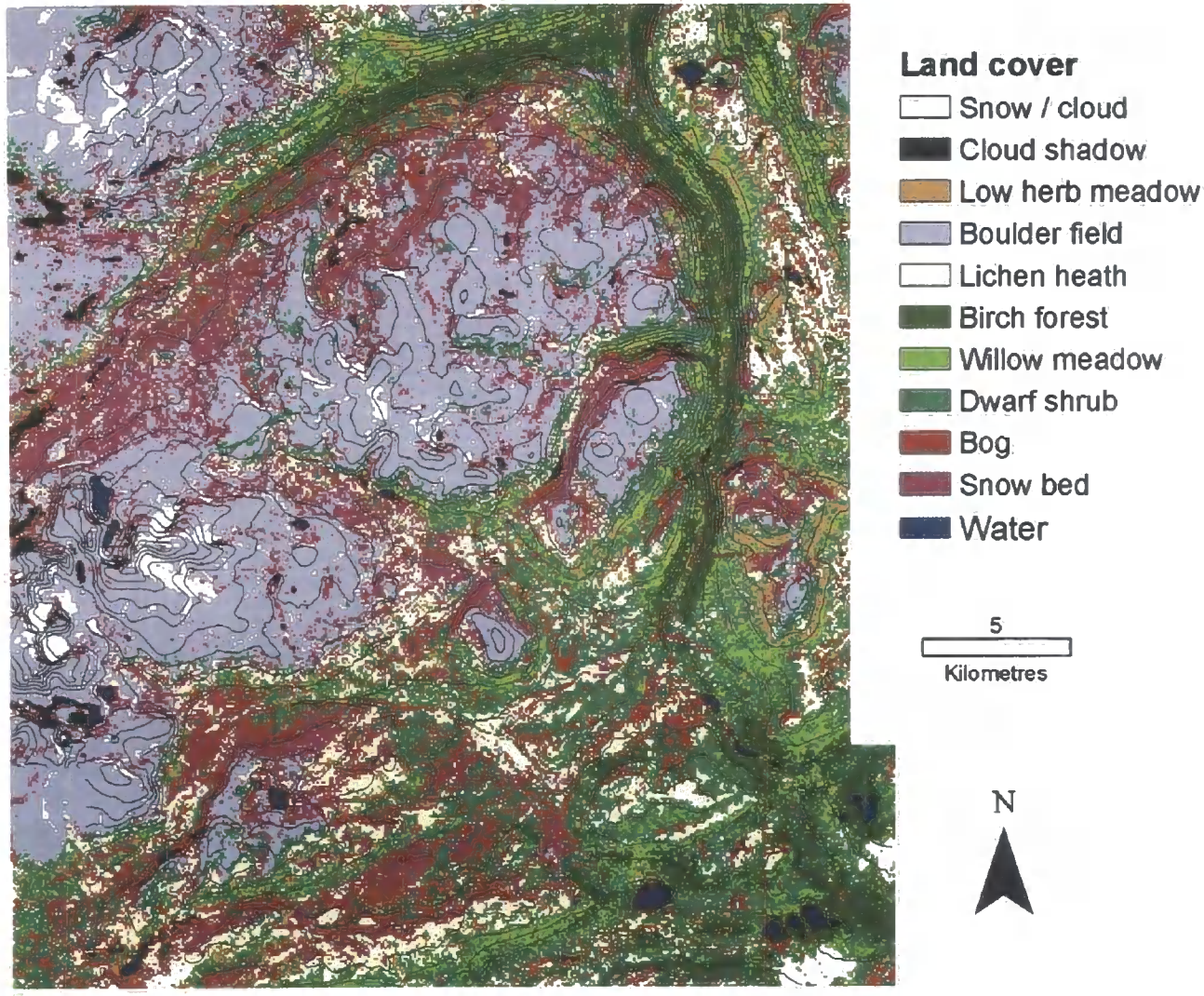

Figure 6.8. Vegetation classification at Dovrefjell. Classification using MLC method using Landsat ETM data, acquired 06/08/99

6.4 Abisko Classification

At Abisko the unsupervised classification indicated a serious problem with spectral separability of classes. The timing of the image acquisition (late September) meant that even forest and tundra classes were difficult to separate, demonstrating the problem of acquiring contemporary data given the return frequency of the satellite, cloud cover and the dynamic phenology of seasonal vegetation change at high latitudes. However, as a substitute for the Landsat TM classification, it was possible to distinguish tundra and forest sites using aerial photos and a digitised vegetation classification (figure 6.9) referred to in Chapter 3.

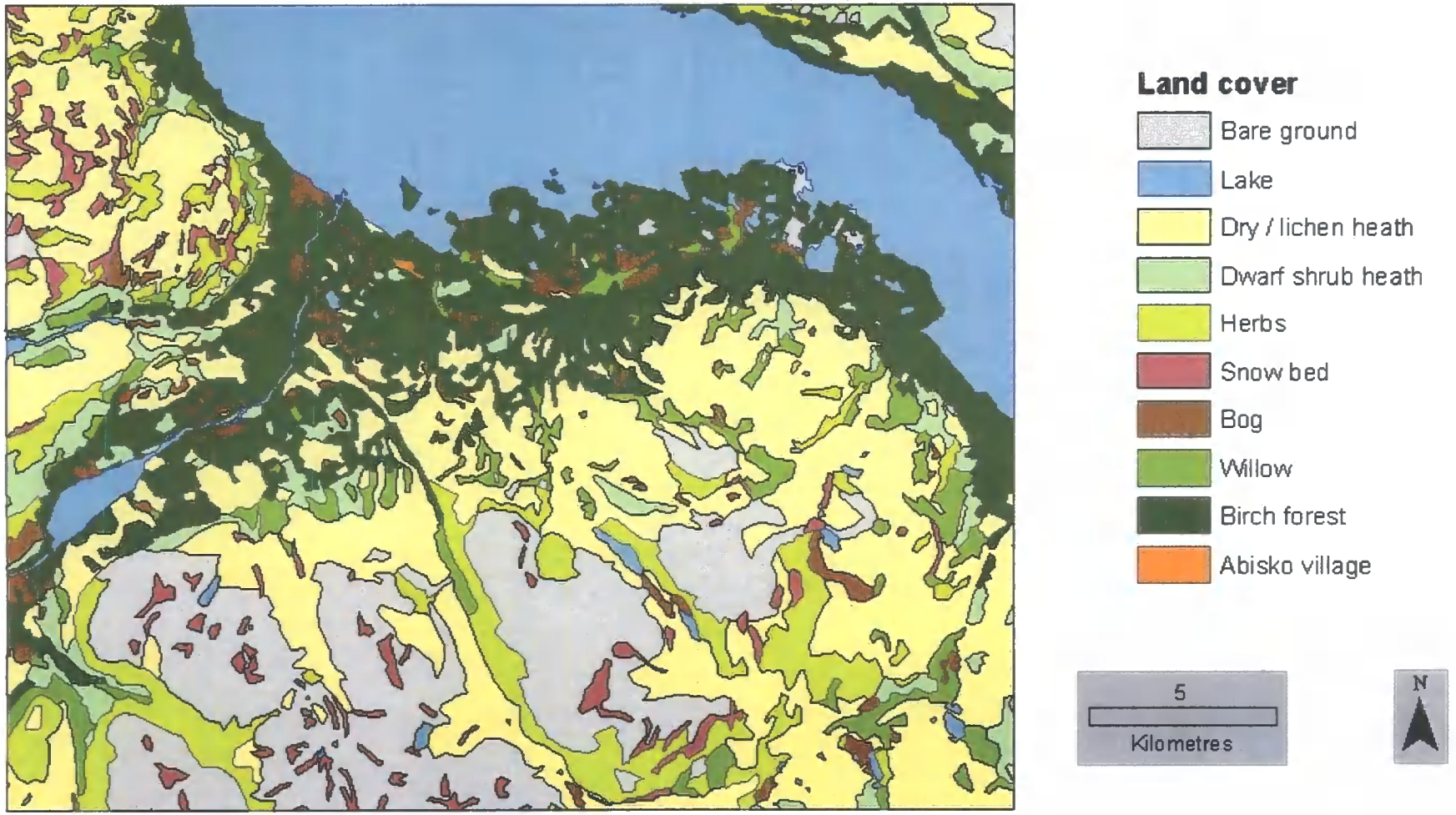

Figure 6.9. Abisko vegetation classification. Source Lantmäteriet.

6.5 Discussion

The aim of the hierarchical method of classification was to alter the level of detail in the classification hierarchy and to discriminate the number of classes depending upon their spectral separability. Therefore, classes at each site could be combined in a consistent way to facilitate comparison. However, additional difficulties were encountered related to the remotely sensed data and the high spatial complexity of vegetation at each site.

The identification of the treeline was relatively straightforward at Dovrefjell, given the steep slope gradient and resulting narrow width of the ecotone; the contrast between forest and tundra heath classes was distinctive. At Joatka, the spatial structure of the vegetation was more complex, with patches of forest often smaller than the measurement scale of Landsat sensor and also at a low density. At Joatka and Dovrefjell, the dominant PFT was often determinable. An overall accuracy of above 70% at Joatka and Dovrefjell represents a successful classification, especially given the challenges of complexity in the spatial patterns of vegetation relative to the resolution of Landsat TM. The main source of error is probably the misclassification of mixed pixels. Dominant PFT classes are often distinct but the reality of mapping an ecotone is that there are subtle transition zones between PFT types and characteristic assemblages of PFTs. Indeed, some difficulty in sample collection was experienced because of heterogeneity of land cover and assemblages of PFTs. The classification at of the ecotone may have been improved by accepting that mixed pixels will occur and boundaries between vegetation types are not discrete. Several approaches have been made using sub-pixel information to more accurately represent land cover, so called fuzzy classification (e.g. Foody *et al.*, 1992).

Rees *et al.* (2002) acknowledge the "trade-off" of between temporal and spatial resolution and the difficulty that cloud cover causes for acquiring an image of the necessary high spatial resolution. In addition to cloud cover, the spectral separation of vegetation classes is significantly affected by the timing of the image acquisition relative to the dynamic vegetation phenology at the study sites. Indeed, at Abisko the image was unsuitable for vegetation classification and the Joatka and archive image was selected to improve separability of vegetation classes. Use of elevation data might have considerably improved the classification, either using DEM-derived variables as additional information in the class allocation or for post-processing. However, if the

vegetation classes are to be used for predictive modelling, then it was important that they were independent of other data that may be incorporated into a GIS.

Ultimately, the classification results at Joatka and Dovrefjell were satisfactory for the purpose of this research. The hierarchical approach to classification would require significantly more information than a single image if all classes were to be discriminated. Tall shrubs (> 2 m) may be distinguished in a winter image (when they are above the snow) and additional VIR data may improve classification if an image from a different part of the growing season were available. However, a significant part of the hierarchy is based on structural information of the vegetation. Therefore, most potential comes from remote sensing techniques that directly provide information of the structure of vegetation. Spaceborne imagery from the planned PALSAR L-band SAR may provide such information. Airborne techniques might include LIDAR, which can provide detailed information on canopy structure (e.g. Means *et al.* (1999), Naesset and Okland (2002)) and thereby enable a 3-dimensional approach to classification of the forest-tundra ecotone (Callaghan *et al.*, 2002).

Chapter 7. Results: monitoring progression of snow melt using temperature and snowpack measurements

This chapter presents the results of the field measurements collected to monitor evolution of snow melt across the forest-tundra ecotone. The methods of measurement collection were discussed in chapter 3. These measurements included continuous measurement of air, ground surface, and soil temperature. I also recorded measurements of snow density, depth, temperature, permittivity, and measures of snow stratigraphy, grain size and snow roughness. Limited measurements of soil permittivity were also recorded where possible.

To aid inter-site comparison, the continuous temperature data are available and presented for each site in 1999, 2000, and 2001, whereas snow measurements were only available for the year of ERS-2 SAR image acquisition.

7.1 Air temperature

Mean air temperature for a nominal "snow-melt period" is shown in figures 7.1 and figure 7.2 for 1999 and 2000; these values are the mean of the four air temperature measurements across the forest-tundra ecotone.

The TinyTag temperature loggers did not record data between 7th May to 10th June 1999 at Joatka and 7th May to 29th May 1999 at Abisko because the memory of the loggers had become unexpectedly full. Unfortunately, this period coincides with important changes in temperature related to the snow melt. However, air temperature measurements were taken with the hand-held temperature probe coincident with SAR image acquisition within this period and measurements from the meteorological station at Abisko Research Station were also acquired for this period.

The data show the impact of both continentality and latitude on air temperature extremes: Joatka has the coldest temperatures and lowest maximum temperatures, followed by Abisko and Dovrefjell respectively. At Joatka, daily mean temperatures remain consistently below 0 °C for a substantially longer period than both Abisko and Dovrefjell. There is considerable variation in air temperature at each study site, with

several periods where daily mean temperature is above 0 °C, followed by periods below 0 °C. Such variation is important for the melting of the snowpack and evolution of snowpack stratigraphy.

There is large diurnal variation in temperature at both forest and tundra locations at each site. Diurnal variation at Abisko and Dovrefjell for 2 days prior to and including the day of SAR image acquisition is shown in figure 7.3 and 7.4. There are clearly melt-freeze events on a diurnal scale, which could impact on snow properties at the time of SAR image acquisition. In addition, figures 7.3 and 7.4 shows higher air temperature for the forest site compared to the tundra location, a pattern generally repeated across the sites but certainly not consistently. This may be a result of differences in elevation between the sites. However, the difference in albedo between snow-covered forest and snow-covered tundra should not be dismissed as an explanation. Even a sparse birch forest canopy will absorb solar radiation and warm; this heat is transferred to the lower atmosphere through convection (Harding *et al.*, 2002). Over the snow-covered tundra, the albedo is probably higher, which may lead to lower temperatures. However, the melting of snow cover will dramatically reduce albedo and lead to heat fluxes from the tundra surface into the lower atmosphere. However, the data available here are insufficient to determine the cause of temperature differences, but it is clear that such differences may influence the presence of wet snow in the forest and on the tundra.

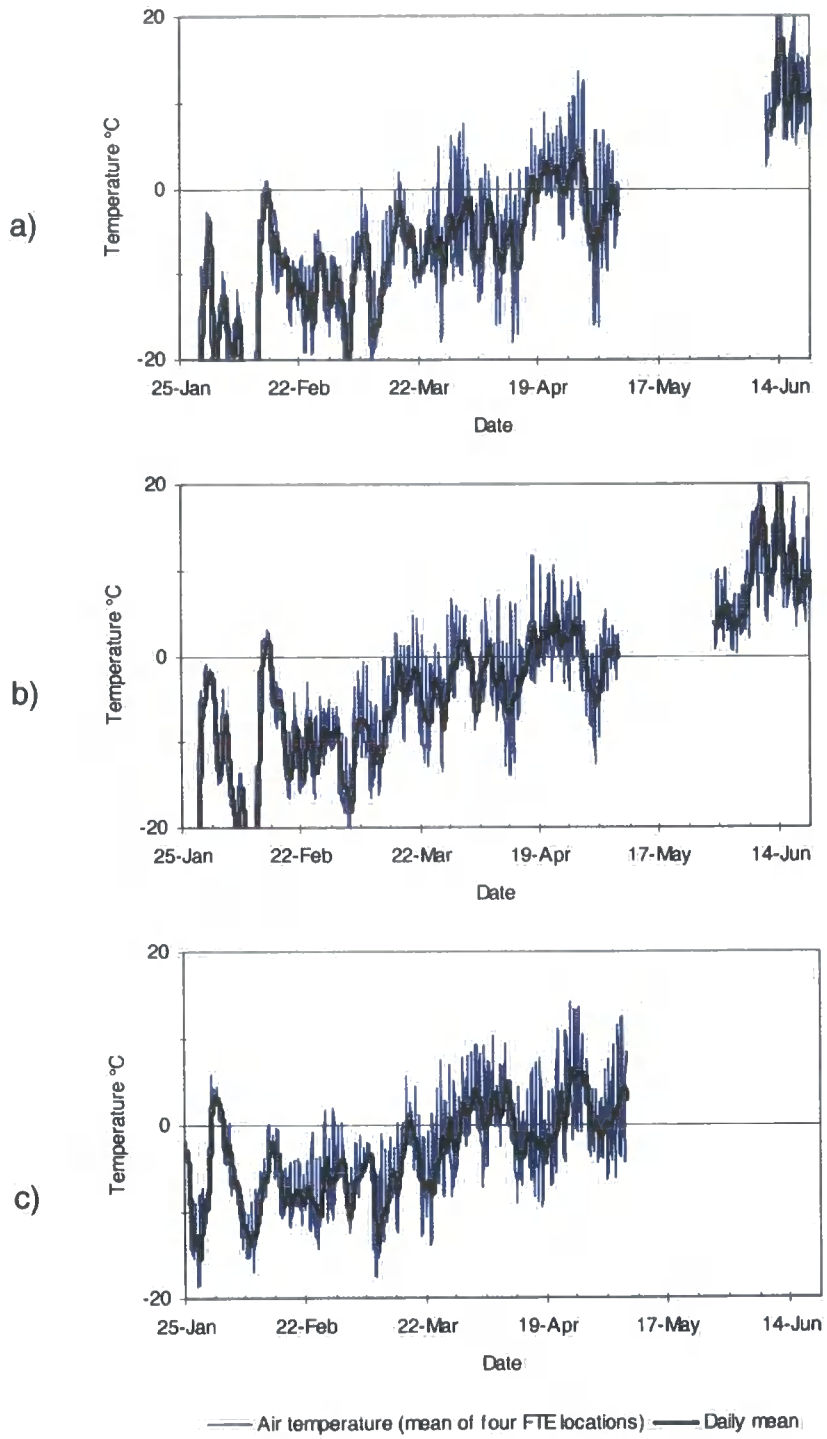

Figure 7.1. Hourly mean air temperature and daily mean air temperature (1999): a) Joatka, b) Abisko and c) Dovrefjell. Temperature measurements are the mean of the four forest-tundra ecotone locations.

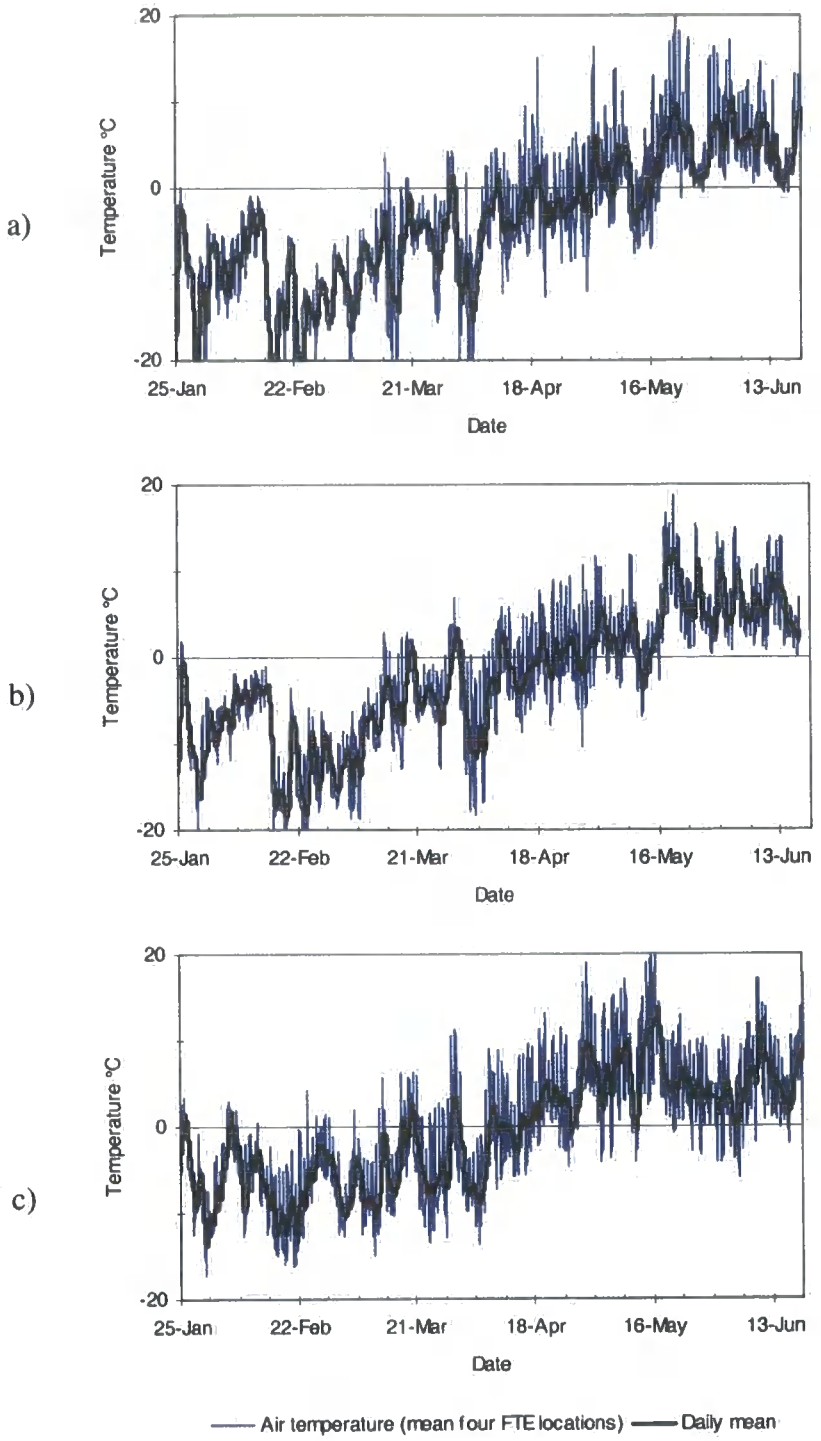

Figure 7.2. Hourly mean air temperature and daily mean air temperature (2000): a) Joatka, b) Abisko and c) Dovrefjell. Temperature measurements are the mean of the four forest-tundra ecotone locations.

(a)

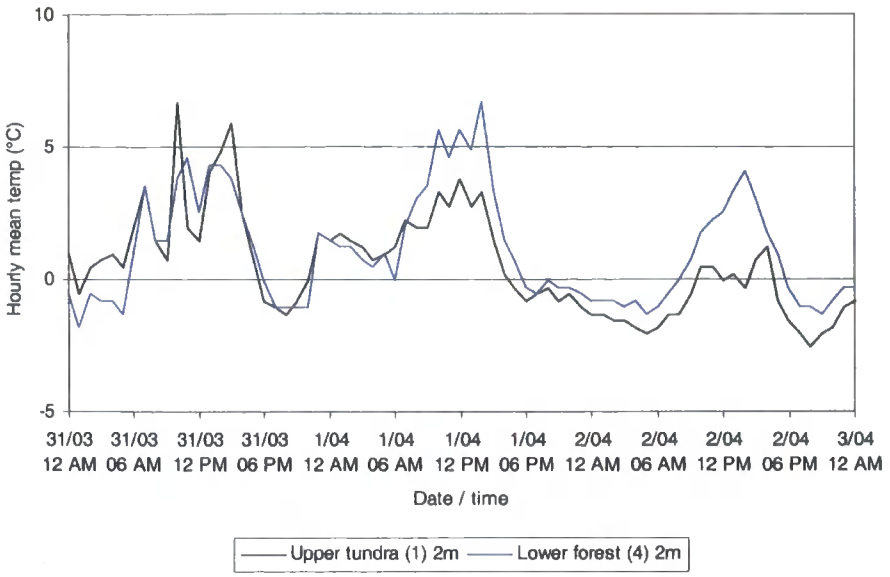

(b)

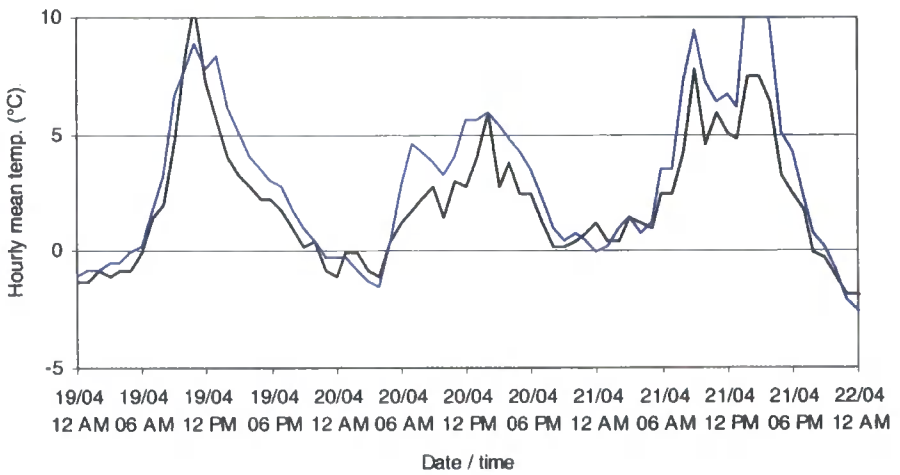

(c)

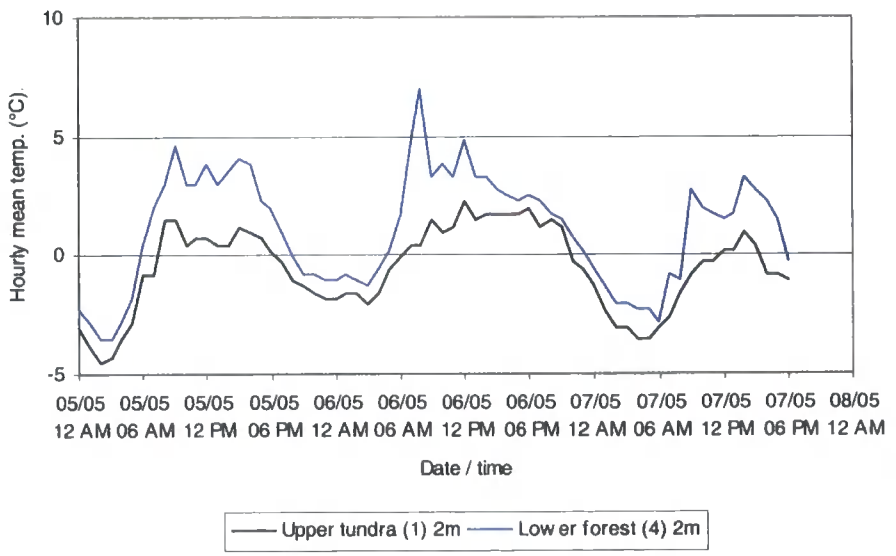

Figure 7.3. Example of diurnal temperature change: Abisko SAR image acquisition on (a) 02/04, (b) 21/04 and (c) 07/05 1999.

(a)

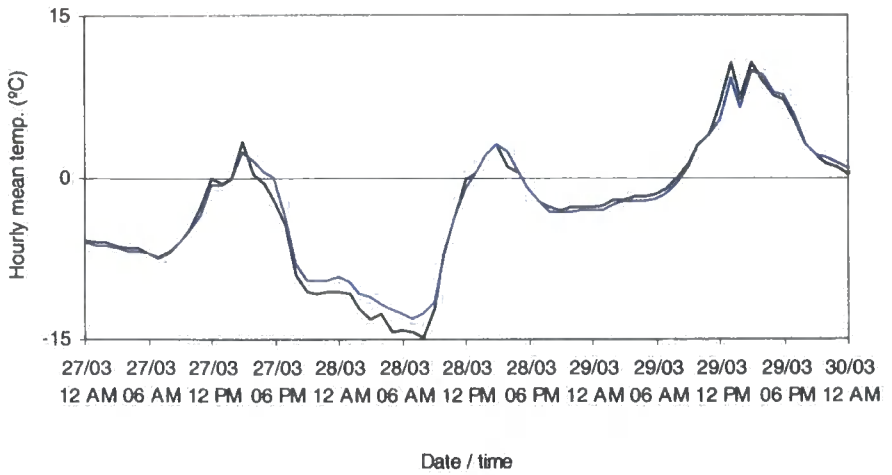

(b)

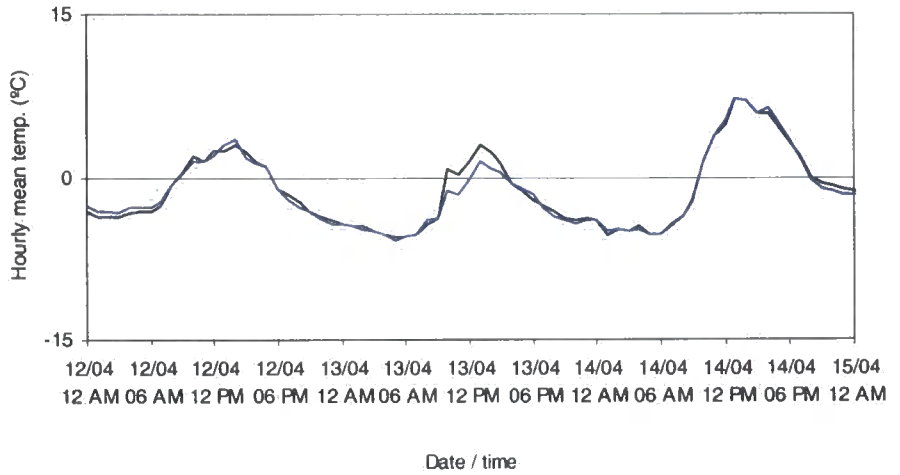

(c)

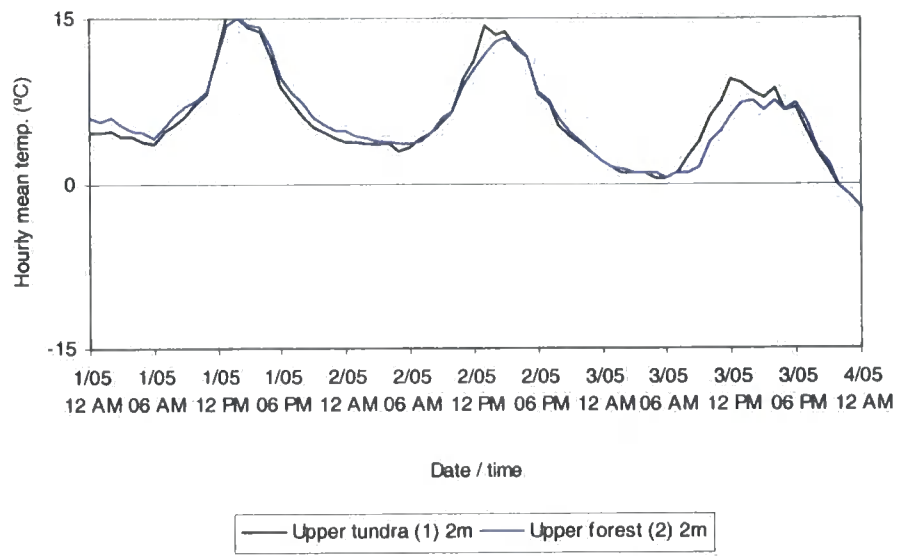

Figure 7.4. Example of diurnal temperature change at Dovrefjell: SAR image acquisition on (a) 29/03, (b) 14/04 and (c) 03/05 2000

7.2 Ground surface temperature

Ground surface temperature at each site is indicative of the timing of snow-free conditions. Unfortunately, measurements were not stored in the ground temperature loggers at Joatka during the same period that air temperature was missing; available measurements at each location across the forest-tundra ecotone are shown in figure 7.5 for the year relevant to SAR image acquisition. The ground surface temperature variation at each study site displays a characteristic "signature" of emerging snow-free conditions across the forest-tundra ecotone. This information allows the determination of the date of snow-free conditions at each location across the forest-tundra ecotone. For example, ground surface temperature variation at Dovrefjell in 2000 indicates that snow-free conditions emerged in the tundra from 23rd – 25th April and in the forest on 18th May. In addition, figure 7.5 shows evidence that there was also a short snow-free period at the lower tundra site at Dovrefjell in 2000 (from 30th – 31st March).

The ground surface temperature data for additional years allowed an overview of the patterns of snow melt across the forest-tundra ecotone to be formed (Table 7.1 to 7.3). The limitations this set of measurements in terms of poor spatial resolution and temporal resolution (in terms of annual variability) is understood, but a generalisation of the patterns of snow melt across the forest-tundra ecotone is useful for interpretation of SAR data. Joatka typically has longer snow duration in the forest sites than tundra sites, with the lower tundra snow-melt completing first. No data is available for the exact timing of snow-free conditions in 1999, when SAR imagery was acquired. At Abisko, the pattern of snow-cover duration reveals that tundra sites are typically snow-free first, with forest sites becoming free up to 40 days later, the upper forest remaining snow-covered longest. At Dovrefjell, the tundra sites typically became snow-free first, followed by the upper tundra.

Tables 7.1 to 7.3 also reveal that there is considerable inter-annual variability in duration of snow cover across the forest-tundra ecotone. For example, at Abisko snow-free conditions occurred 13 days earlier in the upper tundra in 2000 compared to 1999 and 2001. At Joatka, snow-free conditions also came earlier at each site in 2000 compared to 2001. Such annual variability in snow duration is expected and has been recorded, for example, on hemispheric (Robinson, 1997) and regional (Frei and Robinson, 1999) scales.

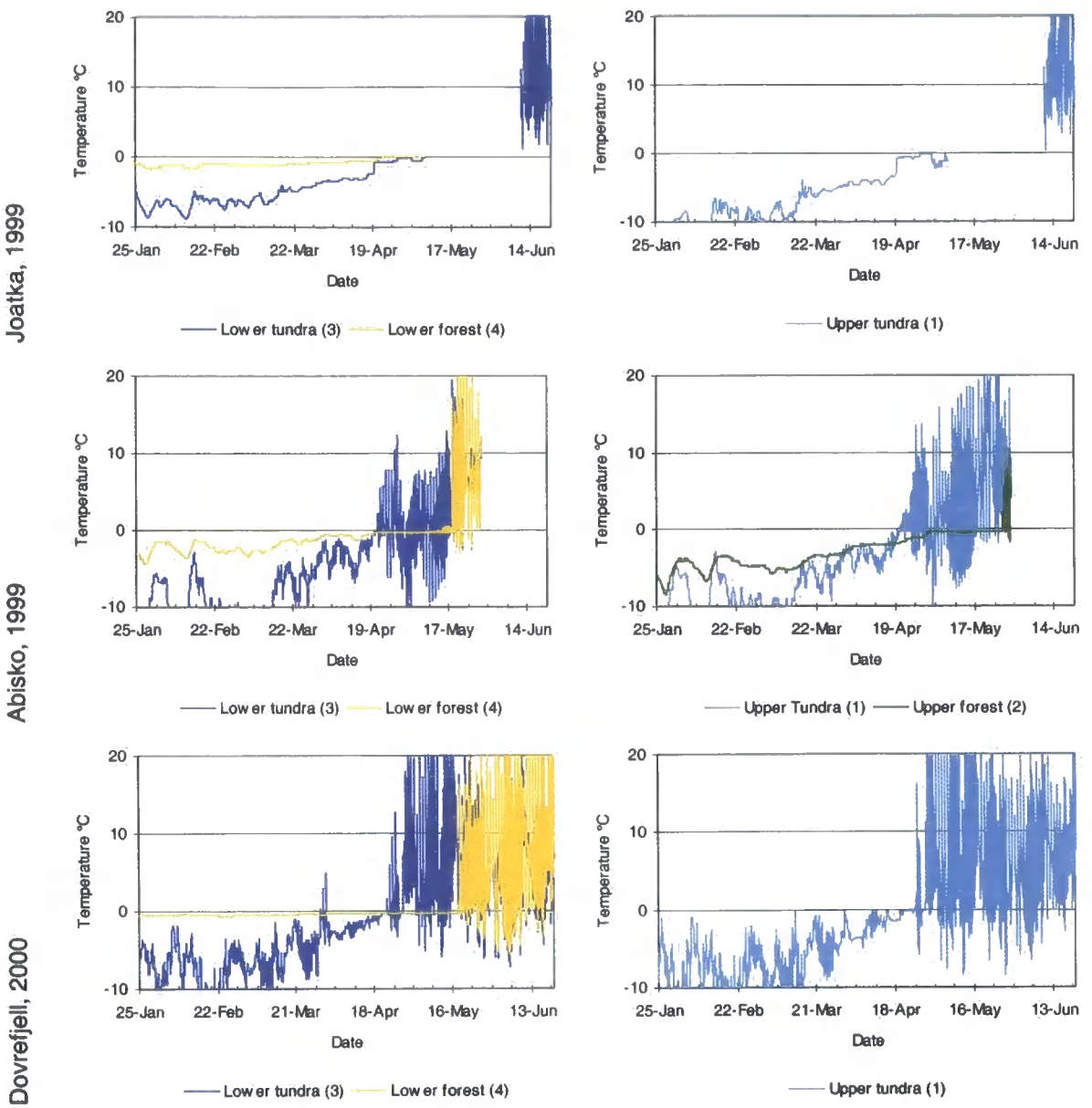

Figure 7.5. Ground surface temperature (where available) across the forest-tundra ecotone for each site.

Table 7.1. Duration of snow cover at Joatka relative to lower forest.

Year	Forest-tundra location	Date continuously snow-free	Duration relative to lower forest (4)
1999	All locations	No data	No data
2000	1. Upper tundra	31st May	-10
	2. Upper forest	12th June	+2
	3. Lower tundra	22nd May	-18
	4. Lower forest	10th June	-
2001	1. Upper tundra	8th May	-23
	2. Upper forest	7th June	+6
	3. Lower tundra	8th May	-23
	4. Lower forest	1st June	-

Table 7.2. Duration of snow cover at Abisko relative to lower forest.

Year	Forest-tundra location	Date continuously snow-free	Duration relative to lower forest (4)
1999	1. Upper tundra	20th April	-28
	2. Upper forest	27th May	+9
	3. Lower tundra	20th April	-28
	4. Lower forest	18th May	-
2000	1. Upper tundra	9th April	-40
	2. Upper forest	No data	No data
	3. Lower tundra	20th May	+1
	4. Lower forest	19th May	-
2001	1. Upper tundra	23rd April	-11
	2. Upper forest	20th May	+16
	3. Lower tundra	27th April	-7
	4. Lower forest	4th May	-

Table 7.3. Duration of snow cover at Dovrfjell relative to lower forest.

Year	Forest-tundra location	Date continuously snow-free	Duration relative to lower forest (4)
1999	1. Upper tundra	4th May	-17
	2. Upper forest	6th May	-15
	3. Lower tundra	6th May	-15
	4. Lower forest	21st May	-
2000	1. Upper tundra	25th April	-23
	2. Upper forest	No data	No data
	3. Lower tundra	23rd April	-25
	4. Lower forest	18th May	-
2001	1. Upper tundra	2nd May	-15
	2. Upper forest	23rd May	+6
	3. Lower tundra	3rd May	-14
	4. Lower forest	17th May	-

Despite snow acting as an insulating medium between ground surface temperature and air temperature, a clear relationship between air temperature and snow-covered ground surface temperature is apparent (figure 7.1, 7.2 and 7.5). There are differences in this relationship between the locations across the forest-tundra ecotone. The characteristic signature revealed that snow cover buffers the ground surface from air temperature "extremes", but that tundra locations show much greater amplitude of variation than the forest locations and much lower minimum temperature. This is likely a result of shallower snow depths on the tundra compared to the forest because shallow snow covers do not provide the same insulation from air temperature (Brown, 1998; Sokratov and Barry, 2002). There is also evidence that the variability in ground surface temperature was reduced substantially for a short period before snow disappeared; often ground surface temperature stabilises at 0 °C before disappearing from both forest and tundra snowpacks. This is evidence that the snowpack is in temperature equilibrium at 0 °C before it completely disappears.

For example, figure 7.5 shows that ground surface temperature at Abisko at the lower forest varies around –1 °C until 19th April, when the temperature stabilises at 0 °C. This

is reasonably a consequence of the increase in mean air temperature on 16th April (figure 7.1). Indeed, the tundra locations became snow-free on 20th April as a result of high air temperatures. The ground surface temperature of the upper forest snowpack does not reach temperature equilibrium until 1st May, despite the high air temperatures, before disappearing 9 days after the lower forest snowpack on 27th May.

A similar pattern can be seen at Joatka before the equipment failure. Tundra snowpacks are manifestly shallower than the forest snowpacks with greater amplitude in ground surface temperature variation. Tundra sites appear to reach temperature equilibrium before the forest sites, in response to the increase in air temperature. At Dovrefjell, forest ground surface temperature is relatively stable at 0 °C for the entire period of observation, perhaps indicating a very deep, insulating snowpack.

7.3 Snowpack measurements

Snow pits were excavated on days coincident with SAR image acquisition with the exception of the "reference" SAR images; on these dates the snow is reasonably assumed to be dry and homogenous because of consistent sub-zero temperatures for the period preceding SAR image acquisition.

The total number of snow pits that could be excavated at each site was limited because of logistical difficulties, and limited human resources (i.e. people to help to dig the snow pits), especially later in the snow melt period. Regardless of such limitations, the rapid change in air temperature around the time of acquisition means that the "window" when snowpack measurements will be representative of snow conditions is likely to be short (figure 7.2 and 7.3). Nevertheless, between 5-12 snow pits were excavated on any given day of SAR acquisition across the forest-tundra ecotone. From this number of snow pits excavated, results are presented here from a representative snow pit from a forest and tundra location for each study site at a time closest to the SAR image acquisition. Later in the snow melt period a tundra snow pit was not excavated because the tundra was generally snow-free, therefore only the forest snow pit is presented.

Firstly, measurements of temperature, density and liquid water content are investigated in the context of each site. Snow surface roughness and stratigraphy are discussed qualitatively.

7.3.1 Joatka

Figure 7.6 shows density, temperature, and water content with depth for forest and tundra sites. It is not possible to determine the rate of decrease in depth because of the small number of time points and difficulty determining exact location of previous pits.

In both forest and tundra, snow density increased over the melt period, mainly in the surface and near-surface layers, but also in the layers closest to the bottom of the snowpack due to the presence of melt water. Density variation may be due to ice lens within the snowpack, which can significantly increase the density, however this is difficult to determine using the volumetric method. A decrease in density with depth is apparent in the tundra snowpack on 17th May and the snowpack comprises large columnar grains (*ca.* 4 mm) with many air spaces, being a depth hoar.

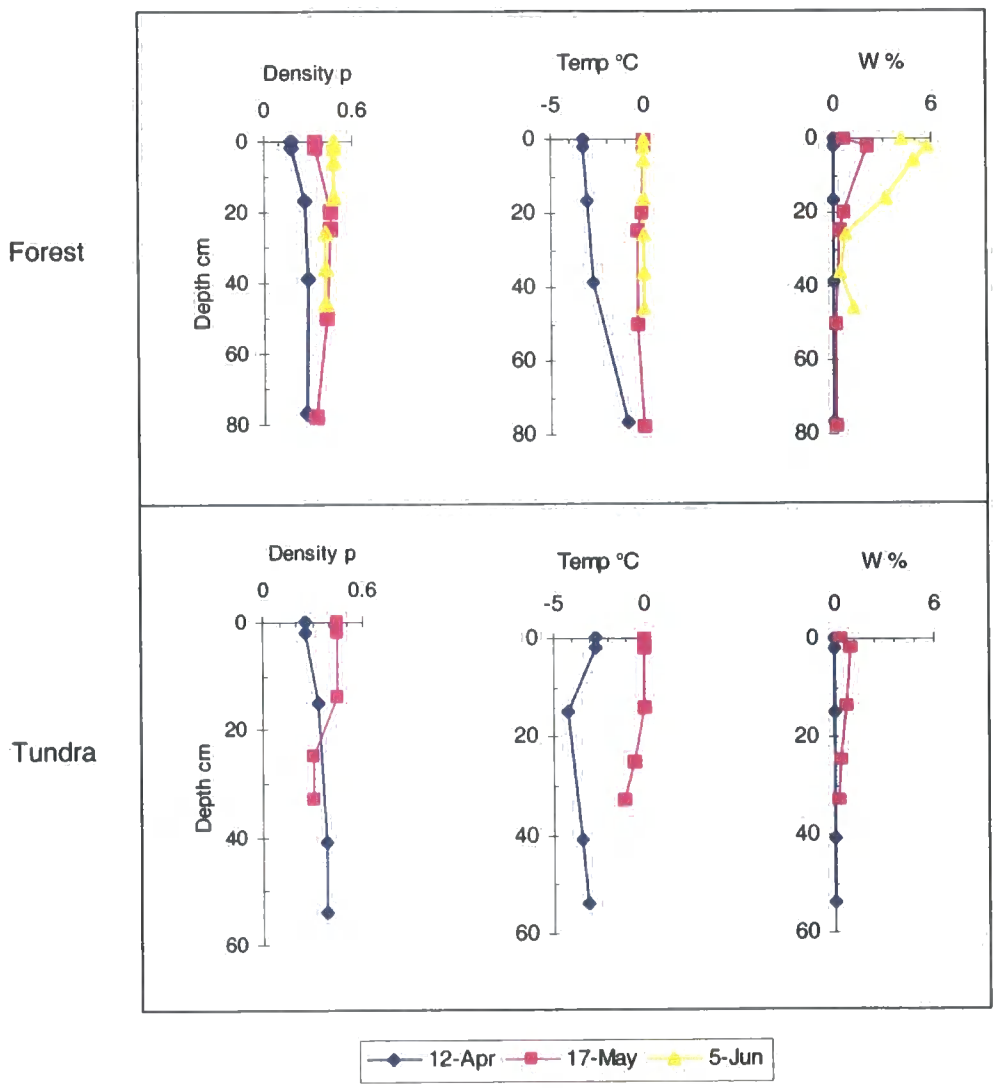

Figure 7.6. Snow measurements at a representative forest and tundra location at Joatka.

Snowpack temperature profiles reveal how the snowpack can insulate from relatively high or low air temperatures and soil temperatures. On 12th April, when the air temperature was low (–3.5 °C at the time of excavation), snowpack temperature increases at lower depth in the forest. The temperature of the tundra snowpack (air temperature –3.1 °C at the time of excavation) is lower than the forest at the ground surface, perhaps as a result of colder night air temperatures (see figures 7.1 and 7.5). On 17th May, the forest snowpack is effectively isothermal at 0 °C (air temperature is 1.2 °C). The shallower tundra snowpack temperature decreases with depth, and could be acting as an insulating medium between the warmer air mass and cold tundra soils. On 5th June, the forest site snowpack is isothermal at 0 °C, with air temperature of 4.1 °C.

Volumetric water content shows an increase in forest and tundra locations. On 12th April, both snowpacks were dry, but by 17th May the water content increased at both locations. The upper layers had the highest water content, which may have been associated with a layer of relatively fresh homogenous wet powder. This layer was deeper in the forest (8 cm) compared to the tundra (1-2 cm). Below this layer the water content decreases and the snow was essentially depth hoar, as reflected in lower snow density. By 5th June the forest snowpack was very wet in the upper layer. The water content and density decrease with depth, probably because water percolated through the air spaces to the ground surface.

In general the size (diameter) of snow grains increased with time, which is a well-known process. Development of ice layers due to melt-freeze metamorphism was evident in some snow pits. Snow properties were found to vary little spatially at each location, but there were differences between forest and tundra locations; tundra snowpack typically has a thin surface wind crust. As melt-freeze occurs, strata develop and the location and frequency of strata was often correspondent at each location, indicating that consistency of melt-freeze processes within the study area. By the 5th June the stratigraphy was degraded (round grains, polycrystals) due to a prolonged melt associated with high temperatures.

7.3.2 Abisko

Pits were excavated at a tundra and upper forest location on each SAR image acquisition date, but not at the exact location of the temperature loggers because of

access restrictions. Snow became free at the location of the loggers slightly earlier than the sites where snow pits could be excavated, but temperatures are considered representative. Results are shown in figure 7.7. It is not possible to determine the rate of decrease in depth because of the small number of time points and difficulty determining exact location of previous pits.

Density increased during melting, mainly in the surface and near-surface layers at the tundra location, but throughout the snowpack in the forest. Density may be lower with increased depth because melt-freeze processes cause development of depth hoar. Wind processes at the tundra location can increase density in the upper layer through formation of a wind crust. For example, when the tundra snowpack was dry on 2nd April, the upper layers had a pronounced wind crust with lower density, dry powder below.

Snowpack temperature is lower in the tundra snowpack on 2nd April, a result of lower air and soil temperatures compared to the forest (see figure 7.5). Snowpack measurements on 21st April coincided with a period of warm weather; air temperature was over 5 °C at the time of SAR image acquisition and had exceeded 10 °C in the previous few days. As a result, the snowpack is isothermal at 0 °C in the upper layers at each location, but temperature decreases slightly at the tundra location with depth. Ground temperatures in figure 7.5 are high at the tundra, but the tundra snowpack at the location of the logger was about to become snow-free and these temperatures may not be representative. On 7th May, air temperature is lower and the shallow tundra snowpack has re-frozen. The deeper, forest snowpack temperature decreases slightly with depth, but by 26th May it effectively in temperature equilibrium at 0 °C in response to high air temperatures (3.4 °C at time of SAR image acquisition; daily minimum and maximum 0.9 and 11.8 °C respectively from nearby Abisko Research Station).

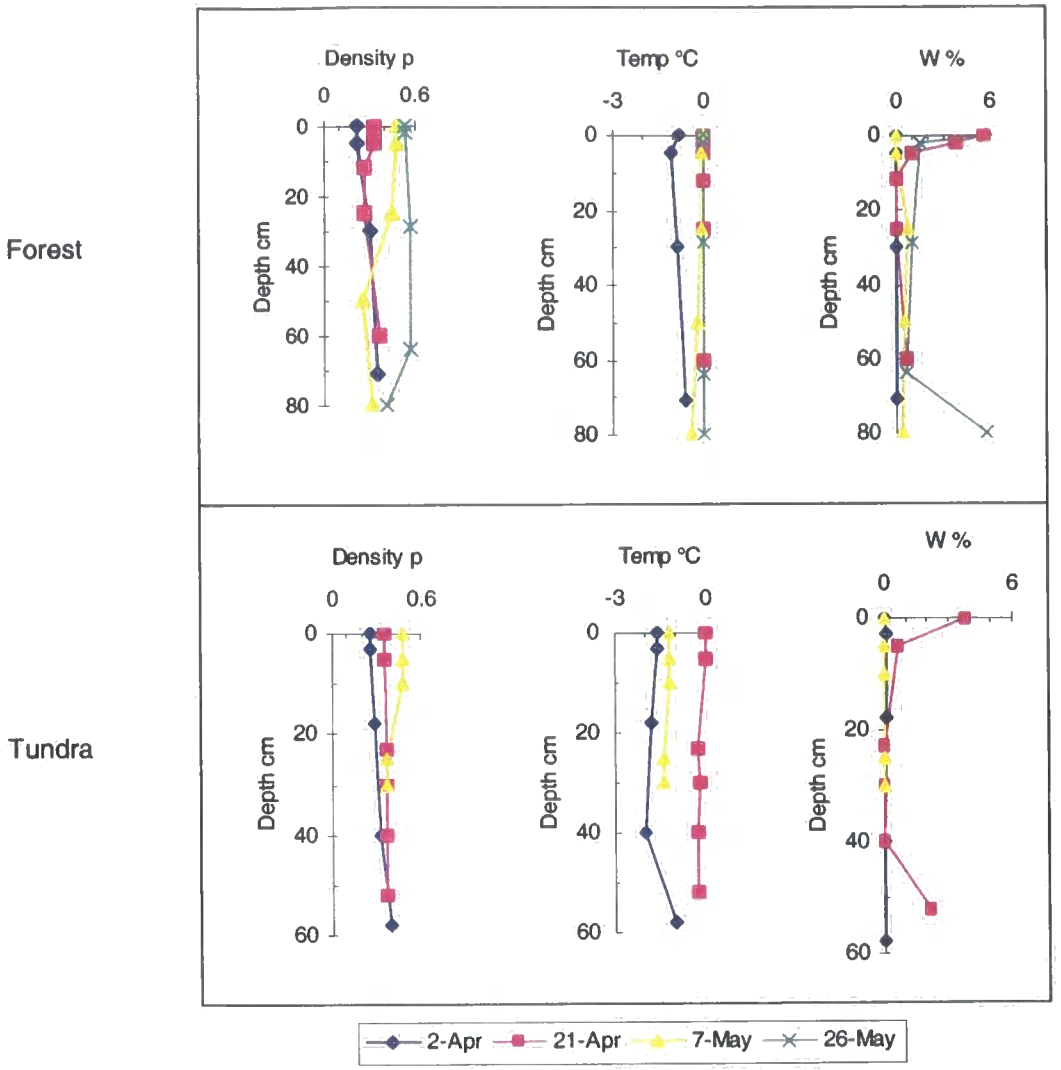

Figure 7.7. Snow measurements at a representative forest and tundra location at Abisko.

Water content in both forest and tundra is negligible on 2nd April and 7th May, as a consequence of low air temperatures. On 21st April, warm air temperature resulted in wet surface layers, but the water content declines with depth. At the tundra site, there is significant increase in water at the bottom of the snowpack, a result of percolation of melt water through the snowpack. On 26th May the entire snowpack in the forest is wet, most prominently in the upper layer. Percolation of water through the snowpack has occurred and there is a slush layer at the bottom with standing water at the ground surface.

Temperature fluctuations caused significant melt-freeze events at Abisko. On 2nd April the tundra had a noticeable wind crust and ice layers at depth, perhaps evidence of melt-freeze events. The forest snowpack was more homogeneous, with deep powder layer at

the surface. Significant ice layers were apparent in the tundra snowpack on 21st April and there was also an ice layer at the ground surface. On 7th May, the tundra snowpack was very icy, with an wind crust and upper layer of depth hoar (large grains with large air spaces as a result of refreezing). A ground surface ice layer was also apparent in the forest on 21st April, and the upper layer was comprised of relatively large grains of 2-3 mm diameter. On 7th May the upper layer in the forest comprises polycrystals, below this depth hoar is typical. By 25th May, the upper layer is very degraded and wet, with large snow grains and air spaces apparent where the water content is slightly lower.

7.3.3 Dovrefjell

Due to constraints of human resources, snow pits were only excavated at Dovrefjell coincident with the SAR image acquisitions on 29th March and 14th April. However, the measurements did include daily monitoring of a single snow pit over 3 days from 27th – 29th March (figure 7.8) and measurements of diurnal changes in snowpack conditions on 14th April in relation to air temperature (figure 7.9).

Figure 7.8 of snow properties and 7.4 of air temperature demonstrate the insulating properties of a forest snowpack. On 28th March extremely low air temperatures have resulted in relatively low snowpack temperature, but below approximately 30 cm temperatures are broadly similar to 27th and 29th March. On 29th March, air temperatures were not low overnight and the snowpack temperature increased significantly in the upper layer and throughout the profile. At the base of the snowpack, temperatures on each day were close to 0 °C, and liquid water was detectable. On 29th March higher air temperature caused an increase in liquid water at the surface of the snowpack, but the majority of the snowpack remains dry. This profile was typical of other snowpacks measured on 29th March and by the time of image aquisition the snowpack was becoming considerably wet. Density remains relatively consistent throughout the snowpack over the three days.

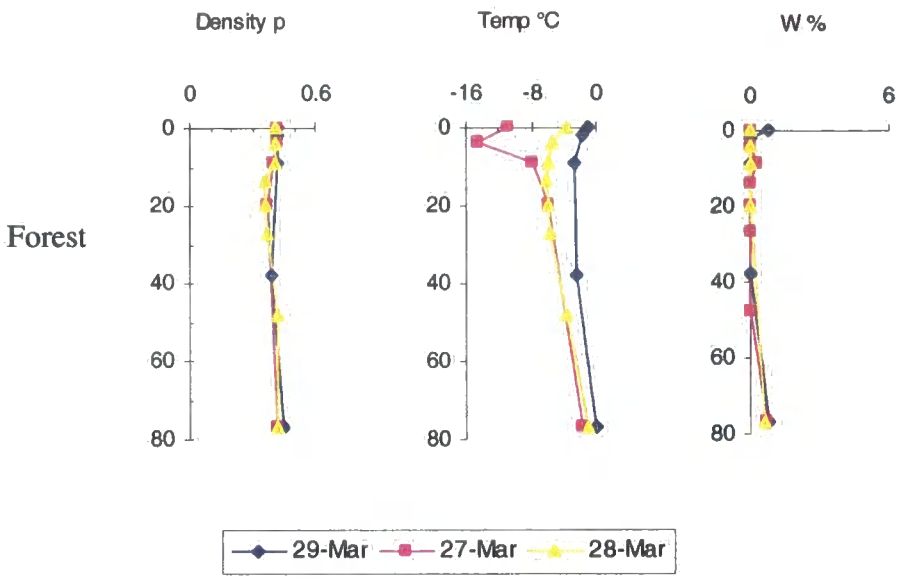

Figure 7.8. Snow measurements from 27-29th March at Dovrefjell forest location.

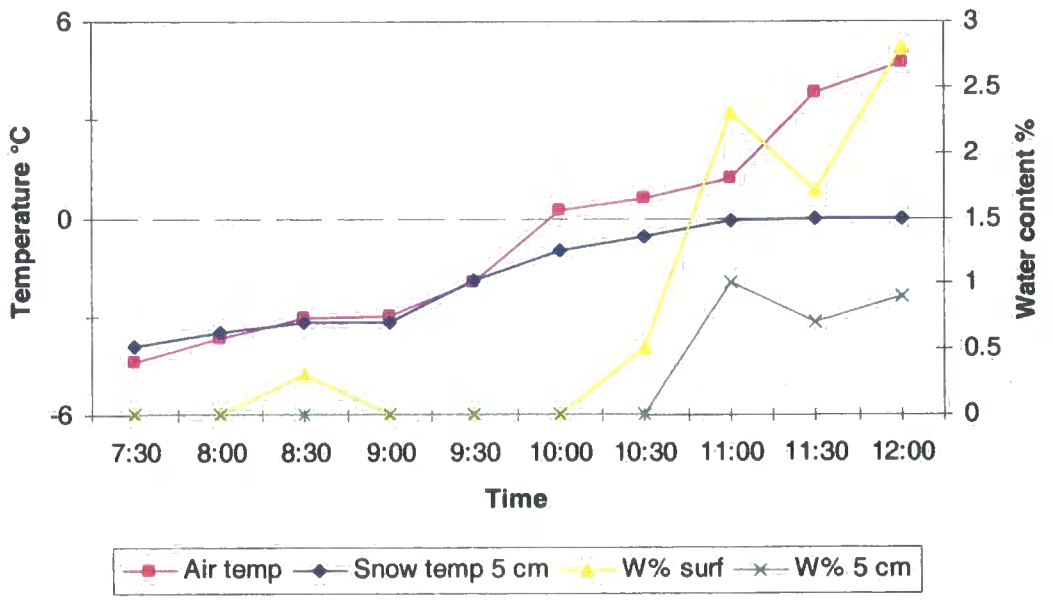

Figure 7.9. Evolution of snow properties at tundra location in relation to temperature. Dovrefjell, 14th April.

In order to investigate the potential of rapid change in the liquid water content of a snowpack to change in temperature, a tundra site was monitored on 14th April over several hours, coincident with SAR image acquisition. Snow temperature, air temperature, density, and permittivity were monitored every 30 minutes in the upper snowpack (surface and 5 cm); overall depth was 37 cm. The weather conditions were overcast and temperatures during the monitoring period varied from –5.3 °C at 6 am to 7 °C at 1 pm. As shown in figure 7.9, snow temperature lagged behind increases in air temperature, but the snowpack temperature did reach 0 °C in response to air temperature. Liquid water content increased in response to higher air and snow temperature; surface water content increased most rapidly, whereas a significant lag was measured at 5 cm.

7.4 Discussion

Seasonal and diurnal change in air temperature causes metamorphosis of a snowpack and changes in snow density, liquid water content and grain size, and results in metamorphosis of a relatively homogenous snowpack to one that is heavily stratified.

Variation in mean daily air temperature, with significant periods below and above freezing, causes melt-freeze cycles; snowpack stratigraphy is predominantly melt-influenced with development of ice lens through percolation of melt water. Diurnal melt-freeze events also frequently occur, even when mean daily air temperature is below 0 °C. Diurnal variation in temperature can rapidly influence the water content of the snowpack in the upper layer, while at depth the snowpack may remain frozen. At Dovrefjell water content in the upper 5 cm rose from 0 to 3 % in one hour in response to air temperature increasing to 5 °C. Longer periods of high mean air temperature can result in an isothermal snowpack at 0 °C, but re-freezing can occur, as demonstrated at Abisko between 2nd April and 7th May and evidence from other sites provided by ground surface temperature measurements. The forest snowpack is consistently deeper than the tundra, and as a result ground surface and soil temperature is colder and more variable at tundra locations because the cold temperatures penetrate the shallow snowpack.

Reflection and absorption of microwaves is likely to be dominated by liquid water content in the upper layer of a snowpack. Therefore, variation in snow wetness in the upper few centimetres in response to temperature is important for interpretation

temporal change in radar backscatter. Diurnal variation in liquid water content could influence the backscatter since liquid water content in the upper layer can increase rapidly in response to air temperature. ERS-2 overpass is typically around 11 am local time, which is often a period of rapid change in snowpack conditions. Depending on the rapidity of the diurnal increase in temperature and the mean daily temperature on the day of SAR image acquisition, snow may be wet or dry. In addition, temperature will also vary with elevation, because of the known relationship between temperature and topography, and perhaps between forest and tundra because of differences in albedo and radiation balance. Other topographic factors, such as topographic shelter and slope aspect may also influence temperature radiation and therefore across a topographically complex landscape the pattern of snow wetness may show considerable variation. Interpretation of backscatter will therefore be complex and snow mapping must consider melt and re-freeze, such as the pattern of snow-melt that occurred at Abisko. At Joatka, in 1999, there were two periods of substantial snow-melt with daily mean air temperature above 0 °C, in late April and early May. Dovrefjell showed more frequent, short periods of daily mean air temperature above 0 °C. However, using temperature as a proxy for liquid water content could lead to uncertainties. There is a significant lag between liquid water content increases and temperature above 0 °C. Further, the insulating properties of the snowpack mean that liquid water can be present in the snowpack at depth, despite air temperatures being considerably lower than 0 °C. If liquid water is present at the base of the snowpack, then this could decrease backscatter through absorption. Therefore, in order to monitor the development of snowpacks at the Arctic forest-tundra ecotone, substantial ground control data are required to interpret the properties of the snowpack at the time of SAR image acquisition.

The return cycle of the ERS-2 satellite is too infrequent to capture these important melt-freeze events, despite its weather-independent capabilities. In addition, meteorological measurements from other years indicate that the timing of snow-free conditions can vary significantly (22, 12, and 17 days at Joatka, Abisko and Dovrefjell respectively). This variation is not surprising given knowledge of hemispheric and regional variation in snow duration from satellite observations (Frei and Robinson, 1999; Robinson, 1997), but makes planning acquisition of satellite imagery difficult, even cloud independent SAR imagery. Many experiments and applications of SAR have monitored a snow melt that lasts for several months (e.g. Nagler and Rott (2000) in the Austrian Alps), or the slow progression of the firn line of a glacier e.g. Adam *et al.* (1997).

Alternatively, airborne systems or SIR experimental data have been used where the return period is improved. The return period of SAR systems, such as Envisat or Radarsat with steerable beam capabilities may be used to acquire more frequent imagery. However, the imaging geometry will be more complex in comparison to the consistent imaging geometry of ERS-2.

Chapter 8. Results: Modelling ERS-2 backscatter from a ground surface and seasonally varying snowpack

To extract information on seasonally changing snow conditions from SAR imagery, it is necessary to understand the degree to which the environment and natural processes we are observing and variables regarding the SAR system itself might influence the backscatter. The landscape features known to affect SAR are topography, the dielectric constant of the snowpack and ground surface, surface roughness, and vegetation cover. SAR system parameters are (reference) incidence angle, frequency, and polarisation. If we are to investigate the seasonal changes in snow conditions, then we must understand (and possibly account for) the part of the total backscatter attributed to other factors, which may be of greater magnitude than the parameter of interest.

In chapter 5 several commonly used correction functions for incidence angle were investigated and the magnitude of different corrections investigated. In this chapter, physically based backscatter models are introduced in order to explore possible backscatter mechanisms from ground surface and from seasonally varying snowpacks. Ulaby *et al.* (1982a; 1982b; 1986) have introduced several models of radar backscatter from snow-covered and ground surfaces. Backscatter models are applied here that have been commonly applied in applications of SAR for snow cover monitoring (e.g. Barber and Ledrew, 1994; Guneriussen, 1997). However, for monitoring snow-melt over tundra surfaces a model sensitivity analysis has not been undertaken. The aim of this chapter is a thorough examination of theoretical backscatter models, in order to further understanding of the scattering mechanisms that may result from the dynamics observed in the environment and to determine what might be the most important influences on backscatter. Analysis of such model enables the theoretical importance of physical parameters such as surface roughness and dielectric properties of the snowpack and the ground surface to be investigated.

8.1 Surface scatter models incorporating surface roughness and dielectric properties

As discussed in chapter 5, the simplest backscatter models interpret topographically dependent backscatter $\sigma^0(\theta)$ as being equal to topographically normalised backscatter

σ_n^0 and some function of incidence angle $f(\theta)$ (e.g. Shi and Dozier (1994); Guneriussen (1997)), see equation 5.2.

Other surface scatter models include surface roughness and dielectric parameters and the modelled backscatter is not simply a function of incidence angle. They can also be used to normalise SAR relative to a reference incidence angle (for the same surface roughness and dielectric properties). The theoretical backscattering models employed were the two variants of the Kirchhoff model, the Geometric Optics (GO) model and Physical Optics (PO) model. In a general sense, the GO model is best suited for very rough surfaces and the PO model is suited for surfaces with intermediate roughness. Another model, the small perturbation model (SPM), is suited for surfaces with small roughness and short roughness correlation lengths. The surface models introduced were used to explore the effect of changing surface conditions. It is important to consider that the assumptions inherent in the models mean that they are only valid within a certain range of surface roughness parameters.

8.1.1 Surface roughness

The roughness of a surface can be described by the standard deviation of the surface height, Δh, which is used to classify a surface as smooth or rough according to the Rayleigh criterion (Ulaby *et al.*, 1982b). A surface is smooth according to Rayleigh criterion if:

$$\Delta h < \frac{\lambda}{8\cos\theta} \qquad \textbf{Equation 8.1}$$

In some cases the Fraunhofer criterion is used:

$$\Delta h < \frac{\lambda}{32\cos\theta} \qquad \textbf{Equation 8.2}$$

where λ is the wavelength in metres. In the case of ERS-2 SAR ($\theta = 23°$ and $\lambda = 0.0565$ m), a surface is smooth if $\Delta h < 0.0077$ or 0.0019 m for the Rayleigh and Fraunhofer criteria respectively. However, this reveals nothing about the *scale* of the irregularities (Rees, 2001). The surface correlation length l is used to quantify the distance beyond which variation is approximately statistically independent. This is assumed to be isotropic and is represented by a Gaussian or exponential function.

Qualitatively, tundra presents a rough surface relative to ERS-2 SAR wavelength, but measurements were not obtained to verify this. However, within the literature, surface roughness is often defined in terms of a single parameter m, which is the root mean square (rms) surface slope. This parameter often takes on no more than a few values representing relatively rough and smooth surfaces. Assuming a Gaussian autocorrelation function (Rees, 2001) with correlation length l and standard deviation of surface height Δh the value of m is calculated according to:

$$m = \sqrt{2} \cdot \frac{\Delta h}{l} \qquad \textbf{Equation 8.3}$$

8.1.2 Kirchhoff geometric optics model

The Kirchhoff geometric optics (GO) model (or stationary phase) is an approximation of the Kirchhoff integral (Ulaby *et al.*, 1986). The Kirchhoff GO model has a restricted validity domain, being only applicable for rough surfaces relative to wavelength. The validity domain for the Kirchhoff GO model is related to surface roughness according to the following rules:

$$\begin{aligned} kl &> 6 \\ kl^2 &> 17.3 \cdot \Delta h \\ k \cdot \Delta h \cdot \cos\theta &> 1.58 \end{aligned} \qquad \textbf{Equation 8.4}$$

(See Rees (2001) equation 3.56).

where k is the wave number, given as:

$$k = 2\pi/\lambda \qquad \textbf{Equation 8.5}$$

and λ is the wavelength (m). ERS (λ = 0.0566 m) has a value of k = 111.21 m^{-1}.

Therefore, l must be greater than 0.054 m and Δh greater than 0.015 m (θ = 23°), but there is also interaction between values of l and Δh to consider (see figure 8.1).

Backscatter is calculated using the Kirchhoff GO model by:

$$\sigma^0_{\parallel}(\theta) = \left|\Gamma_{\parallel}(0)\right|^2 \cdot \frac{\exp\left[-\tan^2\theta / 2m^2\right]}{2m^2 \cdot \cos^4\theta} \qquad \textbf{Equation 8.6}$$

(e.g. see Barber (1994); Guneriussen (1997); Rees (1999); and Rees (2001))

where

|| denotes vertical (parallel) polarisation

$\Gamma_{\|}(0)$ is the Fresnel reflection coefficient for *normally incident* radiation, i.e. at nadir.

m is the rms surface slope.

The Fresnel reflective coefficient is determined using the dielectric properties of the surface ε_2 and the assumption that ε_1 (air) = 1:

$$\Gamma_{\|}(\theta) = \frac{\sqrt{\varepsilon_{r2} - \sin^2\theta} - \varepsilon_2 \cos\theta}{\sqrt{\varepsilon_{r2} - \sin^2\theta} + \varepsilon_2 \cos\theta} \qquad \textbf{Equation 8.7}$$

(see Rees (2001), equation 3.32.3 and Appendix A)

The Kirchhoff GO model enables examination of the sensitivity of ERS-2 to ground surface roughness parameters and surface dielectric properties.

8.1.3 Kirchhoff physical optics model

A relatively smooth surface can be appropriately modelled using the Kirchhoff PO model, or scalar approximation. The validity conditions of the PO model are such that:

$$\begin{aligned} &m < 0.25 \\ &kl > 6 \\ &l^2 > 2.76h\lambda \end{aligned} \qquad \textbf{Equation 8.8}$$

The PO model for vertically polarised radiation and a Gaussian autocorrelation function is given by Rees (1999; 2001) and Ulaby *et al.* (1986):

$$\sigma^o_{\|}(\theta) = 2k^2\cos^2(\theta)\cdot\left|\Gamma_{\|}(\theta)\right|^2 \exp\left[-4k^2h^2\cos^2(\theta)\right] \cdot\sum_{n=1}^{\infty}\left[\frac{\left(4k^2h^2\cos^2(\theta)\right)^n}{n!n}\right]\cdot\exp\left[-k^2l^2\sin^2(\theta)/n\right] \qquad \textbf{Equation 8.9}$$

where

|| denotes vertical (parallel) polarisation

$\Gamma_{\|}(\theta)$ is the Fresnel reflection coefficient at incidence angle θ

8.1.4 Other surface scatter models

The small perturbation model (SPM) is appropriate for modelling scattering where surface height variation Δh and correlation length l are small compared to the wavelength; the slope parameter m is also small. The validity domain is given by:

$$k\Delta h < 0.3$$
$$kl < 3$$

Equation 8.10

(see Rees (2001), equation 3.53)

$$m < 0.3$$

Equation 8.11

(see Ulaby (1982b), equation 12.71).

Therefore, using ERS-2, Δh less than 0.0027 m and l must be less than 0.027 m. However, Ulaby *et al.* (1982b) emphasise that no precise conditions of validity have been obtained for the SPM.

The validity domains of the surface scatter models introduced above are can be limiting for certain circumstances. The integral equation model (IEM) (Fung, 1994) is less restrictive in its validity domain and the model can account for a wide range of surface roughness parameters. Usually, some sort of simplification is employed, which limits the validity, however, the IEM is still complex. It is not considered here because the Kirchhoff GO and PO models are considered adequate for this investigation of radar interaction with snow and ground surfaces (see figure 8.2).

8.2 Volume backscatter model

Scatter from a snow-covered surface must also include a contribution from the snow volume. Commonly used volume scattering models are Rayleigh *cloud analogy* models (Ulaby *et al.*, 1986), which assume that individual scatterers (snow grains) are spherical and distributed evenly throughout a medium. The assumptions of such models can be summarised as follows (Nagler and Rott, 2000):

1. Single scattering
2. A single particle size of snow grains that act as independent scatterers
3. Homogenous snow layer, which means that all reflections and interactions between snow layers are neglected

Given these assumptions, the contribution from volume scattering σ^0_{vol} is given by:

$$\sigma^0_{vol}(\theta') = \frac{N\ \sigma^0_b \cdot \cos\theta'}{2\kappa_e}\left(1 - \frac{1}{L^2(\theta')}\right)$$ **Equation 8.12**

(see Barber (1994) equation 24[1])

where σ^0_b is the average scattering cross section from a snow grain and N is the number density of the scatterers, which is calculated from:

$$N = \frac{3v}{4\pi r^3}$$ **Equation 8.13**

(see Barber (1994), equation 27)

where v is the fractional volume of the particular scatterer and r is the radius of the average scatterer. The fractional volume of snow is given by:

$$v_{snow} = \frac{p_{snow}}{p_{ice}}$$ **Equation 8.14**

where the density of ice is 0.917 gm/cm^3.

The value of σ^0_b is calculated according to:

$$\sigma^0_b = \frac{64\pi^5 r^6}{\lambda^4}|K|^2$$ **Equation 8.15**

(see Barber (1994), equation 28).

where K relates the dielectric properties of the scatterer ε within the background dielectric (ε_b):

$$|K| = \left|\frac{\varepsilon - \varepsilon_b}{\varepsilon + 2\varepsilon_b}\right|^2$$ **Equation 8.16**

(see Barber (1994) equation 29.

The extinction coefficient κ_e is calculated using:

$$\kappa_e = \frac{1}{\delta_p}$$ **Equation 8.17**

[1] Notation altered.

where δ_p is the penetration depth, which is calculated as follows:

$$\delta_p = \frac{\lambda\sqrt{\varepsilon'}}{2\pi\varepsilon''} \qquad \textbf{Equation 8.18}$$

(e.g. Ulaby *et al.* (1982b), equation 11.45; Guneriussen (1997), equation 2[2])

The one-way propagation loss $L(\theta')$ term is defined as:

$$\begin{aligned} L(\theta') &= \exp\left(\kappa_e d \sec(\theta')\right) \\ &= \exp\left(\kappa_e d \frac{1}{\cos\theta'}\right) \end{aligned} \qquad \textbf{Equation 8.19}$$

(e.g. Barber (1994), equation 24; Forster *et al.* (1999), equation 6).

where d is the thickness of the snowpack

Guneriussen (1997) presented a simplified equation:

$$\begin{aligned} \sigma^0_{vol} &= \frac{3v}{4\pi r^3} \cdot \frac{64\pi^5 r^6}{\lambda^4} |K|^2 \cdot \frac{\cos\theta'}{2\kappa_e} \left(1 - \frac{1}{L^2(\theta')}\right) \\ &= \frac{24\pi^4 r^3 v \cos\theta'}{\lambda^4 \kappa_e} |K|^2 \left(1 - \frac{1}{L^2(\theta')}\right) \end{aligned} \qquad \textbf{Equation 8.20}$$

8.3 Integrated snow backscatter model

A model of backscatter from a snowpack must take into account backscatter from the snow surface (air-snow interface), the ground surface (snow-ground interface), and scattering from between the two boundaries (snow volume) (Ulaby *et al.*, 1982b). A model for combined backscatter from a snowpack, $\sigma^0_{pack}(\theta)$ was introduced by Ulaby *et al.* (1982b):

$$\sigma^0_{pack}(\theta) = \sigma^o_{ss}(\theta) + T^2(\theta)\left[\sigma^o_{vol}(\theta') + \frac{\sigma^o_{sg}(\theta')}{L^2(\theta')}\right] \qquad \textbf{Equation.8.21}$$

where

$\sigma^o_{ss}(\theta)$ = the snow surface backscattering coefficient,

$T^2(\theta)$ = transmissivity of the air-snow interface,

$\sigma^o_{vol}(\theta')$ = backscattering coefficient of the snow volume,

[2] Equation in publication contained an error. Correct equation is presented here.

$\sigma^{\circ}_{sg}(\theta')$ = backscattering coefficient of the underlying ground surface,

(θ') = angle of refraction in snow,

$L(\theta')$ = one-way propagation loss in snow volume

Most of the terms in the equation 8.21 have been previously defined. The angle of refraction is dependent on the dielectric contrast at the air-snow interface, and is calculated from equation A.5 in appendix A, being a part of the calculation of the Fresnel reflection coefficient. Transmissivity has a simple relation to the Fresnel reflection coefficient:

$$T(\theta) = 1 - \left|\Gamma_{\parallel}\right|^2 \qquad \textbf{Equation 8.22}$$

8.4 Analysis design

A sensitivity analysis was conducted to investigate the effect of geophysical properties and dielectric properties on backscatter from snow covered and snow-free surfaces. The range of parameters for the sensitivity analysis was determined from field measurements and with recourse to the literature.

8.4.1 Surface roughness

Roughness of the snow surface was interpreted qualitatively, with the surface generally becoming rougher as the melt season progressed. Such qualitative measures of snow surface roughness are quantitatively parameterised within the literature. In the subsequent simple models, parameters for ground and snow surface roughness were considered relative to those shown in table 8.1 and 8.2 respectively.

Table 8.1. Qualitative ground surface roughness and quantitative parameters.

Qualitative classification	Δh (metres)	l (metres)	m	Source
	0.0158	0.117	0.19	Nagler and Rott (2000)
Rough	-	-	0.4	
Medium	-	-	0.2 and 0.3	Ulaby *et al.* (1982b figure 12.2)
Smooth	-	-	0.1	

Table 8.2. Qualitative interpretation of snow surface roughness and quantitative parameters.

Qualitative Classification	Δh (metres)	l (metres)	m	Source
Smooth snow	0.0015	0.085	0.025	
Medium-rough snow	0.0037	0.085	0.062	Drinkwater and Crocker (1988)
Rough snow	0.0081	0.082	0.14	
Wet or dry snow	0.0044	0.116	0.054	Nagler and Rott (2000)
Smooth	0.001	0.06	0.024	
Medium	0.01	0.08	0.177	Barber and Ledrew (1994)
Rough	0.017	0.24	0.1	
Smooth snow	-	-	0.1	Guneriussen (1997)
Rough snow	-	-	0.4	

8.4.2 Ground permittivity / soil moisture

The emphasis on acquiring snowpack measurements resulted in a relatively sparse dataset for soil permittivity. Measurements at Abisko and Joatka are given in table 8.3, and were only recorded on 26th May and 5th June respectively. These data illustrate the difference in dielectric constant for wet and dry tundra soils. The Abisko measurements were taken at the time of SAR image acquisition following a significant period of rainfall. At Joatka, relatively well drained tundra soils were measured on 5th June. These measurements are in accordance with measurements by Sjogersten and Wookey (2002) during a measurement period at Abisko from mid June to the end of August 2000; average volumetric soil water content (integrated 0-10 cm) was 24 % and 31 % for the tundra and forest respectively.

Table 8.3. Soil dielectric measurements at Abisko and Joatka.

	Abisko 26/05/99 (n=24)		Joatka 05/06/99 (n=11)	
	Mean	Standard dev.	Mean	Standard dev.
Ground permittivity ε_g	24.9	5.8	9.3	3.8
Soil moisture W_s%	43.3	5	27.2	5.2

Table 8.4. Measured snowpack parameters during seasonal evolution compared with parameters from literature.

Qualitative classification	Permittivity	Permittivity[3]	Penetration depth[4]	Density	Depth	Grain radius	Volumetric water[5]	Reference
			metres	g/cm^3	metres	metres		
	ε'	ε''	δ	p	d	R	$W\%$	
Dry	1.623	0.0004	31.09	0.327	1	0.001	0	Abisko 02/04/99
Slightly wet	2.083	0.021	0.65	0.418	1	0.001	1.1	Joatka 17/05/99
Med. Wet	2.958	0.0933	0.38	0.534	1	0.001	3.9	Abisko 26/05/99
Very wet	2.9466	0.1065	0.14	0.475	1	0.001	4.5	Joatka 5/6/99
Dry	1.53	0.0002	55.61	0.35	2	0.0005	0	(Nagler and Rott, 2000)
Dry (a)	1.8	0.01	Set to ∞	0.55	n/a	0.002	0	(Guneriussen, 1997)
Dry (b)	1.6	0.0004	28.44	0.35	-	-	0	(Guneriussen, 1997)
Wet (a)	1.9	0.08	0.155	0.35	-	-	3	(Guneriussen, 1997)
Wet (b)	2.2	0.15	0.089	0.35	-	-	5	(Guneriussen, 1997)
Wet (c)	2.6	0.28	0.052	0.35	-	-	8	(Guneriussen, 1997)
Wet (d)	2.7	0.38	0.039	0.55	n/a	0.002	6	(Guneriussen, 1997)
Wet	2.61	0.38	0.038	0.35	0.5	0.00075	4.28	(Nagler and Rott, 2000)

[3] Calculated from Fung (1994).

[4] Values in Guneriussen (1997) corrected because of error in calculation of penetration depth in publication.

[5] All volumetric water values calculated according to Denoth (1994) except values from Guneriussen (1997), which were calculated using a relationship in (Tiuri *et al.*, 1984).

8.4.3 Snowpack parameters

Measured values of snowpack parameters are given in table 8.4. The reference gives the source sites of the field measurements, as reported in chapter 7. Table 8.4 also includes published values for comparative purposes. For dry snow measurement (a), Guneriussen (1997) set the one-way propagation loss to 0, which means that the depth parameter is irrelevant. For wet snow measurement (d), Guneriussen (1997) does not give parameters for depth because it is assumed that the penetration depth is such that the ground surface component is not a contribution to total backscatter.

8.4.4 Parameters for sensitivity analysis

The sensitivity analysis was completed by systematically assessing the impact a set of 5 values for each geophysical and dielectric parameter and also the evaluation of two sets of typical seasonal variables. Sensor parameters were held constant: wavelength 0.0565 m and VV polarisation.

The sets of values for the ground sensitivity analysis are presented in table 8.5. When a parameter is being tested the other associated variables are held constant, as shown in table 8.6. The combinations of h and l values in from table 8.5 and 8.6 produce minimum and maximum values of m of 0.07 and 0.44 respectively.

Table 8.5. Variable sets of ground surface parameters for sensitivity analysis.

Variable set	Soil permittivity	h	l
	ε_g	metres	metres
1	5	0.008	0.07
2	8	0.015	0.1
3	12	0.022	0.15
4	18	0.029	0.2
5	25	0.036	0.25

Table 8.6. Combination of ground surface parameters for sensitivity analysis. *Variable* indicates the set of values from table 8.5.

Soil moisture ε_g	h metres	l metres
Variable	0.022	0.15
12	*Variable*	0.15
12	0.022	*Variable*

The variable sets for snow properties are given in table 8.7. The values for W% are derived from the dielectric constant according to Denoth (1994) and the imaginary part of dielectric constant for use in volume model is calculated according to Fung (1994). The values of ε' and ε'' for values of W% are shown in table 8.8 and the combination of parameters are shown in table 8.9. Table 8.7 and 8.9 produce minimum and maximum values of m for snow surface roughness of 0.02 and 0.18 respectively. A parameterisation of the snow properties for typical seasonal snow properties was also conducted using the field values for *very wet* and *dry* snow from table 8.4 and the snow and ground surface roughness measures from table 8.6 and 8.9.

Table 8.7. Variable sets of snow parameters for sensitivity analysis.

Variable set	*W%*	ρ g cm^{-3}	h metres	l metres	d metres	r metres
1	0	0.2	0.001	0.06	0.3	0.0001
2	1	0.3	0.002	0.07	0.7	0.0005
3	2.5	0.4	0.004	0.08	1	0.001
4	4	0.5	0.008	0.1	1.3	0.002
5	6	0.6	0.01	0.2	1.7	0.005

Table 8.8. Typical values of real and imaginary part of dielectric constant for snow water content. Calculated for p = 0.4.

W	Dielectric constant	
%	ε'	ε''
0	1.8	0.0003
1	2	0.02
2.5	2.3	0.05
4	2.7	0.08
6	3.1	0.12

Table 8.9. Combination of Snow parameters for sensitivity analysis. *Variable* indicates the set of values from table 8.7.

W%	ρ	h	l	d	r
	g cm^{-3}	metres	metres	metres	metres
Variable	0.4	0.004	0.08	0.5	0.001
2.5	*Variable*	0.004	0.08	0.5	0.001
2.5	0.4	*Variable*	0.08	0.5	0.001
2.5	0.4	0.004	*Variable*	0.5	0.001
2.5	0.4	0.004	0.08	*Variable*	0.001
2.5	0.4	0.004	0.08	0.5	*Variable*

The validity domains of the SPM, Kirchhoff GO and PO models, which are calculated from equations 8.4, 8.8, 8.10 and 8.11, are graphically presented in figure 8.1. Depending on the validity domain, the Kirchhoff GO or PO models was implemented. For ground surface roughness the Kirchhoff PO was used for h = 0.01 and 0.015 m (l = 0.15 m), for other values the Kirchhoff GO model was used. This is more rigorous consideration of model validity domain than that given by Guneriussen (1997), who only considers values of m (rms surface slope); consideration of Δh and l is required to properly validate use of the Kirchhoff GO model. The Kirchhoff PO model was used for the snow surface model.

Models were implemented using Visual Basic Working Model 6.0 (Microsoft Corp.); program code is presented in Appendix B.

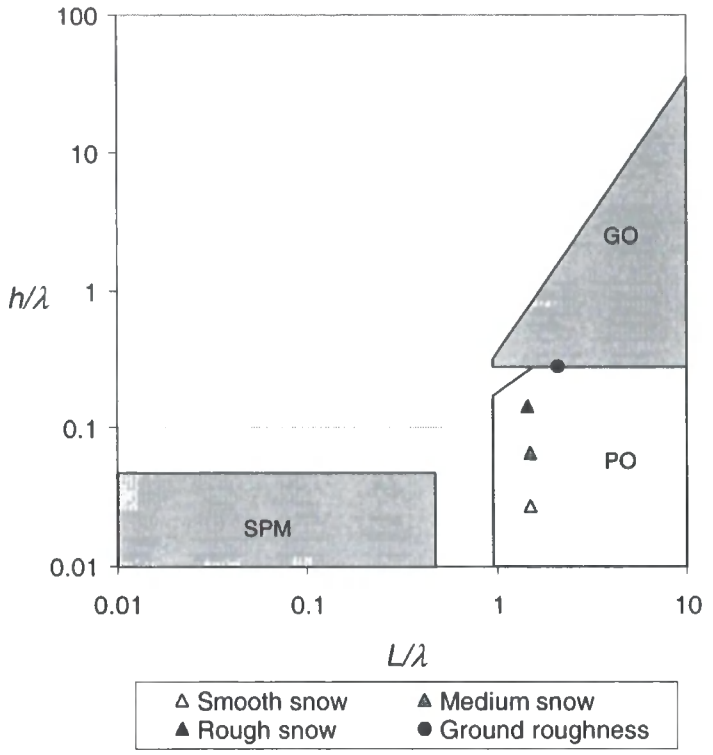

Figure 8.1. Validity domain of the small perturbation model (SPM) and Kirchhoff physical optics (PO) and geometric optics (GO) models of surface scattering. For the GO model the incidence angle is 23° (adapted from Rees (2001)). The values of snow roughness are from Drinkwater and Crocker (1988) and the ground roughness value is from Nagler and Rott (2000).

8.5 Results: ground surface model

The sensitivity of backscatter to ground surface parameters is considered independently from the integrated backscatter model, (i.e. a snow-free surface), however the results can be considered when evaluating the integrated backscatter model when there is an important ground surface backscatter component.

8.5.1 Ground surface roughness

The influence of ground surface roughness, parameterised using values of h and l from table 8.5 is shown in figure 8.2. Backscatter generally decreases considerably as incidence angle increases, but is highly dependent on surface roughness. Smoother surfaces (low values of h, high values of l) produce enhanced *specular* scattering and higher backscatter at lower incidence angles. Increased surface roughness results in reduced angular dependence of backscatter for lower incidence angles; a rougher surface will have more *diffuse* re-radiation. While these results may be instructive in terms of a potential relationship between spatial variation of backscatter and surface

roughness values, the roughness of ground surface will not change significantly during the snow melt period.

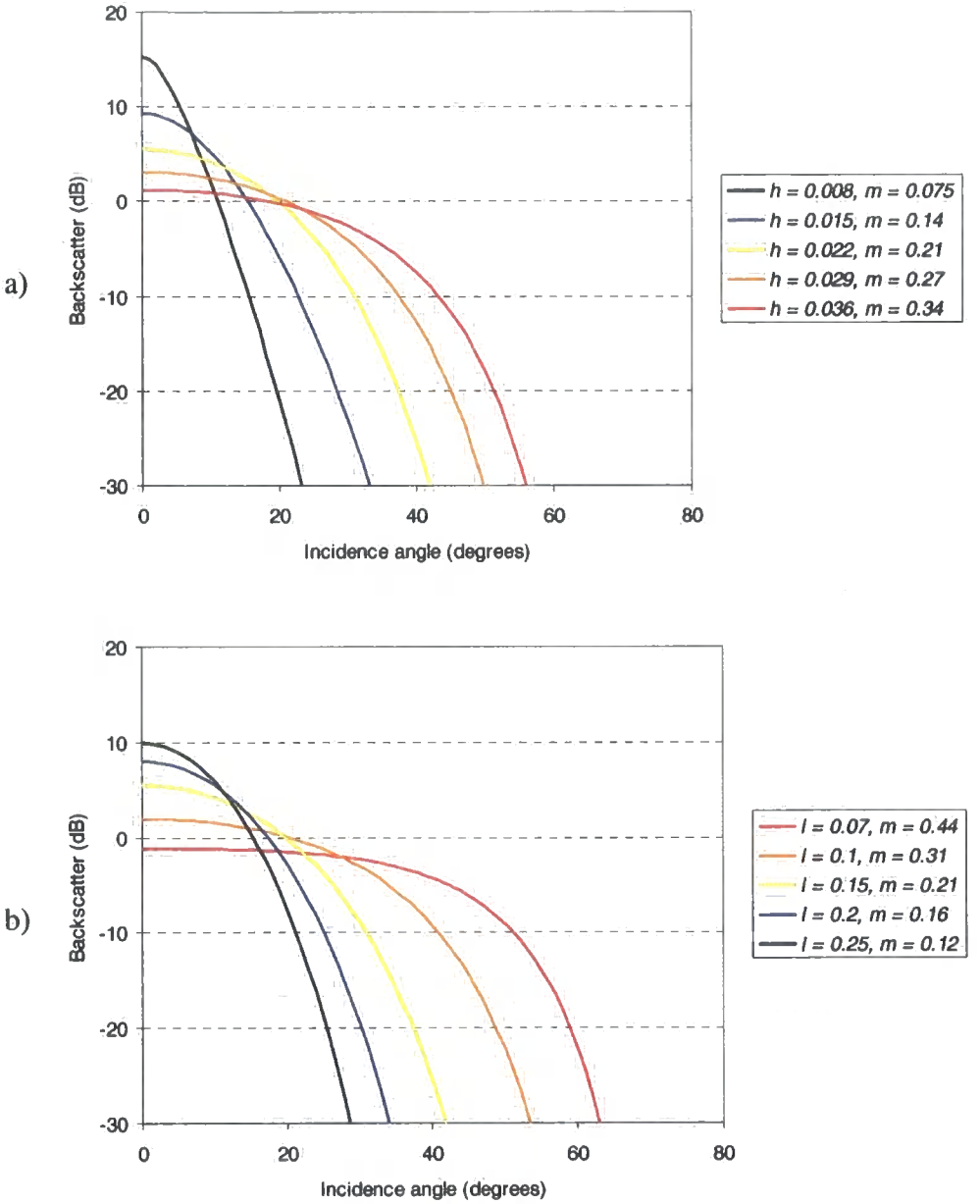

Figure 8.2. Ground surface backscatter model for variable roughness a) std. dev. surface height b) correlation length.

8.5.2 Ground dielectric constant

The importance of ground surface dielectric constant was examined using values of soil permittivity from table 8.5. A modelled difference in backscatter of over 4 dB (at 23°) is shown in figure 8.3 for a change in volumetric soil moisture between approximately 25 to 45 % (see also table 8.3). Based on the ground surface parameters used in table 8.5 it is clear that variation in ground surface roughness may more important than soil

moisture and that variation in surface roughness may mask changes in radar backscatter due to soil moisture.

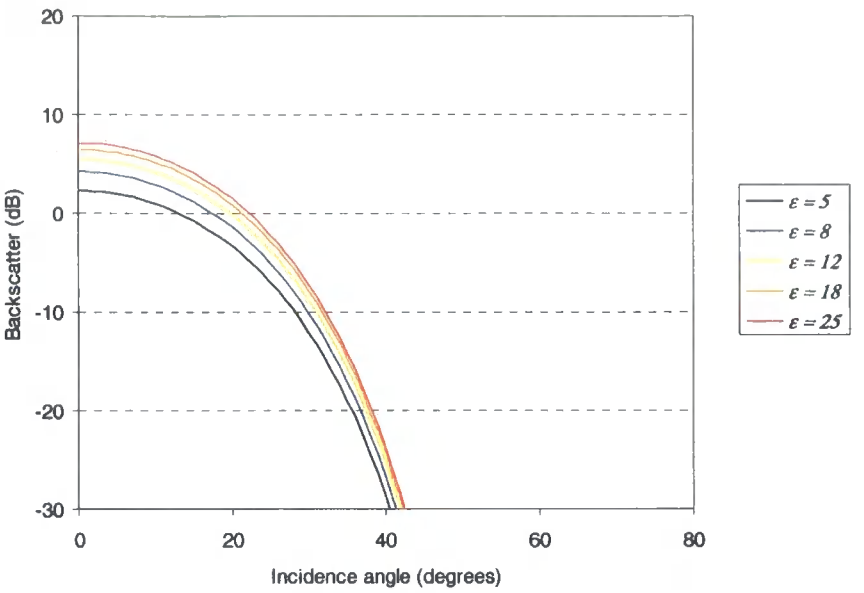

Figure 8.3. Ground surface backscatter model for variable ground permittivity.

8.6 Results: integrated snow backscatter model

For the investigation of backscatter for snow-covered ground, surface scattering from snow and ground must be considered in relation to scattering and dielectric loss from the snow volume. The integrated snow backscatter model presented in equation 8.21 was used with parameters from table 8.9. The snow surface was modelled using the Kirchhoff PO model and the ground surface scattering component was modelled using the Kirchhoff GO model. The ground surface parameters were consistent (see set 3 in table 8.5), but sensitivity of backscatter to ground surface parameters as in figure 8.3 should be considered depending on the contribution of the ground surface to total backscatter.

8.6.1 Snow dielectric properties

Change in snow liquid water content is shown to have a dramatic impact on total backscatter, as shown in figure 8.4. As a snowpack becomes wet, the total backscatter significantly decreases; this is mainly the result of dielectric loss within the snow volume because of the presence of liquid water.

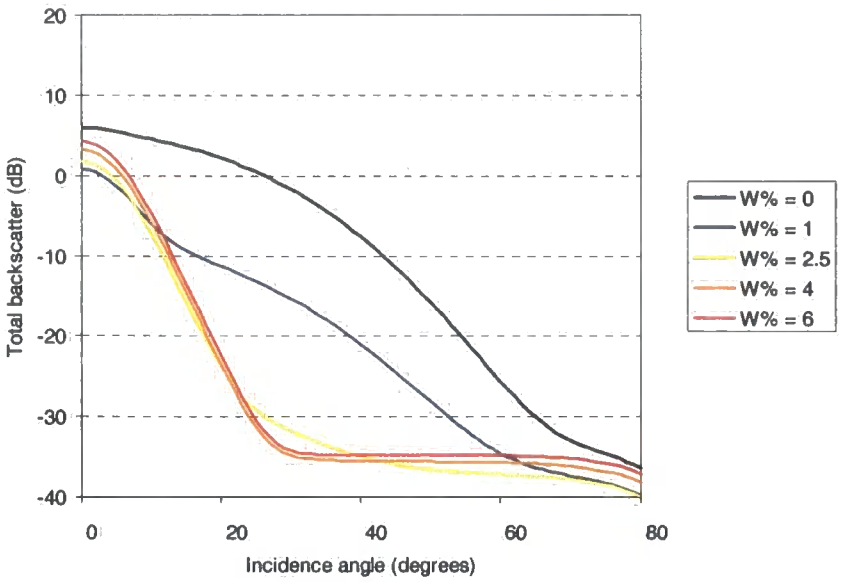

Figure 8.4. Integrated snow backscatter model with variable snow water content.

Figures 8.5 and 8.6 show the relative proportion of total backscatter from snow surface, snow volume and ground surface for snow with W% = 6 and W% = 0 respectively. When the snowpack is wet, scattering from the snow surface is enhanced (because of increased reflectivity) and is relatively the largest contribution to the total backscatter between approximately 0 to 28°. Subsequently, backscatter can increase at lower incidence angle when water content increases because of increased reflectivity. At higher incidence, volume scatter is the dominant contribution to total backscatter, because surface backscatter is reduced and the contribution of scatter from the ground surface can be neglected because the penetration depth is very small. The reduction in penetration depth with increased water content is shown using empirical data in figure 8.7.

For the dry snowpack, backscatter is dominated by the contribution from the ground surface, until high incidence angles when volume backscatter is most important. Transmissivity through a dry snowpack is high; Guneriussen (1997) suggests that the term representing one-way propagation loss, $L(\theta')$, may be set to 1 for dry snow. The relative contribution of the snow surface is to total backscatter is low, except near-nadir, because the dielectric contrast between the air and snow is low.

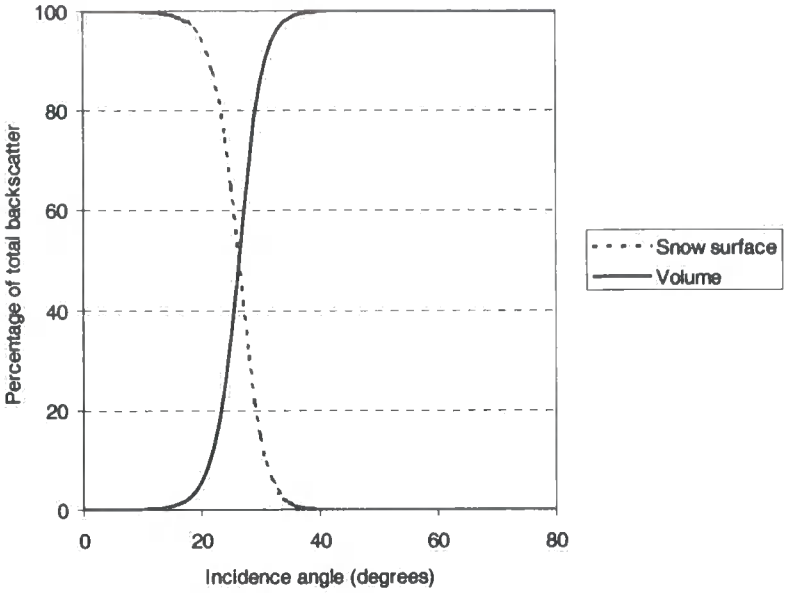

Figure 8.5. Relative proportion of snow surface and snow volume scatter to total backscatter for wet snow (W% = 6).

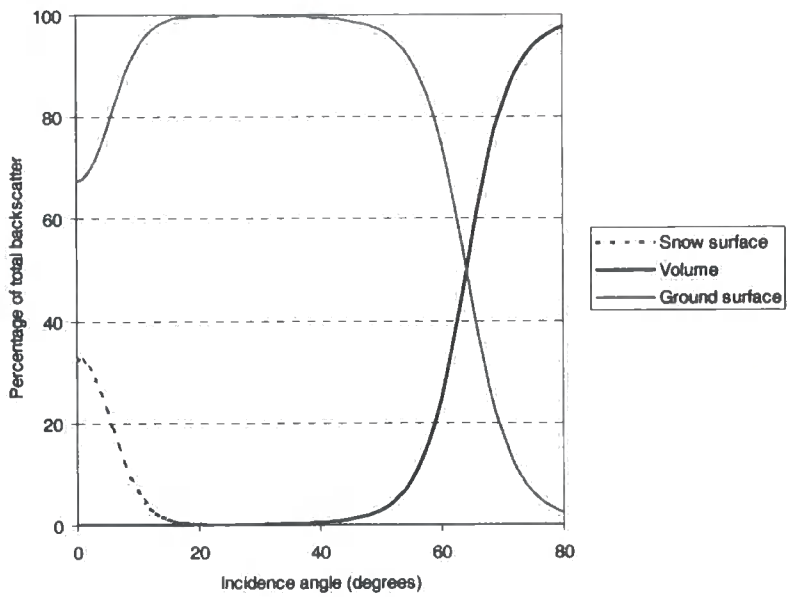

Figure 8.6. Relative proportion of snow surface, snow volume and ground surface scatter to total backscatter for dry snow (W% = 0).

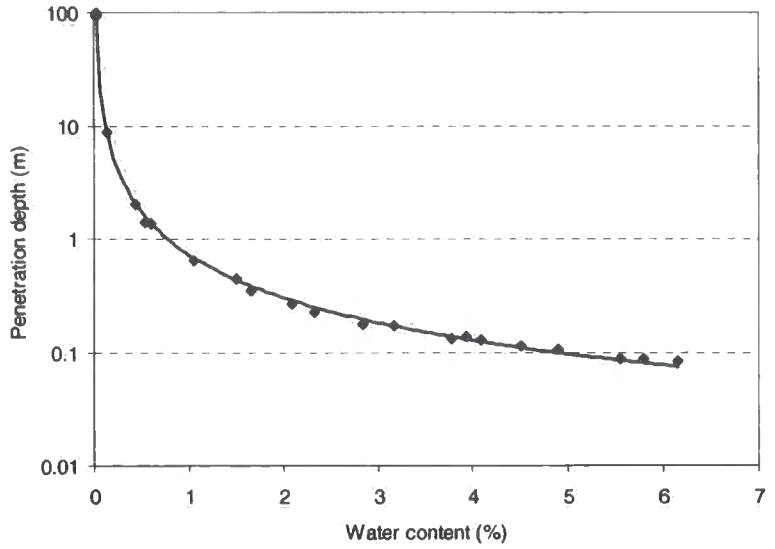

Figure 8.7. Penetration depth of ERS-2 into a snowpack for different dielectric and density properties (see table 8.4 and equation 8.18).

Figure 8.8 shows that for dry snow, the dielectric properties of the ground surface can be important in determining total backscatter. Higher soil moisture content can increase backscatter for dry snow, because the snowpack is essentially transparent.

A dry snowpack will typically have drier soil, because of the cold temperatures. Therefore, figure 8.8 also demonstrates the possibility that a ground surface covered by dry snow may be distinguished from a wet, snow-free surface based on changes in the soil moisture. However, at higher incidence angles the volume scatter from the dry snowpack means that snow covered ground may have a higher backscatter than the snow-free surface. As shown in figure 8.2, this difference in backscatter may depend on the roughness of the ground surface, a rougher surface has reduced angular dependence of backscatter.

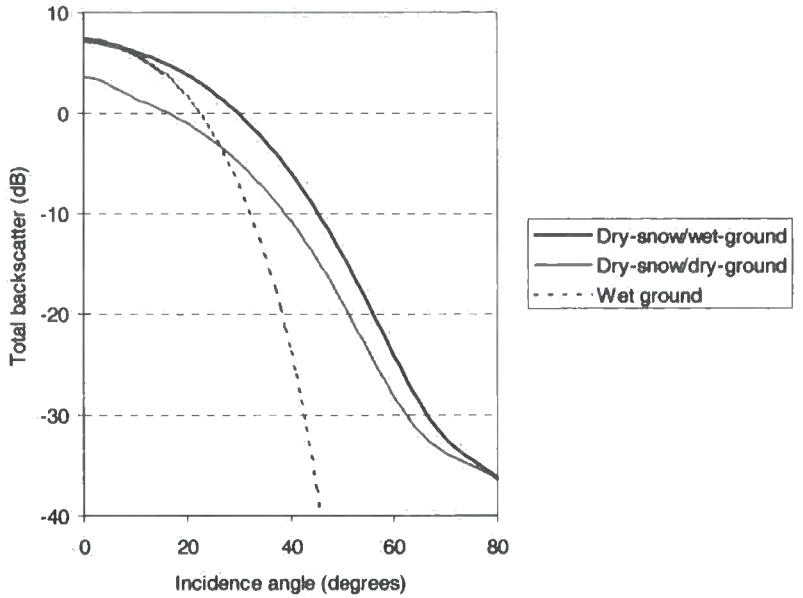

Figure 8.8. Variation in backscatter for a dry snow covered surface with dry (ε_g = 5), wet (ε_g = 25) ground surfaces compared to a wet, snow-free surface. In each case ground roughness parameters are l = 0.15 m and h = 0.022 m.

8.6.2 Snow surface roughness

The sensitivity of backscatter to snow surface roughness was investigated with a snow dielectric constant typical for W% = 2.5. For dry snow, surface scattering may be neglected in comparison to other contributions, except perhaps at near normal incidence (Ulaby *et al.*, 1986).

Results demonstrate that snow surface roughness is important when snow is wet, at least for incidence angles below 40°; at higher incidence angles total backscatter is very low and the volume scattering component is most important. The ground surface is relatively unimportant in this analysis because the backscatter component from the ground surface is small. For variation in h and l in figures 8.9 and 8.10 (m between 0.018 and 0.18) the backscatter can vary significantly – up to 18 dB at 16°. A rough surface for wet snow affects not only the level of backscatter, but also the shape of the curve.

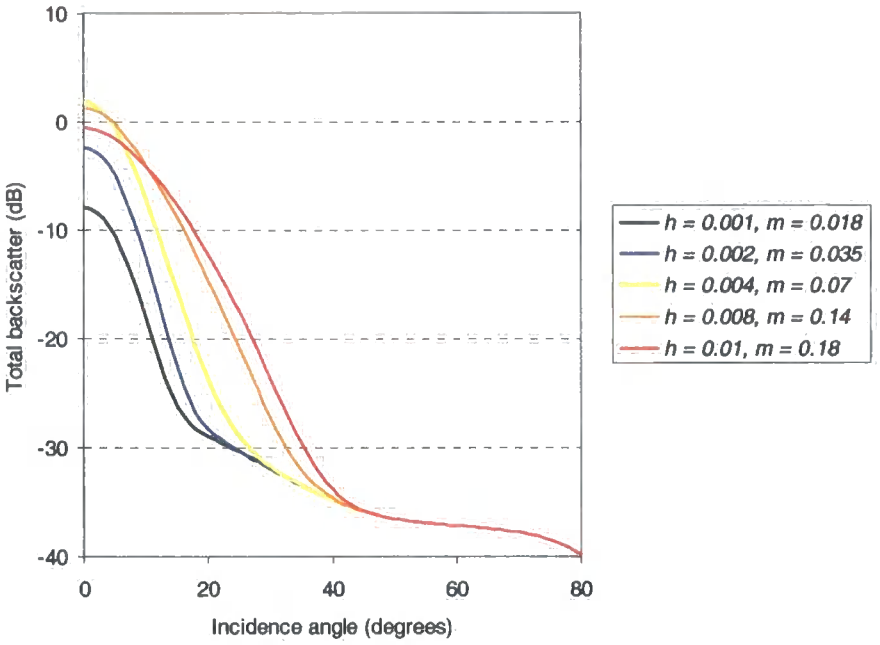

Figure 8.9. Integrated snow backscatter model with variable snow surface roughness (std. dev. surface height).

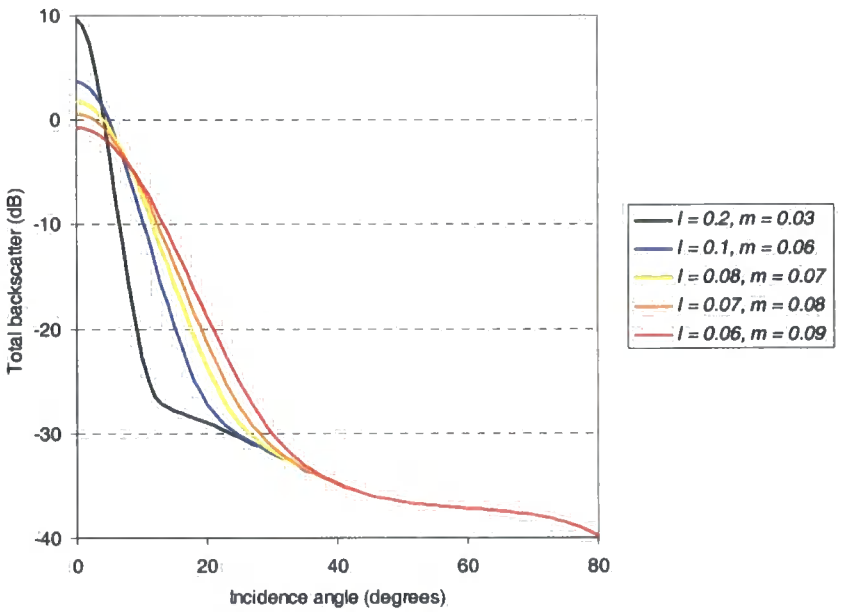

Figure 8.10. Integrated snow backscatter model with variable snow surface roughness (surface correlation length).

8.6.3 Snow density, grain radius and depth

Snow density is shown to have a minimal effect on backscatter, except at high incidence angles where backscatter from the snow volume is the dominant contribution (see figure

8.11). Even then, the maximum difference is about 5 dB at 80° when volume scatter dominates but total backscatter is very low.

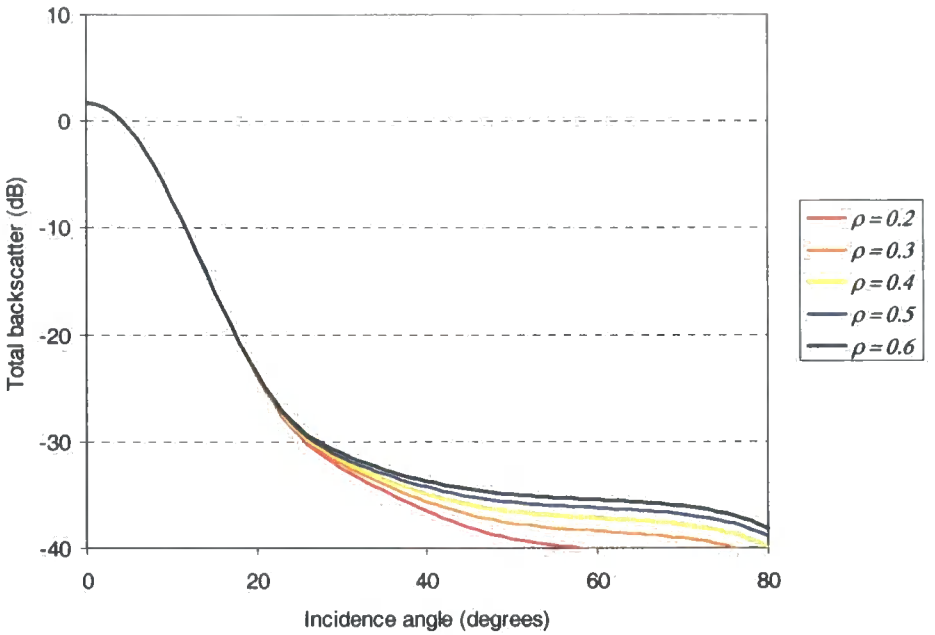

Figure 8.11. Integrated snow backscatter model with variable snow density.

Figure 8.12 shows that snow grain radius produces considerable variation in backscatter over the range of parameters tested. The difference increases from a negligible difference at low incidence to a maximum difference over 35 dB at 60°. The increase in backscatter with increasing snow grain radius is caused by an increase in the scattering cross section of the snow grain, which creates an increase in the volume scattering coefficient. Volume scattering in the snow layer is primarily governed by the size of the ice crystals relative to wavelength (Ulaby *et al.*, 1986).

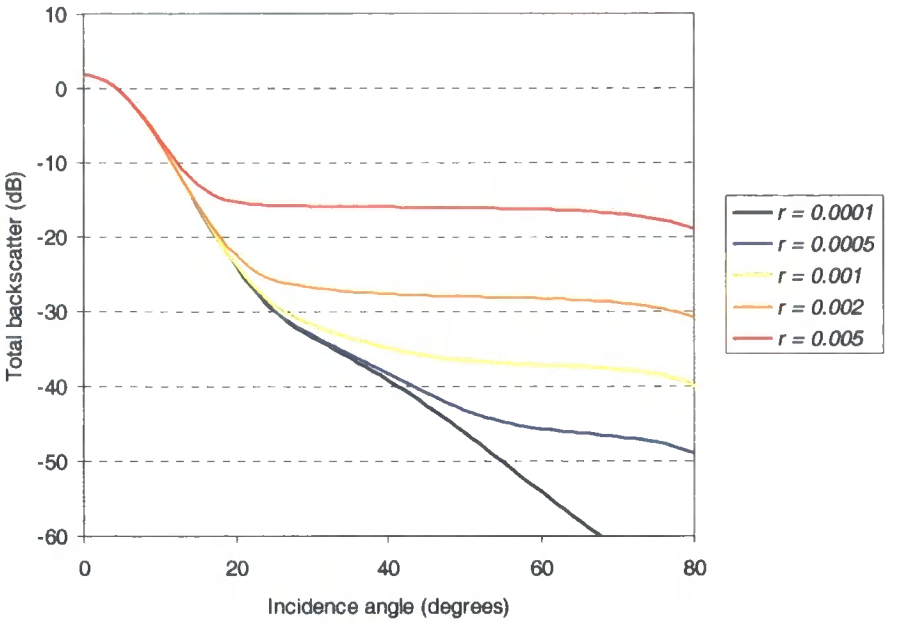

Figure 8.12. Integrated snow backscatter model with variable snow grain radius.

Snow depth is also shown to have a dramatic effect on backscatter for the parameters tested in figure 8.13a, which contrasts with findings in other studies (e.g Barber and Ledrew, 1994; Guneriussen, 1997). This is partly due to the volumetric water content parameter (W% = 2.5), which means that the value of the one-way propagation loss (equation 8.21) is small enough to allow penetration of microwave radiation to the ground surface for shallower snowpacks. This results in a significant ground surface scattering component, meaning that snow depth is an important consideration if the snowpack is only slightly wet. Most parameterisations of snowpacks (see table 8.4) consider deep snowpacks that are either dry or very wet (with a particularly high value of ε'). For example, in figure 8.13b the snowpack is wetter (W% = 6) and there is a significant difference in backscatter only for a snow depth of 0.3 m.

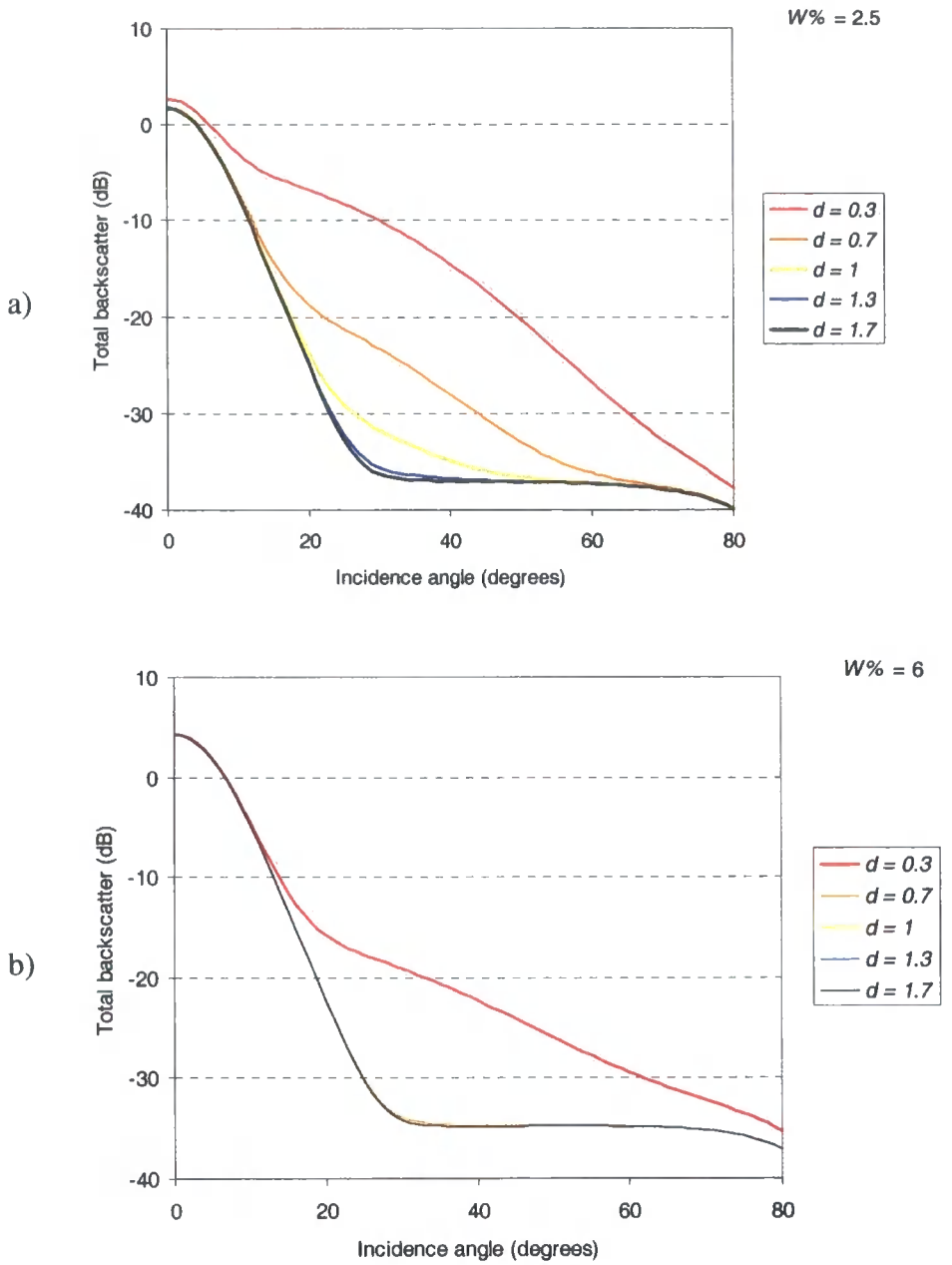

Figure 8.13. Integrated snow backscatter model with variable snow depth for a) W% = 2.5% and b) W% = 6%.

8.6.4 Seasonal change in backscatter

The sensitivity analysis allowed a thorough examination of individual parameters that may impact on backscatter from snow covered ground, however it did not examine combinations of parameters that are considered typical of seasonal snowpack conditions. Using values from table 8.4 for *very wet* and *dry* snow parameters and snow roughness parameters for *rough* and *smooth* snow surfaces (Drinkwater and Crocker, 1988), the seasonal change in backscatter was investigated.

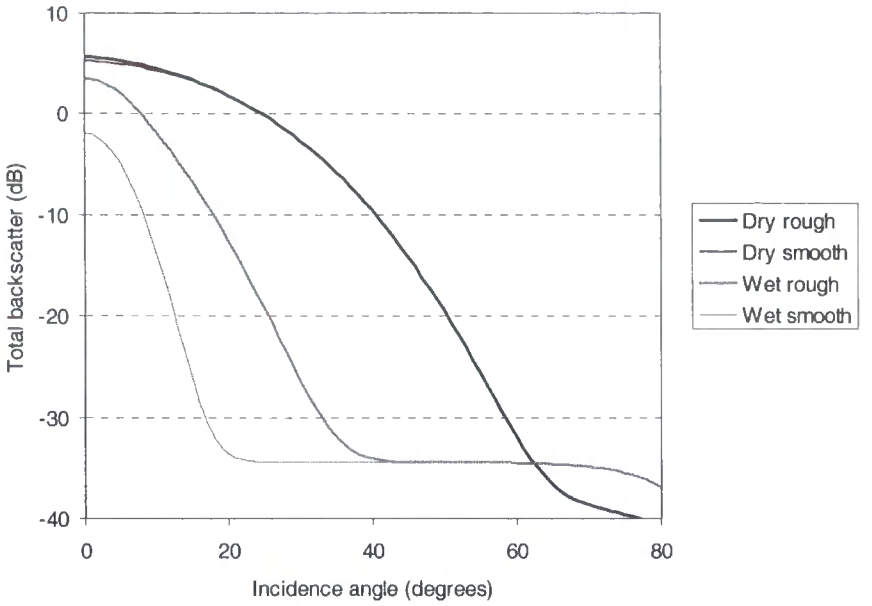

Figure 8.14. Integrated snow backscatter model with for wet and dry and dry snowpacks with roughness from Drinkwater and Crocker (1988).

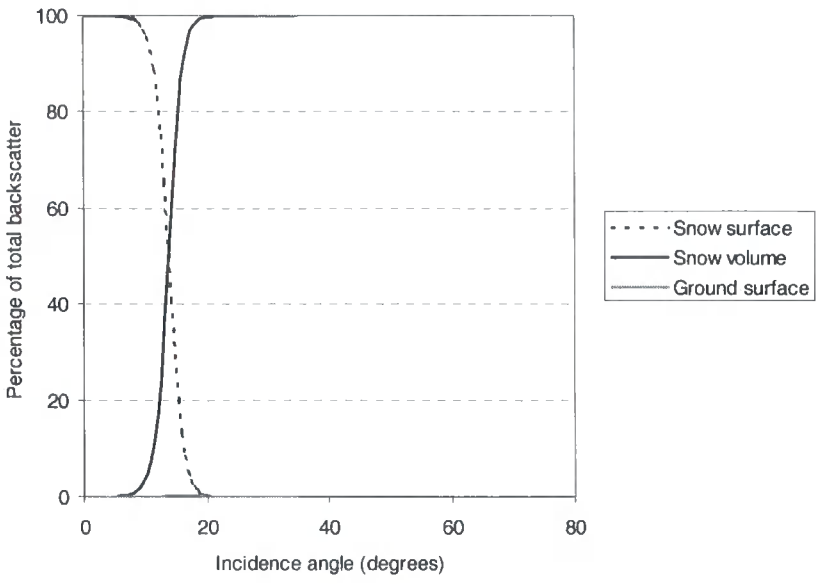

Figure 8.15. Relative proportion of snow surface, snow volume and ground surface scatter to total backscatter for *very wet* snow (W% = 4.5, table 8.5).

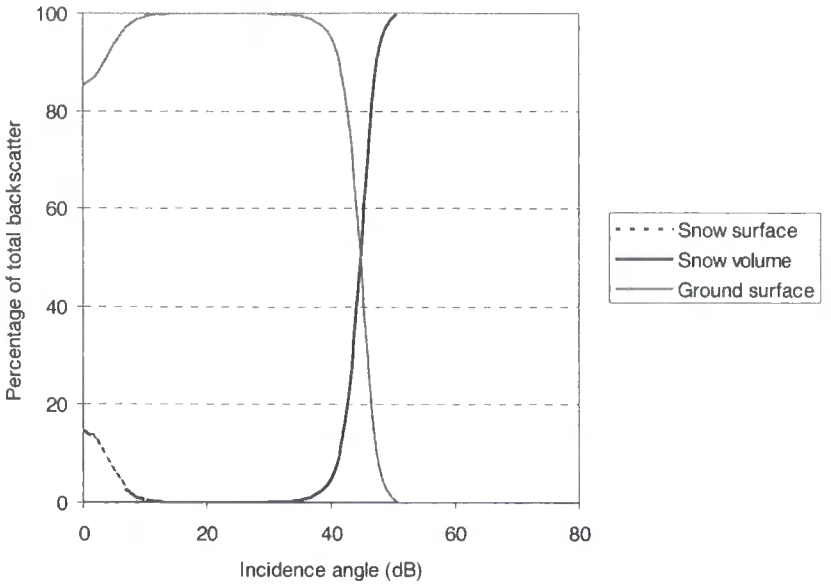

Figure 8.16. Relative proportion of snow surface, snow volume and ground surface scatter to total backscatter for dry snow (W% = 0, table 8.5).

Figure 8.14 shows the expected decrease in backscatter from wet snow compared to dry snow cover. A small difference is apparent for rough and smooth dry snow, but when snow is wet the change in surface roughness results in significant differences in backscatter. It is anticipated that snow will become increasingly rough as snow-melt progresses, which may reduce the difference in backscatter between wet and dry snow cover depending on ground surface conditions.

The proportion of snow surface, snow volume and ground surface scattering to total backscatter is presented in figure 8.15 for *very wet* snow with medium roughness (Drinkwater and Crocker, 1988). For wet snow, scattering from the snow surface is most important at lower incidence angles. Volume scatter becomes important at about 15° although total backscatter is much reduced because of dielectric loss with the snowpack. The contribution of scatter from the ground surface can be neglected because the penetration depth is very small.

In figure 8.16, dry snow with medium roughness (Drinkwater and Crocker, 1988) has surface a scattering contribution only at very low incidence angles and scattering is dominated by ground surface scattering. Volume scattering is most important at incidence angles above 45°. The relative contribution of the snow surface is low because

the dielectric contrast between the air and snow is low. Increased roughness of the snow surface does not significantly enhance this contribution.

8.7 Discussion

Simple modelling can help us to understand the nature of microwave interactions with the ground surface and a snowpack and to extract information from radar images. Physically based surface backscatter models were introduced that included parameters for surface roughness and dielectric constant, in addition to incidence angle. The SPM, Kirchhoff GO and PO models, and IEM are each appropriate under specific conditions related to surface roughness. Results are contingent upon the correct implementation of the physical surface and scattering models (Barber and Ledrew, 1994), particularly in relation to the validity domain of the implemented models. The Kirchhoff GO and PO models were implemented depending on the roughness values investigated in relation to the domains of validity of the models. Through appropriate application of models and a systematic sensitivity analysis, the parameters that can make the largest difference in backscatter were identified and the results can be related to physical conditions encountered during snow-melt.

Results from the Kirchhoff PO and GO models demonstrate the importance of ground surface roughness for received backscatter. Indeed, very rough surfaces may limit the sensitivity of backscatter to incidence angle, at least at low incidence angles. However, ground surface roughness is relatively stable over a period of snow-melt and temporal change in backscatter is not likely to be a function of the roughness properties of the surface. Temporal change in ground surface moisture may have a more significant impact on backscatter. The magnitude of change is less than that for surface roughness, but soil moisture is expected to change significantly over the period of snow-melt. In addition, the effective transparency of dry snow means that ground surface moisture should be considered when a surface is covered with dry snow. This may be important in terms of detecting a difference in backscatter between a ground surface covered in dry snow, which may have low soil moisture because of cold temperatures, and a snow-free surface with higher soil moisture. A significant difference in backscatter might be expected, but results are dependent on ground surface roughness. Typical changes in surface dielectric properties obtained from field measurements, and surface roughness for a medium-rough tundra surface showed a major influence on the backscatter.

In the sensitivity analysis, an increase in snow liquid water content showed that we could expect a significant decrease in backscatter. Indeed, a significant decrease in backscatter occurs for volumetric water content of only 1%. At 2.5% the backscatter was further decreased, but subsequent higher values for water content do no significantly further decrease backscatter. These results demonstrate the importance of small increases of snow water content, which can occur very rapidly through diurnal changes in air temperature. Surface roughness has a strong influence when the snow is wet (Ulaby *et al.*, 1986), which is due to the increase in the dielectric contrast at the snow surface. The (intensity) reflection coefficient of wet snow (W% = 6) is 3.5 times higher than dry snow (W% = 0) at 23°. At higher incidence angles, the snow surface scatter component is less important and snow surface roughness does not affect backscatter regardless of water content. The roughness of the snow surface exercises a negligible effect on the backscattering from snow when the snow is dry; surface scattering is only important near nadir incidence.

Other snowpack parameters investigated were snow density, grain radius and depth. Variation of snow density over the range tested showed little impact on received backscatter and effect of snow density are likely to be masked by other factors. However it is important to accurately measure snow density for determination of liquid water content (Denoth, 1998). In contrast, snow grain radius was shown to have a considerable impact over the range of parameters tested, particularly at higher incidence when the importance of volume scattering is recognised. However, the range of values used was instructive in terms of sensitivity analysis but is perhaps unlikely in terms of values likely due to seasonal metamorphosis in a snowpack. Undoubtedly, an important variable is snow depth, which is often overlooked in modelling studies. When the snowpack is slightly wet (e.g. W% = 2.5) as in the sensitivity analysis, depth is shown to have an important effect. In determining the dielectric loss by means of the one-way propagation loss, depth can be important dependent upon the value ε''; therefore, the method of calculation of ε'' is important. At higher snow water content, snow depth was shown to be less important, but it is clear that the spatial variation in snow depth, even when snow is very wet, may influence backscatter. The patchiness of snow cover and variability in depth relative to the topography and the imaging resolution must be considered.

The combination of parameters in a sensitivity analysis must be limited. Therefore, a combination of parameters from field measurements was also modelled for wet and dry snow. The combined backscatter model demonstrated a clear decrease in backscatter due to the increase in liquid water content and dielectric loss within the snowpack. The importance of surface roughness for a typical wet snowpack was also identified, but the decrease in backscatter for was still considerable compared to backscatter from a dry snowpack.

Limitations must be acknowledged in the application of such models with the data collected. A lack of quantitative field data concerning surface roughness produces uncertainties when comparing model results to images values. However, there is generally a paucity of quantitative values in the literature and Baghdadi *et al.* (2002) acknowledge that correlation length is not only the least accurate parameter but also the most difficult to measure. Another limitation relates to the metamorphism of snowpacks, with distinct layering of even shallow snow covers, which is not incorporated into the models. There may be a significant impact of stratification of snowpacks, even for relatively wet snow given the very small penetration depths. A model proposed by (Forster *et al.*, 1999) to incorporate multiple snow layers is identified as an area for future research. The impact of vegetation on backscatter is not considered, but backscatter can be empirically investigated by comparing backscatter from different vegetation types. Despite the acknowledged limitations, the models illustrate that the dynamic properties of snow and ground surface are critical to understanding the seasonal scattering mechanisms that produce pattern in the ERS-2 data.

Chapter 9. Results: Change in ERS-2 SAR backscatter in relation to seasonally varying snowpack and ground properties

The aim of this chapter is to assess whether changes in ERS-2 backscatter can be detected in relation to the change in snow properties, as reported in chapter 7. The results of snow backscatter modelling in chapter 8 suggest that significant changes in backscatter may be attributable to change in snow and ground surface dielectric properties and snow roughness. In this chapter, the difference between backscatter from tundra and forest vegetation is considered simply by investigating the temporal change in backscatter separately for these vegetation types. Comparison of backscatter between forest and tundra was not conducted because of the complicating effects of, for example, differences in incidence angle, surface roughness and dielectric properties between the vegetation types.

9.1 Sampling methodology

The ERS-2 SAR imagery, vegetation maps, and DEM-derived incidence angle and layover/shadow masks were imported into ArcInfo (version 8.02: ESRI(UK) Ltd., Aylesbury, UK). The raster format of the data means that the data were manipulated using the GRID functionality within ArcInfo.

The reference images for each study site (refer to table 3.1) were reasonably assumed to have dry snow conditions. For other images acquired during the snow melt period, only certain locations had field "ground control data", which meant that samples of backscatter values could only reasonably be investigated from these locations where surface properties were known. Even in dry snow images there may be some exposed ridges and areas of bare rock. Therefore samples were only extracted from the areas of ground control, which were reasonably known to be snow covered.

A ratio of each of these images was made with the reference image. The resultant ratio images were used to investigate temporal change in backscatter. Images known to contain wet snow were used to investigate a wet snow backscatter "signature" and the snow-free images were used to investigate a "snow-free" backscatter signature. The latter signature is based upon the fact that since dry snow is essentially radar

transparent, and we are observing a difference between a relatively dry surface under dry snow and a wet ground surface. This phenomenon was modelled in chapter 8, which demonstrated the physical plausibility. The difference in backscatter may partly depend upon the roughness of the ground surface. Empirical evidence has been noted by Koskinen *et al.* (1997), who observed an increase in backscatter when snow-free areas start to form because of a wet, rough ground surface. This adventitious difference in backscatter from the dry snow covered surface and snow-free surface is referred to as a "snow-free signature".

When access and movement was easier (early-melt and snow-free conditions) more ground control locations were possible, so there is a larger sample size for these conditions. Using the GRID Edit onscreen digitising tools, samples (comprising numerous pixels) were extracted from each of the GRID layers at the location of ground control data. Sampling was undertaken with the following protocol:

- A contiguous area of classified vegetation around the ground control point (GCP).
- Layover and shadow were masked.
- Areas of high and low incidence angle were excluded by limiting the local incidence angle limited to 23 ± 10° (i.e. relative to ERS-2 incidence angle).

The samples were exported for statistical analysis within SPSS (version10; SPSS Inc., Chicago, USA); the following information was exported:

- Backscatter value
- Vegetation code: forest or tundra (dwarf shrub / lichen heath)
- Local incidence angle (for the relevant orbit path)

Temporal change in backscatter was analysed using a paired Student's t-test. The pixels in the (multi-temporal) image ratio were inherently paired and the t-test was a very simple way of comparing the average difference between the backscatter for the sample from reference image and each image later in the melt. The Student's t-test procedure actually tests the null hypothesis of no difference in backscatter between two image dates. A separate t-test was carried out for forest and tundra samples.

The sampling from the images, statistical analysis, and comparison of backscatter values to ground control data and modelling results gives rise to a number of issues:

- Speckle – The use of a paired pixel-by-pixel analysis means that the presence of radar speckle might influence statistics. However, given the use of the Gamma Map speckle filter and the fact that samples were typically of several hundred samples, this should not lead to significant ambiguities.
- Vegetation – there is considerable spatial and temporal variation in vegetation. Only simple empirical consideration of vegetation is made and pixels are paired; the use of image ratios should reduce the effect of variation in vegetation.
- Surface roughness – the surface roughness of the snowpack is known to change and image ratios do not account for this change. The modelling of snow backscatter in chapter 8 suggested that change in snow dielectric properties due to increasing water content is expected to dominate changes in backscatter.
- There are differences between the support (size) of field measurements and the support (size) of the image pixels and samples. This problem cannot be resolved, however. The aim is not direct regression of snow properties (e.g. wetness) to backscatter values, but empirical comparison of values in order to develop classification rules for snow mapping.
- The spatial and temporal limitations of the measurements. With a small training area, caution is required when extrapolating to a larger area.

9.2 Wet snow signature detection

For the detection of a wet snow signature, samples were extracted from the study area where the snow properties were known. The number of pixels in a sample is shown in each table in parentheses next to the vegetation type.

9.2.1 Joatka

The field measurements (chapter 7) established that there was wet snow on 17th May for forest and tundra vegetation (liquid water *ca.* 1 – 2%) and wet snow in the forest on 5th June, but that the water content was considerably higher (*ca.* 4 – 6%). The wet snow signatures on each of these dates were assessed using a paired t-test between the reference image sample and the corresponding sample from the wet snow image.

Table 9.1. Descriptive statistics for wet snow and dry snow samples from 12th April and 17th May (Joatka).

	Forest (n = 395)			Tundra (n = 565)		
	Jan 17	Apr 12	May 17	Jan 17	Apr 12	May 17
Mean (dB)	-10.41	-10.83	-13.73	-11.00	-11.19	-13.09
Std. Deviation	2.01	1.95	2.46	1.95	1.97	2.59
σ_M	.10	.10	.12	.08	.08	.11

(σ_M = Std. Error Mean)

Table 9.2. Paired t-test to evaluate difference in mean backscatter of 12th April and 17th May from reference image (Joatka).

	Forest		Tundra	
	Apr 12	May 17	Apr 12	May 17
Mean (dB)	-.42	-3.32	-.19	-2.08
Std. Deviation	2.53	2.59	2.31	2.59
σ_M	.13	.13	.10	.11
Sig. (2-tailed)	< 0.01	< 0.01	ns	< 0.01

(ns = not significant)

Tables 9.1 and 9.2 show that there was a clear reduction in backscatter for forest and tundra on 17th May. It is also clear that the mean reduction in backscatter is greater for the forest compared to the tundra. There was no significant difference in average backscatter on 12th April on the tundra, although there was considerable variation in all values.

Tables 9.3 and 9.4 indicate that there was a significant decrease in mean backscatter on 5th June within forest; however, there is large variation in the backscatter values. Furthermore, the average decrease in backscatter was lower on 5th June than the 17th May, even though the former snowpack had higher liquid water content.

Table 9.3. Descriptive statistics for wet snow and dry snow sample from 5th June (Joatka).

	Forest (n = 294)	
	Jan 17	June 5
Mean (dB)	-10.37	-11.76
Std. Deviation	2.11	3.18
σ_M	.16	.24

Table 9.4. Paired t-test to evaluate difference in mean backscatter of 5th June from dry snow sample (Joatka).

	Forest
Mean (dB)	-1.39
Std. Deviation	3.50
σ_M	.26
Sig. (2-tailed)	< 0.01

9.2.2 Dovrefjell

At Dovrefjell there were only two dates of field snowpack measurements, but these were used to investigate backscatter values. An identical sample of pixels was used for each image date, although field measurements on 14th April were only conducted at a single location to monitor diurnal changes in snowpack properties. However, the snow cover within the study area was continuous on both dates.

Tables 9.5 and 9.6 show that on 29th March, the mean backscatter from the forest was not significantly different from the reference image in the forest, whereas it was significantly lower from the tundra. However, the difference between the mean backscatter from the tundra is not large (-1.11 ±0.17 dB).

Table 9.5. Descriptive statistics for wet snow and dry snow samples from 29th March, and 14th April (Dovrefjell).

	Forest (n = 330)				Tundra (n = 528)			
	Dry (Feb)	29th March	Dry (March)	14th Apr	Dry (Feb)	29th March	Dry (March)	14th Apr
Mean (dB)	-11.6	-11.71	-11.27	-10.32	-11.6	-12.62	-11.76	-10.22
Std. Dev.	1.82	1.96	1.78	2.00	1.86	2.19	1.92	1.77
σ_M	.10	.11	.10	.11	.08	.10	.08	.08

Table 9.6. Paired t-test to evaluate difference in mean backscatter of 29th March and 14th April from mean dry snow sample (Dovrefjell).

	Forest		Tundra	
	29th March	14th Apr	29th March	14th Apr
Mean (dB)	-.12	.95	-1.03	1.55
Std. Deviation	2.44	2.21	2.43	2.19
σ_M	.13	.12	.11	.10
Sig. (2-tailed)	ns	< 0.01	< 0.01	< 0.01

On 14th April, tables 9.5 and 9.6 show that mean backscatter significantly increased compared to the reference image in both the forest and tundra. At the time of acquisition liquid water content had increased to *ca.* 1 – 2 % in the upper 5 cm of the snowpack meaning a decrease in backscatter due to dielectric loss was expected.

On 3rd May air and ground surface temperature data suggested that the forest was covered by wet snow cover (mean air temperature was significantly above 0 °C in the period before acquisition) and that the tundra snowpack might have disappeared up to a week before this date. A sample of pixels was extracted from the 3rd May image from the same locations as the previous dates and results are shown in table 9.7 and 9.8. There was a significant decrease in mean backscatter from the forest, but also considerable variation in values. The tundra signature also demonstrated a decrease in mean backscatter and large variation in values. This indicates that where the samples were extracted the tundra may not have been completely snow-free.

Table 9.7. Descriptive statistics for wet snow and dry snow sample from 3rd May (Dovrefjell).

	Forest (n = 330)		Tundra (n = 528)	
	Dry	3rd May	Dry	3rd May
Mean (dB)	-11.60	-13.40	-11.60	-14.01
Std. Deviation	1.82	2.50	1.86	2.66
σ_M	.10	.14	.08	.12

Table 9.8. Paired t-test to evaluate difference in mean backscatter of 3rd May from mean dry snow sample (Dovrefjell).

	Forest	Tundra
Mean (dB)	-1.96	-2.33
Std. Deviation	2.98	3.08
σ_M	.16	.13
Sig. (2-tailed)	< 0.01	< 0.01

9.2.3 Abisko

Field measurements at Abisko indicated an interesting pattern of dry snow on 2nd April, with wet snow on 21st April and a refrozen snowpack on 7th May.

Ground temperature data and field observations of tundra areas confirm that they were mostly snow-free before 7th May, particularly at lower elevations and by 26th May only upper forest locations had any wet snow. Sampling was taken where field measurements were obtained and samples of snow-free tundra sites were also analysed in these images because locations of patches of snow-free tundra were known.

Tables 9.9 and 9.10 show difference in mean backscatter for 21st April, when the sampling areas comprised wet snow (liquid water *ca.* 4%). There is a significant decrease in mean backscatter for forest and tundra, but a lower decrease for the tundra. The lower decrease for the tundra may relate to the typically shallow tundra snowpack, which had numerous areas where boulders and vegetation protruded through the snow surface.

Table 9.9. Descriptive statistics for wet snow and dry snow sample on 21st April (Abisko).

	Forest (n = 564)		Tundra (n = 972)	
	Dry	21st April	Dry	21st April
Mean (dB)	-10.89	-12.37	-11.56	-12.40
Std. Deviation	1.89	2.44	1.93	2.46
σ_M	.08	.1	.06	.08

Table 9.10. Paired t-test to evaluate difference in mean backscatter from dry snow cover and 21st April (Abisko).

	Forest	Tundra
	21st Apr	21st Apr
Mean (dB)	-1.48	-.84
Std. Deviation	2.7	2.82
σ_M	.11	.09
Sig. (2-tailed)	< 0.01	< 0.01

The low temperature and low liquid water content of the forest snowpack on 7th May are reflected in the results shown in table 9.11 and 9.12. There is actually a slight increase in backscatter, which may be caused by changes to the properties of the refrozen snowpack. The mean backscatter from snow-free tundra samples reveals a larger increase in backscatter, probably because of snow-free conditions and changes in the relative roughness.

Table 9.11. Descriptive statistics for wet snow and dry snow sample on 7th May (Abisko).

	Forest (n = 564)		Tundra (n = 637)	
	Dry	7th May	Dry	7th May
Mean (dB)	-10.89	-10.55	-11.75	-10.11
Std. Deviation	1.89	2.20	1.76	2.42
σ_M	.08	.09	.07	.10

Table 9.12. Paired t-test to evaluate difference in mean backscatter of 7th May from mean dry snow sample (Abisko).

	Forest	Tundra
Mean (dB)	-.34	1.64
Std. Deviation	2.67	2.70
σ_M	.11	.11
Sig. (2-tailed)	< 0.01	< 0.01

Finally, snow conditions on May 26th were represented by high liquid water content (4 – 6%) in the upper forest. Substantial overnight rain had also fallen, meaning that snow-free areas should have high backscatter due to ground surface reflectivity and provide a contrast with the rapidly melting forest snowpack. However, tables 9.13 and 9.14 indicate that the forest sample has substantially higher mean backscatter than the reference image, and relatively low variation in values. The tundra also showed increased backscatter, higher than on 7th May, perhaps indicating snow-free conditions and a wet reflective surface because of the overnight rain.

Table 9.13. Descriptive statistics for wet snow and dry snow sample from 26th May (Abisko).

	Forest (n = 166)		Tundra (n = 637)	
	Dry	26th May	Dry	26th May
Mean (dB)	-10.13	-7.96	-11.75	-9.15
Std. Deviation	1.62	2.00	1.76	2.09
σ_M	.13	.16	.07	.08

Table 9.14. Paired t-test to evaluate difference in mean backscatter of 26th May from mean dry snow sample (Abisko).

	Forest	Tundra
Mean (dB)	2.17	2.6
Std. Deviation	2.42	2.5
σ_M	.19	.10
Sig. (2-tailed)	< 0.01	< 0.01

9.3 Snow-free signature detection

For the investigation of a snow-free signature, samples were extracted from the study area where the previous snow properties had been known to improve temporal consistency of samples. The number of pixels in a sample is shown in each table.

9.3.1 Joatka

Using the same samples used for wet snow detection on 17th May, the backscatter values on 21st June are used to evaluate a potential snow-free signature. Ground conditions on 21st June were wet because light drizzle had occurred throughout the night. Table 9.15 and 9.16 show the difference between mean backscatter for snow-free and dry snow conditions. Results show that there was a significant increase in mean backscatter in both the snow-free forest and tundra compared to the reference image.

Table 9.15. Descriptive statistics for snow free and dry snow samples (Joatka).

	Forest (n = 395)		Tundra (n = 565)	
	17th Jan	21st June	17th Jan	21st June
Mean (dB)	-10.41	-8.18	-11.00	-8.33
Std. Deviation	2.01	2.17	1.95	1.87
σ_M	.10	.11	.08	.08

Table 9.16. Paired t-test to evaluate difference in mean backscatter of snow-free from mean dry snow sample.

	Forest	Tundra
Mean (dB)	2.23	2.68
Std. Deviation	2.60	2.35
σ_M	.13	.10
Sig. (2-tailed)	< 0.01	< 0.01

9.3.2 Dovrefjell

Air temperature measurements on 19th May had been significantly above 0 °C for several weeks and the ground temperature measurements suggest that the forest was snow-free, although only on the previous day. However, this is the only image available and it is useful in investigate the presence of a snow-free signal, as shown in table 9.17

and 9.18. Results indicate substantially increased mean backscatter from forest and tundra correspondent with snow-free conditions.

Table 9.17. Descriptive statistics for snow free and dry snow samples (Dovrefjell).

	Forest (n = 330)		Tundra (n = 528)	
	10th Mar	19th May	10th Mar	19th May
Mean (dB)	-11.27	-9.33	-11.76	-9.20
Std. Deviation	1.78	1.93	1.92	1.79
σ_M	.10	.11	.08	.08

Table 9.18. Paired t-test to evaluate difference in mean backscatter of snow-free from mean dry snow sample at Dovrefjell.

	Forest	Tundra
Mean (dB)	1.94	2.56
Std. Deviation	2.04	2.37
σ_M	.11	.10
Sig. (2-tailed)	< 0.01	< 0.01

9.3.3 Abisko

Snow-free conditions at Abisko are also related to an increase in mean backscatter from forest and tundra, see table 9.19 and 9.20. The forest has higher backscatter, but the change is very similar in both forest and tundra.

Table 9.19. Descriptive statistics for snow free and dry snow samples (Abisko)

	Forest (n = 398)		Tundra (n = 972)	
	Dry	Free	Dry	Free
Mean (dB)	-11.20	-8.56	-11.56	-9.24
Std. Deviation	1.91	2.17	1.93	2.18
σ_M	.10	.11	.06	.07

Table 9.20. Paired t-test to evaluate difference in mean backscatter of snow-free from mean dry snow sample at Abisko.

	Forest	Tundra
Mean (dB)	2.64	2.32
Std. Deviation	2.55	2.68
σ_M	.13	.09
Sig. (2-tailed)	< 0.01	< 0.01

9.4 Discussion

The analyses in this chapter were possible because the SAR images were geo-referenced using a high resolution DEM and the field measurements were coincident with the SAR image acquisition and accurately located with a GPS. The evaluation of wet snow and snow-free signatures was therefore made using a reasonable spatial distribution of field measurements, which is contrast to many studies that have used meteorological station air temperature data (Baghdadi *et al.*, 1997) and used data from different years to infer snow-melt statistics (Koskinen *et al.*, 1997). The samples were typically of several hundred pixels, which should not mean that the pixel-by-pixel approach and the contribution of radar speckle were problematic. Indeed, the variation in the backscatter was acknowledged in each analysis.

Backscatter from ESR-2 SAR showed seasonal variation, which is interpreted as primarily the result of changes in the liquid water content of the snowpack. The magnitude of the decrease in backscatter due to wet snow appears consistent with the snowpack model results from chapter 8. Backscatter variation was consistent with dielectric loss due to liquid water in wet snow in the forest and tundra on 3rd May at Dovrefjell and 17th May at Joatka; backscatter was significantly reduced in both forest and tundra. However, comparison of field measurements and backscatter values also demonstrate the difficulty of interpreting observed backscatter response because of complex changes in snow properties on diurnal and seasonal temporal scales. For example, at Dovrefjell on March 29th and Abisko on 7th May (in the forest), the backscatter was broadly similar to that from the reference snowpack because the snowpack consisted of re-frozen snow. The possibility to detect wet snow under the forest is in agreement with several authors, who suggest that in low density forest the backscatter is dominated by the dielectric properties of the ground surface (Koskinen *et al.*, 1999; Rignot *et al.*, 1994). Indeed, on 17th May at Joatka, the mean difference in

backscatter was significantly lower in the forest compared to the tundra. This difference may be due to higher liquid water content of the forest snowpack and typically deeper "wet powder" layer in the forest.

The wet-snow signature was less clear in images acquired later in the snow-melt. On 5th June at Joatka a decrease in mean backscatter was detected in the forest, but there was considerable variation in values and the decrease was not large. This could be explained by variation in snowpack properties, but it is likely that forest vegetation had a significant effect. At Abisko on May 26th, wet snow was recorded in the upper forest in field measurements and so we would expect clear wet snow signature, however, the mean backscatter actually significantly increased. The backscatter signature from snow-covered forest areas is the aggregate of backscatter from a number of pathways. The effect of forest cover includes contributions from the forest canopy, and depending on the canopy transmissivity, there is a contribution from the ground including trunk-ground reflection (Koskinen *et al.*, 1997). The results presented here suggest that the density and biomass of the trees at the forest-tundra ecotone does not affect the possibility to detect a wet snow, but that there may be a significant effect on backscatter due to the canopy. An increase in canopy moisture might increase scattering from the canopy and reduce transmissivity of microwaves through to the ground surface (Moghaddam and Saatchi, 1999). Substantial rain fell over the Abisko site on 25th and 26th May, which supports this interpretation. This suggests that the potential of ERS-2 to map snow duration within the forest might be limited by changing canopy conditions.

Despite robust statistically significant signatures for wet snow and snow-free conditions, compared to dry snow cover, there was substantial variation in backscatter values. Higher variation in values is apparent when surfaces are covered by wet snow. The implication that snow dielectric properties may vary over relative short distances in complex topography is realistic; later in the snow-melt, variation in depth and patchiness of cover may also have an effect, although effort was made to extract samples from areas of predominantly continuous snow cover. It is clear that results are somewhat dependent upon the spatial homogeneity of the radar backscatter properties of the snow cover and ground surface. The difference in backscatter between vegetation types was not considered explicitly because of the complexities involved in isolating the vegetation component of the signal. The somewhat higher backscatter from the forest can be qualitatively understood because of the potential of multiple scatter from forest

canopy elements (Rees and Steel, 2001). However, in general little variability in backscatter can be attributed to vegetation, probably because of the low woody biomass of the forest.

Surface roughness of the snowpack was also an important consideration. Image ratios may remove some of the variation in backscatter due to surface roughness, but we know that surface roughness changes because of snowpack evolution. Variation in backscatter due to snowpack surface roughness cannot be ignored; increased snow surface roughness may have been the cause of increased backscatter observed on 14th April at Dovrefjell. The model results in chapter 8 indicated that snow surface roughness could increase backscatter by the amount observed. Nagler and Rott (2000) observed a large increase in ERS-2 backscatter in an experiment by creating a periodic roughness component at wavelength scale in wet snow.

ERS-2 SAR is able to provide regular information on the snowpack, which is important for operational applications, but the snowpack conditions may not be conducive to straightforward snow mapping. Analysis of backscatter signatures and simple modelling shows the complexity of backscatter mechanisms. Based on signatures of SAR backscatter and field measurements, an algorithm for mapping wet and dry snow cover can be developed that is consistent between study sites. A typical difference in backscatter from a dry reference image is –2 to –3 dB for wet snow and a typical increase is 2 dB for snow free conditions. However, there appears to be difficulty when a snowpack is mature and possibly patchy, or due to effects of a wet canopy associated with rain during image acquisition. Any attempt to map wet snow must consider the temporal variation in snow conditions and how this relates to snow duration. Furthermore, the area from which samples were extracted was from a relatively small area with the study site. Applying a mapping algorithm to the larger study area means that there will be an increased variety of targets; consequently there is potential for increased variability in the backscatter response.

Chapter 10. Results: Snow melt mapping

This chapter applies the knowledge gained from the field measurements and snow backscatter signatures to undertake mapping of snow melt at each study site. Chapter 9 demonstrated empirical evidence of a significant wet-snow and snow-free backscatter signature at each site, and chapter 8 demonstrated the physical basis of the backscatter response.

It is clear that critical to the success of any snow-mapping algorithm is to understand the nature of melt-freeze cycles at each site and their effects on received backscatter. In is also necessary to consider the large variation in the backscatter values that was apparent in the wet-snow and snow-free signature from the ratio images. The application of snow mapping over a larger area must be treated with caution given the likely increase in the variety of targets, the greater range of incidence angles and the possibility of altitudinal effects on snow properties.

10.1 The effect of missing coverage

The variation in local incidence angle at each study site is presented in table 6.1 for forest and tundra (which encompasses all the low-growing vegetation types). Values of missing coverage are low for Abisko and Joatka, mainly because the DEM extent at these sites is focused on the area encompassing the forest-tundra ecotone where the topography is less extreme. At Dovrefjell the extent of missing coverage is greater, particularly within the forest, mainly because the study site has more mountainous topography at the FTE and the also because the larger digitised DEM has a larger extent encompassing more varied topography.

Table 10.1. Layover, shadow and other topographic information for each site.

	Joatka		Dovrefjell		Abisko	
	Forest	Tundra	Forest	Tundra	Forest	Tundra
Total area (km^2)	121		1280		106	
Study site elevation range (m)	380-670		450-2200		350-1300	
FTE Elevation (m)	400		1050-1100		700-800	
Mean incidence angle (μ)	24.14°	23.93°	27.77°	21.65°	25.75°	25.97°
$\mu \pm 1.96\sigma$	14.63 - 33.64°	16.74 - 31.1°	3.93 - 51.61°	6.74 - 36.57°	15.29 - 36.2°	14.36 - 37.67°
Total missing coverage (%)	5.5	2.3	33	12	7.8	11.2

10.2 Snow mapping algorithm

The decreased backscatter of wet snow and increased backscatter of snow-free ground in relation to dry snow is the basis for the snow-mapping algorithm. In previous studies, application of radar data for snow mapping has proceeded by assuming continuous dry snow cover and implementing a single rule based on the identification of wet snow; once the snow has been classified as wet, the absence of a wet snow signature given appropriate temperature data is understood to represent snow-free conditions (e.g. Nagler and Rott (2000). In chapter 9 the evaluation of backscatter signatures at each study site indicated a discernable wet snow signature, but also the possibility to identify snow-free conditions perhaps without the prerequisite of a wet snow signature; this is potentially important given the identified rapidity of snowmelt and melt-freeze effects at each site.

A threshold of –3 dB was selected for wet snow, a value compatible with the wet snow signature detected in chapter 9 and with values in the literature (e.g. Nagler and Rott (2000); Baghdadi *et al.* (1997)) and therefore useful for comparative purposes. A value of +2 dB was selected for an initial classification of snow-free conditions, but this was subject to additional rules based on temporal integrity of snow cover, which are discussed in section 10.2.2

The conceptual temporal pattern of snow melt is a period of dry snow conditions followed by persistent wet snowpack, concluded by snow-free conditions. However, ground control data provided evidence that the progression of snowmelt is far from simple and a snow-mapping algorithm must have the capacity to map a snowpack that may become wet and refreeze before snow-free conditions. There is also the possibility that ground covered by dry snow in an initial image acquisition may melt rapidly during the satellite return period, becoming snow-free for the subsequent image acquisition; no characteristic wet snow signature would be detected.

The snow-mapping algorithm can be formalised as follows:

If $\sigma^0_{dif} < -3$ dB then classify as wet snow

If $\sigma^0_{dif} > +2$ dB then classify as snow-free

Otherwise, assume dry/refrozen snow. This classification algorithm is illustrated in figure 10.1.

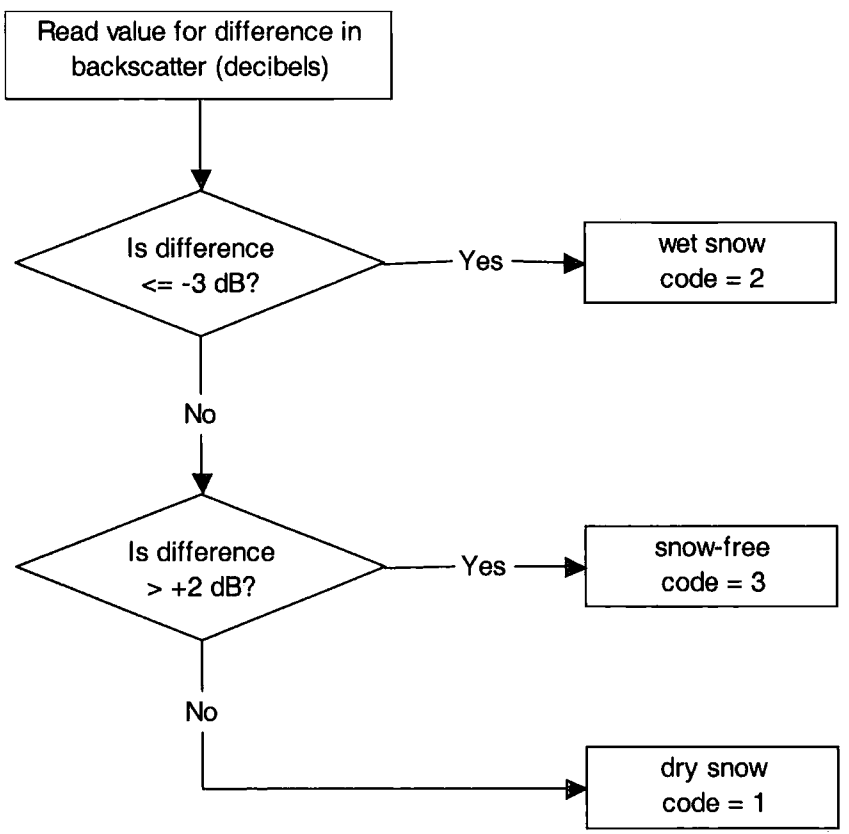

Figure 10.1. The algorithm used to classify snow cover using difference in backscatter.

10.2.1 Transition codes

Using snow-mapping thresholds given above, initial transition images can be constructed that describe how the snow cover state changes between each image based solely on the backscatter thresholds; from dry/refrozen snow, to wet-snow, to snow-free. Depending on the number of images for a site, this will produce several new images with unique codes defining how the snow conditions changed from the previous image, as shown in table 10.2.

Table 10.2. Snow-state transition codes.

Transition Code	Change in state
1	Dry to Dry
2	Dry to Wet
3	Dry to Free
4	Wet to Wet
5	Wet to Free
6	Wet to Dry
7	Free to Free
8	Free to Wet
9	Free to Dry

The physical basis for the snow-mapping algorithm has been discussed, but in reality some transitions in state in table 10.2 are unlikely and potentially difficult to detect. In particular, transition from snow-free to dry snow (9) almost certainly did not occur at each study site; we have no ground control data, but it is unlikely that a unique signature could be detected because the new dry snow cover would probably be over wet ground and have different properties to the reference snowpack. Other changes in state can be reasonably detected, including dry to free (3) if dry-snow completely disappears within the return period of the ERS-2 satellite. A wet to dry (6) transition can reasonably occur if we consider the re-freezing of a wet snowpack and have compatible ground control data (in this case the difference in backscatter would be between –3 dB and +2 dB having previously been below –3 dB). Classification algorithms were written in Arc Macro language (AML), see appendix C. The transition codes are supported by substantial ground control information, which should enable a realistic pattern of snow

melt to be mapped. For simplicity of interpretation, the codes in table 10.2 were recoded as 1 = dry/frozen, 2 = wet snow, and 3 = snow-free (see appendix C).

10.2.2 Temporal consistency and additional rules

The transition codes for each image were produced very simply using only the defined backscatter thresholds. However, considerable variation in backscatter was identified in chapter 9 and field measurements of snow properties indicated that an understanding of the temporal consistency was necessary; this provides the basis for additional classification rules. Two additional rules are implemented at each site to improve the temporal consistency of snow maps, in particular to assess the novel use of a snow-free threshold. Classification algorithms were written in AML, see appendix C.

1. Additional snow-free classification rule: A typical snow-mapping algorithm would consider wet snow (code 2) followed by the absence of wet-snow in a subsequent image to indicate snow-free conditions (code 3) (e.g. Baghdadi *et al.* (1997); Nagler and Rott (2000)). However, I implemented a snow-free classification. Under circumstances where snow was previously wet and field measurements indicated that any snow present should be wet, then it was assumed that the snow had melted, but the snow-free signature was not clear. Therefore, dry/refrozen snow (code 1) was recoded as snow-free (code 3) if the ground data indicated it should not be dry snow (see figure 10.2).
2. Snow-free consistency: Without fresh snowfall, it was assumed that pixels that become snow-free should remain snow-free. If a pixel was snow-free on a particular date (code 3) but subsequently wet snow (code 2) or dry/frozen snow (code 1), then it was reclassified as snow-covered. An illustration of the algorithm is given in figure 10.3 and the AML is detailed in Appendix C.

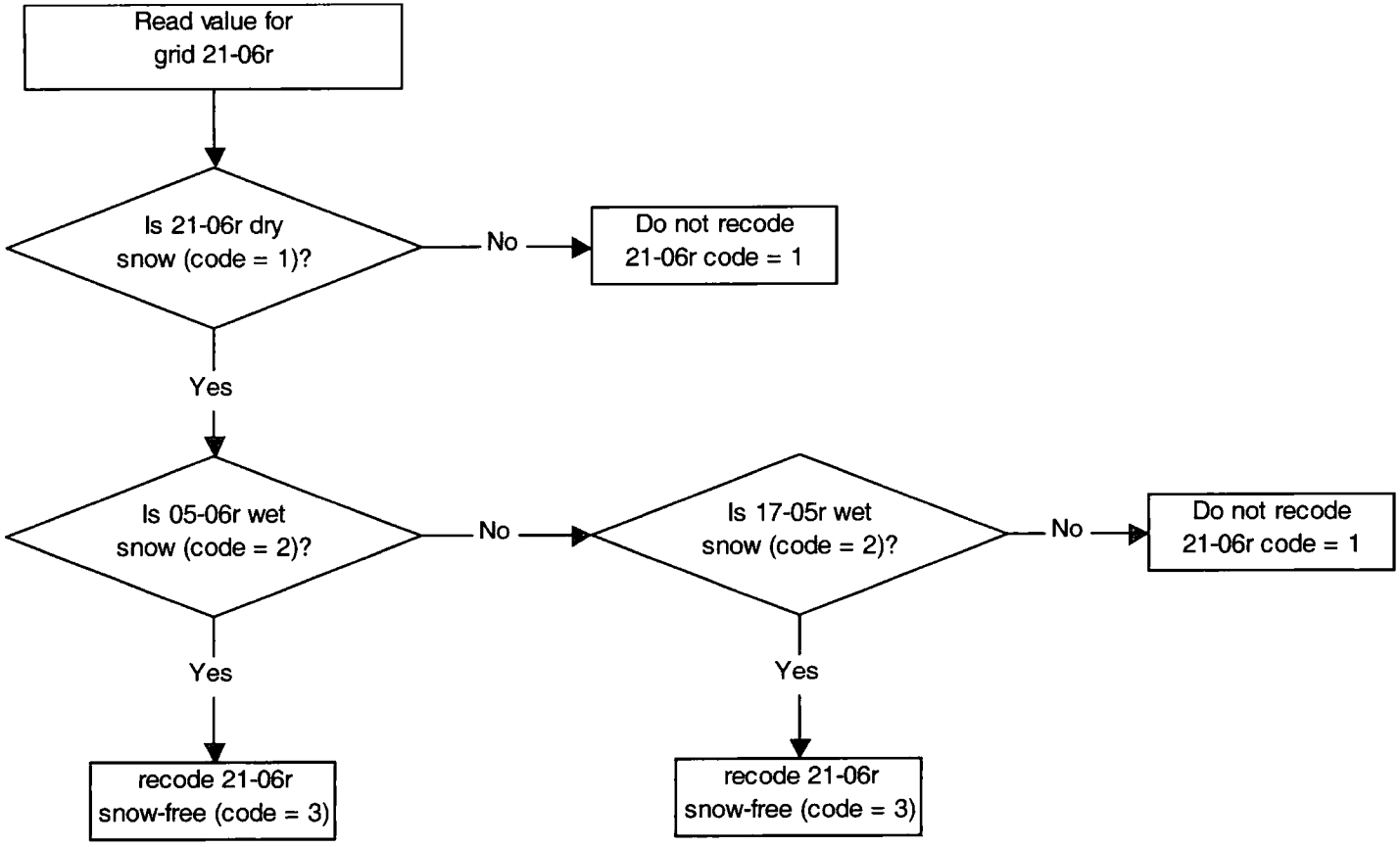

Figure 10.2. The algorithm to recode cells that are dry/frozen snow in the image acquired on 21st June to snow-free if they previously contained wet snow in an earlier image.

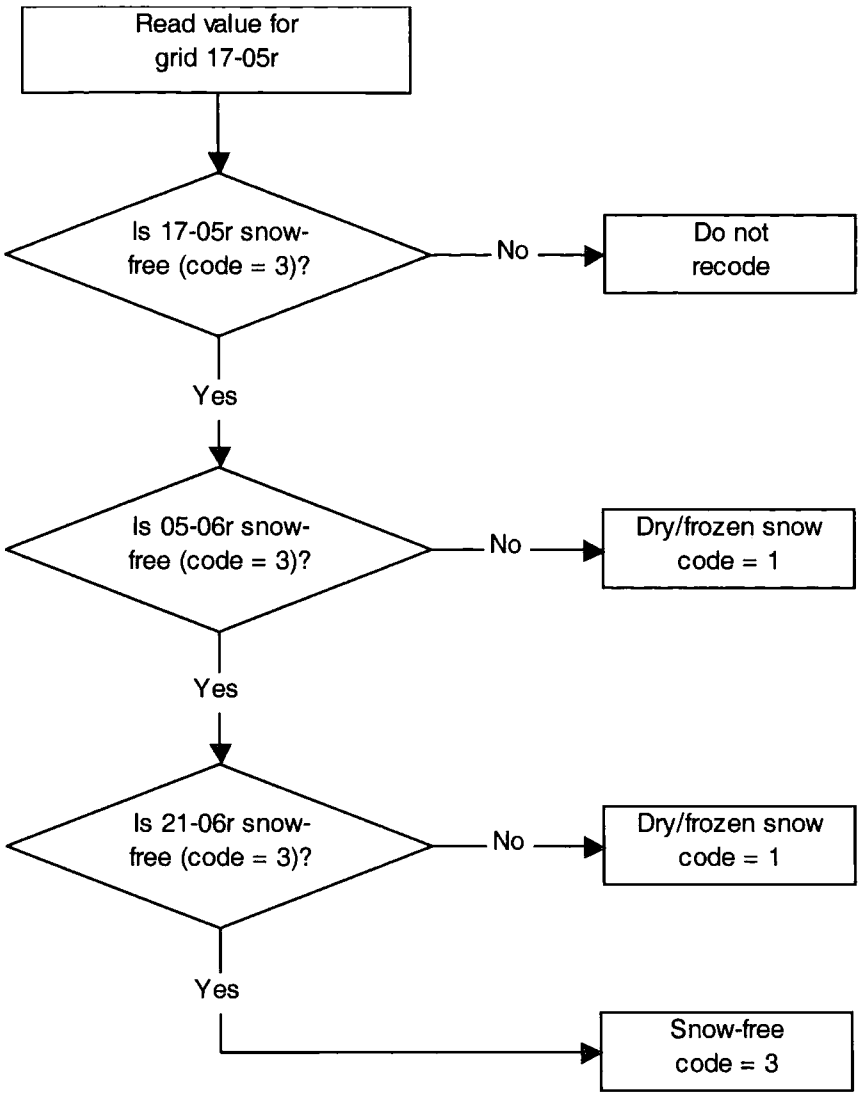

Figure 10.3. The algorithm to ensure temporal consistency of snow cover. Example for Joatka image acquired on 17th May.

10.3 Snow mapping

Snow maps were created with and without the additional rules and were created for each date of wet snow, dry snow, and snow-free ground cover. SAR backscatter images are single channel grey-scale images. Colour density slicing was also employed to the ratio images so that temporal change in backscatter within each study area could be interpreted through change in colour. In order to help interpretation of the pattern of snow melt, the relevant images have been "draped" over the DEM. In addition, the vegetation, elevation, slope gradient and solar index maps are also displayed in this form; these maps comprise figures 10.4-10.7 and figures 10.14-10.17 at Joatka and Dovrefjell respectively. At Abisko, a larger area of the SAR images is simply presented

in two dimensions because backscatter changes are predominant over Lake Torneträsk, which is not covered by the DEM. The conventional two-dimensional representation of Joatka and Dovrefjell snow maps are presented in appendix D.

At Joatka, a clear pattern of snow melt can be recognised in figures 10.8 to 10.13. On 17th May, there was a decrease in backscatter at lower elevations, particularly on the south-facing forested slope, but the study site was predominantly snow-covered. By 5th June, there were substantial areas of decreased backscatter on the highland plateau and also to the south. Many areas showed an increase in backscatter, and others little change; snow cover on the 5th June characterised a snow-covered and snow-free mosaic. By 21st June the study area was mostly snow-free.

Temporal change in backscatter and snow maps for Dovrefjell are shown in figures 10.18 to 10.23; in each figure, the grey shading in the body of the image is layover (see appendix D). Backscatter on 14th April at Dovrefjell showed an increase across most of the study area, apart from a decrease in the north at lower elevations within the Drivdalen valley, however this area is affected by layover. By 5th May, there was a substantial decrease in backscatter in many areas, particularly at higher elevations. An increase in backscatter at lower elevations to the south of the study area was also evident and demonstrates lower elevation areas of snow-free cover and a snowline retreating to higher elevations. By 19th May there remained substantially lower backscatter at high elevations, but the area encompassing the forest-tundra ecotone appeared to be snow-free.

At Abisko, changes in backscatter in figure 10.24 can be seen very clearly over Lake Torneträsk as the snow-cover overlaying thick ice became wet. Variation in backscatter occurred across the area encompassing the forest-tundra ecotone. On 21st April most of the study site showed a decrease in backscatter associated with wet snow. On May 7th, cold temperatures result in much of the area having little change in backscatter. However, some areas showing increased backscatter are probably snow-free. In figure 10.25, it is clear that by 26th May much of the study site was snow-free, as indicated by increased backscatter. At high elevations a decrease in backscatter represented wet snow.

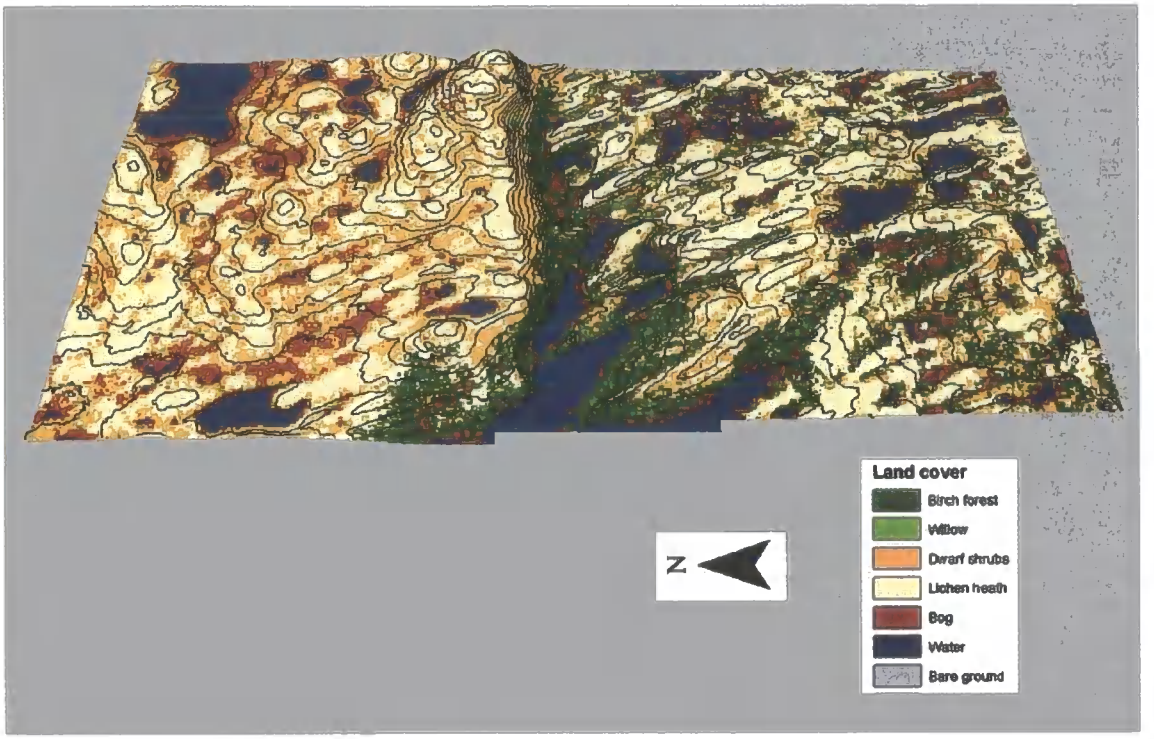

Figure 10.4. Vegetation at Joatka study site.

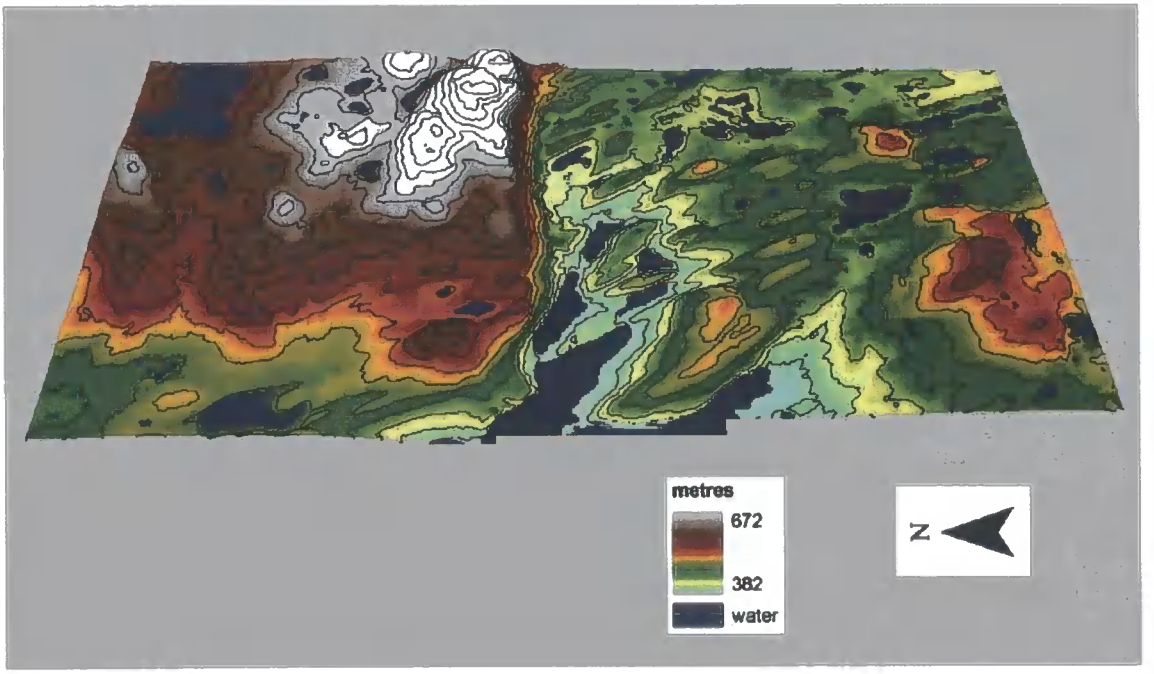

Figure 10.5. Elevation at Joatka study site.

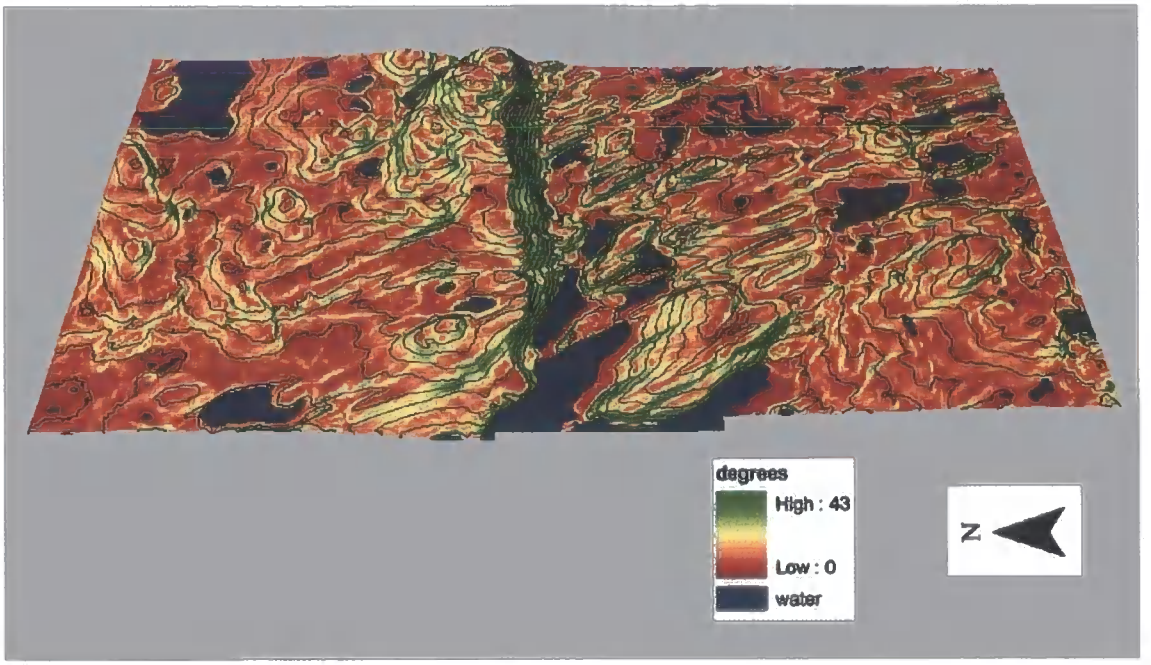

Figure 10.6. Slope gradient at Joatka study site.

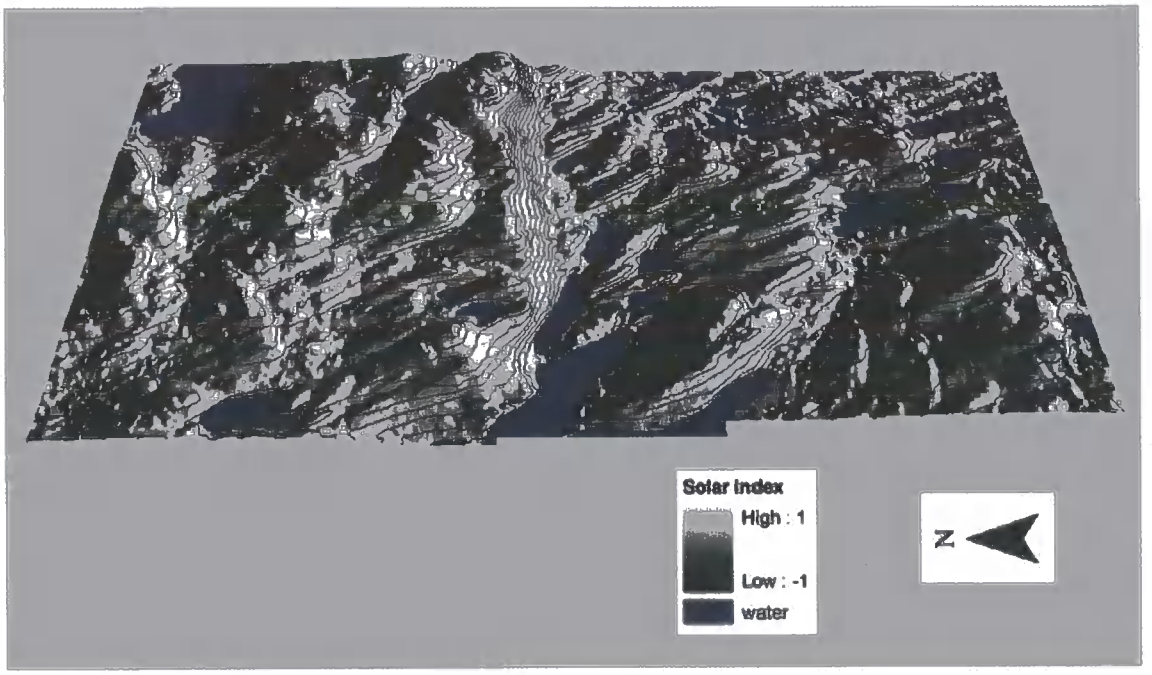

Figure 10.7. Slope aspect (solar radiation index) at Joatka study site

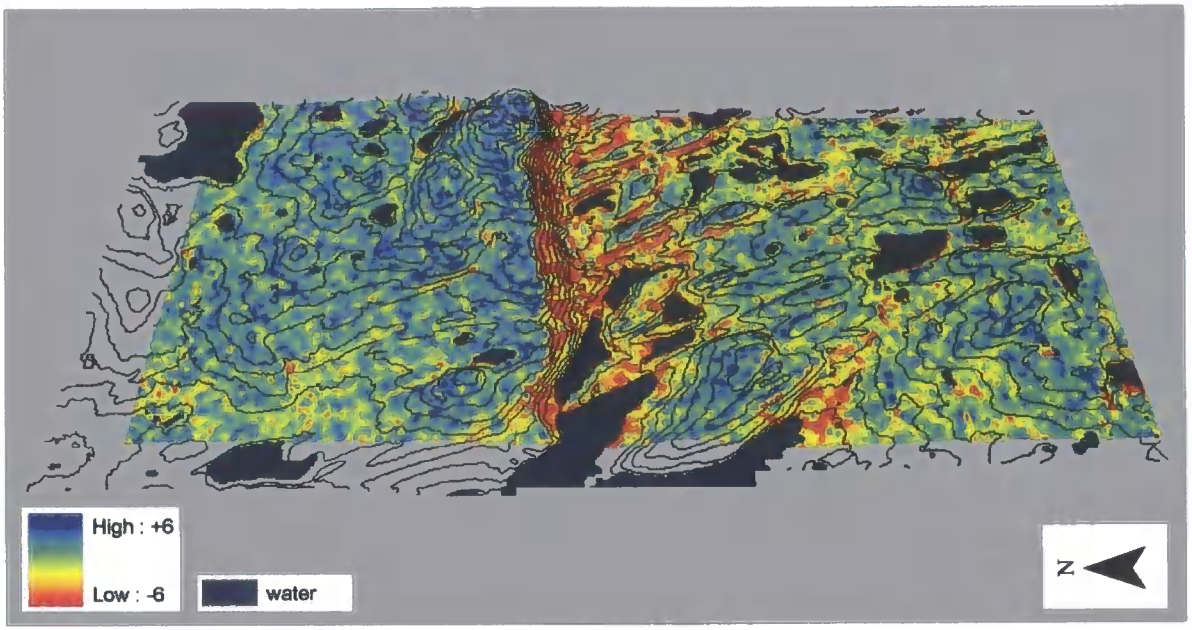

Figure 10.8. Spatial variation in backscatter difference (decibels) at Joatka, 17th May.

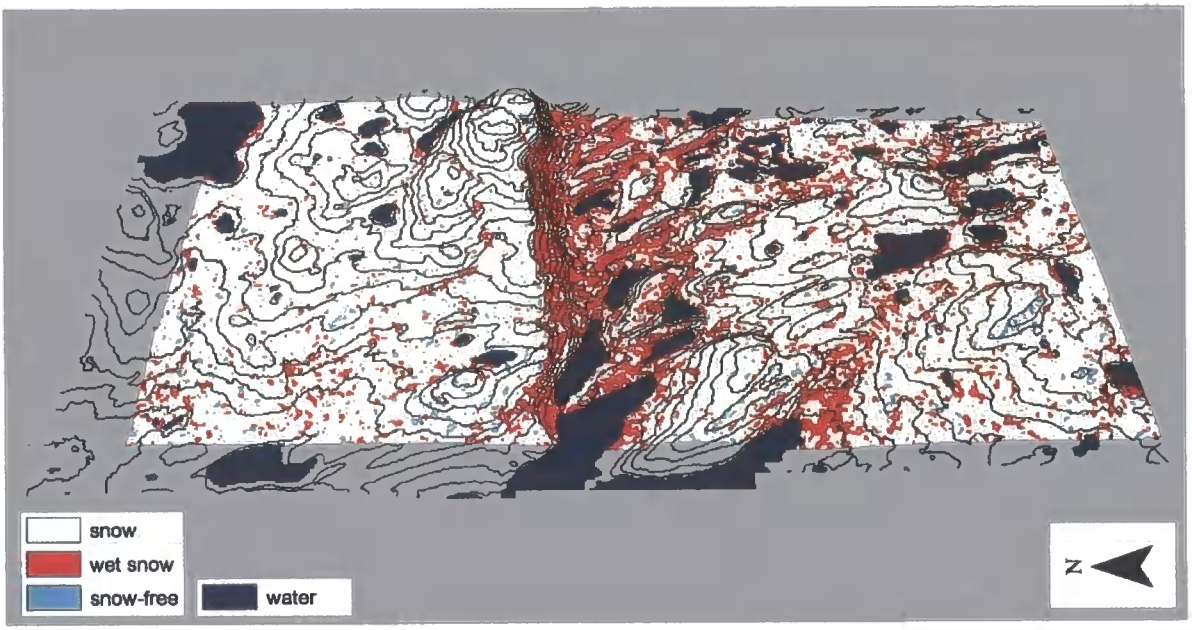

Figure 10.9. Snow map for Joatka, 17th May.

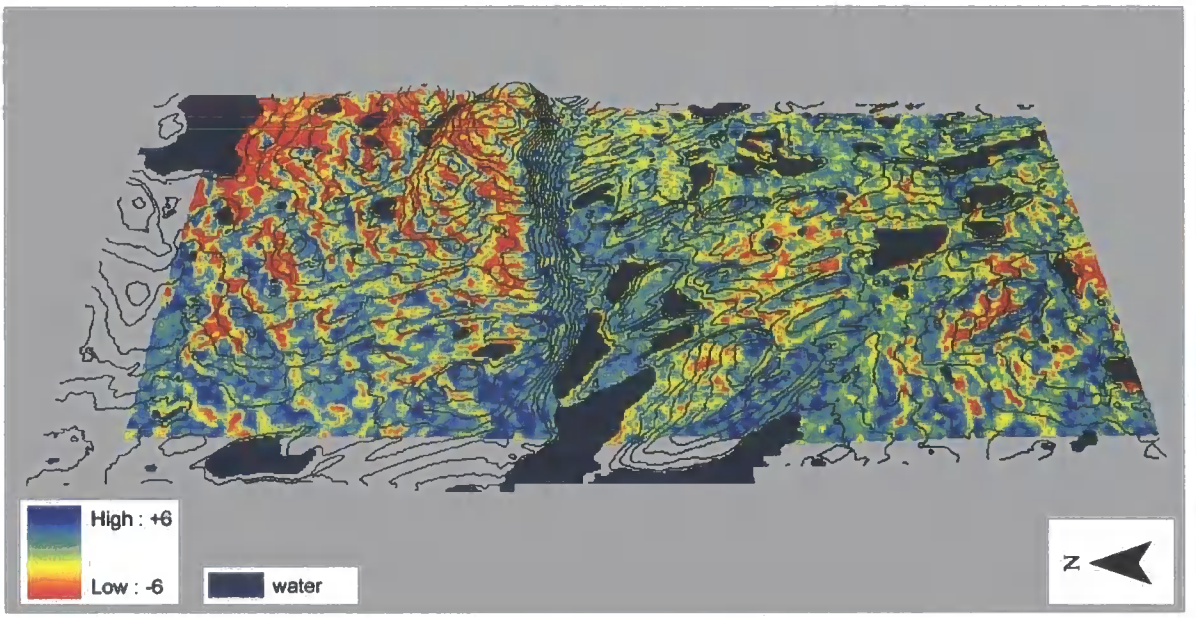

Figure 10.10. Spatial variation in backscatter difference (decibels) at Joatka, 5th June.

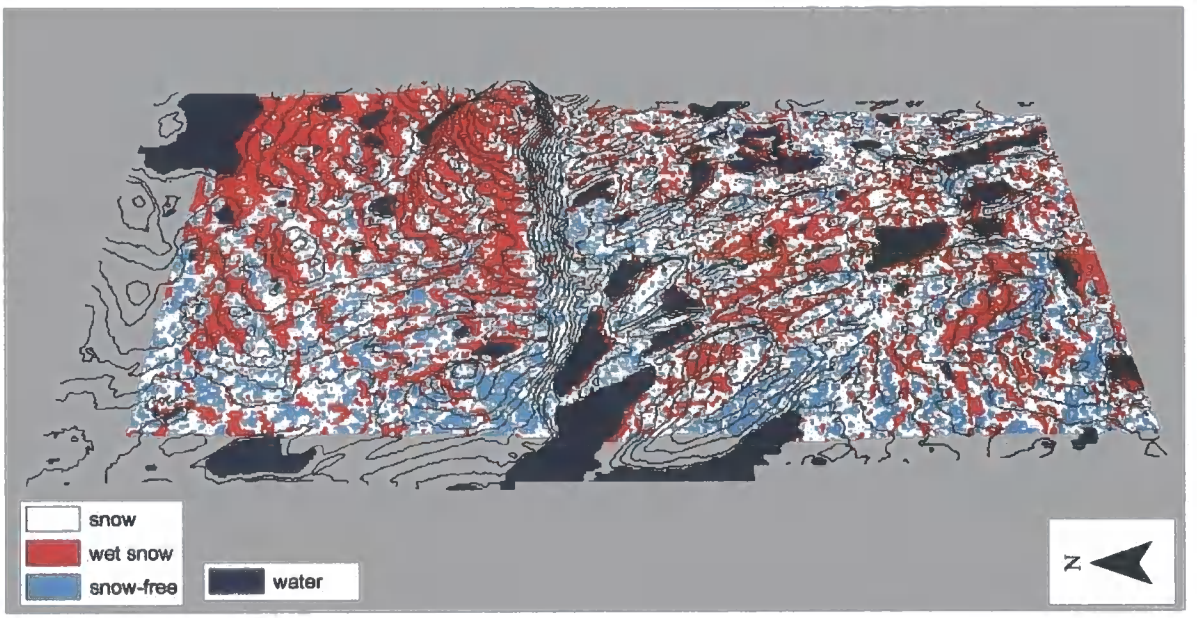

Figure 10.11. Snow map for Joatka, 5th June.

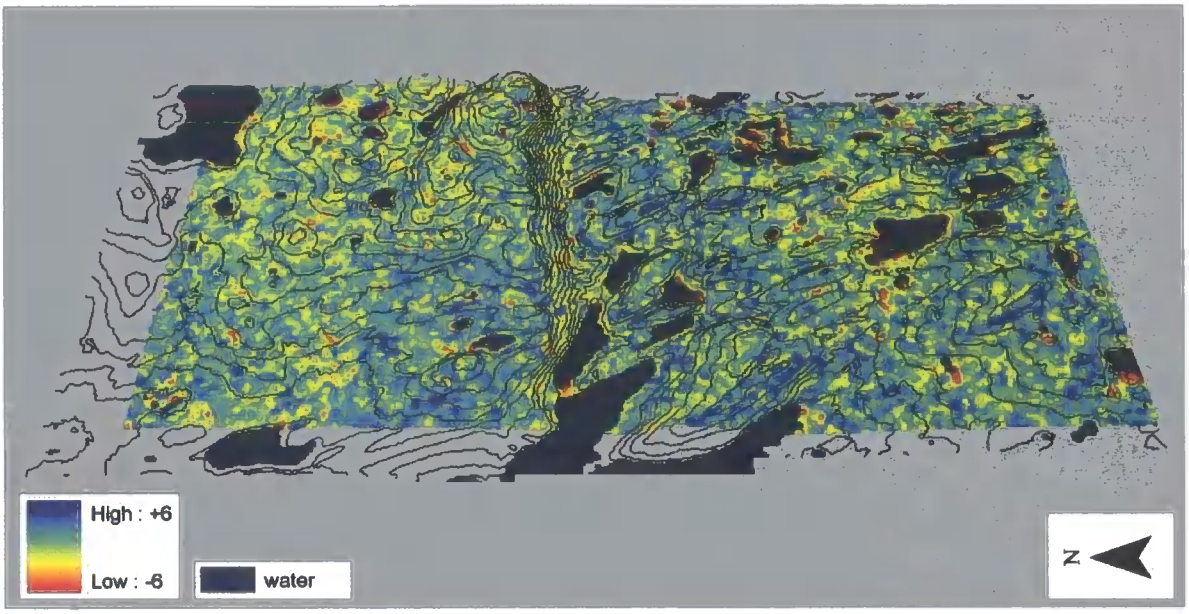

Figure 10.12. Spatial variation in backscatter difference (decibels) at Joatka, 21st June.

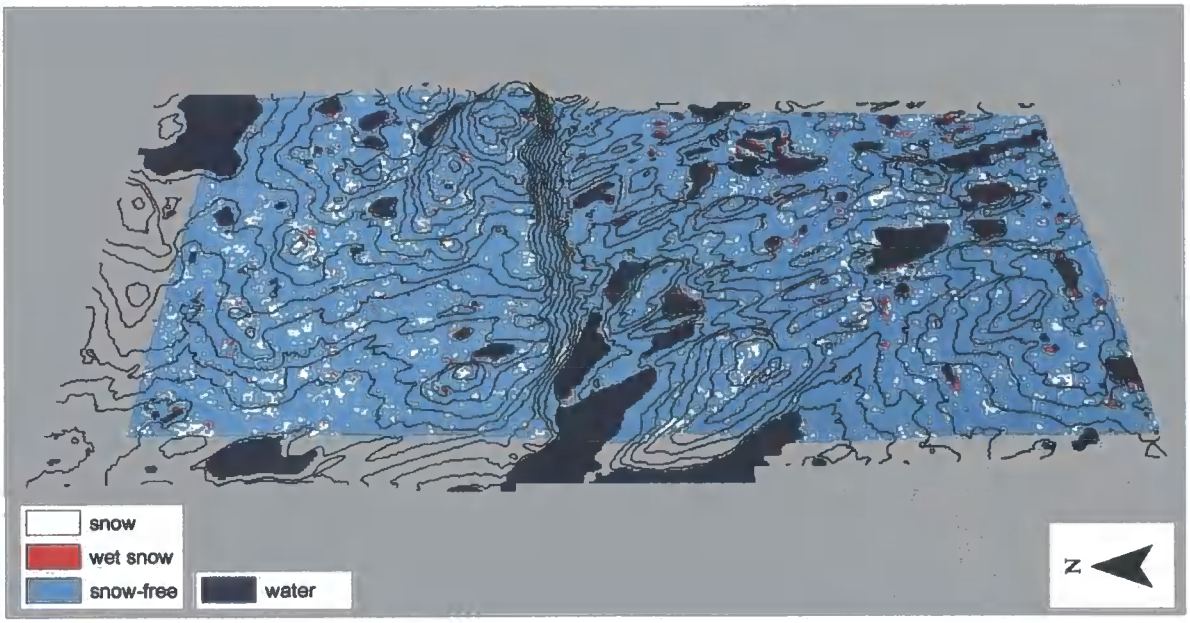

Figure 10.13. Snow map for Joatka, 21st June.

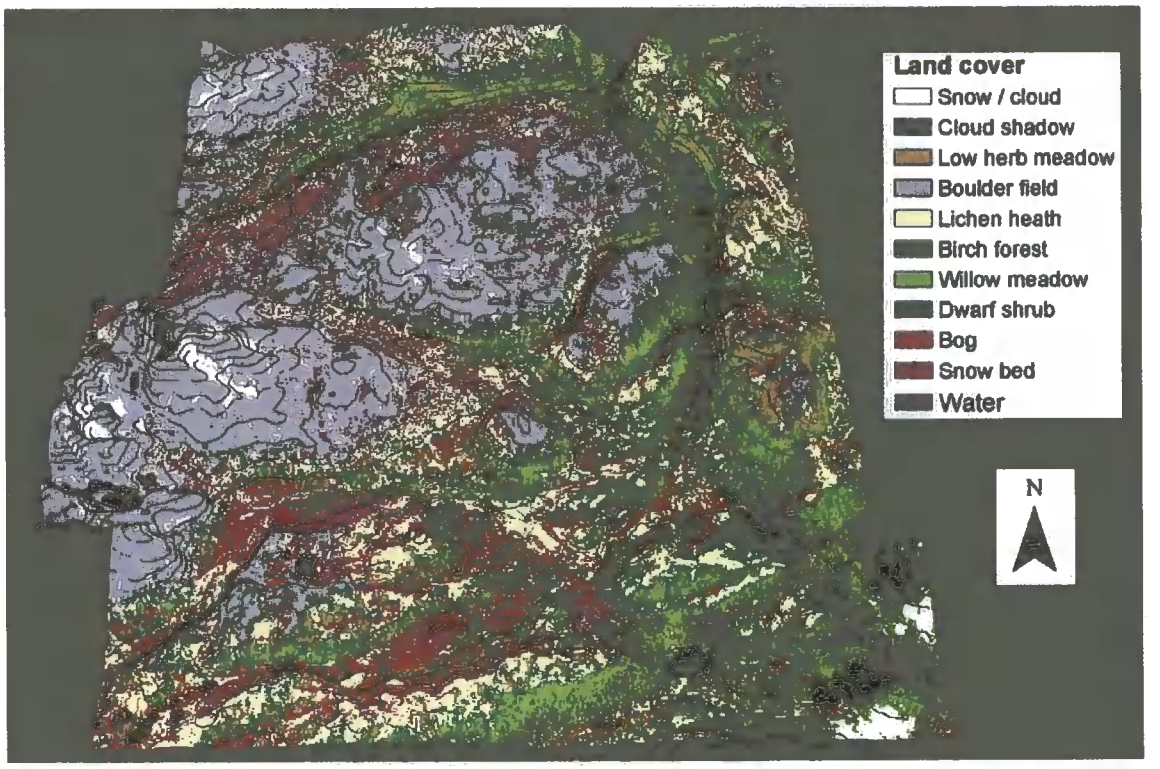

Figure 10.14. Vegetation at Dovrefjell study site.

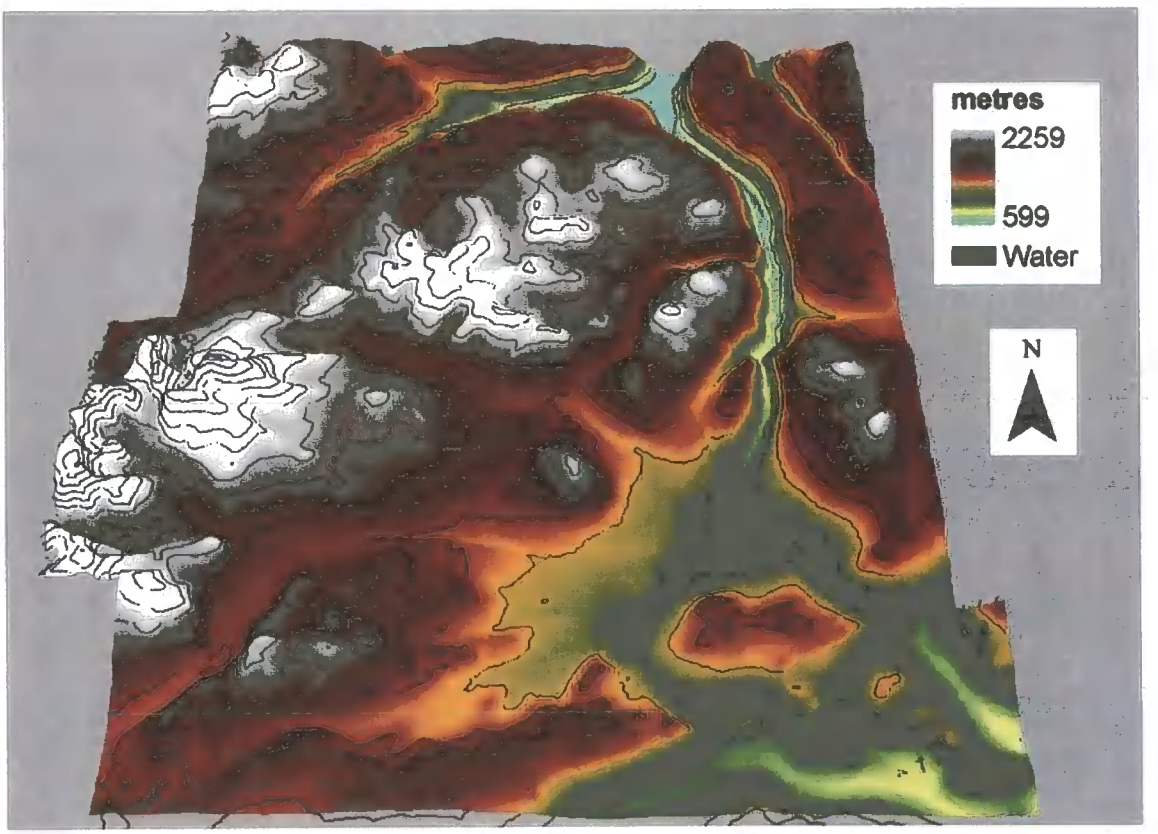

Figure 10.15. Elevation at Dovrefjell study site.

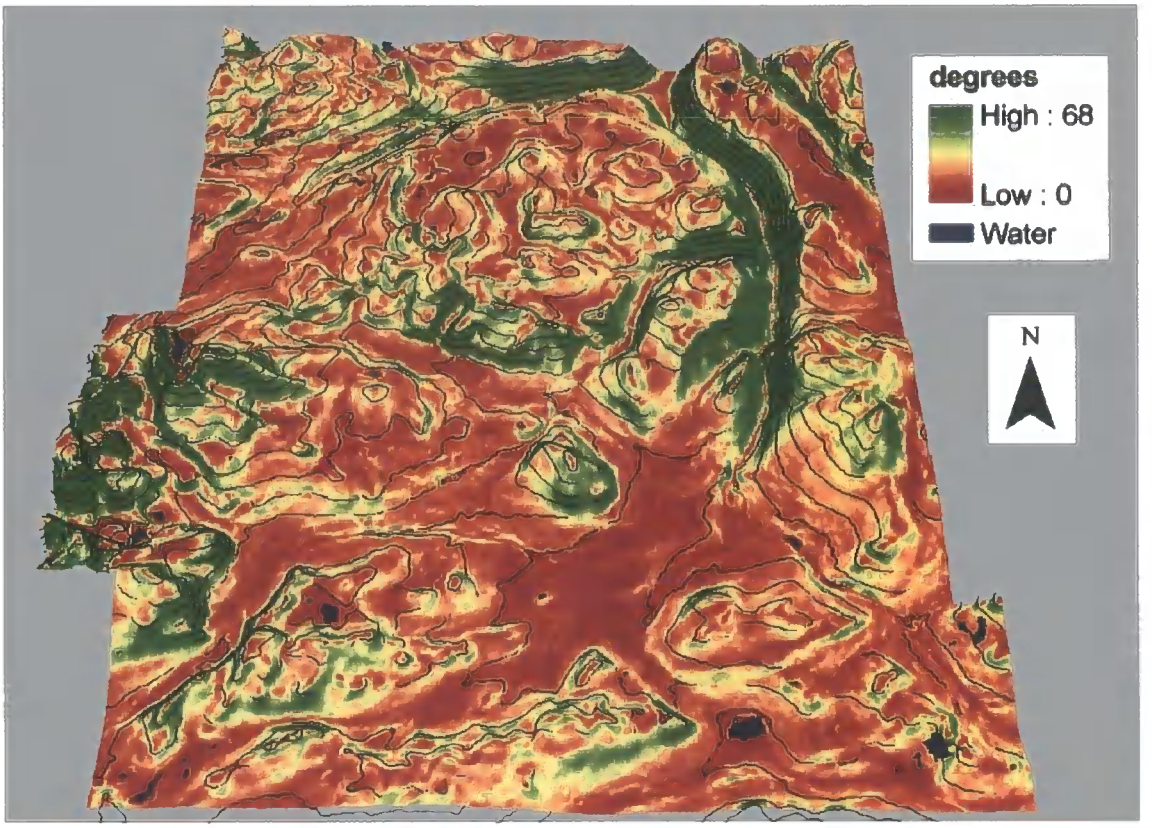

Figure 10.16. Slope gradient at Dovrefjell.

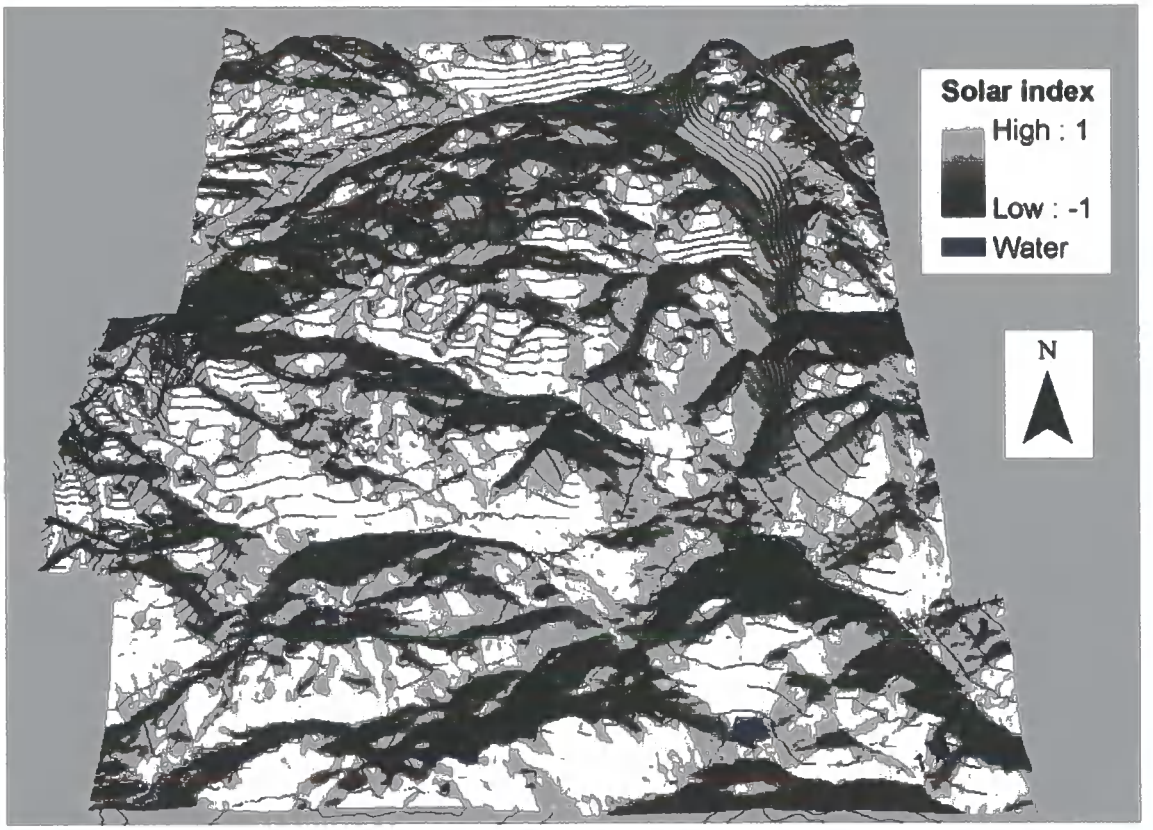

Figure 10.17. Slope aspect (solar radiation index) at Dovrefjell.

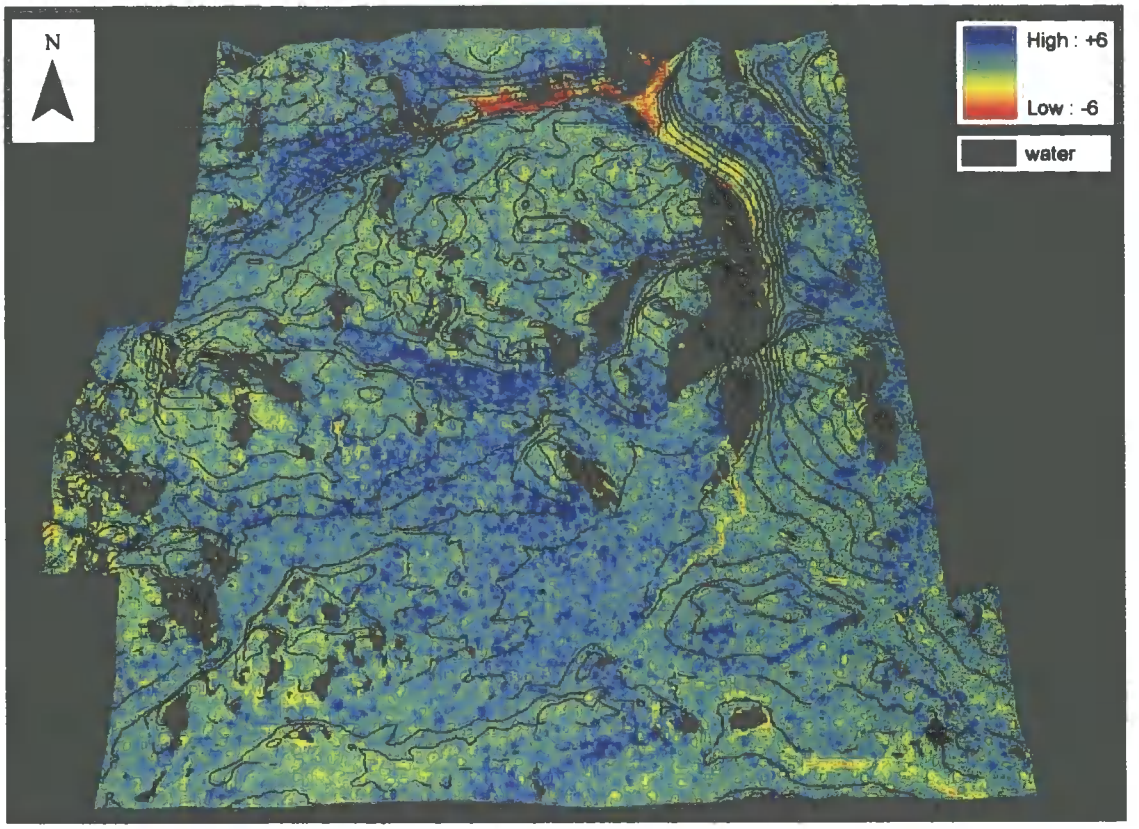

Figure 10.18. Spatial variation in backscatter difference at Dovrefjell, 14th April.

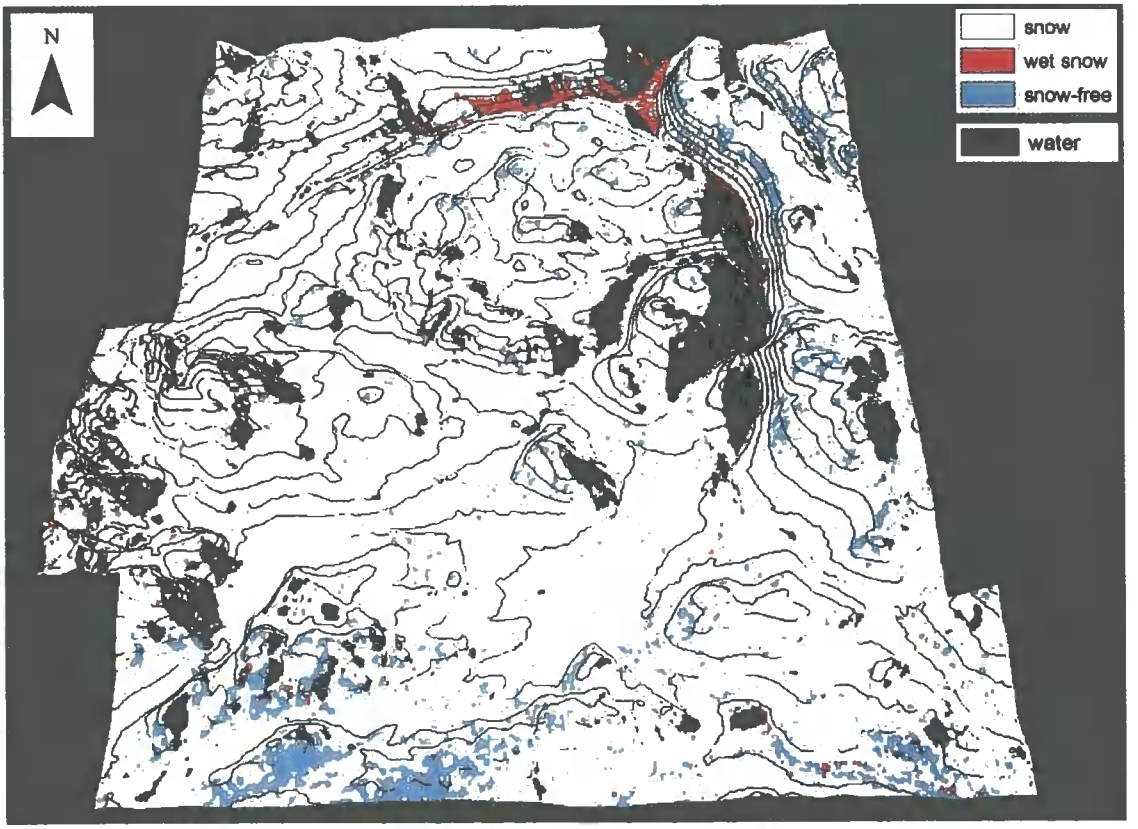

Figure 10.19. Snow map for Dovrefjell, 14th April.

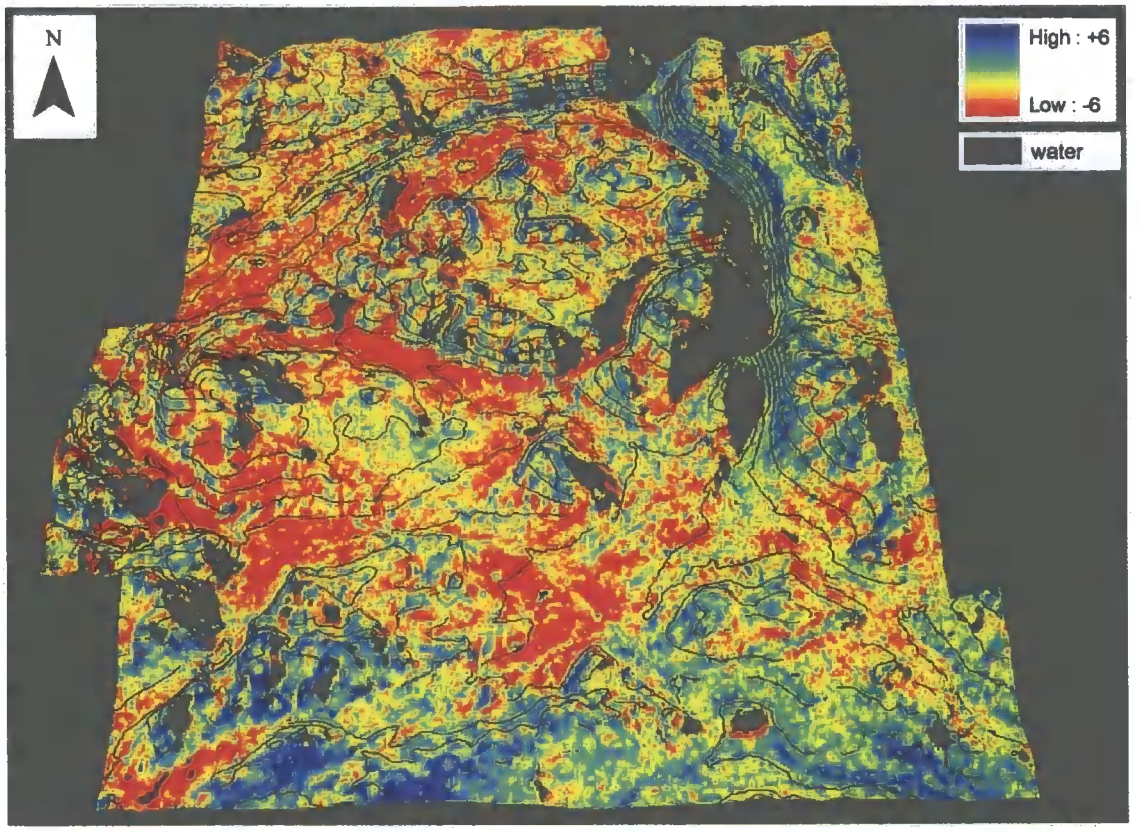

Figure 10.20. Spatial variation in backscatter difference at Dovrefjell, 3rd May.

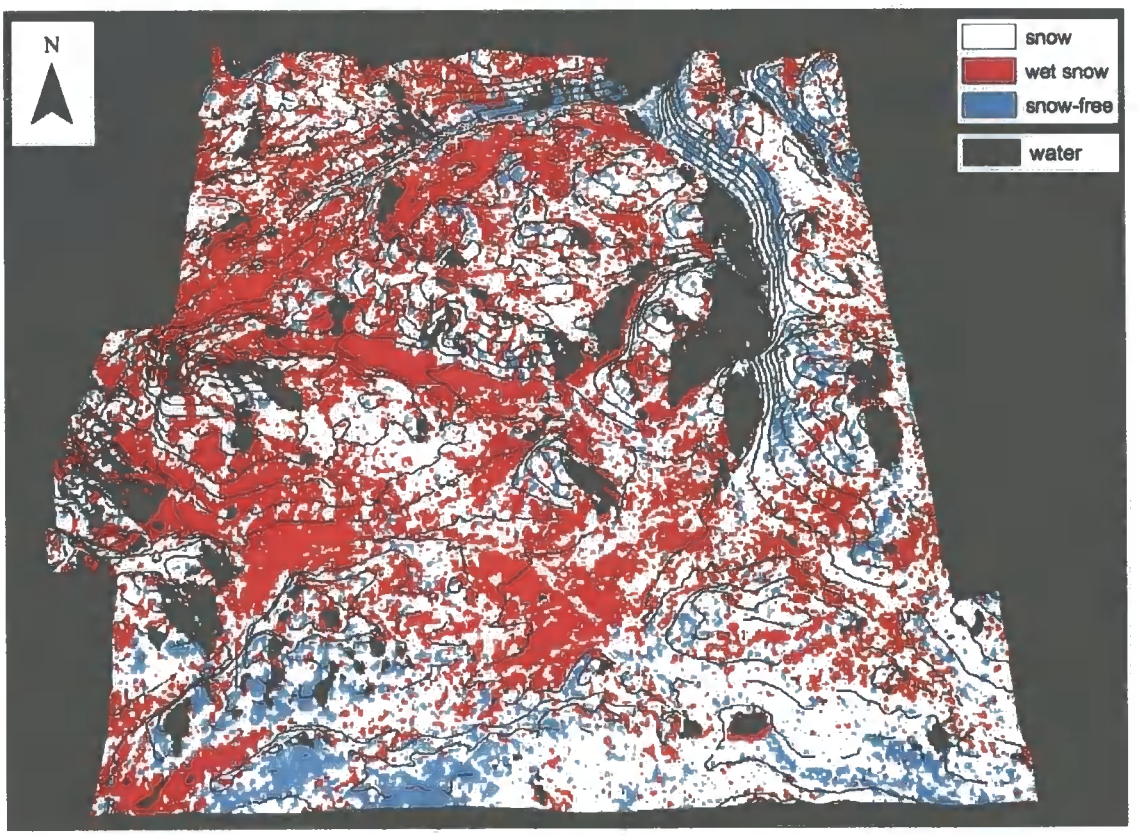

Figure 10.21. Snow maps for Dovrefjell, 3rd May.

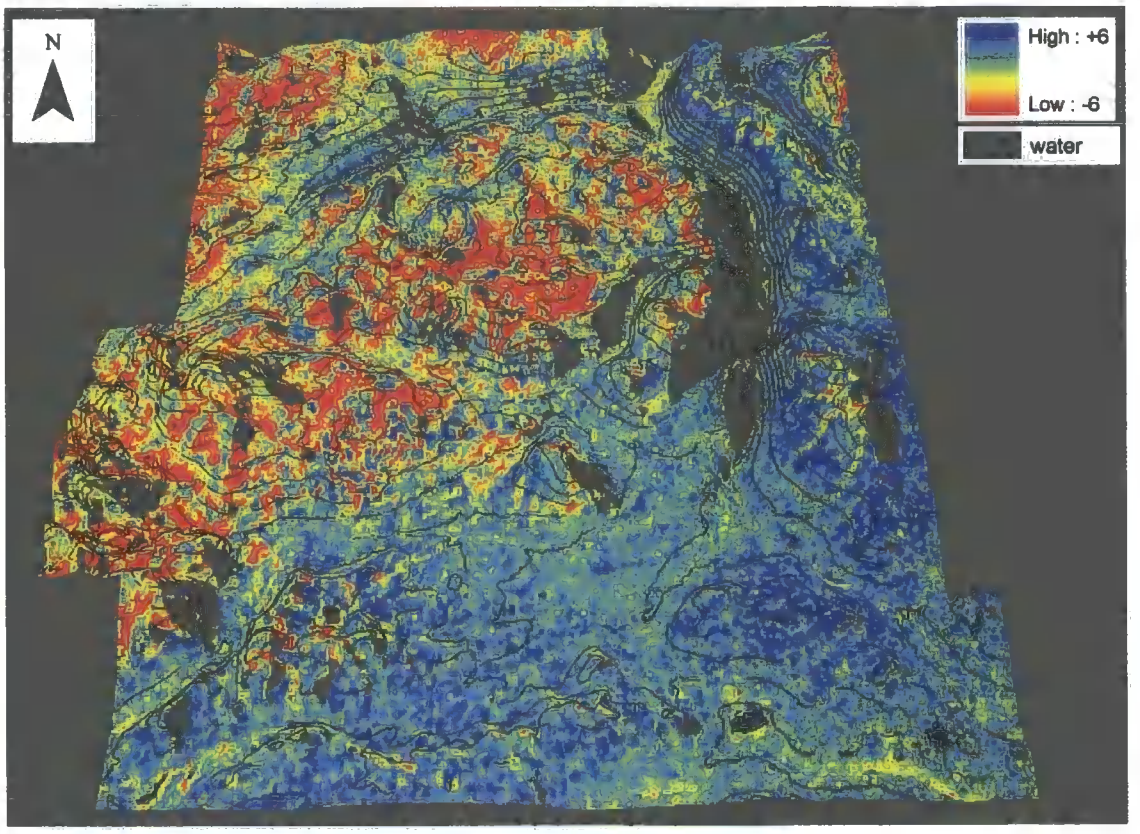

Figure 10.22. Spatial variation in backscatter difference at Dovrefjell, 19th May.

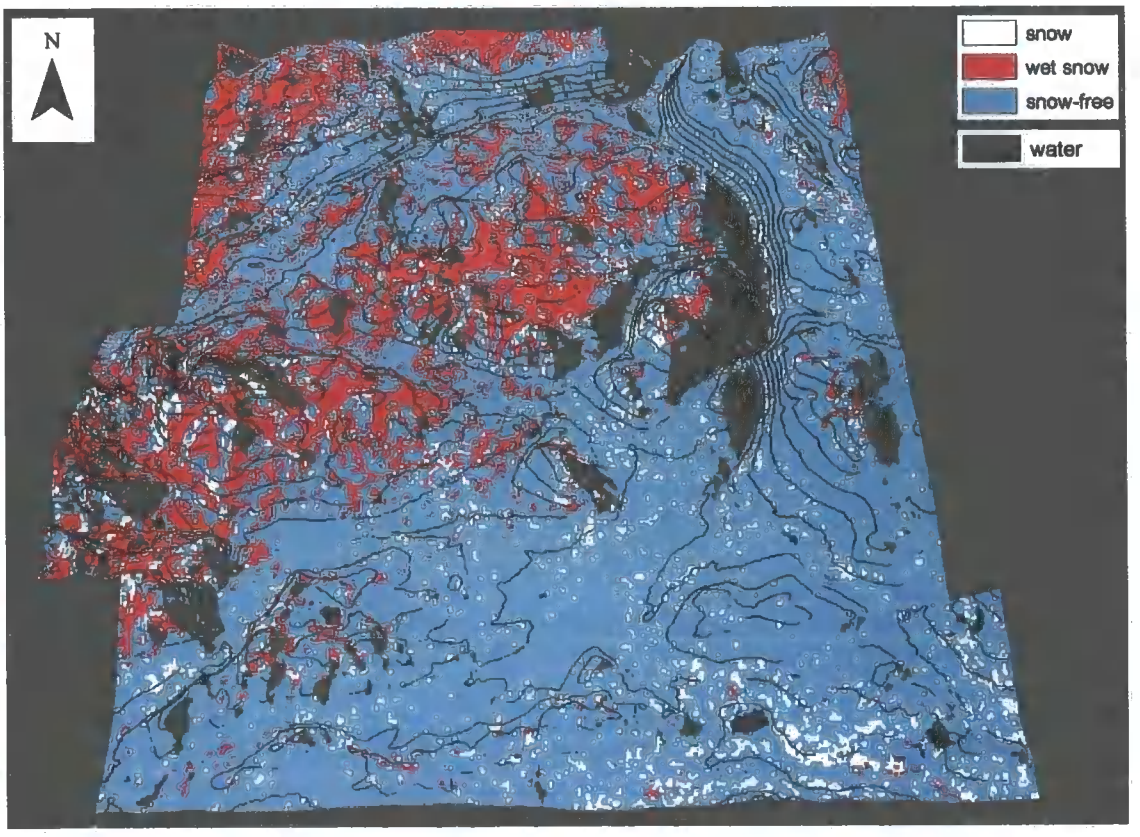

Figure 10.23. Spatial variation in backscatter difference at Dovrefjell, 19th April.

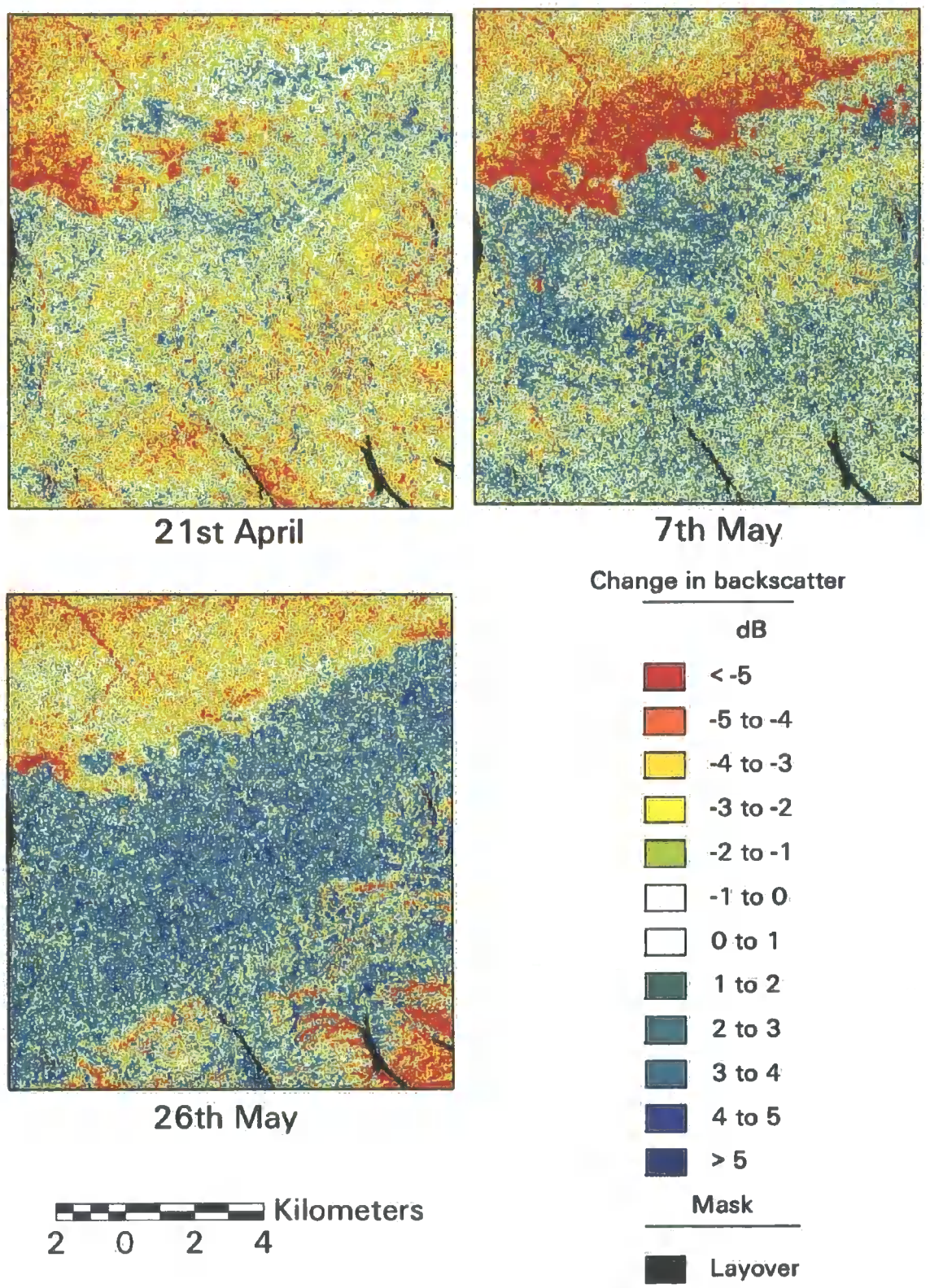

Figure 10.24. Spatial variation in backscatter difference at Abisko.

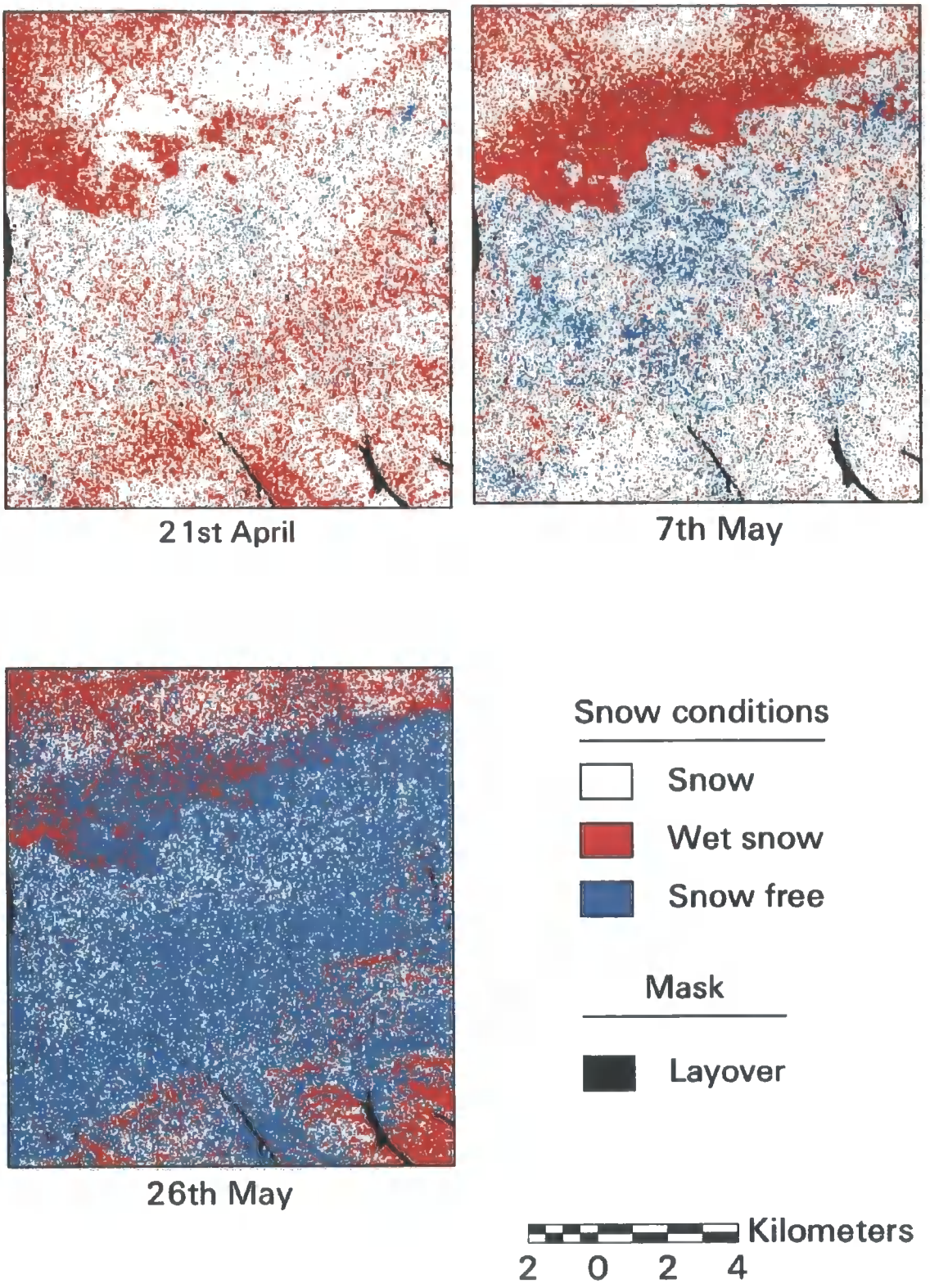

Figure 10.25. Snow maps for Abisko.

10.4 Validation

Validation of the final snow maps should ideally be conducted using an independent source of spatial snow data. As discussed in section 2.4.4, an option is the use of snow covered area (SCA) data derived from optical sensors such as Landsat TM or SPOT XS. However, given the trade-off between satellite return frequency and resolution and the cloud attenuation of VIR sensors, the availability of concurrent VIR data at a resolution compatible with the SAR data is likely to be limited. Indeed, the availability of cloud-free VIR data at each site for the period of interest was investigated and it was concluded that this was not a reasonable option; VIR data was too limited and the few available dates not sufficiently close to radar acquisitions.

Therefore, validation consisted of a quantitative assessment of snow mapping results based on two components, omission (exclusion) and commission (inclusion) error; there is also scope for a qualitative assessment based on knowledge of snow distribution. Evaluating commission and omission error is relatively straightforward when the algorithm is applied to images with known conditions i.e. a dry snow or snow-free image. While this provides a reasonable basis for accuracy assessment, determining errors when the snow conditions are characterised by a mosaic of dry-snow, wet-snow, and snow-free conditions is more difficult and when a qualitative assessment is beneficial.

10.4.1 Joatka validation

It was assumed that the image acquired on 12th April was completely covered by dry snow meaning that wet snow or snow-free pixels were commission errors. This may be an overstatement because wet snow was probably present, perhaps associated with bogs because of their thermal properties, and there were a few snow-free ridges. Table 10.3 contains results of applying the basic snow-mapping algorithm (i.e. with the two thresholds for wet and snow-free cover).

Table 10.3. Contingency table for 12th April image at Joatka. It is likely that there is some accurately classified wet snow, but this cannot be validated.

		Knowledge		
		Dry snow	Wet snow	Snow-free
Class	Dry snow	70.0	0	0
	Wet snow	15.6	0	0
	Snow-free	14.4	0	0

Without the implementation of the additional rules, snow mapping is *ca.* 70 % accurate in terms of overall accuracy, but this is probably a conservative value. Temporal consistency of snow-free conditions was assessed between each image date; there was no fresh snowfall between 17th May and 21st June, but fresh snow did fall between 12th April and 17th May meaning that figures between these dates must be treated with more caution. Of snow-free cover on 12th April, only 4.9 % was temporally consistent with snow-free conditions on 17th May. Reclassification of snow-free ground cover that was not temporally consistent with the later image improves the accuracy of snow mapping to a around 88 %. On 17th May snow-free cover was classified as 16.5 % of the total area, with 6.9 % consistent with snow-free conditions on 5th June and 6.1 % consistent on both 5th June and 21st June. By 5th June, 28.2 % of cover is classified as snow-free, with 21.8 % consistent with snow-free conditions on 21st June (28 % consistent with non-wet snow classification on 21st June).

These inconsistencies were reclassified. If a pixel was classified as snow-free, but was not classified as snow-free in subsequent images then it was recoded from snow-free conditions to dry/refrozen. Additional recoding was made on 21st June for areas that had wet snow cover on 2nd April, 17th May, or 5th June but were classified as dry or refrozen snow on 21st June; this recoded an additional 1.5 % of the total area to snow-free cover. Even using the snow mapping algorithm and the two additional rules, some areas were never classified as wet snow and remain classified as dry snow on 21st June; this "no change" area was 15.6 %, and was uniquely recoded for further investigation.

10.4.2 Dovrefjell validation

There was no additional dry snow image available of the same geometry as the reference images at Dovrefjell to evaluate commission error for wet snow and snow-free conditions; field measurements indicated likelihood of some wet snow cover on 29th

March and 14th April and ground temperature measurements in chapter 7 suggested some snow-free ground emerging on 30th March.

The temporal consistency of snow-free conditions was assessed and is particularly important at Dovrefjell because of the melt-freeze cycles resulting in predominantly frozen snow on 29th March and 14th April coincident with image acquisition. Approximately 50% of the total area was never classified as wet snow, an outcome that appears to have an altitudinal relationship with the majority of the unclassified area at lower elevations. It is likely that these area had a frozen snowpack in early images but mostly snow-free by 3rd and 19th May when snow would have been wet due to high air temperatures. The temporal consistency of snow-free classification is complex at Dovrefjell. The increase in backscatter on 14th April that was detected in signature evaluation is evident across the study site. Indeed, 40.6 % of the total area was initially classified as snow-free if temporal consistency of snow cover is not enforced; the snow-free area is 12.8 % on 14th April if both additional rules are employed. By 19th May the total area remaining classified as dry/frozen snow was high at 21.1 %.

10.4.3 Abisko validation

The snow mapping at Abisko must account for the melt/freeze of snowpack from 21st April to 7th May. Snow conditions on 21st April should be dominated by wet snow, with limited patches of snow-free ground. On 7th May snow-free patches on the tundra were evident, but the frozen snowpack meant that the contrast between the snow covered areas (forest and tundra) and the areas of snow-free tundra relied on the snow-free signature being detected.

On 21st April, 13.7% of the area was classified as snow-free, with 7.6% consistent with later images. On 7th May, snow-free area increased to 32.1%, with 22.7% consist with later images. Since the snowpack was frozen on 7th May, classifying previously wet snow areas as snow-free could not be applied. By 26th May, 23.2 % of the area was classified as dry/refrozen snow in error, which is partly due to the small number of images during the melt period (i.e. the rapidity of snow-melt). In addition, at Abisko the topographic variation is very complex and there is considerable variation in slope and aspect at a number of spatial scales, with areas of hummock tundra, the fluvio-glacial moraine deposits and larger landscape features.

10.5 Discussion

The variation in topography at each site means that some coverage is lost due to layover. Dovrefjell is a particularly mountainous site, with higher variation in relief and the forest-tundra ecotone at Dovrefjell is much more abrupt given the steepness of the topography. Much of the forest is located in sheltered Drivdalen valley, which is most severely affected by layover, however since ground control data was collected across more gentle slopes, missing coverage is not a severe problem at this or the other two sites.

The basis of snow mapping using radar remote sensing is the reduction in backscatter as a result of wet snow; this was identified in chapters 8 and 9. The wet snow threshold of 3 dB is empirically defined, and the snow-free classification based on an increase in backscatter is based on empirical and modelling evidence regarding an increase in backscatter from a wet ground surface. Field measurements showed that monitoring progression of snow melt required knowledge of melt-freeze cycles. Indeed, in several images the snowpack was frozen and a clear wet snow signature could not be detected.

It is difficult to answer the question of accuracy of the final snow maps without an independent source of spatial snow data. An option is the use of SCA data derived from optical sensors such as Landsat TM or SPOT XS. However, given previously discussed limitations of the return period and coincident cloud cover, this is not a reasonable option. Validation is best considered with recourse to the ground data and temporal consistency of the snow cover and also through a qualitative interpretation of accuracy.

Transition codes offer a simple method of quantifying change between thematic layers. At Joatka, applying the snow-mapping algorithm to a dry image on 12th April was used to evaluate the commission error for wet snow, which was estimated as 12%. The use of the novel snow-free threshold had commission error of 13.8%. However, this means that accuracy in terms of commission error for wet and snow-free conditions was *ca.* 70%. The error reveals the variation in backscatter that occurs between SAR images. One reason for the errors in the temporal stability of snow maps might be the SAR image statistics, which depend on level of multi-looking and speckles filter. Improvements in mapping would be expected if several reference scenes were available and an average taken to reduce the effects of speckle on multi-temporal analysis.

Another reason is inaccuracy in geometric correction, perhaps due errors in the DEM or the effect of the different imaging geometry of some images.

Improvement in the snow maps was made by the enforcement of temporal consistency in snow-free conditions. It was reasonably assumed that no areas transformed from snow-free to snow-covered during image acquisition and so snow-free conditions had to be consistent. An increase in backscatter at Dovrefjell on 14th April was detected in backscatter signatures in chapter 9 and results in over 40 % of the total area being classified as snow-free. When temporal consistency of snow cover was enforced, the snow-free area was reduced to 12.8%. Other studies have found a higher temporal consistency in snow mapping, e.g. Nagler and Rott (2000), which may be due to re-sampling to a relatively coarse DEM.

Qualitatively, the snow maps indicate an expected transition from continuous dry snow cover to patchy wet snow and finally to snow-free conditions. However, a more focused examination reveals potential errors. At each site, snow duration was recorded longest within the forest, but in general this was not the result of snow cover classification. For example, at Joatka, lower elevations where the forest is located are predominantly classified as snow-free on 5th June. The problem of detected a wet snow signature within the forest was highlighted in chapter 9 and the resultant classification suggests that the potential to map snow cover using ERS-2 SAR at the forest-tundra ecotone may be limited. In addition, a relatively large area of each study site showed no characteristic wet snow signature and no increase in backscatter empirically associated with snow-free conditions; they had similar dielectric and roughness properties as when dry snow-covered.

Chapter 11. Results: Relationship between topography, vegetation and radar-derived snow melt at the forest-tundra ecotone

The analysis of overall accuracy of snow maps in chapter 10 suggested reasonable accuracy of snow maps, but also indicated significant areas that were unclassified. This chapter undertakes further analysis of the transition of snow cover between different states within biophysical zones related to topography and vegetation. By stratifying by elevation, slope aspect, and vegetation the occurrence of wet snow (incorporating transition codes 2, 4, and 8) or occurrence of snow-free (incorporating transition codes 3, 5, and 7) can be calculated for each zone.

11.1 Sampling scheme

A systematic sampling scheme was used to reduce the level of spatial autocorrelation. Spatial variation in the topographic variables detailed in chapter 6 (elevation, slope gradient and solar radiation index) was characterized by the semivariance, which is a measure of the deviation between pairs of (z) values at a certain distance and direction. The spatial variation was quantified by the semivariogram. The value of semivariance for a separation distance of h (referred to as the lag) is half the average squared difference in z value between pairs of values separated by distance h. It was assumed that semivariance is a function only of distance h and not of position and that there was stationarity of difference. When using gridded data we have a sample for each location in the grid. The semivariogram is modelled by fitting a theoretical function to the sample semivariogram and semivariograms were calculated using Arc/Info GRID; the method is detailed in appendix E.

There are several important features in a semivariogram. At relatively short lag distances of h, the semi-variance is small, but increases with the distance between the pairs of sample points. At a distance referred to as the range, the semi-variance levels off to a relatively constant value referred to as the sill. This implies that beyond this range distance, the variation in z values is no longer spatially correlated. Within the range, the z value variation is smaller when the pairs of sample points are closer together. Even at a lag of zero there will probably be a positive value for semivariance, which is known as the "nugget" and represents spatially correlated variation over

distances less than the smallest sampling interval, measurement error and any purely random variation (Oliver, 2001).

The extent of the x-axis of the semivariogram could be determined by the distance between the most widely separated pair of points in the input sample data. Example semivariograms for topographic variables and backscatter values at Joatka are presented in figure 11.1 and 11.2. These variograms clearly show that the spatial dependence is different depending on the variable under examination. The sill for elevation is not reached until 8 km, which is expected given the wide range of elevation values in the study area, from the high summit of the ridge, to the low elevation of the lakes. Solar radiation index shows spatial independence at a smaller lag, demonstrating variation in slope aspect at a different spatial scale than regional elevation change, as shown in the elevation data. In figure 11.3 it is interesting to note that the spatial dependence in backscatter values is characterised by a large nugget, perhaps representing unfiltered radar speckle, and that the semivariance is considerably higher for the image acquired on the 5th June. The higher semivariance may be a result of the distribution of patchy wet snow causing higher spatial variation in backscatter compared to the dry snow image.

By increasing the distance between samples, the spatial dependence in the samples was reduced. Oliver (2001) suggests that a useful "rule of thumb" is to sample at an interval that is half of the range. This balances the need for reduction in spatial autocorrelation in the data and the need to generate a sufficient sample size. Following examination of the semivariograms for each topographic variable at each site, a sampling interval was defined. A sampling interval of 300 m was used at Joatka and Abisko study sites and 500 m at Dovrefjell.

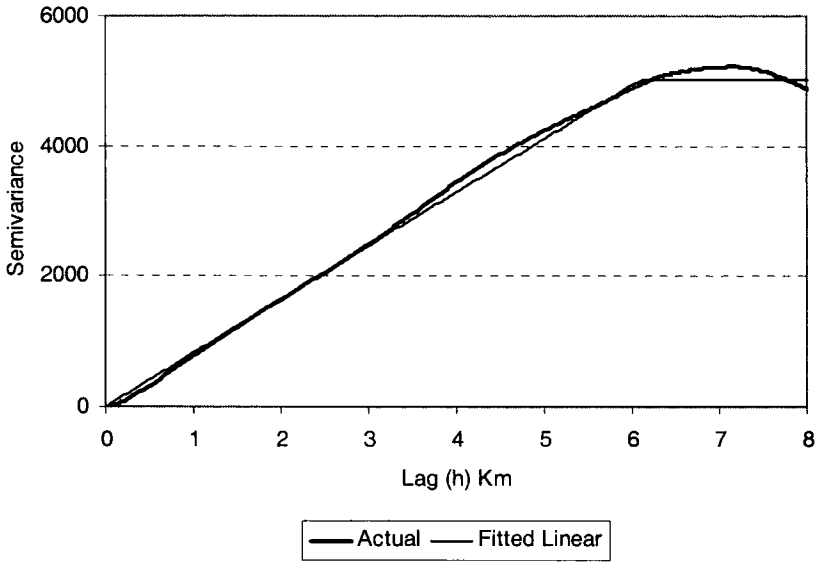

Figure 11.1. Semivariogram of elevation at Joatka.

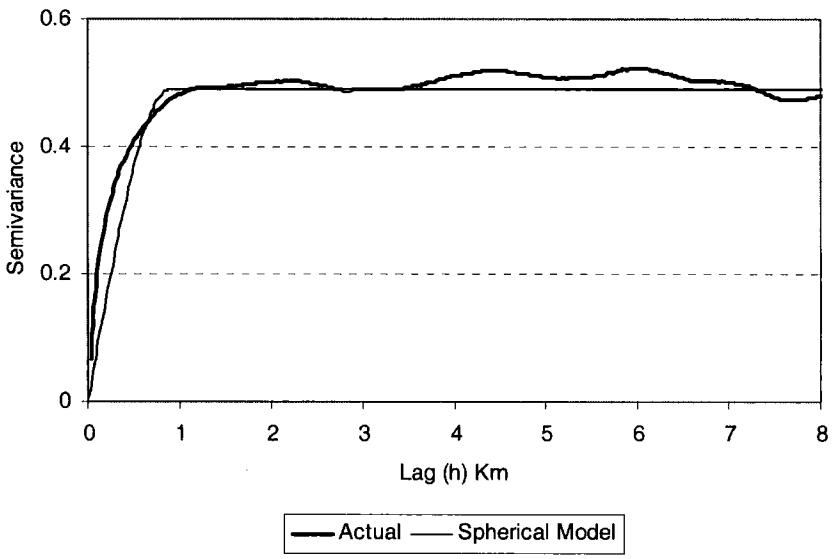

Figure 11.2. Semivariogram of solar radiation index at Joatka

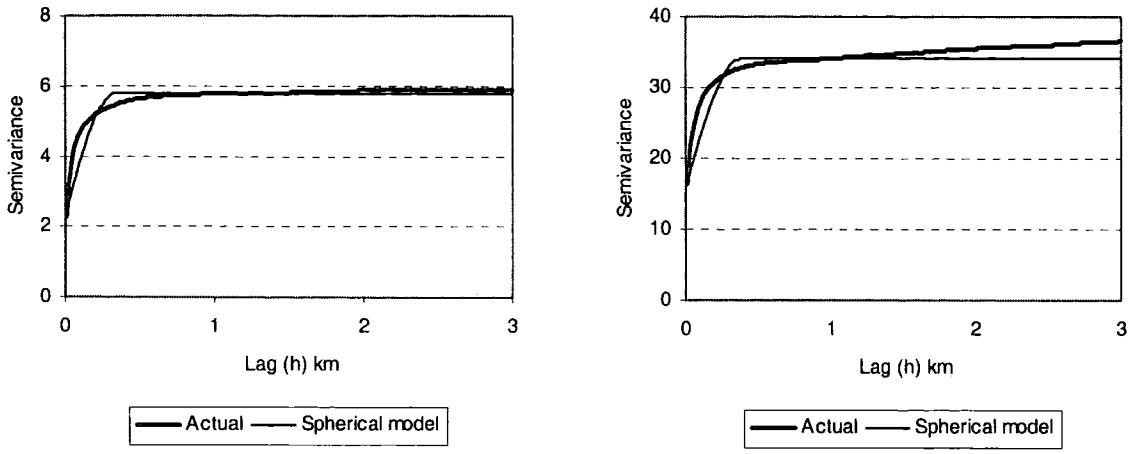

(a) 17/01 (b) 05/06

Figure 11.3. Semivariograms and fitted models of backscatter values (dB) on (a) 17th January and (b) 5th June at Joatka.

11.2 Topography and patterns of snow cover

The influence of elevation and slope aspect on the pattern of snow cover was investigated. Elevation was stratified in to pertinent zones for a particular study area, whereas slope aspect was classified from the solar radiation index, in which values range from 1 (south-facing) to –1 (north facing). The classes 1 to 4 for solar index are equal interval classes with a value of 1 representing high solar index and 4 representing very low solar index. The co-occurrence of snow properties for each topographic zone was calculated.

11.2.1 Joatka

Table 11.1 and figure 11.1 indicate a pattern of wet snow emerging at lower elevations on 17th May, with a higher proportion of wet snow at higher elevations on 5th June, indeed, over 50 % of the area is covered by wet snow above approximately 530 m. Table 11.1 indicates increasing likelihood of snow-free conditions at lower elevations as snow-melt progresses.

Table 11.1. Proportion of wet snow by elevation (Joatka).

Elevation (m)	12th April	17th May	5th June	21st June
375-425	0.159	0.361	0.203	0.026
425-475	0.107	0.211	0.262	0.020
475-525	0.14	0.154	0.288	0.017
525-575	0.097	0.08	0.524	0.015
575-625	0.086	0.118	0.542	0.034
625-675	0.09	0.09	0.598	0.033

Table 11.2. Proportion snow-free by elevation (Joatka).

Elevation (m)	17th May	5th June	21st June
375-425	0.043	0.275	0.841
425-475	0.062	0.249	0.818
475-525	0.084	0.277	0.814
525-575	0.052	0.145	0.83
575-625	0.05	0.113	0.815
625-675	0.049	0.115	0.869

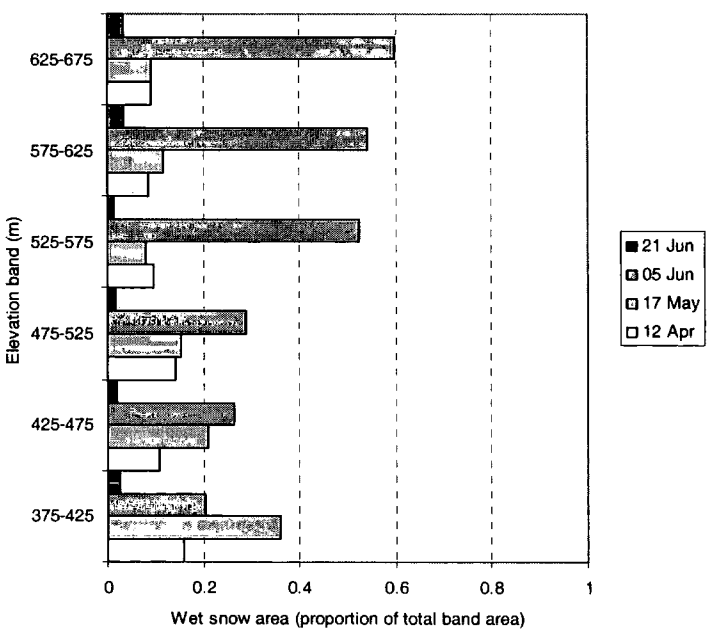

Figure 11.4. Area of wet snow by elevation (Joatka).

Slope aspect is shown to have an effect on proportion of wet snow and snow-free conditions in table 11.3 and table 11.4. Wet snow is most likely on south facing slopes on May 17th and on north facing slopes on 5th June. Similarly, snow-free conditions are more likely on south facing slopes.

Table 11.3. Proportion wet snow by slope aspect (Joatka).

	12th April	17th May	5th June	21st June
1 (North)	0.104	0.135	0.428	0.018
2	0.128	0.172	0.334	0.025
3	0.120	0.192	0.247	0.023
4 (South)	0.139	0.318	0.181	0.021

Table 11.4. Proportion snow-free by slope aspect (Joatka).

	17th May	5th June	21st June
1 (North)	0.054	0.179	0.841
2	0.064	0.22	0.823
3	0.066	0.251	0.792
4 (South)	0.064	0.315	0.818

11.2.2 Dovrefjell

An elevation dependence of wet snow and snow-free conditions appears evident at Dovrefjell in table 11.5 and table 11.6 and figure 11.2. Wet snow is most likely at low elevations on 29th March and 14th April. On 3rd May, wet snow covers the largest area and is present at all elevations, particularly at higher elevations. By 19th May, wet snow has retreated to predominantly higher elevations and snow-free conditions are more likely at lower elevations.

Table 11.5. Proportion of wet snow by elevation zone (Dovrefjell).

Elevation (m)	29th March	14th April	3rd May	19th May
< 900	0.271	0.259	0.112	0.112
900-1050	0.119	0.048	0.237	0.047
1050-1200	0.131	0.029	0.315	0.035
1200-1350	0.127	0.034	0.369	0.115
1350-1500	0.114	0.051	0.404	0.254
> 1500	0.131	0.068	0.362	0.434

Table 11.6. Proportion snow-free by elevation (Dovrefjell).

Elevation (m)	14th April	3rd May	19th May
< 900	0.182	0.381	0.626
900-1050	0.124	0.172	0.673
1050-1200	0.145	0.176	0.734
1200-1350	0.137	0.167	0.69
1350-1500	0.113	0.149	0.57
> 1500	0.103	0.138	0.387

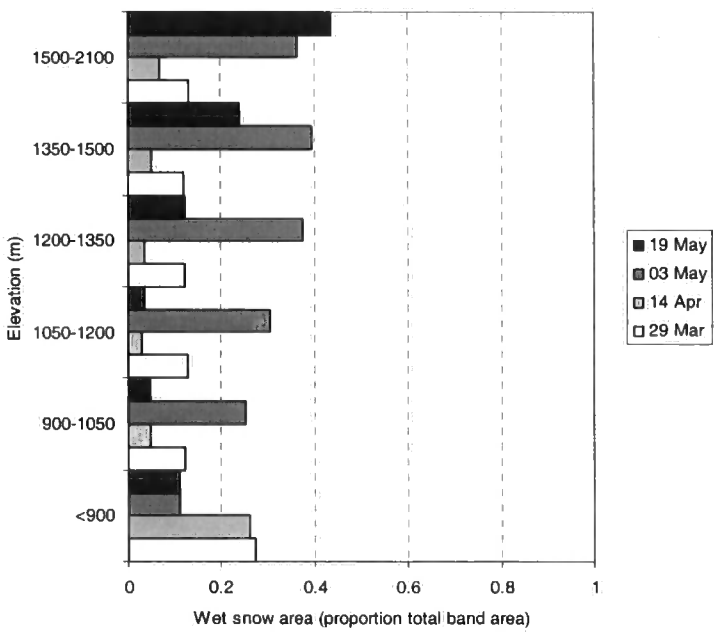

Figure 11.5. Area of wet snow by elevation (Dovrefjell).

A relationship between snow cover and slope aspect is also evident in tables 11.7 and 11.8. Wet snow is more likely on north-facing slopes on later dates, and snow-free conditions are more likely to emerge on south-facing slopes.

Table 11.7. Proportion of wet snow by slope aspect (Dovrefjell).

	29th March	14th April	3rd May	19th May
1 (North)	0.104	0.054	0.37	0.188
2	0.126	0.059	0.347	0.183
3	0.141	0.045	0.306	0.151
4 (South)	0.149	0.047	0.312	0.144

Table 11.8. Proportion snow-free by slope aspect (Dovrefjell).

	14th April	3rd May	19th May
1 (North)	0.101	0.140	0.606
2	0.124	0.161	0.61
3	0.141	0.183	0.638
4 (South)	0.149	0.191	0.639

11.2.3 Abisko

Tables 11.9 and 11.10 indicate elevation dependence of snow cover at Abisko, but the proportion of wet snow is not high for any date. Proportion of wet snow decreases with elevation on 7th May, but there is little relationship on 21st April. Snow-free conditions are also elevation dependent. Wet snow is noticeable at higher elevations on 26th May.

Table 11.9. Proportion of wet snow by elevation (Abisko)

Elevation (m)	21st April	7th May	26th May
< 500	0.201	0.089	0.02
500-600	0.249	0.129	0.025
600-700	0.366	0.118	0.11
700-800	0.321	0.083	0.125
800-900	0.273	0.073	0.123
>900	0.222	0.083	0.20

Table 11.10. Proportion snow-free by elevation (Abisko) .

Elevation (m)	21st April	7th May	26th May
< 500	0.081	0.265	0.758
500-600	0.088	0.257	0.782
600-700	0.071	0.237	0.670
700-800	0.077	0.271	0.610
800-900	0.063	0.228	0.616
>900	0.047	0.144	0.508

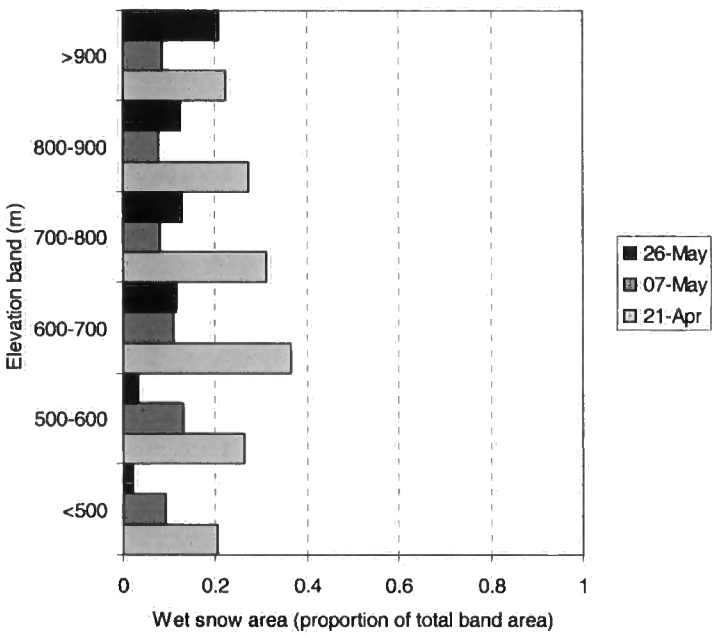

Figure 11.6. Area of wet snow by elevation (Abisko).

At Abisko, slope aspect demonstrates similar results to the other study areas; snow-free conditions in particular are more likely on south-facing slopes, as shown in tables 11.11 and 11.12.

Table 11.11. Proportion of wet snow by slope aspect (Abisko).

	21st April	7th May	26th May
1 (North)	0.275	0.105	0.09
2	0.268	0.096	0.058
3	0.245	0.075	0.043
4 (South)	0.261	0.059	0.022

Table 11.12. Proportion snow-free by slope aspect (Abisko).

	21st April	7th May	26th May
1 (North)	0.069	0.223	0.672
2	0.084	0.252	0.717
3	0.1	0.315	0.755
4 (South)	0.109	0.331	0.768

11.3 Vegetation and patterns of snow melt

Co-occurrence of vegetation types at the forest-tundra ecotone and snow conditions was investigated, but no causality between the distribution of snow and vegetation can be inferred. The results are not independent of topography, although simple stratification into elevation and slope aspect classes was made.

11.3.1 Joatka

An increased occurrence of wet snow in the forest compared to tundra can be identified on 17th May in table 11.13, which was identified in signature analysis in Chapter 8 and provides a clear indication that ablation was happening in the forest. Emergence of snow-free conditions for vegetation types in table 11.14 provides evidence that substantial areas of all vegetation types were becoming free on 5th June, but that forest had higher proportion being classified as snow-free. However, these tables include the entire study area and tables 11.15 and 11.16 stratify the study area into three elevation classes that enclose the forest-tundra ecotone. The pattern of snow-free cover is complex, and other topographic factors may be an important influence, but in the higher elevation classes, lichen heath has the highest proportion of snow-free conditions but forest also has a relatively high proportion classified as snow-free.

Table 11.13. Proportion of wet snow by vegetation type (Joatka).

	12th April	17th May	5th June
Forest	0.131	0.336	0.22
Dwarf shrubs	0.112	0.177	0.348
Bog	0.17	0.253	0.382
Lichen heath	0.104	0.139	0.319

Table 11.14. Proportion snow-free by vegetation type (Joatka).

	5th June	21st June
Forest	0.336	0.854
Dwarf shrubs	0.28	0.832
Bog	0.263	0.799
Lichen heath	0.269	0.814

Table 11.15. Proportion snow-free by vegetation type and elevation.

Elevation Zone (m)	Vegetation	5th June	21st June
375-425	Forest	0.363	0.872
	Dwarf shrubs	0.284	0.88
	Bog	0.276	0.73
	Lichen	0.281	0.838
425-475	Forest	0.309	0.845
	Dwarf shrubs	0.35	0.815
	Bog	0.342	0.791
	Lichen	0.258	0.813
475-525	Forest	0.381	0.825
	Dwarf shrubs	0.316	0.821
	Bog	0.216	0.815
	Lichen	0.388	0.806

11.3.2 Dovrefjell

Vegetation at Dovrefjell includes an additional class of bare ground. Table 11.16 shows a low proportion of wet snow for most vegetation types, the highest being for bare ground on 3rd and 19th May. Snow-free conditions in table 11.17 are most likely for the

low/dwarf shrubs and lichen heath, with herbaceous cover also having a lower proportion snow-free. When elevation is stratified in table 11.18, forest cover at lower elevations is least likely to be snow-free, but again the pattern is complex and other topographic factors may be important.

Table 11.16. Proportion of wet snow by vegetation type (Dovrefjell).

	29th March	14th April	3rd May	19th May
Forest	0.127	0.091	0.202	0.062
Low/dwarf shrubs	0.159	0.05	0.285	0.066
Herbaceous	0.111	0.046	0.388	0.15
Lichen	0.143	0.036	0.277	0.08
Unvegetated	0.114	0.061	0.399	0.413

Table 11.17. Proportion snow-free by vegetation type (Dovrefjell).

	14th April	3rd May	19th May
Forest	0.116	0.185	0.677
Low/dwarf shrubs	0.162	0.209	0.708
Herbaceous	0.113	0.148	0.649
Lichen	0.154	0.196	0.683
Unvegetated	0.095	0.126	0.413

Table 11.18. Proportion snow-free by vegetation type and elevation (Dovrefjell).

Elevation zone		14th April	3rd May
< 900	Forest	0.141	0.345
	Low/dwarf shrubs	0.209	0.412
	Herbaceous	0.156	0.377
	Lichen	0.343	0.4
900-1050	Forest	0.09	0.125
	Low/dwarf shrubs	0.136	0.191
	Herbaceous	0.143	0.188
	Lichen	0.12	0.171
1050-1200	Forest	0.188	0.21
	Low/dwarf shrubs	0.154	0.189
	Herbaceous	0.125	0.156
	Lichen	0.147	0.171

11.3.3 Abisko

The vegetation classes at Abisko are those obtained from a simple classification of birch forest and tundra classes. Because of the low proportion of wet snow at Abisko in all images, only the proportion of snow-free conditions is assessed In table 11.19 snow free conditions are perhaps more likely on the tundra, but this pattern is clearer when elevation is considered in table 11.20.

Table 11.19. Proportion snow-free by vegetation type (Abisko).

	21st April	7th May	26th May
Tundra	0.088	0.27	0.661
Forest	0.048	0.174	0.754

Table 11.20. Proportion snow-free by vegetation type and elevation.

Elevation zone (m)		21st April	7th May	26th May
< 500	Tundra	0.174	0.435	0.739
	Forest	0.07	0.202	0.715
500-600	Tundra	0.125	0.353	0.79
	Forest	0.044	0.19	0.783
600-700	Tundra	0.094	0.283	0.699
	Forest	0.03	0.117	0.743

11.3.4 Unclassified snow cover and vegetation / topography

It is clear that a significant proportion of each study site was not classified as wet snow in any of the temporal sequence of images and did not show a consistent snow-free signature. This lack of change in backscatter was investigated in relation to topography and vegetation. Examination of unclassified area within vegetation types in table 11.21 reveals that tundra vegetation at Joatka and Abisko has the highest proportion, but that forest has the highest proportion at Dovrefjell. Unclassified area may be topographically dependent (tables 11.22-11.25). At Dovrefjell unclassified is increased at lower elevations, whereas at Joatka a relationship is more complex and may be related to the prominent exposed ridge and south facing slopes at 450-500 m. At Abisko there appears to be no discernable pattern in the unclassified area

Table 11.21. Percentage of unclassified pixels at each site.

	Joatka	Dovrefjell	Abisko
Forest	13.1	26.1	21.9
Dwarf/low shrubs	15.2	22.5	23.8
Bog	15.7	20.1	
Lichen heath	16.8	23.7	
Bare ground		17.4	

Table 11.22 Percentage of unclassified pixels by elevation at Joatka

Elevation (m)	Unclassified %
375-425	13.3
425-475	16.2
475-525	16.9
525-575	15.5
575-625	15.2
625-675	10

Table 11.23. Percentage of unclassified pixels by elevation at Dovrefjell.

Elevation (m)	Unclassified %
< 900	26.2
900-1050	28
1050-1200	23.1
1200-1350	19.5
1350-1500	17.7
> 1500	17.9

Table 11.24. Percentage of unclassified pixels by elevation at Abisko.

Elevation (m)	Unclassified %
< 500	25.5
500-600	19.6
600-700	20.8
700-800	27.3
800-900	26
>900	29.2

Table 11.25. Percentage of unclassified pixels by slope aspect at Joatka.

	Joatka	Dovrefjell	Abisko
1 (North)	14.1	20.6	23.7
2	15.2	20.7	22.6
3	18.5	21.1	20.3
4 (South)	16.1	21.7	21

11.4 Statistical modelling of vegetation, topography and snow-melt

The interdependence of topographic variables and vegetation distribution means that there is limited value in continuing with statistical approaches based on cross tabulation of two or three variables. A modelling approach that accounts for redundancy in predictive variables and can operate with a combination of categorical and continuous variables is required. For example, the spatial distribution of snow in relation to topography and vegetation could be investigated by logistic regression. In contrast, given the influence of vegetation on snow distribution, the spatial pattern of vegetation can be predicted using topographic and snow cover variables.

The latter approach was undertaken using the Joatka data, where the snow cover data appear most reliable. In order model plant functional type in relation to topography, several additional topographic variables were derived from the DEM using Arc/Info. These were sampled in accordance with the interval specified in section 11.1, which was 300 m, and imported into SPSS for statistical analysis and modelling.

11.4.1 Profile and planform curvature

Slope *profile* curvature is the rate of change of slope for each cell in the direction of the slope, whereas slope *planform* curvature is the rate of change of slope for each cell in the direction of the surface perpendicular to the slope direction. They are the second derivative of the surface (i.e., the slope of the slope) and can be used to describe the physical characteristics of a drainage basin in an effort to understand erosion and runoff processes. Slope profile curvature affects the acceleration and deceleration of flow, and therefore influences erosion and deposition. Slope planform curvature influences convergence and divergence of flow and soil water content. They may also be expected to influence wind exposure.

Each curvature measure is calculated using the *curvature* function in Arc/Info. It operates on a cell-by-cell basis for a 3x3 neighbourhood. A positive curvature indicates that the surface is upwardly convex at that grid cell. A negative curvature indicates that the surface is upwardly concave at that grid cell. A value of zero indicates that the surface is flat.

11.4.2 Upslope area

Upslope area is the catchment area above a location and is important in terms of runoff volume and steady state runoff. This is the equivalent of a grid of accumulated flow to each cell, based upon the number of cells flowing into each cell in the output grid.

Upslope area is calculated using the *flowdirection* and *flowaccumulation* functions in Arc/Info. The current processing cell is not considered in this calculation, and therefore cells with a flow accumulation of zero are local topographic highs and may be used to identify ridges. Cells with a high flow accumulation are areas of concentrated flow and may be used to identify stream channels. The identification of ridges has implications for wind exposure.

11.4.3 Topographic soil moisture

The soil moisture index was developed to model the effects of subsurface throughflow on water accumulation and soil moisture. It provides a surrogate for soil moisture potential (Bevan and Kirkby, 1979; Brown, 1994). In a simplified form, the soil *moisture* variable is the natural logarithm of the ratio between the upslope area and the slope gradient (in degrees).

11.4.4 Topographic shelter

Topographic shelter is the extent to which a location is surrounded by higher elevation terrain. It can affect local climate because sites surrounded with and elevated horizon may be shades from direct solar radiation, effectively reducing photosynthetic period. In contrast, emitted longwave radiation from surrounding slopes may be absorbed at a sheltered site (Joyce, 2000). Topographically sheltered sites may also have reduced exposure to high wind speeds.

A topographic *shelter* variable was calculated within Arc/Info using the *focal max* function. It is designed to quantify the elevation difference between each grid cell and the higher ground in the immediate vicinity. Therefore, the elevation of the cell was

subtracted from the result of the *focalmax* operation to calculate local topographic shelter. A neighbourhood of 29x29 cells (900 metres) was used based upon the analysis of spatial dependence of topography within the study area.

11.4.5 Redundancy in topographic variables

The derived topographic variables are significantly correlated, for example at the 0.01 level, as shown in table 11.26. To reduce redundancy and the potential problem of multicollinearity in regression analyses, principal component analysis (PCA) was employed within SPSS.

Table 11.26. Pearson Correlations for topographic variables at Joatka (shaded cells significant at the 0.01 level.

	DEM	Gradient	Solar	Upslope	Profile	Planform	Moisture	Shelter
DEM		.029	-.028	-.006	.043	-.010	-.025	-.081
Gradient	.029		.274	-.001	-.006	.007	-.335	.540
Solar	-.028	.274		-.006	-.010	.012	-.055	.252
Upslope	-.006	-.001	-.006		-.221	-.254	.705	.186
Profile	.043	-.006	-.010	-.221		.740	-.354	-.307
Planform	-.010	.007	.012	-.254	.740		-.389	-.152
Moisture	-.025	-.335	-.055	.705	-.354	-.389		.060
Shelter	-.081	.540	.252	.186	-.307	-.152	.060	

11.4.6 Principal component analysis

PCA is a parametric method that requires all variables are continuous. The procedure involves the derivation of uncorrelated variables (principal components) formed by linear components of the original variables. The first principal component is associated with the maximum variation in the data set, with succeeding principal components explaining maximum residual variation in directions orthogonal to previously defined components (Miller et al., 1984). The PCA was an un-rotated solution, because otherwise collinearity is not removed because axes are not orthogonal. The variance explained and the component matrix is shown in tables 11.27 and 11.28 and given the eigenvalues in table 11.27 only the first four components were used (eigenvalue > 1). The interpretation of the loading is given in table 11.29, with no interpretation given for PCs 7 and 8 because there is no clear information.

Table 11.27. PCA: Total variance explained

Component	eignevalue	% of Variance	Cumulative %
1	2.426	30.324	30.324
2	1.802	22.521	52.846
3	1.098	13.724	66.569
4	1.008	12.597	79.167
5	.811	10.132	89.299
6	.442	5.520	94.819
7	.231	2.894	97.712
8	.183	2.288	100.000

Table 11.28. Component Matrix

	Component							
	1	2	3	4	5	6	7	8
DEM	-.057	-.058	-.130	.982	.057	.095	-.008	-.004
Gradient	-.040	.858	.052	.137	-.282	-.357	-.001	.183
Solar	.025	.562	.257	-.004	.785	-.013	-.018	-.017
Upslope	.689	-.121	.602	.133	-.151	-.208	-.156	-.199
Profile	-.782	-.126	.494	.072	-.055	-.100	.322	-.084
Planform	-.778	-.021	.492	-.009	-.106	.234	-.266	.126
Moisture	.771	-.379	.384	.037	.062	.104	.146	.277
Shelter	.367	.756	.125	-.025	-.265	.431	.108	-.099

Table 11.29. Interpretation of PCA loadings.

Component	Interpretation - high values
1	High potential moisture and runoff; sheltered depressions
2	Steep, predominantly south-facing slopes; well sheltered; somewhat low potential moisture
3	High runoff potential; rounded topography; reasonably high moisture potential
4	High elevations
5	High solar radiation potential
6	Sheltered; relatively flat areas

11.4.7 Logistic regression at Joatka

Vegetation was specified as the dependent variable, with the topographic principal components and snow cover information being the predictors; details are given in table 11.30.

Table 11.30. Predictor variables for logistic regression at Joatka.

Variable name	Description
PC1	Principal component 1
PC2	Principal component 2
PC3	Principal component 3
PC4	Principal component 4
Snow17	Binary variable, snow or snow free on May 17th
Wet17	Binary variable, wet snow or dry/snow free on May 17th
Dwf17	Categorical variable, dry snow, wet snow and snow free on May 17th
Snow5	Binary variable, snow or snow free on June 5th
Wet5	Binary variable, wet snow or dry/snow free on June 5th

The sample of values was divided into two samples using random selection in SPPS. One sample was used for model building and the other was an independent validation sample. A backward-stepwise model building procedure was undertaken and predictors were included only if significant at the 0.05 level using the difference in -2 log-likelihood between the current model and a reduced model (the reduced model is the model formed by omitting a predictor from the current model). Table 11.31 provides

details of the variance explained by different models. The classification of the dependent variable is different for each model.

Table 11.31. Residual analysis (Nagelkerke R^2) and prediction accuracy (Kappa).

Model	Dependent variable (Vegetation classes)	Predictors (Topographic PCs)	R^2	Overall accuracy	$\hat{k}$
1	Non-vascular (lichen heath) and other	PC1, PC2	.145	.62	.19
2	Lichen heath, herbaceous and shrubs	PC1, PC2, PC3	.157	.55	.19
3	Lichen heath, herbaceous, dwarf shrubs and other shrubs	PC1, PC2, PC3, PC4	.322	.486	.203
4	Non-forest and forest	PC1, PC2, PC3, PC4	.361	.85	.368

Overall the models performed relatively poorly at predicting the dependent variable. SAR derived now cover was not a significant variable in any of the models; snow cover did not explain any variation in vegetation in addition to that explained by topography. Table 11.32 provides details of the intercept and coefficients for each model.

The most consistent predictor was PC2, which represents steep, sheltered, south-facing slopes. It is a significant predictor for each model, with lichen heath less likely to occur for high values of PC2. When the vegetation is separated into lichen heath, herbaceous and shrub types, high values of PC2 reveal an increased likelihood of shrubs. A key predictor for Lichen heath is PC1, which identifies depressions with high runoff and moisture potential; lichen heath is much less likely in such locations. It is interesting that this predictor is not significant in discriminating between herbaceous vegetation, which are associated with bogs at this site, and shrubs. Both are positively associated with higher moisture potential. PC4 is dominated by elevation. It is interesting that elevation is only significant when tall shrubs (forest) is identified as a distinct vegetation class; other PFTs are more likely at higher elevations than low and tall shrubs.

Table 11.32. Model parameter estimates. Empty cells for a model indicate a predictor was not significant as an overall model predictor.

Model		Intercept	PC1	PC2	PC3	PC4
1	Lichen heath	-.466	-.546	-.602		
	Other	-	-	-	-	-
2	Lichen heath	-.218	-.515	-.693	-.133	
	Herbaceous	-1.409	.172	-.515	-.216	
	Shrubs	-	-	-	-	
3	Lichen heath	1.514	-.649	-1.012	-.481	1.502
	Herbaceous	.320	.045	-.816	-.544	1.310
	Dwarf shrubs	1.235	-.200	-.516	-.475	1.764
	Low/tall shrubs	-	-	-	-	-
4	Non-forest	2.299	-.311	-.729	-.456	1.575
	Forest	-	-	-	-	-

11.5 Discussion

At each study site, it is clear that the pattern of snow-melt was topographically mediated. However, the patterns of snow-melt are complex and numerous topographic factors are likely to influence snow distribution. Multivariate approaches were investigated, which make full use of the information available in topographic data and reduce redundancy in variables.

Principal component analysis can produce topographic predictors that are "ecologically meaningful". Logistic regression models using the principal components at Joatka showed the potential of such an approach to predict vegetation type. However, in each model there was considerable unexplained variance in the data. This may be the result of errors in the vegetation classification, which may propagate and lead to reduced accuracy in the models. Further problems may result from the use of indirect gradients (topo-climatic predictors) and other important variables such as soil type were not available. The resolution of the DEM and vegetation data may also limit the explanatory and predictive power of the models.

The SAR-derived snow cover maps were not significant predictors when topography was included in the logistic regression. This is further evidence of errors in the

classification of snow cover. There is clear evidence that detection of wet snow in the forest is problematic, with an increased proportion of snow-free conditions from areas of forest when a lower proportion was expected. On 5th June at Joatka and 26th May at Abisko it was identified through field measurements that there was significant wet snow in the forest at the tree line. However, this is not detected in the classification of the images. Despite problems with the snow data, it is clear that snow-free conditions were more likely to occur earlier at lower elevations and on south facing slopes at each site. Wet snow was significantly associated with south-facing slopes early in the melt-period and snow cover is associated with north facing slopes at the end of the melt-period. Vegetation and snow conditions also had significant co-occurrence at each site, but the results at Joatka demonstrate the importance of topography.

Chapter 12. General Discussion

This chapter aims to synthesise the findings of the previous chapters and provides the main conclusions from this thesis and identifies some areas for future work.

At landscape scales, the spatial and temporal persistence of snow cover is known to be an important factor affecting the composition and spatial patterns of vegetation at the forest-tundra ecotone (Allen and Walsh, 1993). The aim of this research was to map spatial and temporal patterns of snow melt at landscape scale across the forest tundra ecotone in Arctic Europe. Therefore, data on snow cover were required at a high temporal and spatial resolution over relatively large areas; remote sensing provided the only reasonable method for such data collection. With independence of cloud cover and solar illumination, and especially given sensitivity to liquid water content, data from C-band ERS-2 SAR was utilised for snow mapping. The operational research context of the DART project necessitated study sites at three distinct and remote sites in the Fennoscandian mountain range, which introduced practical constraints that restricted image acquisition and field measurements of snow cover to a single year at each site. Furthermore, the DART study sites, each with considerable topographic variation at a number of scales, provided challenging environments in which to map the spatial pattern of snow melt with ERS-2 SAR.

The temporal and spatial measurement scales were a key consideration in the research design. The measurement scale of the spatial pattern of vegetation was effectively limited by the resolution of Landsat TM. Using ground control data a complex mosaic of communities at the forest-tundra ecotone was identified, which provided a challenge not only for vegetation classification but also because of likely vegetation influence on the SAR backscatter. The observed complexity in vegetation might be problematic for environmental monitoring using of SAR; however, to some extent the use of multi-temporal imagery and change detection mitigates this problem. Using a supervised classification, vegetation classes that could be determined varied at each site, depending on timing of the acquisition of imagery (related to highly dynamic vegetation phenology) and spatial variation in the structure of the forest-tundra ecotone. Multi-spectral VIR satellite imagery provided a suitable means of classification, although the aim of developing a classification generalised across all sites based on a hierarchical PFT classification (Chapin III *et al.*, 1996; Walker, 2000) was unrealistic. In particular,

the topography and climate at Joatka has resulted in a structure of vegetation with no distinct tree line and a patchy mosaic of communities that were difficult to classify given the resolution of Landsat TM. Each study site had characteristic assemblages of PFTs, which meant that inter-site comparison was qualitative.

It was anticipated that the temporal resolution of ERS-2 would be limited only by the return frequency of the satellite and restrictions on human resources; the return frequency at high latitudes was identified as approximately every 2 weeks. It was known that inherent system effects would limit the spatial resolution of ERS-2, most notably speckle, which requires filtering, and geometric distortion. Considerable inter-annual variation in snow duration was identified using ground surface temperature measurements, which was congruent with longer-term studies at regional and hemispheric scales (Frei and Robinson, 1999; Robinson, 1997). Clearly this variation cannot be accounted for with a single year of image acquisition and field measurements, nor if data had been acquired at a single study site over a period of three years. This variation makes planning acquisition of satellite imagery difficult, even with cloud independent SAR systems.

Snow and temperature measurements were made across the forest-tundra ecotone coincident with image acquisition. There were limitations with this data collection because the temporal "window" in which measurements are representative of the time of data acquisition was short, which limits the spatial distribution of measurements. In addition, given the known dependence of temperature on elevation and other topographic factors (Joyce, 2000) there is considerable spatial variation in snow properties across a complex landscape. Given such limitations and practical constraints, a data set was acquired that could be used to characterise snow conditions, at least within a small area.

A physically based model of C-band VV polarised microwave backscatter from a snowpack demonstrated a clear decrease in backscatter due to dielectric loss because of the measured increase in liquid water content within wet snowpacks. Surface roughness of both ground surface and snow surface was also shown to be an important parameter, but this aspect of the modelling was limited by lack of empirical data. Given the limitations of modelling, especially in relation to a lack of quantitative data on snow roughness, the model results were not compared directly to the received ERS-2

backscatter. However the pattern of the response was clear and future work was identified to model the potential impact of snowpack stratigraphy on backscatter.

Despite the capability of ERS-2 SAR to provide regular information on the snowpack, which is important for operational applications, it was clear that snowpack conditions were not conducive to straightforward interpretation. At each site, depending on the rapidity of the diurnal increase in temperature and the mean daily temperature on the day of SAR image acquisition, snow may be wet or dry. The return frequency of the ERS-2 satellite cannot capture such snow-melt dynamics, despite its weather independent capabilities. At Joatka, in particular, the snowmelt was characterised by a rapid progression from snow-covered, to snow patch mosaic, to snow-free conditions. Indeed, there might only be a few weeks difference between early and late melting areas, which is typical of Arctic ecosystems (Walker *et al.*, 1999). If snow melt lasts for several months (e.g. Nagler and Rott(2000) in the Austrian Alps), the temporal frequency of imagery is less important.

Analysis of multi-temporal backscatter signatures in relation to field measurements illustrated the complexity of the backscatter response. ERS SAR has the potential to measure change in conditions within forest, as noted by (Rignot *et al.*, 1994). However, there are many other factors that may confound the signal, for example, there is difficulty when a snowpack is mature and possibly patchy, or due to effects of a wet canopy associated with rain close to image acquisition. Based on signatures of SAR backscatter and field measurements, an algorithm for mapping wet and dry snow cover was developed that was consistent between study sites. The wet snow threshold was similar to that implemented in other studies (e.g. Rott and Nagler, 1995; Turpin *et al.*, 2000) and a typical increase of 2 dB was identified for snow-free conditions, which is consistent with the findings of Koskinen *et al.* (1997). Mapping wet snow had to consider the temporal variation in snow conditions and how changes related to snow duration and not just in terms of snow wetness. Temporal consistency in snow-free conditions between images was enforced to improve snow mapping.

The landscape was stratified into zones of elevation and slope aspect to evaluate the spatial and temporal change in snow cover along environmental gradients. In earlier images at each site, lower elevation had the highest probability of wet snow, even at sites with a relatively small elevation gradient. Differential ablation of snow appears to

occur as a function of slope orientation, with late lying snow characteristic of north facing slopes and snow wetness in earlier images characteristic of south facing slopes. The impact of slope aspect reflects the importance of snow properties at the time of image acquisition. Given the effects of diurnal change in temperature at the time of acquisition, we might expect the pattern of snow wetness to be influenced by the orientation of slope because of variation in solar radiation; this might differentially influence the speed of increase in water content. The study areas were also stratified in relation to vegetation communities. The image acquired on 17th May at Joatka provided a striking example of the potential of SAR to monitor snow melt under the birch canopy. However, other images, notably at Abisko on 26th May and Joatka on 5th June, demonstrated the difficulties in interpreting the backscatter from birch forest. There was some evidence that snow-free conditions emerged first in tundra areas and the potential of snow mapping using ERS-2 SAR may be limited to tundra / low growing vegetation; ERS-2 / C-band SAR does not provide a suitable means of monitoring snowmelt across the forest-tundra ecotone.

It was disappointing that the integration of temporal and spatial dimensions was limited by the poor quality of the snow melt data, especially later in the melt period. The spatial-temporal patterns of melt between the three sites cannot be used to suggest whether snow cover is controlling the distribution of tree line components. A richer series of data might allow more sophisticated analysis of snow and vegetation pattern, and enable causal mechanisms to be investigated. Two statistical approaches in particular were considered; generalised linear models and Markov transition matrices. Logistic regression is a type of generalised linear model and has been widely used to develop an understanding of the factors that control species distribution (Brown, 1994; Guisan *et al.*, 1998). An example of logistic regression at Joatka demonstrated that the SAR derived snow cover maps were not significant in predicting vegetation patterns. Markov transition matrices have been used to study a limited series of VIR images of snow cover to determine snow retention probabilities and snow accumulation probabilities in relation to vegetation (Allen and Walsh, 1993). Both approaches have potential for determining the relative importance of factors that influence the spatial pattern of vegetation at the forest-tundra ecotone.

12.1 Future research prospects

Classification of the forest-tundra ecotone was completed by statistical characterisation of spectral vegetation properties, which has known limitations. A more ecologically relevant representation of the forest-tundra ecotone is a three-dimensional approach (Callaghan *et al.*, 2002), which gives information on structure. As such, considerable potential comes from remote sensing techniques that directly provide information of the structure of vegetation and L-band PALSAR from the planned ALOS satellite will provide such data. Airborne techniques may also be valuable, in particular LIDAR, which can provide detailed information on canopy structure (e.g. Means *et al.* (1999), Naesset and Okland (2002)).

Given knowledge of the melt-freeze cycles at each site, we understand more fully the process scale of variation in snow properties that are relevant to SAR imagery. Clearly ERS-2 is not able to measure at a sufficient temporal scale to capture the temporal scale of natural variation. Alternative methods of image acquisition must be considered in order to improve the temporal frequency of imagery. Airborne systems, carrying both VIR sensors and active and passive radars, have been used in previous research with obvious improved control on return frequency (Baghdadi *et al.*, 1998; Balzter *et al.*, 2002; Green *et al.*, 1998). However, costs of airborne image acquisition campaigns are considered prohibitive. The steerable beam capabilities of SAR systems such as Envisat or Radarsat may be used to acquire more frequent imagery. However, the imaging geometry will be more complex, especially in comparison to the consistent imaging geometry of ERS-2. The utility of terrestrial remote sensing must be acknowledged. Spatial and temporal resolutions can be achieved far beyond that of any spaceborne sensor or realistic airborne image acquisition campaign and the costs are potentially low (Gottfried *et al.*, 1998; Hinkler *et al.*, 2002).

If studies are to be extended using spaceborne systems such with as those with complex imaging geometry, then availability of a DEM is crucial. Considerable human and computer resources were required to produce a DEM at each site that was compatible with the resolution of SAR. Poor availability of elevation data for Arctic studies is not likely to be mitigated in the near future. Shuttle Radar Topography Mission (JPL, 2002) will soon produce results, but the orbit of the shuttle limits the availability of data to 60° degrees north and 54° degrees south latitude. The highly variable SAR acquisition geometries made available by Radarsat and Envisat have intensified the need for terrain

correction of images over mountainous terrain. The broadly unchanging geometry of ERS-1 and ERS-2 allowed multi-temporal overlay in radar geometry. Geometric correction is necessary to bring the images from the ground range geometry into map geometry and radiometric correction is required if mixed-mode thematic information is not to be overwhelmed by terrain induced distortions (Small *et al.*, 1997). In the context of SAR systems in which the acquisition geometries are more variable, the correction model is particularly important. Development of software tools to create accurate maps of incidence angle is required, otherwise application of SAR imagery may require processing beyond the capabilities of many current users.

In terms of SAR imagery, it is clear that research at sites with lower relief amplitude than we encountered in DART sites would enable a better understanding of radar interaction with snow and vegetation at the forest-tundra ecotone. However, the spatial analysis of snow-vegetation interactions may benefit from a finer resolution and smaller extent of study area, using intensive sampling on experimental plots on selected slopes. Given that vegetation influences the distribution of snow cover and that much of the environmental variability controlling vegetation patterns might be attributable to topographic factors and their influence on climate, the causality of mechanisms is difficult to determine with an empirical approach. Isolating the effects of each of these physical features is beyond the scope of the present study and is likely to require an experimental approach (Schaefer and Messier, 1995). An improved understanding of ecosystem responses to environmental change, and feedbacks between these responses, could be achieved through measurements and experimental manipulations at fine spatial and temporal scales. Subsequently, the mechanisms of the response can be investigated through process-based modelling (Baxter, *pers. comm.*).

References

Adam, S., Pietroniro, A., and Brugman, M.M. (1997) Glacier snow line mapping using ERS-1 SAR Imagery. Remote Sensing of Environment, 61, 46-54.

Allen, T.R. and Walsh, S.J. (1993) Characterizing multitemporal alpine snowmelt patterns for ecological inferences. Photogrammetric Engineering and Remote Sensing, 59, 1521-1529.

Altese, E., Bolognani, O., Mancini, M., and Troch, P.A. (1996) Retrieving soil moisture over bare soil from ERS 1 synthetic aperture radar data: Sensitivity analysis based on a theoretical surface scattering model and field data. Water Resources Research, 32, 653-661.

Andersson, N.Å., Callaghan, T.V., and Karlsson, P.S. (1996) The Abisko Scientific Research Station. Ecological Bulletins, 45, 11-14.

ASF (2002) Synthetic Aperture Radar Products. Alaska SAR Facility. Accessed: 2002. http://www.asf.alaska.edu/~webweaver/ASF_site/4_3.html.

August, P., Michaud, J., Labash, C., and Smith, C. (1994) GPS for Environmental Applications - Accuracy and Precision of Locational Data. Photogrammetric Engineering and Remote Sensing, 60, 41-45.

Austin, M.P. (2002) Spatial prediction of species distribution: an interface between ecological theory and statistical modelling. Ecological Modelling, 157, 101-118.

Baghdadi, N., Gauthier, Y., and Bernier, M. (1997) Capability of Multitemporal ERS-1 SAR data for wet snow cover mapping. Remote Sensing of Environment, 60, 174-186.

Baghdadi, N., King, C., Chanzy, A., and Wigneron, J.P. (2002) An empirical calibration of the integral equation model based on SAR data, soil moisture and surface roughness measurement over bare soils. International Journal of Remote Sensing, 23, 4325-4340.

Baghdadi, N., Livingstone, C.E., and Bernier, M. (1998) Airborne C-band SAR measurements of wet snow-covered areas. IEEE Transactions on Geoscience and Remote Sensing, 36, 1977-1981.

Baker, W.L., Honaker, J.J., and Weisberg, P.J. (1995) Using aerial photgraphy and GIS to map the forest-tundra ecotone in Rocky Mountain National park, Colorado, for global change research. Photogrammetric Engneering and Remote Sensing, 61, 313-320.

Balzter, H., Baker, J.R., Hallikainen, M., and Tomppo, E. (2002) Retrieval of timber volume and snow water equivalent over a Finnish boreal forest from airborne polarimetric Synthetic Aperture Radar. International Journal of Remote Sensing, 23, 3185-3208.

Barber, D.G. and Ledrew, E.F. (1994) Modeling Synthetic-Aperture Radar (SAR) Scattering from a Seasonally Varying Snow-Covered Sea-Ice Volume at 5.3 and 9.25 Ghz. Polar Research, 13, 35-54.

Barnekow, L. (1999) Holocene tree-line dynamics and inferred climatic changes in the Abisko area, northern Sweden, based on macrofossil and pollen records. Holocene, 9, 253-265.

Bayer, T., Winter, R., and Schreier, G. (1991) Terrain influences in SAR backscatter and attempts to their correction. IEEE Transactions on Geoscience and Remote Sensing, 29, 451-462.

Bernier, M. and Fortin, J.-P. (1998) The potential of time series of C-band SAR data to monitor dry and shallow snow cover. IEE Transactions on Geoscience and Remote Sensing, 36, 226-243.

Bernier, M., Fortin, J.P., Gauthier, Y., Gauthier, R., Roy, R., and Vincent, P. (1999) Determination of snow water equivalent using RADARSAT SAR data in eastern Canada. Hydrological Processes, 13, 3041-3051.

Bevan, K.J. and Kirkby, M.J. (1979) A physically-based variable contributing area model of basin hydrology. Hydrological Sciences Bulletin, 24, 43-67.

Biftu, G.F. and Gan, T.Y. (1999) Retrieving near-surface soil moisture from Radarsat SAR data. Water Resources Research, 35, 1569-1579.

Billings, W.D. and Bliss, L.C. (1959) An alpine snowbank environment and its effects on vegetation, plant development, and productivity. Ecology, 40, 388-390.

Bindlish, R. and Barros, A.P. (2000) Multifrequency soil moisture inversion from SAR measurements with the use of IEM. Remote Sensing of Environment, 71, 67-88.

Bindlish, R. and Barros, A.P. (2001) Parameterization of vegetation backscatter in radar-based, soil moisture estimation. Remote Sensing of Environment, 76, 130-137.

Blöschl, G. (1999) Scaling in snow hydrology. Hydrological Processes, 13, 2149-2175.

Bowman, W.D. (1992) Inputs and Storage of Nitrogen in Winter Snowpack in an Alpine Ecosystem. Arctic and Alpine Research, 24, 211-215.

Brisco, B. and Brown, R.J. (1995) Multidate SAR/TM synergism for crop classification in western Canada. Photogrammetric Engineering and Remote Sensing, 61, 1009-1014.

Brown, D.G. (1994) Predicting vegetation types at treeline using topography and biophysical disturbance variables. Journal of Vegetation Science, 5, 641-656.

Brown, J. (1998) Active layer and permafrost properties, including snow depth, soil temperature, and soil moisture, Barrow, Alaska, USA. International Permafrost Association, Data and Information Working Group. Accessed.

Callaghan, T.V., Crawford, R.M.M., Eronen, M., Hofgaard, A., Payette, S., Rees, W.G., Skre, O., Sveinbjornsson, J., Vlassova, T.K., and Werkman, B.R. (2002a) The dynamics of the tundra-taiga boundary: An overview and suggested coordinated and integrated approach to research. Ambio, Special Report, 12, 3-5.

Callaghan, T.V., Werkman, B.R., and Crawford, R.M.M. (2002b) The tundra-taiga interface and its dynamics: Concepts and applications. Ambio, Special Report, 12, 6-14.

Capstick, D. and Harris, R. (2001) The effects of speckle reduction on classification of ERS SAR data. International Journal of Remote Sensing, 22, 3627-3641.

Castel, T., Martinez, J.M., Beaudoin, A., Wegmuller, U., and Strozzi, T. (2000) ERS INSAR data for remote sensing hilly forested areas. Remote Sensing of Environment, 73, 73-86.

CCRS (2002) CCRS Remote Sensing Glossary. Canada Centre for Remote Sensing. Accessed: 2002. http://www.ccrs.nrcan.gc.ca/ccrs/learn/terms/glossary/glossary_e.html.

Chapin III, F.S., Bret-Harte, M.S., Hobbie, S.E., and Zhong, H. (1996) Plant functional types as predictors of transient responses of Actic vegetation to global change. Journal of Vegetation Science, 7, 347-358.

Cohen, W.B. and Spies, T.A. (1992) Estimating structural attributes of Douglas-fir western hemlock forest stands from Landsat and Spot imagery. Remote Sensing of Environment, 41, 1-17.

Collins, M.J., Wiebe, J., and Clausi, D.A. (2000) The effect of speckle filtering on scale-dependent texture estimation of a forested scene. IEEE Transactions on Geoscience and Remote Sensing, 38, 1160-1170.

Congalton, R.G. (1991) A review of assessing the accuracy of classifications of remotely sensed data. Remote Sensing of Environment, 37, 35-46.

Cramer, W. (2002). Biome Models. In Encyclopedia of Global Environmental Change. The Earth System: Biological and Ecological Dimensions of Global Environmental Change (ed T. Munn), Vol. 2. John Wiley & Sons, Ltd., Chichester.

Cubasch, U. (2001) Climate projections (including regional projections and sea level). In Conference of the Parties to the UNFCCC. IPCC.

Cubasch, U., Meehl, G.A., Boer, G.J., Stouffer, R.J., Dix, M., Noda, A., Senior, C.A., Raper, S., and Yap, K.S. (2001). Projections of Future Climate Change. In Climate Change 2001: The Scientific Basis - Contribution of Working Group I to the Third Assessment Report of the Intergovernmental Panel on Climate Change (IPCC). (eds J.T. Houghton, Y. Ding, D.J. Griggs, M. Noguer, P.J. van der Linden, X. Dai, K. Maskell and C.A. Johnson). IPCC.

Daly, C. (1984) Snow distribution patterns in the alpine krummholz zone. Progress in Physical Geography, 8, 157-175.

Daly, C., Neilson, R.P., and Phillips, D.L. (1994) A statistical topographic model for mapping climatological precipitation over mountainous terrain. Journal of Applied Meteorology, 33, 140-158.

Denoth, A. (1989) Snow dielectric measurements. Advances in Space Research, 9, 233-243.

Denoth, A. (1994) An electronic device for long term snow wetness recording. Annals of Glaciology, 19, 104-106.

Denoth, A. (1998) Product Description: Dielectric Moisture Meter with Flat Capacitive Sensor University of Innsbruck, Innsbruck.

Denoth, A., Foglar, A., Weiland, P., Mätzler, C., Aebischer, H., Tiuri, M., and Shivola, A. (1984) A comparative study of instruments for measuring the liqiud water content of snow. Journal of Applied Physics, 56, 2154-2160.

Dobson, M.C., Ulaby, F.T., and L.E., P. (1995a) Land-cover classification and estimation of terrain attributes using synthetic-aperture radar. Remote Sensing of Environment, 51, 199-214.

Dobson, M.C., Ulaby, F.T., Le Toan, T., Beaudoin, A., Kasischke, E.S., and Christensen, N. (1992) Dependence of radar backscatter on coniferous forest biomass. IEEE Transactions on Geoscience and Remote Sensing, 30, 412-415.

Dobson, M.C., Ulaby, F.T., and Pierce, L.E. (1995b) Land-Cover Classification and Estimation of Terrain Attributes Using Synthetic-Aperture Radar. Remote Sensing of Environment, 51, 199-214.

Domik, G., Lerberl, F., and Cimino, J. (1988) Dependence of image grey values on topography in SIR-B images. International Journal of Remote Sensing, 9, 1013-1022.

Dozier, J. (1984) Snow reflectance from Landsat-4 Thematic Mapper. IEEE Transactions on Geoscience and Remote Sensing, 22, 323-328.

Dozier, J. and Marks, D. (1987) Snow mapping and classification from Landsat Thematic Mapper data. Annals of Glaciology, 9, 97-103.

Drinkwater, M.R. and Crocker, G.B. (1988) Modeling Changes in the Dielectric and Scattering Properties of Young Snow-Covered Sea Ice at GHz Frequencies. Journal of Glaciology, 34, 274-282.

Dubois, P.C., Vanzyl, J., and Engman, T. (1995) Measuring Soil-Moisture with Imaging Radars. IEEE Transactions on Geoscience and Remote Sensing, 33, 915-926.

Engman, E.T. (1991) Applications of Microwave Remote-Sensing of Soil-Moisture for Water-Resources and Agriculture. Remote Sensing of Environment, 35, 213-226.

Engman, E.T. and Chauhan, N. (1995) Status of Microwave Soil-Moisture Measurements with Remote- Sensing. Remote Sensing of Environment, 51, 189-198.

Erdas (1999) The Erdas Field Guide, 5th edn. Erdas Inc., Atlanta.

ESA (1999) The ERS SAR Toolbox User Manual. European Space Agency. Accessed: 2001. http://earth.esa.int/services/best/documentation/manual/stbx_V-5.html.

ESA (2002) Envisat Product Handbook. ESA. Accessed: 2002. http://envisat.esa.int/dataproducts/.

Fily, M., Dedieu, J.-P., and Surdyk, S. (1995) A SAR image study of a snow covered area in the French Alps. Remote Sensing of Environment, 51, 253-262.

Flowerdew, R., Geddes, A., and Green, M. (2001). Behaviour of regression models under random aggregation. In Modelling Scale in Geographical Information Science (eds N.J. Tate and P.M. Atkinson). John Wiley & Sons, Chichester.

Foody, G.M., Campbell, N.A., Trodd, N.M., and Wood, T.F. (1992) Derivation and application of probabilistic measures of class membership from the maximum likelihood classification. International Journal of Remote Sensing, 58, 1335-1341.

Forster, R.R., Jezek, K.C., Bolzan, J., Baumgartner, F., and Gogineni, S.P. (1999) Relationships between radar backscatter and accumulation rates on the Greenland ice sheet. International Journal of Remote Sensing, 20, 3131-3147.

Frank, T.D. (1988) Mapping Dominant Vegetation Communities in the Colorado Rocky- Mountain Front Range with Landsat Thematic Mapper and Digital Terrain Data. Photogrammetric Engineering and Remote Sensing, 54, 1727-1734.

Franklin, J. (1995) Predictive vegetation mapping: geographic modelling of biospatial patterns in relation to environmental gradients. Progress in Physical Geography, 19, 474-499.

Fransson, J.E.S. and Israelsson, H. (1999) Estimation of stem volume in boreal forests using ERS-1 C- and JERS-1 L-band SAR data. International Journal of Remote Sensing, 20, 123-137.

Frei, A. and Robinson, D.A. (1999) Northern hemisphere snow extent: Regional variability 1972-1994. International Journal of Climatology, 19, 1535-1560.

Frolov, A.D. and Macheret, Y.Y. (1999) On dielectric properties of dry and wet snow. Hydrological Processes, 13, 1755-1760.

Fuller, R.M., Groom, G.B., and Jones, A.R. (1994) The land cover map of Great Britain: an automated classification of Landsat Thematic Mapper data. Photogrammetric Engineering and Remote Sensing, 60, 553-562.

Fung, A.K. (1994) Microwave scattering and emission models and their applications Artech House, Boston.

Galen, C. and Stanton, M.L. (1995) Responses of Snowbed Plant-Species to Changes in Growing-Season Length. Ecology, 76, 1546-1557.

Garen, D.C., Johnson, G.L., and Hanson, C.L. (1994) Mean areal precipitation for daily hydrologic modeling in mountainous regions. Water Resources Bulletin, 30, 481-491.

Gens, R. and Van Genderen, J.L. (1996) SAR interferometry - Issues, techniques, applications. International Journal of Remote Sensing, 17, 1803-1835.

Gillman, M. and Hails, R. (1997) An introduction to ecological modelling: putting practice into theory Blackwell Science Ltd., London.

Goering, D.J., Chen, H., Hinzman, L.D., and Kane, D.L. (1995) Removal of Terrain Effects from Sar Satellite Imagery of Arctic Tundra. IEEE Transactions on Geoscience and Remote Sensing, 33, 185-194.

Gottfried, M., Pauli, H., and Grabherr, G. (1998) Prediction of vegetation patterns at the limits of plant life: A new view of the alpine-nival ecotone. Arctic and Apline Research, 30, 207-221.

Goyal, S.K., Seyfried, M.S., and O'Neill, P.E. (1998) Effect of digital elevation model resolution on topographic correction of airborne SAR. International Journal of Remote Sensing, 19, 3075-3096.

Green, R.O., Eastwood, M.L., Sarture, C.M., Chrien, T.G., Aronsson, M., Chippendale, B.J., Faust, J.A., Pavri, B.E., Chovit, C.J., Solis, M.S., Olah, M.R., and Williams, O. (1998) Imaging spectroscopy and the Airborne Visible Infrared Imaging Spectrometer (AVIRIS). Remote Sensing of Environment, 65, 227-248.

Groisman, P.Y., Karl, T.R., and Knight, R.W. (1994) Observed Impact of Snow Cover on the Heat-Balance and the Rise of Continental Spring Temperatures. Science, 263, 198-200.

Guisan, A., Edwards, T.C., and Hastie, T. (2002) Generalized linear and generalized additive models in studies of species distributions: setting the scene. Ecological Modelling, 157, 89-100.

Guisan, A., Theurillat, J.P., and Kienast, F. (1998) Predicting the potential distribution of plant species in an Alpine environment. Journal of Vegetation Science, 9, 65-74.

Guisan, A. and Zimmermann, N.E. (2000) Predictive habitat models in ecology. Ecological modelling, 135, 147-186.

Guneriussen, T. (1997) Backscattering properties of a wet snow cover derived from DEM corrected ERS-1 SAR data. International Journal of Remote Sensing, 18, 375-392.

Guneriussen, T., Hogda, K.A., Johnsen, H., and Lauknes, I. (2001) InSAR for estimation of changes in snow water equivalent of dry snow. IEEE Transactions on Geoscience and Remote Sensing, 39.

Haack, B.N., Herold, N.D., and Bechdol, M.A. (2000) Radar and optical data integration for land-use/land-cover mapping. Photogrammetric Engineering and Remote Sensing, 66, 709-716.

Haefner, H., Holecz, F., Meier, E., Nüesch, D., and Piesbergen, J. (1993) Capabilities and limitations of ERS-1 SAR data for snowcvoer determination in mountainous regions. In Second ERS-1 Symposium - Space at the Service of our Environment, pp. 971-976. ESA, Hamburg, Germany.

Hall, D.K., Foster, J.L., Salomonson, V.V., Klein, A.G., and Chien, J.Y.L. (2001) Development of a technique to assess snow-cover mapping errors from space. IEEE Transactions on Geoscience and Remote Sensing, 39, 432-438.

Harding, R., Kuhry, P., Christensen, T.R., Sykes, M.T., Dankers, R., and van der Linden, S. (2002) Climate feedbacks at the tundra-taiga interface. Ambio, Special Report, 12, 47-55.

Harrell, P.A., Kasischke, E.S., Bourgeau-Chavez, L.L., Haney, E.M., and Christensen, N.L. (1997) Evaluation of approaches to estimating aboveground biomass in southern pine forests using SIR-C data. Remote Sensing of Environment, 59, 223-233.

Haxeltine, A. and Prentice, I.C. (1996) BIOME3: An equilibrium terrestrial biosphere model based on ecophysiological constraints, resource availability, and competition among plant functional types. Global Biogeochemical Cycles, 10, 693-709.

Heegaard, E. (2002) A model of alpine species distribution in relation to snowmelt time and altitude. Journal of Vegetation Science, 13, 493-504.

Hinkler, J., Pedersen, S.B., Rasch, M., and Hansen, B.U. (2002) Automatic snow cover monitoring at high temporal and spatial resolution, using images taken by a standard digital camera. International Journal of Remote Sensing, 23, 4669-4682.

Hinse, M., Gwyn, Q.H.J., and Bonn, F. (1988) Radiometric correction of C-band imagery for topographic effects in regions of moderate relief. IEEE transactions on Geoscience and Remote Sensing, 26, 122-132.

Houghton, J.T., Ding, Y., Griggs, D.J., Noguer, M., van der Linden, P.J., Dai, X., Maskell, K., and Johnson, C.A. (2001) Climate Change 2001: The Scientific Basis - Contribution of Working Group I to the Third Assessment Report of the Intergovernmental Panel on Climate Change (IPCC). IPCC.

Huntley, B., Dean, A.M., Baxter, R., and Thomas, C.J. *et al.* (2003). DART: Dynamic response of the forest-tundra ecotone to environmental change. Final Report, volume 1: Scientific Report. European Union.

Huntley, B. and Webb, T. (1988) Vegetation History Kluwer, Dordrecht.

Imhoff, M.L. (1995) Radar Backscatter and Biomass Saturation - Ramifications for Global Biomass Inventory. IEEE Transactions on Geoscience and Remote Sensing, 33, 511-518.

Johnsen, H., Lauknes, L., and Guneriussen, T. (1995) Geocoding of fast-delivery ERS-1 SAR image mode product using DEM data. International Journal of Remote Sensing, 16, 1957-1968.

Josberger, E.G. and Mognard, N.M. (2002) A passive microwave snow depth algorithm with a proxy for snow metamorphism. Hydrological Processes, 16, 1557-1568.

Joyce, A.N. (2000) Modelling surface climate over complex terrain for landscape ecology, University of Durham, Durham, UK.

JPL (2002) Shuttle Radar Topography Mission. Jet Propulsion Laboratory. Accessed: 2003. http://www.jpl.nasa.gov/srtm/index.html.

Kaplan, J.O. (2001) Geophysical Applications of Vegetation Modelling, Lund University, Lund.

Kasischke, E.S., Bourgeauchavez, L.L., Christensen, N.L., and Haney, E. (1994) Observations on the sensitivity of ERS-1 SAR image intensity to changes in aboveground biomass in young loblolly-pine forests. International Journal of Remote Sensing, 15, 3-16.

Kasischke, E.S., Melack, J.M., and Dobson, M.C. (1997) The use of imaging radars for ecological applications - A review. Remote Sensing of Environment, 59, 141-156.

Kjällgren, L. and Kullman, L. (1998) Spatial patterns and structure of the mountain birch tree limit in the southern Swedish scandes - A regional perspective. Geografiska Annaler, 80A, 1-16.

Koh, G. and Jordan, R. (1995) Subsurface Melting in a Seasonal Snow Cover. Journal of Glaciology, 41, 474-482.

Koskinen, J.T., Metsamaki, S., Grandell, J., Janne, S., Matikainen, L., and Hallikainen, M. (1999) Snow monitoring using radar and optical satellite data. Remote Sensing of Environment, 69, 16-29.

Koskinen, J.T., Pulliainen, J., and Hallikainen, M.T. (1997) The use of ERS-1 SAR data in snow melt monitoring. IEEE Transactions on Geoscience and Remote Sensing, 35, 601-610.

Kudo, G. (1991) Effects of Snow-Free Period on the Phenology of Alpine Plants Inhabiting Snow Patches. Arctic and Alpine Research, 23, 436-443.

Kuntz, S. and Siegert, F. (1999) Monitoring of deforestation and land use in Indonesia with multitemporal ERS data. International Journal of Remote Sensing, 20, 2835-2853.

Kuplich, T.M., Freitas, C.C., and Soares, J.V. (2000) The study of ERS-1 SAR and Landsat TM synergism for land use classification. International Journal of Remote Sensing, 21, 2101-2111.

Laur, H., Bally, P., Meadows, P., Sanchez, J., Schaettler, B., Lopinto, E., and Esteban, D. (1998) ERS SAR Calibration: Derivation of the Backscattering Coefficient in ESA ERS SAR PRI Products ESA Publications Division.

Le Toan, T., Beaudoin, A., Riom, J., and Guyon, D. (1992) Relating forest biomass to SAR data. IEEE Transactions on Geoscience and Remote Sensing, 30, 403-411.

Levens, R. (1966) The strategy of model building in population ecolgy. American Scientific, 54, 421-431.

Lillesand, T.M. and Kiefer, R.W. (1994) Remote Sensing and Image Interpretation, 3 edn. John Wiley & Sons, Inc., Chichester.

Lin, D.S., Wood, E.F., Beven, K., and Saatchi, S. (1994) Soil-Moisture Estimation over Grass-Covered Areas Using Airsar. International Journal of Remote Sensing, 15, 2323-2343.

Lozano-Garcia, D.F. and Hoffer, R.M. (1993) Synergistic effects of combined Landsat TM and SIR-B data for forest resources assessment. International Journal of Remote Sensing, 14, 2677-2694.

Lucas, R.M. and Harrison, A.R. (1994). Snow monitoring in the United Kingdom using NOAA AVHRR imagery. In Environmental Remote Sensing from Regional to Global Scales (eds G.M. Foody and P.J. Curran), pp. 111-130. John Wiley & Sons, Inc., Chichester.

Macdonald, G.M., Edwards, T.W.D., Moser, K.A., Pienitz, R., and Smol, J.P. (1993) Rapid Response of Treeline Vegetation and Lakes to Past Climate Warming. Nature, 361, 243-246.

Macelloni, G., Paloscia, S., Pampaloni, P., Sigismondi, S., De Matthaeis, P., Ferrazzoli, P., Schiavon, G., and Solimini, D. (1999) The SIR-C/X-SAR experiment on Montespertoli: sensitivity to hydrological parameters. International Journal of Remote Sensing, 20, 2597-2612.

Mangolini, M. and Arino, O. (1998) ERS-SAR and Landsat-TM multitemporal fusion for crop statistics.

Means, J.E., Acker, S.A., Harding, D.J., Blair, J.B., Lefsky, M.A., Cohen, W.B., Harmon, M.E., and McKee, W.A. (1999) Use of large-footprint scanning airborne lidar to estimate forest stand characteristics in the Western Cascades of Oregon. Remote Sensing of Environment, 67, 298-308.

Milbert, D.G. (2000) Comparison of Positions With and Without Selective Availability (Full 24 Hour Data Sets). National Geodetic Survey. Accessed: 2002. http://www.ngs.noaa.gov/FGCS/info/sans_SA/.

Miller, G.P., Fuchs, M., Hall, M.J., Asrar, G., Kanemasu, E.T., and Johnson, D.E. (1984) Analysis of seasonal mult-spectral reflectances of small grains. Remote Sensing of Environment, 14, 153-167.

Moeremans, B. and Dautrebande, S. (2000) Soil moisture evaluation by means of multi-temporal ERS SAR PRI images and interferometric coherence. Journal of Hydrology, 234, 162-169.

Moghaddam, M. and Saatchi, S.S. (1999) Monitoring tree moisture using an estimation algorithm applied to SAR data from BOREAS. IEEE Transactions on Geoscience and Remote Sensing, 37, 901-916.

Moore, I.D., Grayson, R.B., and Ladson, A.R. (1991) Digital Terrain Modelling: A review of hydrological, geomorphological, and biological applications. Hydrological Processes, 5, 3-30.

Myneni, R.B., Keeling, C.D., Tucker, C.J., Asrar, G., and Nemani, R.R. (1997) Increased plant growth in the northern high latitudes from 1981 to 1991. Nature, 386, 698-702.

Naesset, E. and Okland, T. (2002) Estimating tree height and tree crown properties using airborne scanning laser in a boreal nature reserve. Remote Sensing of Environment, 79, 105-115.

Nagler, T. and Rott, H. (2000) Retrieval of wet snow by means of multitemporal SAR data. IEEE Transactions on Geoscience and Remote Sensing, 38, 754-765.

Nemani, R. and Running, S.W. (1996) Implementation of a hierarchical global vegetation classification in ecosystem function models. Journal of Vegetation Science, 7, 337-346.

Nezry, E., Mougin, E., Lopes, A., Gastelluetchegorry, J.P., and Laumonier, Y. (1993) Tropical vegetation mapping with combined visible and SAR spaceborne data. International Journal of Remote Sensing, 14, 2165-2184.

NOAA (2002) Polar Operational Environmental Satellite. Accessed: 2002. http://www.oso.noaa.gov/poes/.

Oliver, M.A. (2001). Determining the Spatial Scale of Variation in Environmental Properties using the Variogram. In Modelling Scale in Geographical Information Science (eds N.J. Tate and P.M. Atkinson). John Wiley & Sons, Chichester.

Ostendorf, B. and Reynolds, J.F. (1998) A model of arctic tundra vegetation derived from topographic gradients. Landscape Ecology, 13, 187-201.

Payette, S., Filion, L., Delwaide, A., and Begin, C. (1989) Reconstruction of Tree-Line Vegetation Response to Long-Term Climate Change. Nature, 341, 429-431.

Pierce, L.E., Bergen, K.M., Dobson, M.C., and Ulaby, F.T. (1998) Multitemporal land-cover classification using SIR-C/X-SAR imagery. Remote Sensing of Environment, 64, 20-33.

Pohl, C. and van Genderen, J.L. (1998) Multisensor image fusion in remote sensing: concepts, methods and applications. International Journal of Remote Sensing, 19, 823-854.

Pope, K.O., Reybenayas, J.M., and Paris, J.F. (1994) Radar remote-sensing of forest and wetland ecosystems in the Central-American tropics. Remote Sensing of Environment, 48, 205-219.

Pulliainen, J. and Hallikainen, M. (2001) Retrieval of regional Snow Water Equivalent from space-borne passive microwave observations. Remote Sensing of Environment, 75, 76-85.

Pulliainen, J.T., Mikkelä, P.J., Hallikainen, M.T., and Ikonen, J.-P. (1996) Seasonal dynamics of C-band backscatter of boreal forests with applications to biomass and soil moisture estimation. IEEE transactions on Geoscience and Remote Sensing, 34, 758-769.

Quilfen, Y., Chapron, B., Bentamy, A., Gourrion, J., Elfouhaily, T.M., and Vandemark, D. (1999) Global ERS 1 and 2 and NSCAT observations: Upwind crosswind and

upwind downwind measurements. Journal of Geophysical Research-Oceans, 104, 11459-11469.

Ranson, K.J. and Sun, G.Q. (1994) Northern forest classification using temporal multifrequency and multipolarimetric SAR images. Remote Sensing of Environment, 47, 142-153.

Ranson, K.J. and Sun, G.Q. (1997) An evaluation of AIRSAR and SIR-C/X-SAR images for mapping northern forest attributes in Maine, USA. Remote Sensing of Environment, 59, 203-222.

Rees, G., Brown, I., Mikkola, K., Virtanen, T., and Werkman, B. (2002) How can the dynamics of the tundra-taiga boundary be remotely monitored? Ambio, Special Report, 12, 56-62.

Rees, W.G. (1999) The Remote Sensing Data Book Cambridge University Press, Cambridge.

Rees, W.G. (2001) Physical Principles of Remote Sensing, 2 edn. Cambridge University Press, Cambridge.

Rees, W.G. and Steel, A.M. (2001a) Radar backscatter coefficients and snow detectability for upland terrain in Scotland. International Journal of Remote Sensing, 22, 3015-3026.

Rees, W.G. and Steel, A.M. (2001b) Simplified radar mapping equations for terrain correction of space-borne SAR images. International Journal of Remote Sensing, 22, 3643-3649.

Rignot, E., Salas, W.A., and Skole, D.L. (1997) Mapping deforestation and secondary growth in Rondonia, Brazil, using imaging radar and thematic mapper data. Remote Sensing of Environment, 59, 167-179.

Rignot, E., Way, J.B., McDonald, k., Viereck, L., Williams, C., Adams, P., Payne, C., Wood, W., and Shi, J. (1994a) Monitoring of environmental conditions in taiga forests using ERS-1 SAR. Remote Sensing of Environment, 49, 145-154.

Rignot, E., Williams, C.L., Way, J.B., and Viereck, L.A. (1994b) Mapping of forest types in Alaskan boreal forests using SAR imagery. IEEE Transactions on Geoscience and Remote Sensing, 32, 1051-1059.

Robinson, D.A. (1997) Hemispheric snow cover and surface albedo for model validation. Annals of Glaciology, 25, 241-245.

Rott, H. (1984) The analysis of backscattering properties from SAR data of mountain regions. IEEE Journal of Oceanic Engineering, OE-9, 347-355.

Rott, H. and Davis, R.E. (1993) Multifrequency and polarimetric SAR observations on alpine glaciers. Annals of Glaciology, 17, 98-104.

Rott, H. and Mätlzer, C. (1987) Posibilities and limits of synthetic aperture radar for snow and glacier surveying. Annals of Glaciology, 9, 195-199.

Rott, H. and Nagler, T. (1992) Snow and glacier investigations by ERS-1 SAR. In First ERS-1 Symposium, pp. 577-582. ESA, Cannes, France.

Rott, H. and Nagler, T. (1995) Monitoring temporal dynamics of snow melt with ERS-1 SAR. In IGARSS, pp. 1747-1749.

Saatchi, S.S., Nelson, B., Podest, E., and Holt, J. (2000) Mapping land cover types in the Amazon Basin using 1 km JERS-1 mosaic. International Journal of Remote Sensing, 21, 1201-1234.

Sader, S.A., Waide, R.B., Lawrence, W.T., and Joyce, A.T. (1989) Tropical forest biomass and successional age class relationships to a vegetation index derived from Landsat TM data. Remote Sensing of Environment, 28, 143-.

Schaefer, J.A. and Messier, F. (1995) Scale-dependent correlations of Arctic vegetation and snow cover. Arctic and Alpine Research, 27, 38-43.

Schmullius, C.C. and Evans, D.L. (1997) Synthetic aperture radar (SAR) frequency and polarization requirements for applications in ecology, geology, hydrology, and oceanography: a tabular status quo after SIR-C/X-SAR. International Journal of Remote Sensing, 18, 2713-2722.

Schotten, C.G.J., Vanrooy, W.W.L., and Janssen, L.L.F. (1995) Assessment of the capabilities of multitemporal ERS-1 SAR data to discriminate between agricultural crops. International Journal of Remote Sensing, 16, 2619-2637.

Shi, J. and Dozier, J. (1993) Measurements of snow- and glacier covered areas with single-polarization SAR. Annals of Glaciology, 17, 72-76.

Shi, J. and Dozier, J. (1994) Snow mapping in alpine regions with synthetic aperture radar. IEEE Transactions on geoscience and Remote Sensing, 32, 152-157.

Shi, J. and Dozier, J. (1995) Inferring snow wetness using C-band data from SIR-C's polarimetric synthetic aperture radar. IEEE Transactions on Geoscience and Remote Sensing, 33, 905-914.

Shi, J. and Dozier, J. (1997) Mapping seasonal snow cover with SIR-C/X-SAR in mountainous areas. Remote Sensing of Environment, 59, 294-307.

Shi, J., Hensly, S., and Dozier, J. (1998) Mapping snow cover with repeat pass synthetic aperture radar.

Shi, J.C. and Dozier, J. (2000a) Estimation of snow water equivalence using SIR-C/X-SAR, part I: Inferring snow density and subsurface properties. IEEE Transactions on Geoscience and Remote Sensing, 38, 2465-2474.

Shi, J.C. and Dozier, J. (2000b) Estimation of snow water equivalence using SIR-C/X-SAR, part II: Inferring snow depth and particle size. IEEE Transactions on Geoscience and Remote Sensing, 38, 2475-2488.

Shi, J.C., Wang, J., Hsu, A.Y., Oneill, P.E., and Engman, E.T. (1997) Estimation of bare surface soil moisture and surface roughness parameter using L-band SAR image data. IEEE Transactions on Geoscience and Remote Sensing, 35, 1254-1266.

Shi, Z. and Fung, K.B. (1994) A comparison of digital speckle filters. In IGRASS.

Sjogersten, S. and Wookey, P.A. (2002a) Climatic and resource quality controls on soil respiration across a forest-tundra ecotone in Swedish Lapland. Soil Biology and Biochemistry, 34, 1633-1646.

Sjogersten, S. and Wookey, P.A. (2002b) Spatio-temporal variability and environmental controls of methane fluxes at the forest-tundra ecotone in the Fennoscandian mountains. Global Change Biology, 8, 885-894.

Small, D., Holecz, F., Meier, E., Nüesch, D., and Barmettler, A. (1997) Geometric and radiometric calibration of RADARSAT images. In Geomatics in the era of RADARSAT, pp. 24-30, Ottawa, Canada.

Soares, J.V., Renno, C.D., Formaggio, A.R., Yanasse, C.D.C.F., and Frery, A.C. (1997) An investigation of the selection of texture features for crop discrimination using SAR imagery. Remote Sensing of Environment, 59, 234-237.

Sokratov, S.A. and Barry, R.G. (2002) Intraseasonal variation in the thermoinsulation effect of snow cover on soil temperatures and energy balance. Journal of Geophysical Research-Atmospheres, 107, art. no.-4093.

Stiles, W.H. and Ulaby, F.T. (1980) The active and passive microwave response to snow parameters 1. Wetness. Journal of Geophysical Research, 85, 1037-1044.

Stjernman, A. (1995). Design and devleopment of a microwave multifrequency polarimetric scatterometer for biosphere remote sensing. Swedish Institute of Space Physics, Kiruna.

Strozzi, T., Dammert, P.B.G., Wegmuller, U., Martinez, J.M., Askne, J.I.H., Beaudoin, A., and Hallikainen, M.T. (2000) Landuse mapping with ERS SAR interferometry. IEEE Transactions on Geoscience and Remote Sensing, 38, 766-775.

Strozzi, T., Wegmuller, U., and Matzler, C. (1999) Mapping wet snowcovers with SAR interferometry. International Journal of Remote Sensing, 20, 2395-2403.

Tansey, K.J. and Millington, A.C. (2001) Investigating the potential for soil moisture and surface roughness monitoring in drylands using ERS SAR data. International Journal of Remote Sensing, 22, 2129-2149.

Tappeiner, U., Tappeiner, G., Aschenwald, J., Tasser, E., and Ostendorf, B. (2001) GIS-based modelling of spatial pattern of snow cover duration in an alpine area. Ecological modelling, 138, 265-275.

Teillet, P.M., Guindon, B., Meunier, J.F., and Goodenough, D.G. (1985) Slope-aspect effects in synthetic aperture radar imagery. Canadian Journal of Remote Sensing, 11, 39-49.

Tiuri, M.E., Sihvola, A.H., Nyfors, E.G., and Hallikaiken, M.T. (1984) The complex dielectric constant of snow at microwave frequencies. IEEE Journal of Oceanic Engineering, 9, 377-382.

Townshend, J., Justice, C., Li, W., Gurney, C., and Mcmanus, J. (1991) Global land cover classification by remote-sensing - present capabilities and future possibilities. Remote Sensing of Environment, 35, 243-255.

Tso, B. and Mather, P.M. (1999) Crop discrimination using multi-temporal SAR imagery. International Journal of Remote Sensing, 20, 2443-2460.

Turpin, O.C., Caves, R.G., Ferguson, R.I., and Johansson, B. (2000). Verification of simulated snow cover in an Arctic basin using satellite-derived snow-cover maps. In Annals of Glaciology, Vol 31, 2000, Vol. 31, pp. 391-396.

Ulaby, F.T., Moore, R.K., and Fung, A.K. (1982a) Microwave Remote Sensing Fundamentals and Radiometry Addison-Wesley Publishing Company, London.

Ulaby, F.T., Moore, R.K., and Fung, A.K. (1982b) Radar Remote Sensing and Surface Scattering and Emission Theory Addison-Wesley Publishing Company, London.

Ulaby, F.T., Moore, R.K., and Fung, A.K. (1986) From Theory to Application Addison-Wesley Publishing Company, London.

Walker, D.A. (2000) Hierarchical subdivision of Arctic tundra based on vegetation response to climate, parent material and topography. Global Change Biology, 6, 19-34.

Walker, D.A., Halfpenny, J.C., Walker, M.D., and Wessman, C.A. (1993) Long-term studies of snow-vegetation interactions. Bioscience, 43, 287-301.

Walker, M.D., Walker, D.A., Welker, J.M., Arft, A.M., Bardsley, T., Brooks, P.D., Fahnestock, J.T., Jones, M.H., Losleben, M., Parsons, A.N., Seastedt, T.R., and Turner, P.L. (1999) Long-term experimental manipulation of winter snow regime and summer temperature in arctic and alpine tundra. Hydrological Processes, 13, 2315-2330.

Walsh, S.J., Butler, D., Allen, T.R., and Malanson, G.P. (1994) Influence of snow patterns and snow avalanches on the alpine treeline ecotone. Journal of Vegetation Science, 5, 657-672.

Walsh, S.J., Evans, T.P., Welsh, W.F., Entwisle, B., and Rindfuss, R.R. (1999) Scale-dependent relationships between population and environment in northeastern Thailand. Photogrammetric Engineering and Remote Sensing, 65, 97-105.

Wang, Y., Davis, F.W., Melack, J.M., Kasischke, E.S., and Christensen, N.L. (1995) The effects of changes in forest biomass on radar backscatter from tree canopies. International Journal of Remote Sensing, 16, 503-513.

Wang, Y., Kasischke, E.S., Melack, J.M., Davis, F.W., and Christensen, N.L. (1994) The effects of changes in loblolly-pine biomass and soil-moisture on ERS-1 SAR backscatter. Remote Sensing of Environment, 49, 25-31.

Way, J., Paris, J., kasischke, E., Slaughter, C., Viereck, L., Christensen, N., Dobson, M.C., Ulaby, F., Richards, J., Milne, A., Sieber, A., Ahern, F.J., Simonett, D., Hoffer, R., Imhoff, M., and Weber, J. (1990) The effect of changing environmental conditions on microwave signatures of forest ecosystems: preliminary results of the March 1988 Alaskan aircraft SAR experiment. International Journal of Remote Sensing, 11, 1119-1144.

Way, J., Rignot, E.J.M., McDonald, K.C., Oren, R., Kwok, R., Bonan, G., Dobson, M.C., Viereck, L.A., and Roth, J.E. (1994) Evaluating the type and state of Alaska taiga forests with imaging radar for use in ecosystem models. IEEE Transactions on Geoscience and Remote Sensing, 32, 353-370.

Wiens, J.A. (1989) Spatial scaling in ecology. Functional Ecology, 3, 385-397.

Wilson, L.L., Tsang, L., Hwang, J.N., and Chen, C.T. (1999) Mapping snow water equivalent by combining a spatially distributed snow hydrology model with passive microwave remote-sensing data. IEEE Transactions on Geoscience and Remote Sensing, 37, 690-704.

Winther, J.G. and Hall, D.K. (1999) Satellite-derived snow coverage related to hydropower production in Norway: present and future. International Journal of Remote Sensing, 20, 2991-3008.

Wisel, C. (1992) Aims and limits of ecological modeling. Ecological Modelling, 63, 1-12.

Wivell, C.E., Steinwand, D.R., Kelly, G.G., and Meyer, D.J. (1992) Evaluation of terrain models for geocoding and terrain correction of sythetic aperture radar (SAR) images. IEEE Transactions on Geoscience and Remote Sensing, 30, 1137-1144.

Wooding, M.G. (1995) Satellite Radar in Agriculture: Experience with ERS-1 ESA Publications Division, Noordwijk, The Netherlands.

Woodward, F.I. (1987) Climate and Plant Distribution Cambridge University Press, Cambridge.

Wu, S.T. (1987) Potential application of multipolarization SAR for pine-plantation biomass estimation. IEEE Transactions on Geoscience and Remote Sensing, 25, 403-409.

Appendix A. Calculation of the Fresnel reflection coefficient

The Fresnel reflection coefficient is effectively the measure of reflectivity given dielectric properties. For vertically polarised (parallel) electromagnetic wave incident on a plane interface between two media, the Fresnel reflection coefficient is calculated in terms of the impedances of two media, Z_1 and Z_2:

$$\Gamma_{\parallel}(\theta) = \frac{Z_2 \cos\theta_2 - Z_1 \cos\theta_1}{Z_2 \cos\theta_2 + Z_1 \cos\theta_1} \qquad \textbf{Equation A.1}$$

(Rees, 2001) equation 3.31.3

or

$$\Gamma_{\parallel}(\theta) = \frac{Z_1 \cos\theta_1 - Z_2 \cos\theta_2}{Z_1 \cos\theta_1 + Z_2 \cos\theta_2} \qquad \textbf{Equation A.2}$$

(Barber & Ledrew, 1994) equation 37

Equations A.1 and A.2 are equivalent if we understand that $r_{\parallel}$ is the *fractional amplitude* and the modulus is usually taken and $r_{\parallel}$ is subsequently squared to obtain *fractional intensity* (Rees, 1999). The impedance is calculated according to Rees (1999) and Barber (1994) equation 34 and 35:

$$Z_i = \frac{1}{\sqrt{\varepsilon_i}} \qquad \textbf{Equation A.3}$$

where ε_i is the dielectric constant. Equation A.3 is equivalent to[1]:

$$Z_i = \frac{\sqrt{\varepsilon_i}}{\varepsilon_i} \qquad \textbf{Equation A.4}$$

The value of $\cos\theta_2$ is generally given as in Barber (1994) equation 36:

$$\cos\theta_2 = \sqrt{1 - \frac{\varepsilon_1}{\varepsilon_2} \cdot \sin^2\theta_1} \qquad \textbf{Equation A.5}$$

[1] Using mathematical surd theory

In many cases it is assumed that the first medium Z_1 (air) has a dielectric constant (ε_1) equal to 1 (Rees, 2001), which means that equation can be simplified:

$$\cos\theta_2 = \sqrt{1 - \frac{1}{\varepsilon_2} \cdot \sin^2\theta_1} \qquad \textbf{Equation A.6}$$

$$= \sqrt{1 - \frac{\sin^2\theta_1}{\varepsilon_2}} \qquad \textbf{Equation A.7}$$

We can then insert equation A.4 and A.7 into the general Fresnel reflection equation, A.1:

$$r_{\parallel}(\theta_1) = \frac{\frac{\sqrt{\varepsilon_2}}{\varepsilon_2} \cdot \sqrt{1 - \frac{\sin^2\theta_1}{\varepsilon_2}} - \cos\theta_1}{\frac{\sqrt{\varepsilon_2}}{\varepsilon_2} \cdot \sqrt{1 - \frac{\sin^2\theta_1}{\varepsilon_2}} + \cos\theta_1} \qquad \textbf{Equation A.8}$$

$$= \frac{\frac{1}{\varepsilon_2} \cdot \sqrt{\varepsilon_2 \cdot \left(1 - \frac{\sin^2\theta_1}{\varepsilon_2}\right)} - \cos\theta_1}{\frac{1}{\varepsilon_2} \cdot \sqrt{\varepsilon_2 \cdot \left(1 - \frac{\sin^2\theta_1}{\varepsilon_2}\right)} + \cos\theta_1} \qquad \textbf{Equation A.9}$$

$$= \frac{\frac{1}{\varepsilon_2} \cdot \sqrt{\varepsilon_2 - \sin^2\theta_1} - \cos\theta_1}{\frac{1}{\varepsilon_2} \cdot \sqrt{\varepsilon_2 - \sin^2\theta_1} + \cos\theta_1} \qquad \textbf{Equation A.10}$$

$$= \frac{\sqrt{\varepsilon_2 - \sin^2\theta_1} - \varepsilon_2\cos\theta_1}{\sqrt{\varepsilon_2 - \sin^2\theta_1} + \varepsilon_2\cos\theta_1} \qquad \textbf{Equation A.11}$$

Appendix B. Visual Basic program of combined backscatter model.

```
Option Explicit
'--------------------------------------------------------------------------------
'Combined backscatter model for microwave scatter from a snowpack
'Snow surface - Scalar model
'Snow volume - Rayleigh based cloud model
'Ground surface - Kirchhoff Geometric Optics model
'See Chapter 8 in thesis for physical basis of the models and references
'By Andy Dean 2003!
--------------------------------------------------------------------------------
    ' System and math constants
  Const pi As Single = 3.14159265
  Const wavelength As Single = 0.0565
  Const wavenumber As Single = 111.21
    ' Output filename details
  Dim outputpath As String
  Dim filename As String

    ' Incidence angle
  Dim t As Integer
  Dim X As Integer
  Dim trad(81) As Single
    ' Refracted incidence angle
  Dim cosRFt(81) As Single
  Dim RFt(81) As Single

    ' SNOW variables
    'dielctric constants
  Dim SnowDCreal As Single
  Dim SnowDCimag As Single
  Dim Lsnow As Single
  Dim Hsnow As Single
  Dim Msnow As Single
```

```
Dim Lground As Single
Dim Hground As Single
Dim Mground As Single

Dim dcground As Single

        ' Densities
Const pice As Single = 0.917
Dim psnow As Single

      ' Depth of snowpack
Dim depth As Single
      ' Radius of scatterer
Dim radius As Single
      ' Fractional volume
Dim V As Single
       ' Dielectric mixture model
Dim dielMIX As Single
      ' Extinction coefficient
Dim Kext As Single
      ' Number density of scatterers
Dim NDS As Double
      ' Scatter for single grain
Dim singlegraina, singlegrainb, singlegraint As Single

      ' Penetration depth
Dim pdepth As Single
      ' One-way propagation loss
Dim OneWayLoss(81) As Single
      ' transmissivity
Dim Y(81) As Single

     ' Scalar model total values
Dim scalar(81), scalardB(81) As Double
      ' Total volume backcatter
```

```
    Dim vol(81) As Double
    Dim voldB(81) As Double

        ' Ground surface scatter variables
    Dim validt As Single
    Dim kGO(81) As Double
    Dim kGOdB(81) As Double

        ' Combined total backscatter
    Dim combined(81) As Double
    Dim combineddB(81) As Double
    Dim relativesurface(81) As Double
    Dim relativevol(81) As Double
    Dim relativeground(81) As Doubl

Public Sub combi_Com_Click()
        ' get values from text boxes
Hsnow = Val(Text11.Text)
Lsnow = Val(Text12.Text)

        ' Calculate value of m for snow
Msnow = Sqr(2) * Hsnow / Lsnow
Hground = Val(Text7.Text)
Lground = Val(Text8.Text)

        ' Calculate value of m for ground
Mground = Sqr(2) * Hground / Lground
Text9.Text = CStr(Round(Mground, 3))
Text13.Text = CStr(Round(Msnow, 3))

        ' Output to text boxes
SnowDCreal = Val(Text4.Text)
SnowDCimag = Val(Text5.Text)
dcground = Val(Text10.Text)
radius = Val(Text1.Text)
```

```
psnow = Val(Text2.Text)
depth = Val(Text3.Text)


        ' Derived snow volume values *****************
    V = psnow / pice
    NDS = (3 * V) / (4 * pi * radius ^ 3)
    dielMIX = ((SnowDCreal - 1) / (SnowDCreal + 2)) ^ 2
    pdepth = (wavelength * Sqr(SnowDCreal)) / (2 * pi * SnowDCimag)
    Kext = 1 / pdepth
    singlegraina = 64 * (pi ^ 5) * (radius ^ 6) / (wavelength ^ 4)
    singlegrainb = dielMIX ^ 2
    singlegraint = singlegraina * singlegrainb

        ' Output Filename
    outputpath = "C:\Documents and Settings\Andy\My Documents\VBthesis\"
    filename = Text6.Text

        ' scalar validity information
Call SCALARvalidity

        ' Open the output file
Open outputpath & filename & ".txt" For Output As #1
Print #1, filename & " t refractedt transmissivity onewayloss kGOdB(X) scalardB(X)
voldB(X) combineddB(X) relsurface(X) relvol(X) relground(X)"

        ' Set initial incidence angle to 0
validt = 0
t = 0
' ********** LOOP FOR x array ***********
For X = 0 To 80
            trad(X) = (pi / 180) * t
            Call SCALARsurface
            Call volume
            Call KGOsurface
```

```
        ' for calculating the combined model must find the transmissivity Y
          Y(X) = 1 - (Fresnel(SnowDCreal, trad(X))) ^ 2

          combined(X) = scalar(X) + Y(X) ^ 2 * (vol(X) + (kGO(X) / OneWayLoss(X)
        ^ 2))
          combineddB(X) = (Log(combined(X)) / Log(10)) * 10
          relativesurface(X) = 100 * (scalar(X) / combined(X))
          relativevol(X) = 100 * ((Y(X) ^ 2 * vol(X)) / combined(X))
          relativeground(X) = 100 * ((Y(X) ^ 2 * kGO(X) / OneWayLoss(X) ^ 2) /
        combined(X))

          Print #1, t, 180 / pi * RFt(X), Y(X) ^ 2, OneWayLoss(X), kGOdB(X),
        scalardB(X), voldB(X), combineddB(X), relativesurface(X), relativevol(X),
        relativeground(X)

          'add 1 to incidence angle for next value in array
          t = t + 1
Next X
Close #1

' K GO Validity to keep it out of loop - no need for repeating this
If wavenumber * Lground > 6 And Lground ^ 2 > 2.76 * Hground * wavelength Then
  Label2.Caption = "Ground roughness values are valid up to " & validt & " degrees"
Else
  Label2.Caption = "Ground roughness values are NOT valid"
End If

End Sub

        'Scalar model
Public Sub SCALARsurface()
Dim n As Integer
Dim nfact As Double
Dim a(81) As Single
```

```
Dim b(81) As Single
Dim c(81) As Single
Dim abtmp1(81), abtmp2(81), absum(81) As Single

a(X) = 4 * (wavenumber ^ 2) * (Hsnow ^ 2) * Cos(trad(X)) ^ 2
b(X) = (wavenumber ^ 2) * (Lsnow ^ 2) * Sin(trad(X)) ^ 2
c(X) = (wavenumber ^ 2) * (Lsnow ^ 2) * Cos(trad(X)) ^ 2

' ********** LOOP FOR VALUES OF N **************************
For n = 1 To 100 Step 1
        ' n fact is the value of n factorial
    nfact = n
    Call Factorial(n, nfact)
    abtmp1(X) = (a(X) ^ n) / (nfact * n)
    abtmp2(X) = Exp(-b(X) / n)

        '// keep adding to sum the total for the loop
    absum(X) = absum(X) + (abtmp1(X) * abtmp2(X))
Next n
' ********* END LOOP FOR VALUES OF N ************************

scalar(X) = c(X) * (Fresnel(SnowDCreal, trad(X))) ^ 2 * Exp(-a(X)) * absum(X)
scalardB(X) = 10 * Log(scalar(X)) / Log(10)

End Sub
    ' Volume model
Public Sub volume()
cosRFt(X) = Sqr(1 - ((Sin(trad(X)) ^ 2) / SnowDCreal))
    ' calculate refracted angle in degrees for text file
If cosRFt(X) = 1 Then
  RFt(X) = 0
Else
  RFt(X) = Atn(-cosRFt(X) / Sqr(-cosRFt(X) * cosRFt(X) + 1)) + 2 * Atn(1)
End If
```

```
        ' calculate other angular dependent variables - using cos of refracted angle
OneWayLoss(X) = Exp(Kext * depth * (1 / cosRFt(X)))
vol(X) = ((NDS * singlegraint * cosRFt(X)) / (2 * Kext)) * (1 - (1 / OneWayLoss(X) ^
2))
voldB(X) = (Log(vol(X)) / Log(10)) * 10

End Sub

        'Ground surface model
Private Sub KGOsurface()
Dim d(81) As Single
Dim e(81) As Single
Dim f(81) As Single

Call KGOvalidity

d(X) = -1 * Tan(RFt(X)) ^ 2
e(X) = 2 * (Mground ^ 2)
f(X) = 2 * (Mground ^ 2) * cosRFt(X) ^ 4

kGO(X) = (Fresnel(dcground, 0) ^ 2) * (Exp(d(X) / e(X)) / f(X))
kGOdB(X) = 10 * Log(kGO(X)) / Log(10)
End Sub

        'Validity
Sub SCALARvalidity()
If Msnow < 0.25 And wavenumber * Lsnow > 6 And Lsnow ^ 2 > 2.76 * Hsnow *
wavelength Then
  Label1.Caption = "The snow roughness parameters are valid"
Else
  Label1.Caption = "The snow roughness parameters are NOT valid"
End If
End Sub

        'Fresnel reflection function
```

```
Public Function Fresnel(DielConst As Single, Ang As Single) As Single
' fresnel formula
Fresnel = Abs((Sqr(DielConst - Sin(Ang) ^ 2) - DielConst * Cos(Ang)) / _
   (Sqr(DielConst - Sin(Ang) ^ 2) + DielConst * Cos(Ang)))
End Function

        'work out factorial of an integer
Public Sub Factorial(n As Integer, nfact As Double)
' j is the counter, which reduces n by 1 until n-j is 1

Dim j As Integer
For j = 1 To (n - 1) Step 1
   nfact = nfact * j
Next j
End Sub

        'Validity for Geometric Optics
Sub KGOvalidity()
' check for validity according to incidence angle _
the value of validt is the angle up to which the model is valid
If wavenumber * Hground * cosRFt(X) > 1.58 Then
validt = X
End If
End Sub

        'Function for log 10
Public Function logbase(thevalue As Double, base As Integer) As Double
logbase = Log(thevalue) / Log(base)
End Function
```

Appendix C. Arc/Info AMLs for snow cover classification

C.1 Snow classification

```
/* Arc/info macro, written by Andy Dean
/* Joatka transition codes for 12th April 1999
/* Macro operates on amplitude ratio image called i.e. ratio from reference image
/* Macro produces a grid called 12-04tm

docell

/* DRY TO FREE
if (12-04dif ge 2) 12-04tm = 3

/* DRY to DRY
else if (12-04dif lt 2 and 12-04dif gt -3) 12-04tm = 1

/* DRY TO WET
else if (12-04dif le -3) 12-04tm = 2

/* CODE TO CHECK IF EVERYTHING CLASSIFIED
else 12-04tm = 20

end
&return
```

```
/* Arc/info macro, written by Andy Dean
/* Joatka Transition codes for 17th May 1999
/* Macro operates on ratio image i.e. ratio from reference image
/* Macro produces a grid called 17-05tm

/* DRY TO DRY
if (12-04tm == 1 and 17-05d lt 2 and 17-05dif gt -3) 17-05tm = 1

/* DRY TO WET
else if (12-04tm == 1 and 17-05dif le -3) 17-05tm = 2

/* DRY TO FREE
else if (12-04tm == 1 and 17-05dif ge 2) 17-05tm = 3

/* WET TO WET
else if (12-04tm == 2 and 17-05dif le -3) 17-05tm = 4

/* WET TO FREE
else if (12-04tm == 2 and 17-05dif ge 2) 17-05tm = 5

/* WET TO DRY
else if (12-04tm == 2 and 17-05dif lt 2 and 17-05dif gt -3) 17-05tm = 6

/* FREE TO FREE
else if (12-04tm == 3 and 17-05dif ge 2) 17-05tm = 7

/* FREE TO WET
else if (12-04tm == 3 and 17-05dif le -3) 17-05tm = 8

/* FREE TO DRY
else if (12-04tm == 3 and 17-05dif lt 2 and 17-05dif gt -3) 17-05tm = 9

/* CODE TO CHECK IF EVERYTHING CLASSIFIED
else 17-05tm = 20

end
&return
```

```
/* Arc/info macro, written by Andy Dean
/* Joatka transition codes for 5th June 1999
/* Macro operates on ratio image i.e. ratio from reference image
/* Macro produces a grid called 05-06tm

docell
/* DRY TO DRY
if (17-05tm == 1 and 05-06dif lt 2 and 05-06dif gt -3) 05-06tm = 1
else if (17-05tm == 6 and 05-06dif lt 2 and 05-06dif gt -3) 05-06tm = 1
else if (17-05tm == 9 and 05-06dif lt 2 and 05-06dif gt -3) 05-06tm = 1

/* dry to wet
else if (17-05tm == 1 and 05-06dif le -3) 05-06tm = 2
else if (17-05tm == 6 and 05-06dif le -3) 05-06tm = 2
else if (17-05tm == 9 and 05-06dif le -3) 05-06tm = 2

/* DRY TO FREE
else if (17-05tm == 1 and 05-06dif ge 2) 05-06tm = 3
else if (17-05tm == 6 and 05-06dif ge 2) 05-06tm = 3
else if (17-05tm == 9 and 05-06dif ge 2) 05-06tm = 3

/* WET TO WET
else if (17-05tm == 2 and 05-06dif le -3) 05-06tm = 4
else if (17-05tm == 4 and 05-06dif le -3) 05-06tm = 4
else if (17-05tm == 8 and 05-06dif le -3) 05-06tm = 4

/* wet to free
else if (17-05tm == 2 and 05-06dif ge 2) 05-06tm = 5
else if (17-05tm == 4 and 05-06dif ge 2) 05-06tm = 5
else if (17-05tm == 8 and 05-06dif ge 2) 05-06tm = 5

/* wet to dry
else if (17-05tm == 2 and 05-06dif gt -3 and 05-06dif lt 2) 05-06tm = 6
else if (17-05tm == 4 and 05-06dif gt -3 and 05-06dif lt 2) 05-06tm = 6
else if (17-05tm == 8 and 05-06dif gt -3 and 05-06dif lt 2) 05-06tm = 6


/* FREE TO FREE
else if (17-05tm == 3 and 05-06dif ge 2) 05-06tm = 7
else if (17-05tm == 5 and 05-06dif ge 2) 05-06tm = 7
else if (17-05tm == 7 and 05-06dif ge 2) 05-06tm = 7

/* FREE TO WET
else if (17-05tm == 3 and 05-06dif le -3) 05-06tm = 8
else if (17-05tm == 5 and 05-06dif le -3) 05-06tm = 8
else if (17-05tm == 7 and 05-06dif le -3) 05-06tm = 8

/* FREE TO DRY
else if (17-05tm == 3 and 05-06dif gt -3 and 05-06dif lt 2) 05-06tm = 9
else if (17-05tm == 5 and 05-06dif gt -3 and 05-06dif lt 2) 05-06tm = 9
else if (17-05tm == 7 and 05-06dif gt -3 and 05-06dif lt 2) 05-06tm = 9

/* CODE TO CHECK IF EVERYTHING CLASSIFIED
else 05-06tm = 20
end
&return
```

```
/* Arc/info macro, written by Andy Dean
/* Joatka transition codes for 21st June 1999
/* Macro operates on ratio image i.e. ratio from reference image
/* Macro produces a grid called 21-06tm

docell
/* DRY TO DRY
if (05-06tm == 1 and 21-06dif gt -3 and 21-06dif lt 2) 21-06tm = 1
else if (05-06tm == 6 and 21-06dif gt -3 and 21-06dif lt 2) 21-06tm = 1
else if (05-06tm == 9 and 21-06dif gt -3 and 21-06dif lt 2) 21-06tm = 1

/* DRY TO WET
else if (05-06tm == 1 and 21-06dif le - 3) 21-06tm = 2
else if (05-06tm == 6 and 21-06dif le - 3) 21-06tm = 2
else if (05-06tm == 9 and 21-06dif le - 3) 21-06tm = 2

/* DRY TO FREE according to +2db rule
else if (05-06tm == 1 and 21-06dif ge 2) 21-06tm = 3
else if (05-06tm == 6 and 21-06dif ge 2) 21-06tm = 3
else if (05-06tm == 9 and 21-06dif ge 2) 21-06tm = 3

/* WET TO WET
else if (05-06tm == 2 and 21-06dif le -3) 21-06tm = 4
else if (05-06tm == 4 and 21-06dif le -3) 21-06tm = 4
else if (05-06tm == 8 and 21-06dif le -3) 21-06tm = 4

/* WET TO FREE
else if (05-06tm == 2 and 21-06dif ge 2) 21-06tm = 5
else if (05-06tm == 4 and 21-06dif ge 2) 21-06tm = 5
else if (05-06tm == 8 and 21-06dif ge 2) 21-06tm = 5

/* WET TO DRY
else if (05-06tm == 2 and 21-06dif gt -3 and 21-06dif lt 2) 21-06tm = 6
else if (05-06tm == 4 and 21-06dif gt -3 and 21-06dif lt 2) 21-06tm = 6
else if (05-06tm == 8 and 21-06dif gt -3 and 21-06dif lt 2) 21-06tm = 6


/* FREE TO FREE
else if (05-06tm == 3 and 21-06dif ge 2) 21-06tm = 7
else if (05-06tm == 5 and 21-06dif ge 2) 21-06tm = 7
else if (05-06tm == 7 and 21-06dif ge 2) 21-06tm = 7

/* FREE TO WET
else if (05-06tm == 3 and 21-06dif le -3) 21-06tm = 8
else if (05-06tm == 5 and 21-06dif le -3) 21-06tm = 8
else if (05-06tm == 7 and 21-06dif le -3) 21-06tm = 8

/* FREE TO DRY
else if (05-06tm == 3 and 21-06dif gt -3 and 21-06dif lt 2) 21-06tm = 9
else if (05-06tm == 5 and 21-06dif gt -3 and 21-06dif lt 2) 21-06tm = 9
else if (05-06tm == 7 and 21-06dif gt -3 and 21-06dif lt 2) 21-06tm = 9

/* CODE TO CHECK IF EVERYTHING CLASSIFIED
else 21-06tm = 20

end
&return
```

C.2 Recode snow cover

```
/* Arc/info macro, written by Andy Dean
/* Joatka – recoding of transition codes to dry, wet, free snow cover
/* creates grids with suffix r to denote recoded

12-04r = reclass(12-04tm, recodesnow.rmp, data)
17-05r = reclass(17-05tm, recodesnow.rmp, data)
05-06r = reclass(05-06tm, recodesnow.rmp, data)
21-06r = reclass(21-06tm, recodesnow.rmp, data)

&return
```

Remap file <recodesnow.rmp> shown below:

```
1 : 1
2 : 2
3 : 3
4 : 2
5 : 3
6 : 1
7 : 3
8 : 2
9 : 1
```

C.3 Temporal consistency

```
/* Arc/info macro, written by Andy Dean
/* Joatka temporal consistency rules

/* Start with grid 21-06r
docell
if (17-05r == 2 and 21-06r == 1) 21-06final  = 3
else if (05-06r == 2 and 21-06r == 1) 21-06final  = 3
else 21-06final  = 21-06r
end

/* next do 05-06
docell
if (17-05r == 2 and 05-06r == 1) 05-06final  = 1
else if (05-06r == 3 and 21-06final  ne 3) 05-06final  = 1
else 05-06final  = 05-06r
end

/* then do 17-05
docell
if (17-05r == 3 and 05-06final  ne 3) 17-05final  = 1
else 17-05final  = 17-05r
end

/* and finally 12-04
docell
if (12-04r == 3 and 17-05final  ne 3) 12-04final  = 1
else 12-04final  = 12-04r
end

&return
```

Appendix D. Snow maps at Joatka and Dovrefjell

D.1 Joatka

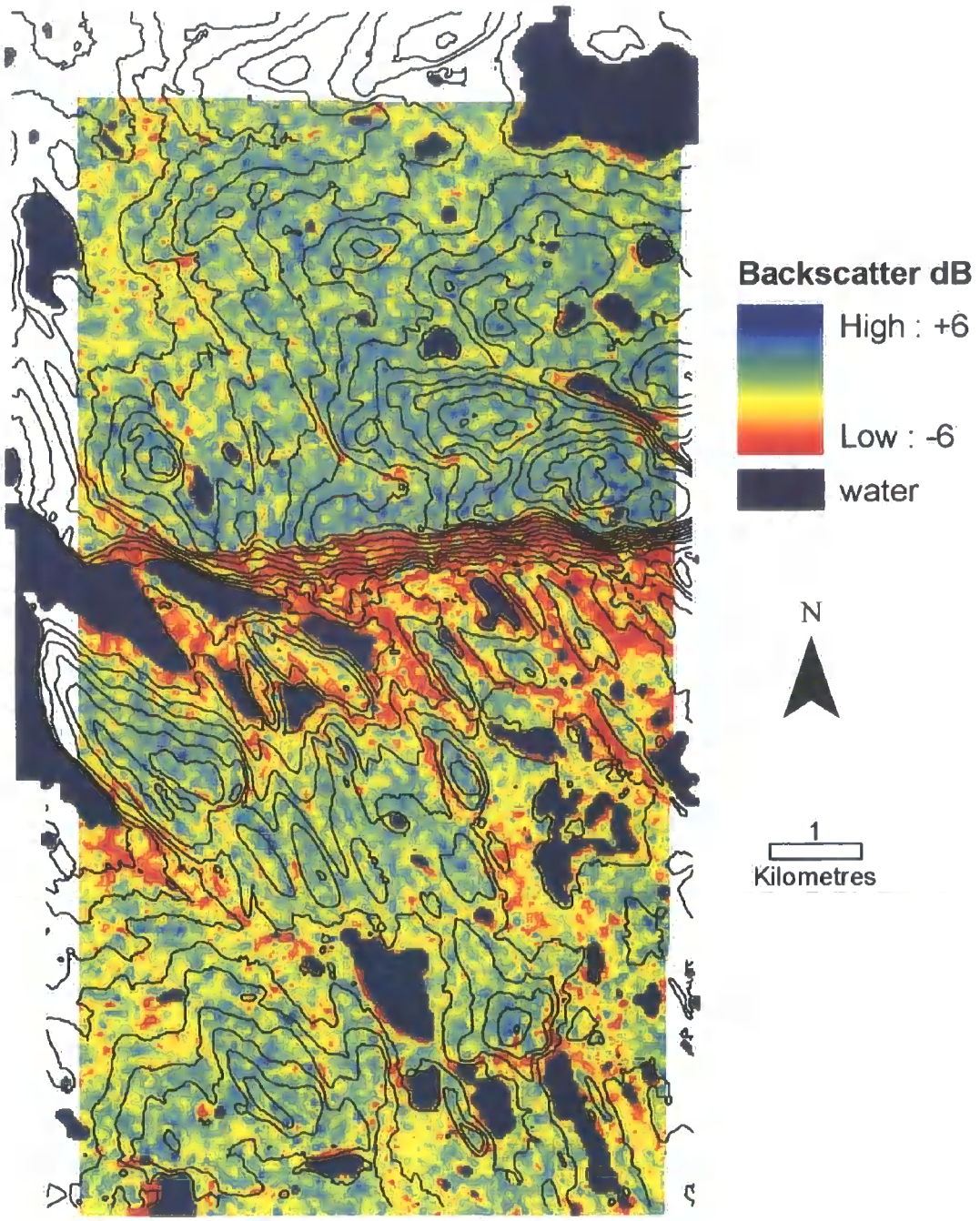

Figure D.1. Difference in backscatter at Joatka on 17th May.

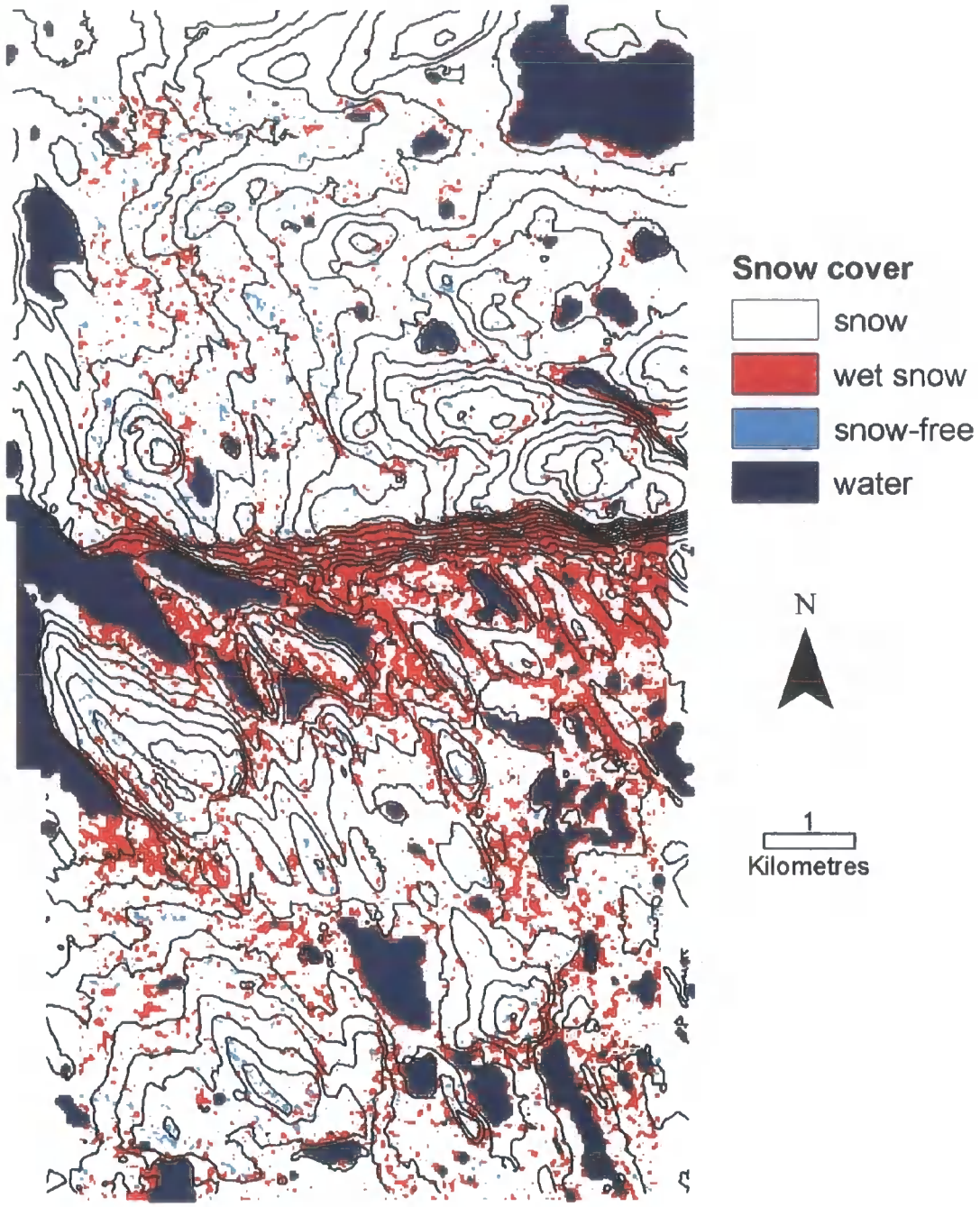

Figure D.2. Snow map at Joatka on 17th May.

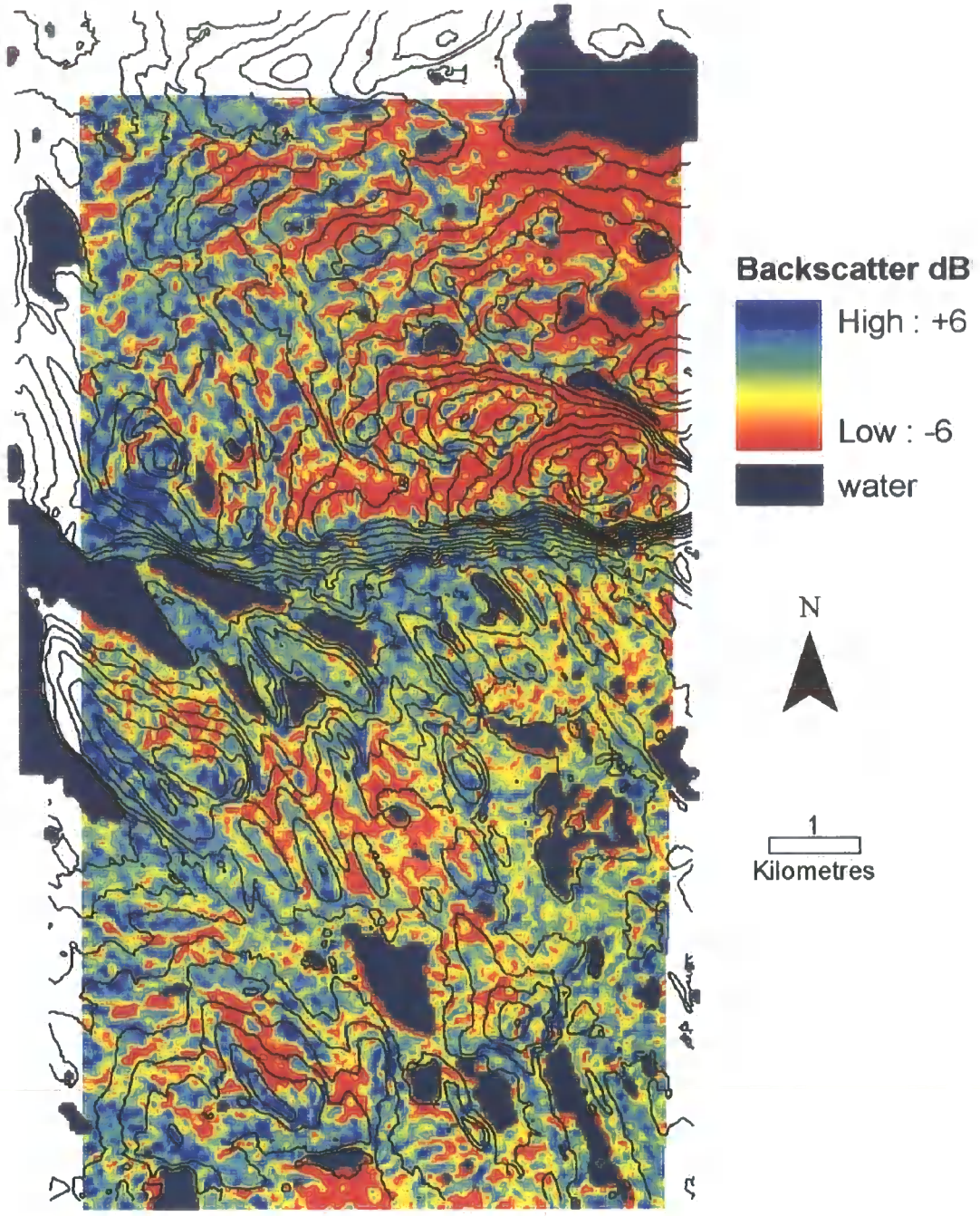

Figure D.3. Difference in backscatter at Joatka on 5th June.

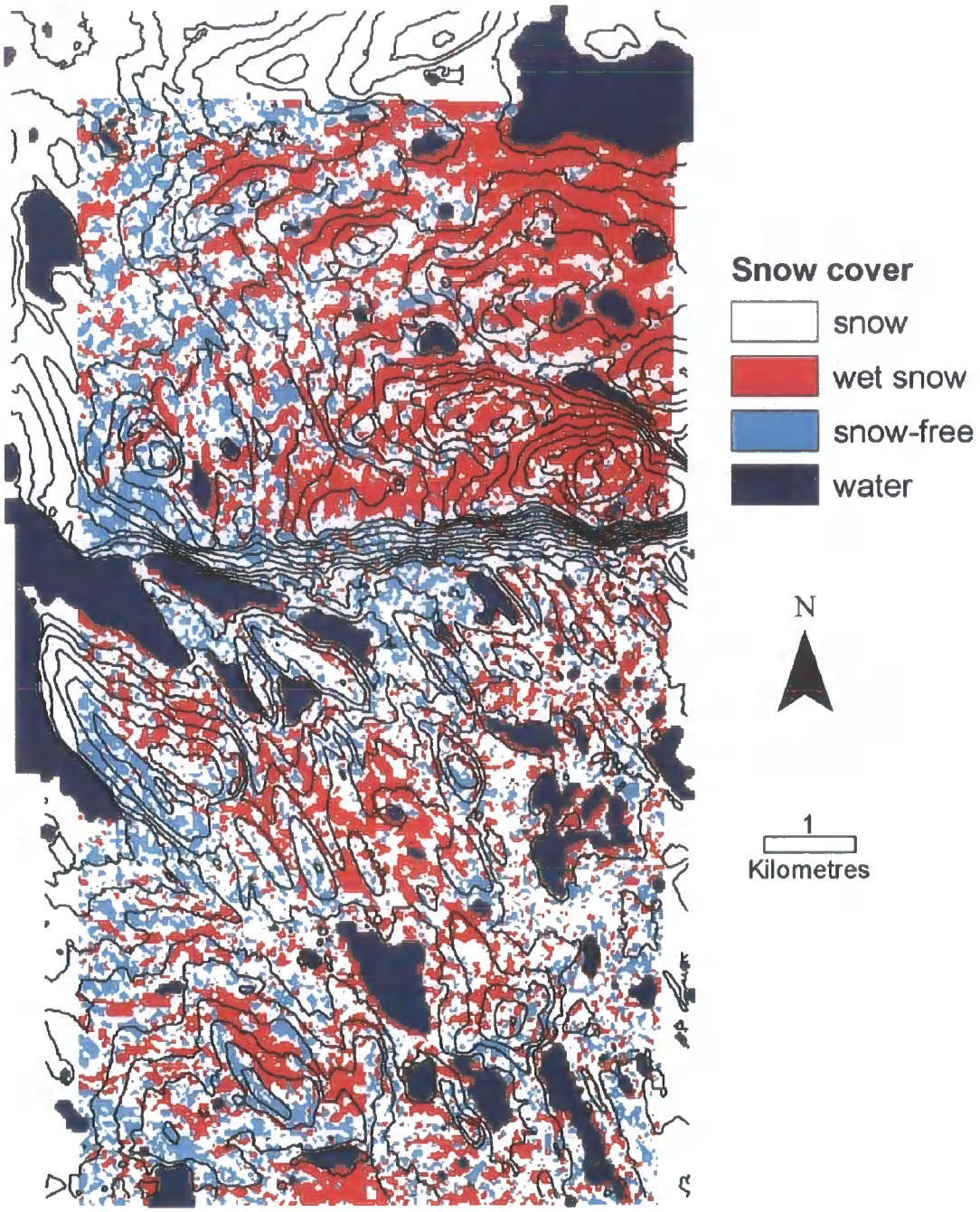

Figure D.4. Snow map at Joatka on 17th May

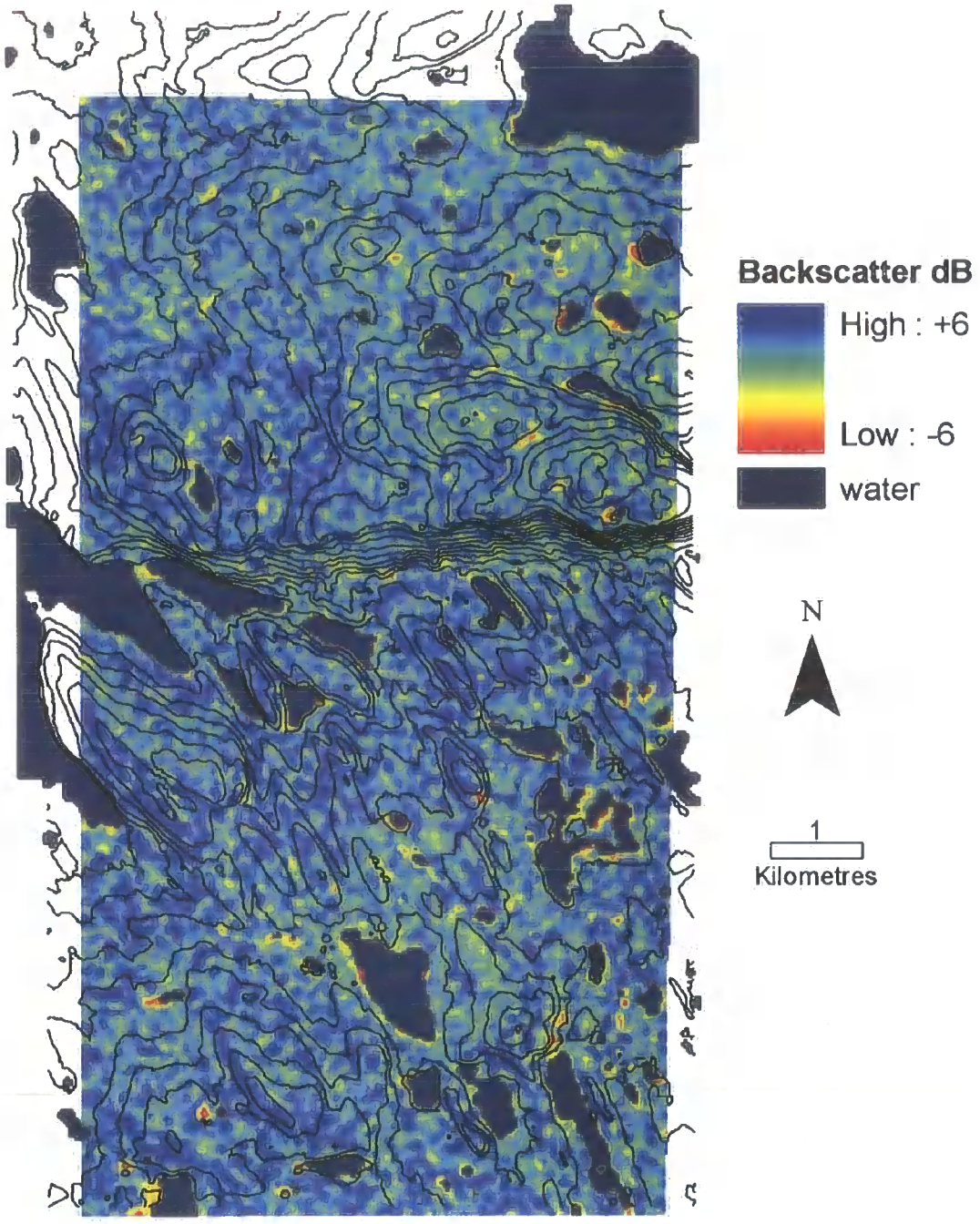

Figure D.5. Difference in backscatter at Joatka on 21st June.

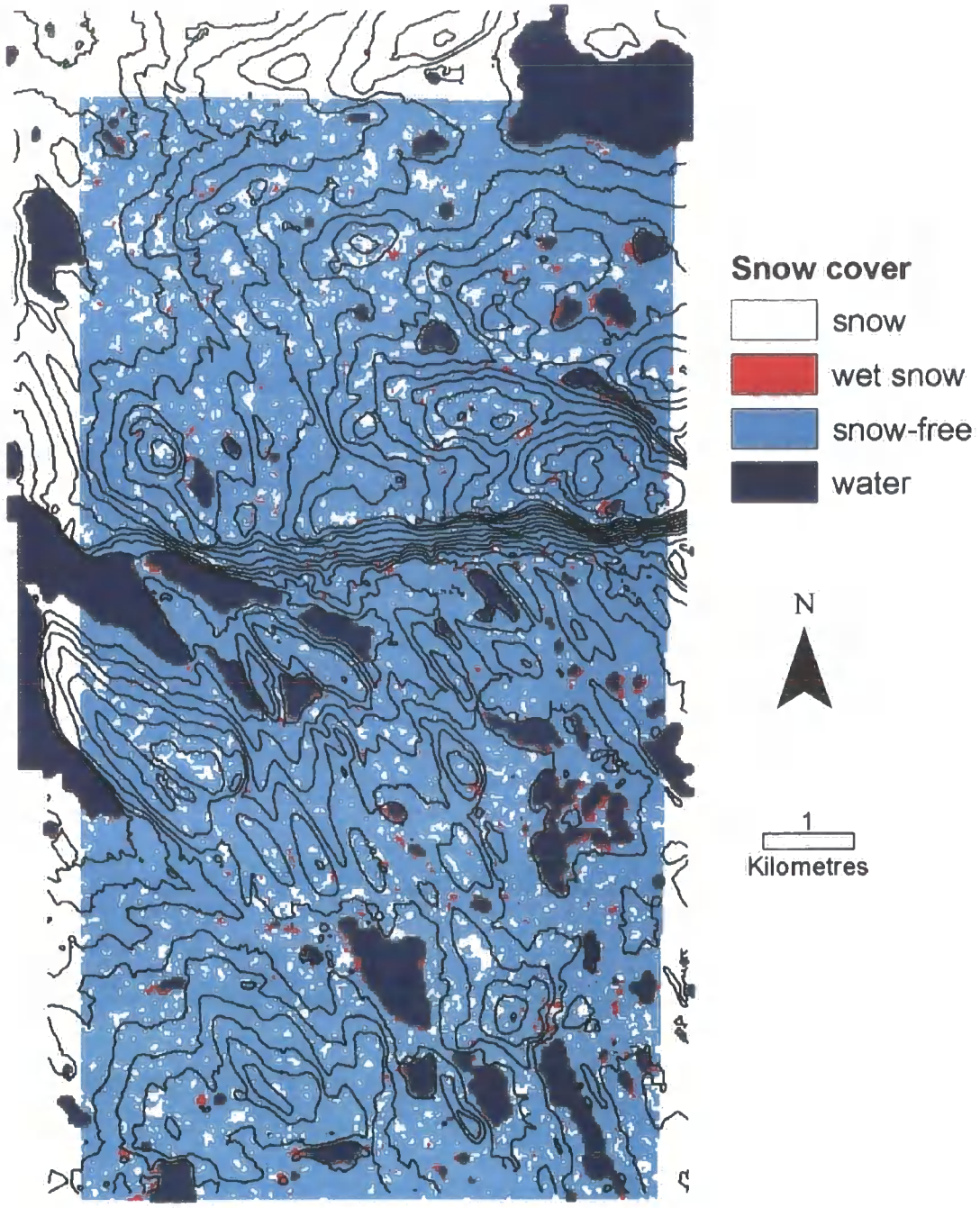

Figure D.6. Snow map at Joatka on 21st June.

D.2 Dovrefjell

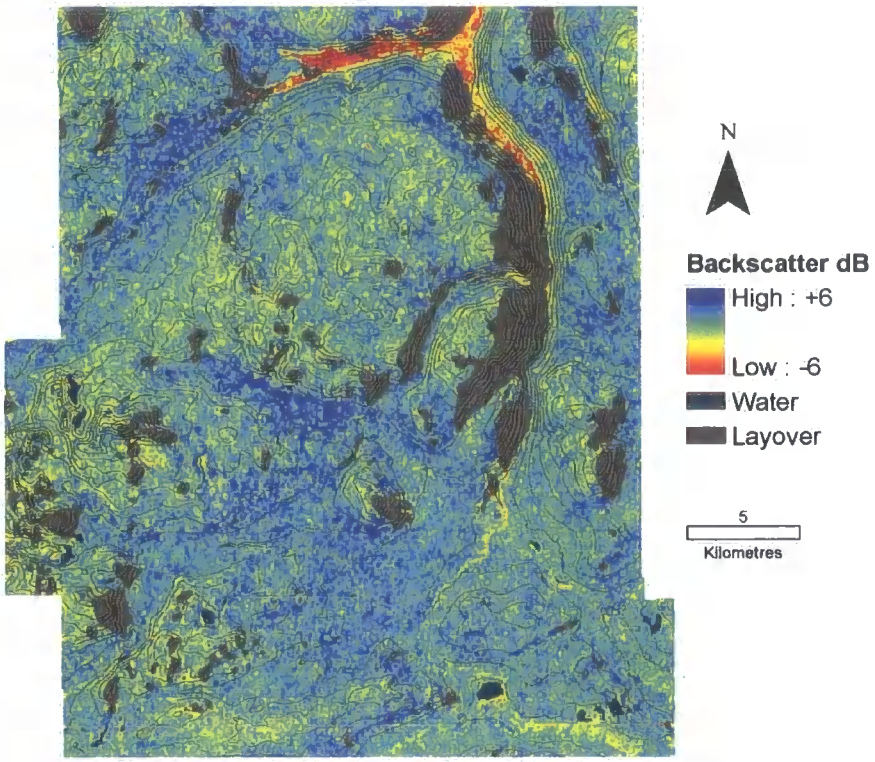

Figure D.7. Difference in backscatter at Dovrefjell on 14th April.

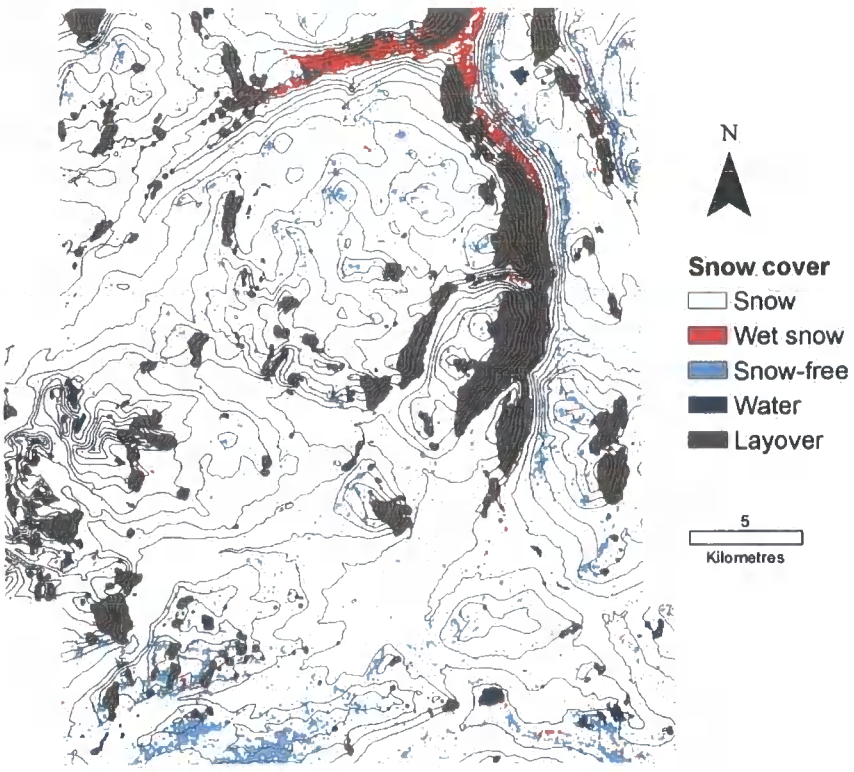

Figure D.8. Snow map at Dovrefjell 14th April.

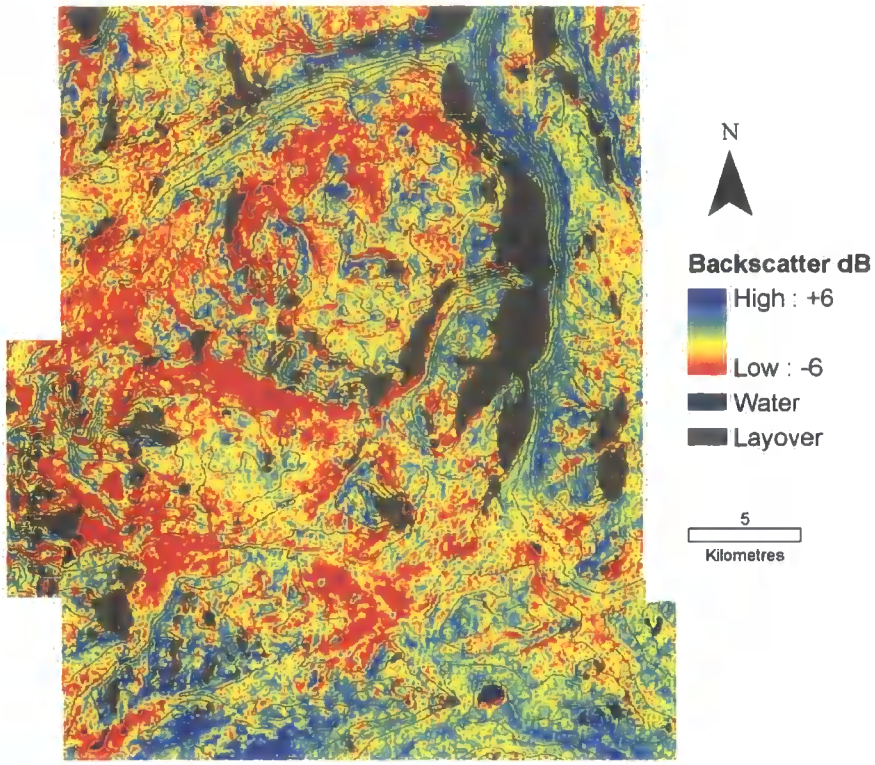

Figure D.9. Difference in backscatter at Dovrefjell on 3rd May.

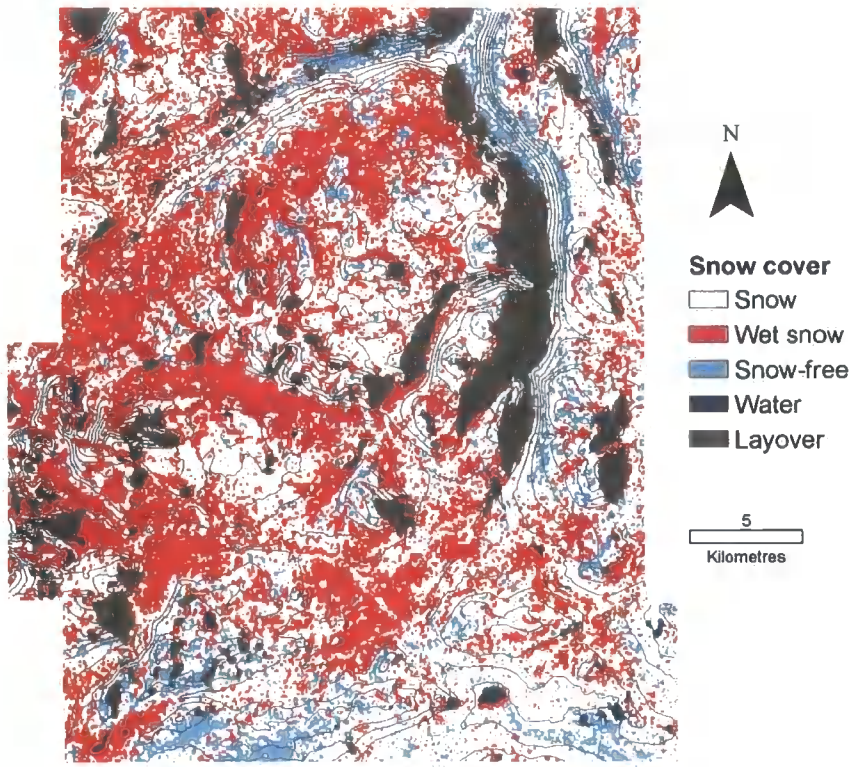

Figure D.10. Snow map at Dovrefjell 3rd May.

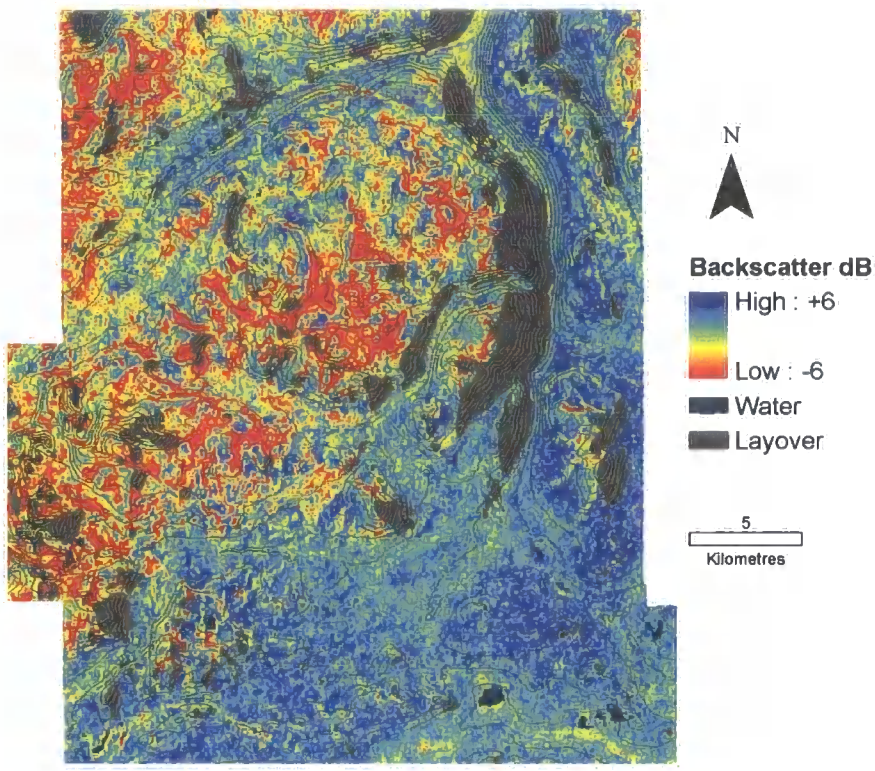

Figure D.11. Difference in backscatter at Dovrefjell on 19th May

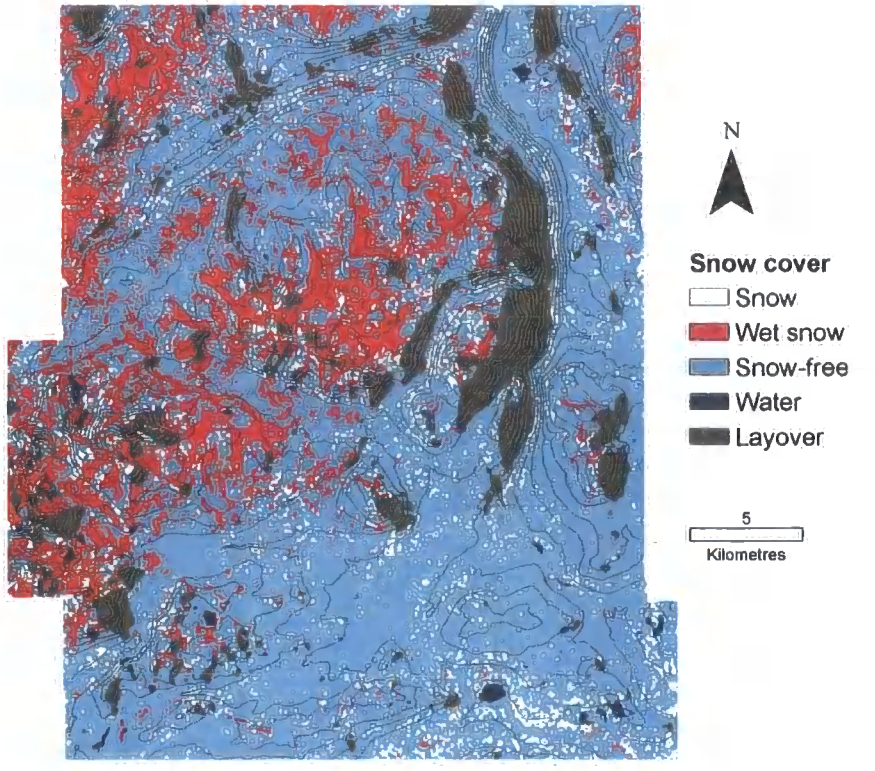

Figure D.12. Snow map at Dovrefjell 19th May.

Appendix E. Calculation of a semivariogram

The Arc/Info KRIGING command implements ordinary kriging and can fit the SPHERICAL, CIRCULAR, EXPONENTIAL, GAUSSIAN and LINEAR models. The aim is not interpolation because we have gridded data, but to use the semivariogram to evaluate the spatially dependent variation in the data. Ordinary Kriging assumes that the variation in z values is free of any structural component (drift).

E.1 Methodology

Example for creating semivariogram for Joatka **elevation** grid:

1. Convert grid to point file using GRIDPOINT

   elevlattice = GRIDPOINT (**elevation**, **item**)

where **item** is the input grids z value (attribute) that will be stored in the output point coverage.

2. Complete Kriging operation. Specify that only that the GRAPH (the semivariogram) will be produced and not the interpolation to save computational time:

   elev-file = KRIGING(**elevlattice**, item, #, GRAPH, #, SPHERICAL, RADIUS, 300, #, 30)

   This creates an Info table called **elev-file.svg**, which can be viewed in Arcplot.

3. In Arcplot and use display the semivariogram:

   SEMIVARIOGRAM **elev-file.svg**

Use Arc/Info TABLES to export (unload) the information from the Info table to a comma separated ASCII file. This can then be imported into Microsoft Excel and an appropriate model fitted using data generated by the Kriging function or experimentation.